Towards motion-insensitive Arterial Spin Labeling perfusion imaging

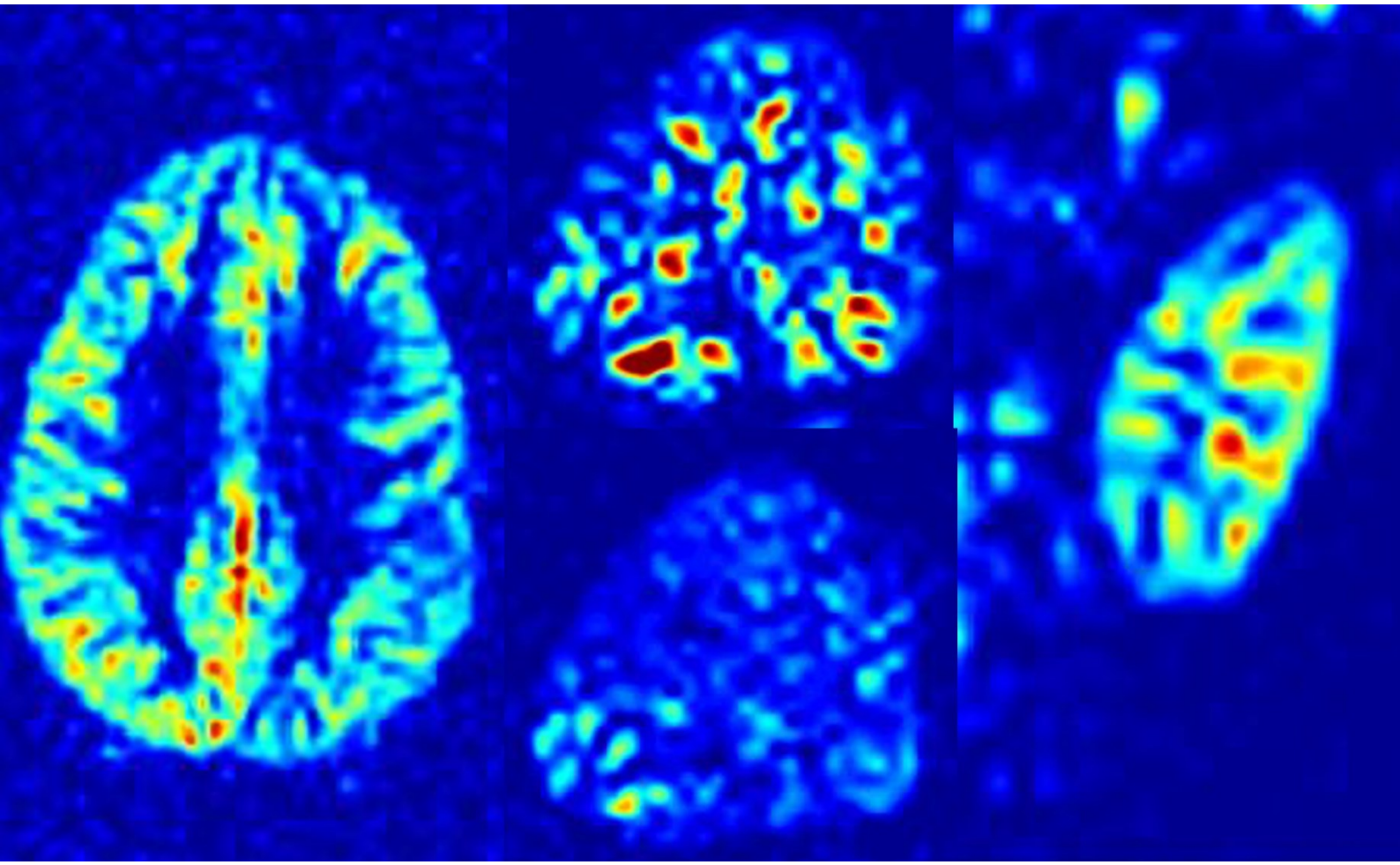

Jörn Huber

Fraunhofer MEVIS

Universität Bremen

Towards motion-insensitive Arterial Spin Labeling perfusion imaging

Dissertation

submitted to the Faculty of Physics

University of Bremen, Germany

for the degree of

Doctor of Natural Sciences (Dr. rer. Nat.)

Jörn Huber

Referees:

Prof. Dr. Matthias Günther

Prof. Dr. Oliver Speck

Date of defense: 31.03.2022

Bremen

Abstract

Perfusion measurements in brain and liver are of high clinical interest. While changes in brain perfusion can by an indicator for neurological diseases such as stroke or Alzheimer's disease, changes in liver perfusion might be correlated with the presence of cirrhosis. In both organs, tumors can also be identified by an increase of perfusion in affected areas. Arterial spin labeling (ASL) magnetic resonance imaging (MRI) has the potential to be an alternative to invasive measurements of perfusion using contrast agent-based techniques. However, the clinical application of ASL is currently limited. This is primarily due to the fact of intrinsically low SNR in perfusion-weighted images, which is especially problematic in liver with low perfusion rates. As a result, long scan times are required, which increase the sensitivity to subject motion. Unfortunately, motion during clinical scans is common and some sources of motion, such as respiration, are almost unavoidable. The goal of this thesis is to develop novel methods which address the motion sensitivity of ASL sequences.

The developed techniques include novel optimized approaches for background suppression, an automatic detection of breathholds during ASL experiments to suppress respiratory motion artifacts, prospective correction of respiratory motion during free-breathing scans as well as three-dimensional retrospective motion correction using a 3D GRASE PROPELLER (3DGP) readout. In addition, a novel 3DGP reconstruction, allowing joint estimation of motion and geometric distortion, is presented. Algorithms are implemented and validated in brain and liver ASL perfusion imaging using healthy volunteers. Finally, recommendations for future improvements of the developed techniques are given.

Contents

General Introduction and Outline

The correct function of the human body heavily depends on the distribution of blood to different types of tissue and organs. The blood fulfills different tasks, such as the distribution of nutrients, the defense from external threats (e.g., bacteria) or the regulation of the body temperature (1). Consequently, many diseases often entail a change in blood supply. Tumorous tissue typically shows a fast rate of growth. The high demand for nutrients and oxygen results in an increased blood supply to the affected region. Other examples are diseases like stroke, Alzheimer's, and liver cirrhosis, which are all accompanied with changes in the blood supply (2)(3)(4). The assessment of the so-called tissue perfusion in brain and liver, which describes the volume of blood flowing through a fixed amount of tissue, is therefore of high clinical interest.

Different methods exist which allow measurement of perfusion (5)(6)(7). Among those methods, perfusion measurements using magnetic resonance imaging achieve a high spatial resolution without ionizing radiation, making it an attractive imaging modality. Typically, the assessment of perfusion using MRI is based on local signal variation as induced by exogenous contrast agents, which were injected prior to the imaging experiment. Unfortunately, these contrast agents are not applicable to subjects with certain diseases. One such example is renal failure (8). Therefore, the potential of non-invasive assessment of tissue perfusion using arterial spin labeling (ASL) MRI as an alternative to contrast agent-based methods began to increase since the early 1990s (9).

In ASL perfusion imaging, inflowing blood is magnetically inverted, making it an endogenous tracer. This results in a so-called label image. The perfusion-weighted information is revealed by subtracting the label image from a control image without blood inversion. Since no contrast agents accumulate in the blood, ASL is suited for repetitive measurements. Although the technique was first described almost 30 years ago, the application of ASL to routine imaging in clinics is still restricted. This especially holds for liver, which shows lower perfusion rates compared to brain. The main reason is the intrinsically low SNR in perfusion-weighted ASL images. Low SNR makes it necessary to average several measurements, which are acquired over a long period of scan time. These long scan times in combination with the subtractive nature result in a high sensitivity to

e.g., random or respiratory subject motion during the scan, which potentially cause strong artifacts in images, making them unusable for diagnostic purposes. The motion sensitivity of ASL is a major factor which currently restricts the general applicability in clinical environments. Hence, the motivation of this thesis is the development of novel techniques for compensation of motion related artifacts in ASL perfusion-weighted images. Novel approaches for improved background suppression, motion correction using 3D GRASE PROPELLER readouts and strategies especially designed for compensation of respiratory motion in abdominal ASL imaging are introduced in Part II of this thesis. Developed techniques are validated in brain and liver ASL imaging using healthy volunteers and a general discussion is finally given.

Outline

Part I introduces fundamental concepts which are needed to understand the novel methods presented in this work.

Chapter 1 gives closer insights into physiological processes in the human body. More precisely, the function of blood and the vascular system as well as key parameters of the perfusion process are reviewed.

Chapter 2 introduces the basic concepts of magnetic resonance imaging in terms of the generation and relaxation of measurable MRI signal as well as spatial image encoding and the principle of adiabatic inversion. Together, these are the fundamental components of ASL perfusion imaging.

Chapter 3 reviews the basic concepts of perfusion measurement using ASL. Furthermore, selected imaging techniques which are applied in this work are briefly discussed.

Part II contains the description and evaluation of novel techniques for motion compensation in ASL perfusion imaging.

Chapter 4 describes the motivation and technical implementation of novel algorithms.

First, novel techniques for background suppression in ASL imaging are introduced. In section 4.1.2, an **optimized fixed background suppression scheme** is proposed. The algorithm allows selective suppression of short T_1 components corresponding to off-resonant fat, while keeping a residual positive on-resonant magnetization of the organ of interest. The algorithm is designed for application in combination with additional motion compensation techniques. In addition, the implementation of an **adaptive background suppression scheme** is described in section 4.1.3. The adaptive background suppression algorithm first estimates and then reduces the magnetization of the actual T_1 spectrum in the region of interest.

Next, novel algorithms for retrospective motion correction in ASL imaging using a 3D GRASE PROPELLER (3DGP) readout are introduced. In section 4.2.2, theory and

implementation of a novel 3DGP image reconstruction algorithm, allowing **joint estimation of in-plane motion and geometric distortion using 3DGP,** are demonstrated. Subsequently, a novel image space-based **estimation and correction of three-dimensional rigid body motion using 3DGP** is presented in section 4.2.3.

Finally, customized solutions for compensation of respiratory motion in liver ASL imaging are presented. In section 4.3.2, the **multi-breathhold technique** is introduced, which allows subjects to personally decide about timepoint and duration of subsequent breathholds during examinations. In addition, the implementation of **a novel technique for prospective compensation of respiratory motion using navigator matching** is described in section 4.3.3, which aims for correction of motion artifacts in free-breathing liver ASL examinations.

Chapter 5 applies and evaluates the novels methods for motion compensation in brain and liver ASL imaging.

As a prerequisite for effective background suppression in ASL imaging, section 5.1.1 describes and evaluates optimal parameters for frequency offset corrected inversion (FOCI) pulses, yielding high inversion efficiencies in both abdominal and brain ASL experiments.

The adaptive background suppression is evaluated in a phantom and brain ASL imaging using two healthy volunteers in section 5.1.2.

Section 5.2.1 covers evaluation of joint estimation of in-plane motion and geometric distortion using 3DGP in brain ASL imaging in combination with the optimized fixed background suppression scheme in a study using five healthy volunteers.

The feasibility of three-dimensional rigid body motion estimation and correction using 3DGP is initially demonstrated in a healthy volunteer in section 5.2.2.

Section 5.3.1 evaluates the multi-breathhold technique for compensation of respiratory motion in combination with the optimized fixed BS scheme in liver ASL experiments of a healthy volunteer.

Finally, section 5.3.2 analyzes the performance of the prospective respiratory motion compensation in liver ASL imaging in combination with the optimized fixed BS scheme in a study using eight healthy volunteers.

Chapter 6 includes a general discussion of the novel techniques and gives a recommendation for future work in the field of motion compensation in ASL perfusion imaging.

Part I

Basic Concept

1 Perfusion and Physiology

Besides changes in the structure of tissue, many diseases manifest themselves in changes of the rate of blood supply to the affected organ or region. These changes can be an important indicator for e.g., stroke, where parts of the brain can be cut from the supply with fresh blood, which is a life-threatening condition (2)(10). Here, assessment of tissue perfusion can deliver valuable information, before changes in the underlying tissue structure might be detected. Perfusion measurements further have the potential as a biomarker in neurodegenerative diseases, such as Alzheimer's, being important for classification of disease progression (3). Besides the potential in neurological diseases, perfusion measurements can also add valuable information for certain liver diseases, such as cirrhosis (11)(12). Cirrhosis describes a chronic liver disease, distorting the hepatic vasculature, which in turn shows as a change in the global perfusion rate (13). If not detected or treated, cirrhosis shows a high lethality. Cirrhosis can also result in the development of liver cancer, which shows overall low survival rates (14). Tumors usually show high demands for arterial blood due to the higher growth rate when compared to healthy tissue. Therefore, tumors are likely to show higher perfusion when compared to healthy surrounding tissue (15), indicating the potential of perfusion measurement for early cancer detection in liver. The same holds for brain tumors such as glioblastomas (16). Perfusion measurement in brain and liver is therefore an ongoing interest with high potential for clinics.

The following sections will give a brief overview over the perfusion processes in both organs. Afterwards, the most important perfusion related parameters are defined, and techniques are introduced which allow to assess the perfusion of tissue.

1.1 Blood, Vascular System and Perfusion

The following description is based on Anatomy & Physiology from the OpenStax College (1). The main job of blood is to deliver oxygen and remove waste from perfused tissue. In addition, blood plays an important role in the regulation of body temperature. Blood is a solution of different components, majorly consisting of so-called plasma, which is composed of water, proteins, hormones etc. The hematocrit, consisting of red blood cells,

represents the second major compartment of blood. Finally, a small fraction of the blood consists of white blood cells and platelets. Taken together, these ingredients make blood a red, viscous fluid. In order to fulfill its purpose, blood needs to be distributed to all parts of the human body. Therefore, a widely branched system of arteries exists, which finally end into smaller microvascular vessels, distributing the oxygen-enriched blood. Blood, carried by arteries, flows away from the heart. In contrast, veins carry blood whose oxygen has already been delivered to cells, and it needs to be enriched in the lungs again. The largest artery in the human body is the aorta, directly exiting the heart. From there, the blood takes different routes to reach body parts with different organs. This work focusses on brain and liver perfusion measurements. The blood supplies of both organs are therefore subsequently described.

1.1.1 Brain Perfusion

Arterial and venous blood supplies of the human brain are shown in Figure 1.1 and Figure 1.2. Coming from the heart, blood travels through the ascending aorta until it reaches the aortic arch, which is connected to the right and left carotid arteries, from where the blood finally reaches the brain. The size of the arteries decreases with increased distance from the heart. Finally, the blood reaches so-called arterioles, which are only about 30 micrometers in diameter. From there, the blood first enters so-called metarterioles before it finally enters the capillary bed, which supplies the blood to the surrounding tissue. Here, the important exchange of substances between blood and the surrounding cells occurs, which is known as perfusion. From the capillary bed, the blood enters distributed venules, which are again only a couple of micrometers in diameter. Many venules finally form a vein, which transports the blood to the heart again. The process of perfusion is visualized in Figure 1.3.

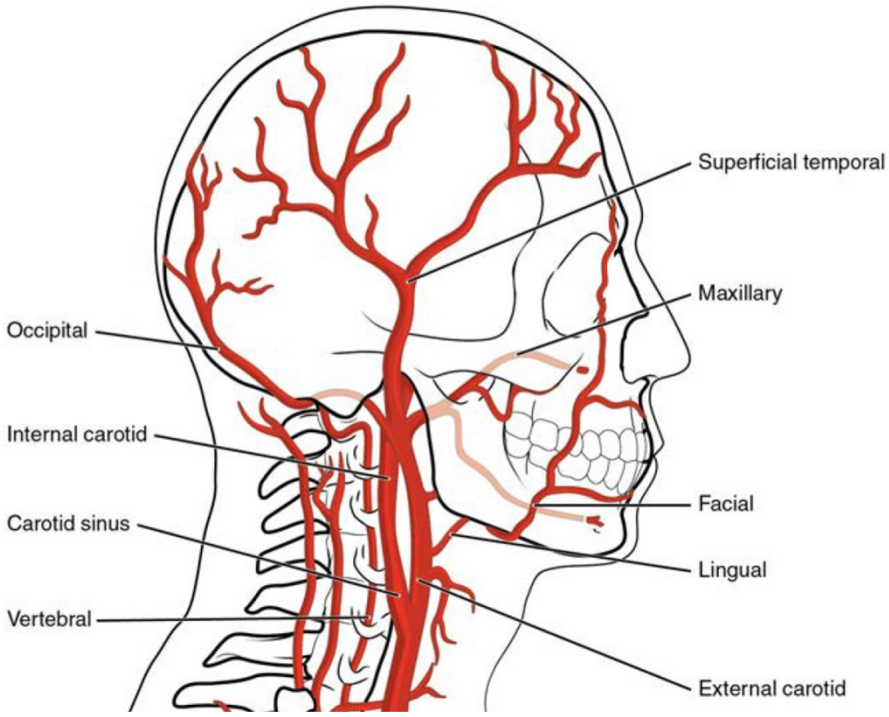

Figure 1.1: Arterial blood supplies of the human brain. The graphic was adapted based on illustrations from Open-Stax College – Anatomy and Physiology (1), which is licensed under CC BY 4.0[1].

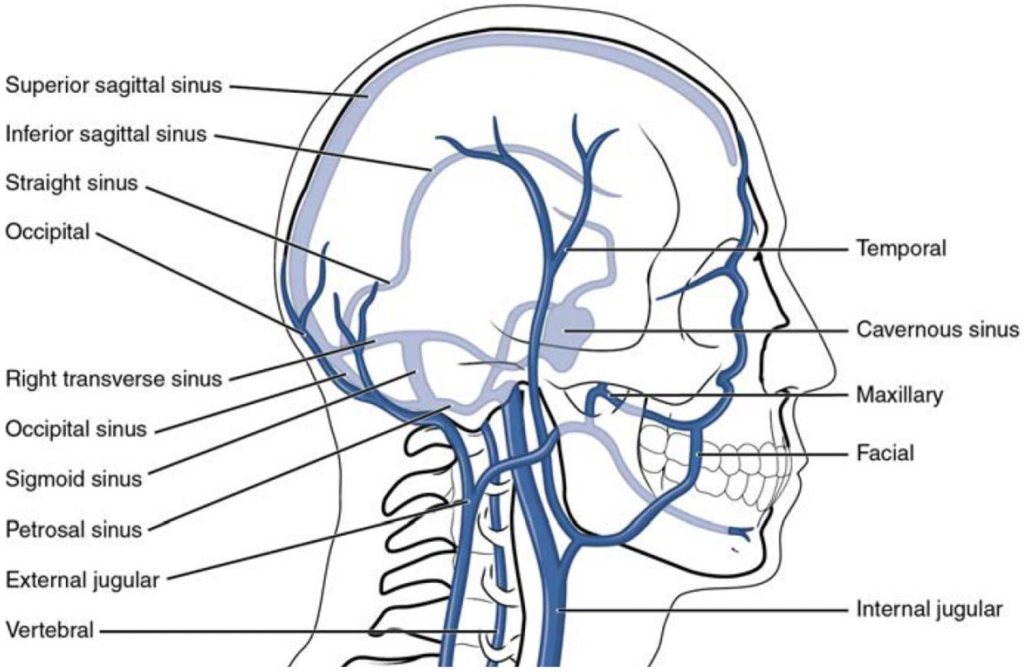

Figure 1.2: Venous blood supplies of the human brain. The graphic was adapted based on illustrations from Open-Stax College – Anatomy and Physiology (1), which is licensed under CC BY 4.0[1].

[1] https://creativecommons.org/licenses/by/4.0/

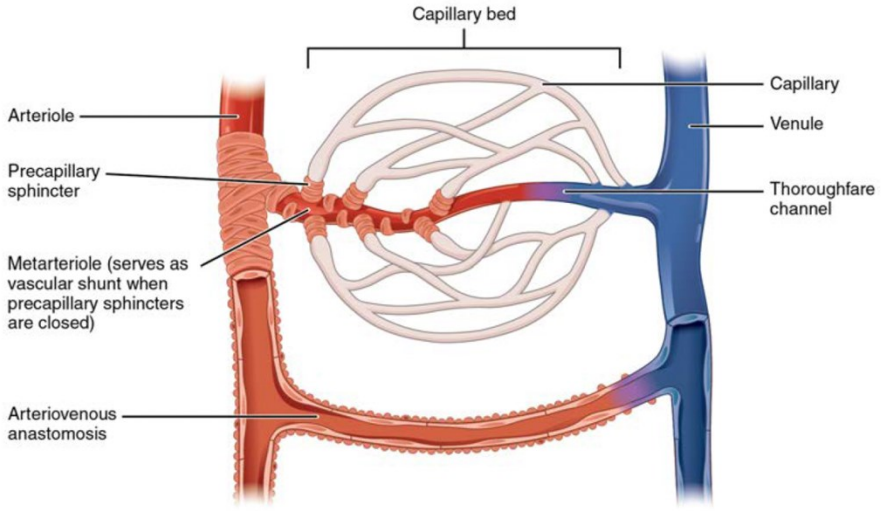

Figure 1.3: Process of perfusion. Blood is distributed to the capillary bed, where exchange processes take place. Afterwards, blood enters so-called venules, which combine to larger veins. The graphic was adapted based on illustrations from Open-Stax College – Anatomy and Physiology (1), which is licensed under CC BY 4.0[2].

1.1.2 Liver Perfusion

The liver is located inferior to the diaphragm in the right upper part of the abdominal cavity (cf. Figure 1.4a). The liver not only plays an important role in the digestive system, but is also important for metabolism and regulation (1). In terms of the digestive function, liver produces bile, which emulsifies lipids. This way, they can be digested in the watery environment. The liver possesses two unique blood supplies to fulfill this function. Besides a hepatic artery, which supplies the organ with oxygenated blood, the liver is also connected to a hepatic portal vein, providing nutrient-rich blood, which is a major difference when compared to other organs in the human body (cf. Figure 1.4b). Note that the total blood flow through the liver is not equally distributed to hepatic artery and portal vein. Instead, only one fifth to one third of the total flow can be traced back to the arterial component (17). The perfusion process in liver is therefore an unequal mixture of blood perfusion processes from portal vein and hepatic artery at the same time.

[2] https://creativecommons.org/licenses/by/4.0/

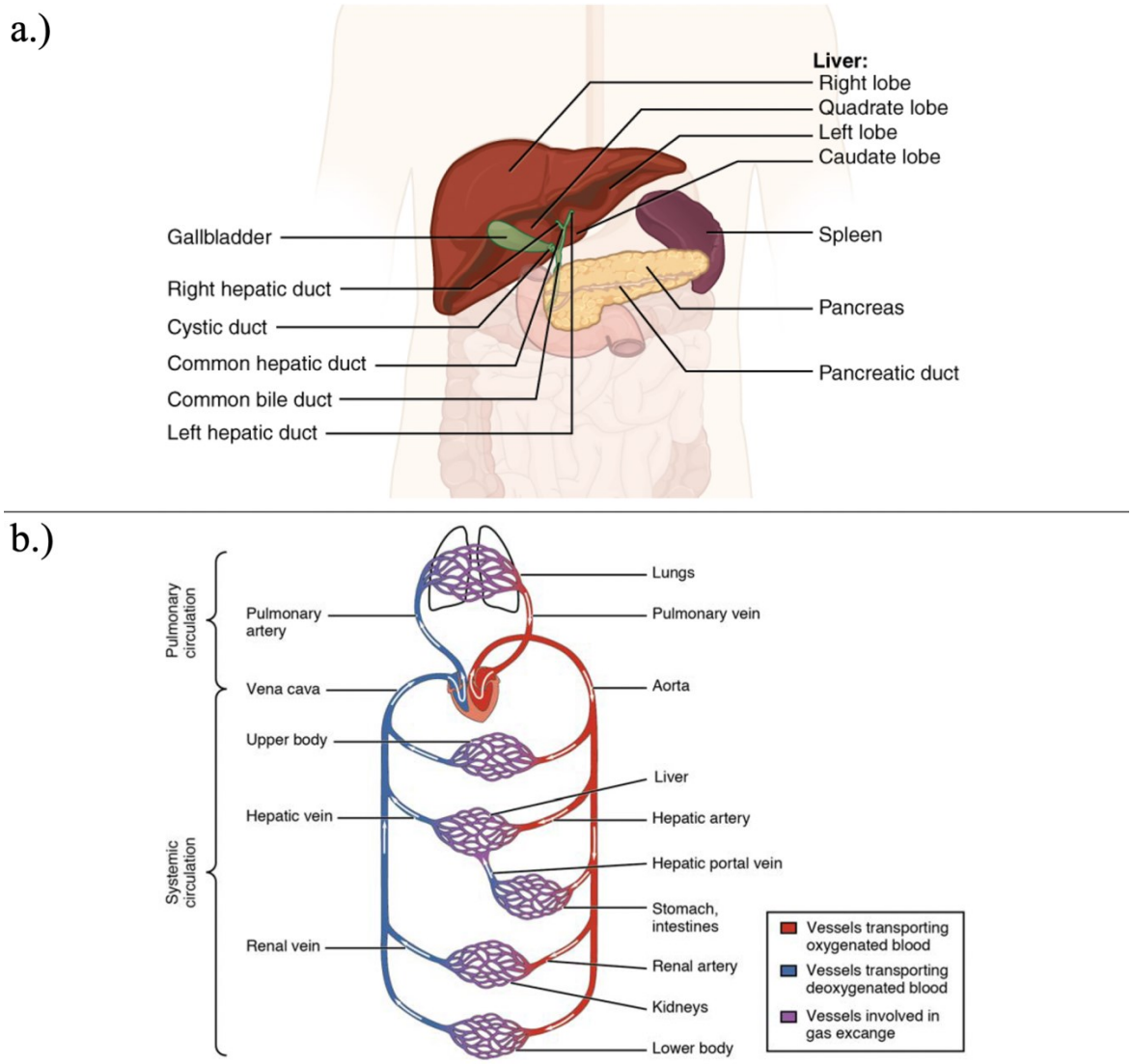

Figure 1.4: a.) Location of the liver in the abdomen; and b.) System of blood supplies in the human body. The liver shows the special characteristic that two supplies, delivering oxygenated blood as well as nutrition-rich blood to the organ while blood leaves the organ through a single vein. The graphic was adapted based on illustrations from Open-Stax College – Anatomy and Physiology (1), which is licensed under CC BY 4.0[3].

[3] https://creativecommons.org/licenses/by/4.0/

1.2 Key Parameters of Perfusion

For better understanding of the concepts described in the following sections, some perfusion related parameters are briefly mentioned and defined, based on the description in (18).

Perfusion is defined as

$$P = \frac{F}{W}. \quad [1.1]$$

Here, F depicts the blood flow rate in milliliters of blood per minute and W is the tissue mass. An alternative definition uses the tissue volume instead of the mass and describes the so-called perfusion rate

$$f = \frac{F}{V}. \quad [1.2]$$

In brain perfusion imaging, f is commonly referred to as cerebral blood flow (CBF).

1.3 Measurement of perfusion

Different methods exist which enable the measurement of tissue perfusion. Early quantitative methods were based on measuring the arterial and venous washout curves of a freely diffusible tracer, such as nitrous oxide using catheters (19)(20). Other techniques relied on the injection (nowadays inhalation) of radioactive agents such as Krypton^{85}. The distribution of the injected agent was followed by measuring the position of corresponding radioactive decay processes (5). Today, Position-Emission-Tomography (PET) is often used to measure perfusion. Here, a tracer is injected which shows β^+ decay. The simultaneous detection of two photons resulting from the annulation of the β^+ with a β^- particle is recorded and transferred to a two- or three-dimensional map of tracer distribution (6). The spatial resolution using PET is however usually restricted. This arises from the fact that the β^+ particle does not immediately interact with the surrounding tissue but travels a certain distance.

In 1973, the concept of magnetic resonance imaging (MRI) was first described, which enables measurement of perfusion with high spatial resolution (7). Here, an external magnetic field acts on the distribution of spin in the body, resulting in formation of a macroscopic magnetization. Application of radiofrequency pulses then allows to excite these spins, which generates a measurable signal in receive coils. The assessment of perfusion using MRI is based on local signal variation as induced by contrast agents. Based on the type of contrast agent or tracer, MRI methods can be divided into two major subgroups (18): Techniques based on exogenous tracers and techniques based on endogenous tracers. Dynamic susceptibility contrast (DSC) and dynamic contrast enhanced (DCE) imaging are the most important representatives of the first group (21)(22)(23). Here, contrast agent is injected, and many images of the region or organ of interest are rapidly acquired. As the contrast agent passes by, a signal change is observed in perfused voxels, depending on the applied image contrast. This change can be fitted to a model to derive quantitative parameters, describing the functional condition of the tissue. Although this technique is quite effective and commonly used in clinical reality, the invasive nature comes with some potential drawbacks. One disadvantage is a potential relation between gadolinium-based contrast agents and the development of nephrogenic systemic fibrosis in patients with renal insufficiency (8)(24). In addition, perfusion measurements using contrast agents cannot be repeated an arbitrary number of times due to the accumulation of the agent in blood. The agent therefore needs to be excreted prior to an additional measurement. Finally, recent discussion about the effects of deposition of gadolinium-based contrast agents in brain increase the demand for a non-invasive alternative in clinical routine (25)(26)(27). Arterial spin labeling (ASL) magnetic resonance imaging (MRI) allows non-invasive measurement and quantification of the perfusion rate by magnetically inverting the blood, flowing into the region of interest, utilizing it as endogenous tracer. Thus, ASL is a potential candidate to overcome the potential risks associated with injection of contrast agents. Unfortunately, ASL shows a high sensitivity to motion during the MRI examinations, which will be addressed in this work. As a basis for understanding the developed methods, the general concept of signal generation and spatial image encoding using MRI is discussed next.

2 Generation of the MRI Signal

Magnetic Resonance Imaging (MRI) is a tomographic technique, which allows to measure and visualize internal chemical and physical characteristics of an object, utilizing the concept of Nuclear Magnetic Resonance (NMR) (28). In contrast to NMR, MRI applies magnetic field gradients to encode additional spatial information into the measured signals. This enables the reconstruction of two-dimensional or three-dimensional images. Unlike other tomographic modalities, such as Computer Tomography (CT) or Ultrasound, MRI does not rely on the principle of screening an object of interest. Instead, the emission of radio frequency signals from precessing spins is measured. The great benefit is that no ionizing radiation is needed, allowing MRI to operate in the radio frequency range, avoiding potential harmful effects. In addition, the measured MRI signal allows to recover many different parameters describing the characteristics of the underlying tissue, such as relaxation times, spin densities and molecular motion in terms of diffusion and perfusion. This makes MRI one of the most versatile imaging techniques.

The following sections describes the fundamental behavior of spins in an external magnetic field and under the influence of external radiofrequency (RF) pulses, which forms the basis of measuring signals in MRI. In addition, the concept of spatial image encoding is briefly introduced. The following sections are based on the descriptions in (18), (28) and (29).

2.1 Magnetization and Spin Precession

All relevant MR phenomena, like excitation, relaxation of signal and precession of magnetization around an external magnetic field, can be described in a classical fashion using the macroscopic magnetization vector $\vec{M}$ (29). This section will briefly describe the underlying concepts which result in a formation of $\vec{M}$ in presence of an external magnetic field.

A biological sample consists of atoms, which in turn consist of nuclei and surrounding electrons. Nuclei with odd atomic numbers or weights possess a so-called spin, which is a quantum mechanical property (30). For MR, hydrogen ^{1}H is most relevant, possessing a spin quantum number $I = \frac{1}{2}$. In absence of an external magnetic field, the three-

dimensional directions of the spin angular momentum $\vec{I}$ of different ^{1}H nuclei are distributed randomly as depicted in Figure 2.1a. $\vec{I}$ is further linked to a magnetic moment

$$\vec{\mu} = \gamma \cdot \vec{I}, \qquad [2.1]$$

with $\gamma = 2\pi \cdot 42.58\ \mathrm{Mhz/T}$ the gyromagnetic ratio in case of ^{1}H (28). The macroscopic magnetization is given by the sum of individual magnetic moments, yielding

$$\vec{M} = \sum_{\vec{r}} \vec{\mu}\,(\vec{r}) = \vec{0}, \qquad [2.2]$$

which means that no macroscopic magnetization $\vec{M}$ builds up in absence of external fields. Therefore, an external magnetic field

$$\vec{B} = B_0 \cdot \vec{e}_z, \qquad [2.3]$$

pointing along the direction of the unit vector $\vec{e}_z$ of the laboratory frame, is introduced. According to quantum mechanics, a proton in such a magnetic field has two energy eigenstates, which form the basis of all possible energy states the proton can populate (29). These eigenstates are known as spin-up $|\uparrow\rangle$ and spin-down $|\downarrow\rangle$. Note, that the eigenstates are not completely parallel or antiparallel to the external field, but also possess a transversal component (29). In addition, it is important to note that this does not imply that all spins are in one of both eigenstates and thus parallel or antiparallel to the external field. Rather, their distribution is given by the combined spin-state $|\Psi\rangle$, which is a linear combination of both eigenstates

$$|\Psi\rangle = c_1 \cdot |\uparrow\rangle + c_2 \cdot |\downarrow\rangle. \qquad [2.4]$$

Here, c_1 and c_2 depict complex numbers. It follows that spins are still distributed randomly, but there is a slight tendency to point along the direction of the external field (cf. in Figure 2.1b). This can be understood, when considering the external field as an additional energy term, which, however, is much smaller than the thermal energies of individual spins (29). It follows that a macroscopic magnetization builds up:

$$\vec{M} = \sum_{\vec{r}} \vec{\mu}\,(\vec{r}). \qquad [2.5]$$

Note that in presence of an external magnetic field, individual magnetic moments experience a torque, which can be readily derived from classical as well as quantum mechanical considerations (29). The equation of motion can be formulated according to

$$\frac{d\vec{\mu}}{dt} = \gamma\vec{\mu} \times \vec{B}_0, \qquad [2.6]$$

which is easily solved by

$$\mu_{xy}(t) = \mu_{xy}(0) \cdot \exp(-i\gamma B_0 t + \Phi_0), \qquad [2.7]$$

and

$$\mu_z(t) = \mu_z(0). \qquad [2.8]$$

It shows that the transverse component $\mu_{xy}(t)$ of individual spins precesses around the external magnetic field with an angular frequency of

$$\omega_0 = \gamma B_0, \qquad [2.9]$$

which is known as the Larmor frequency. This holds for individual spins as well as for the macroscopic magnetization vector $\vec{M}$. The random initial phase Φ_0 of spins explains cancellation of all transverse components of the magnetization vector. A non-zero transverse component however is needed to generate a measurable current in so-called receive coils, based on Faraday's law (31). The next sections will therefore focus on how to generate and manipulate measurable transverse components of the magnetization vector $\vec{M}$.

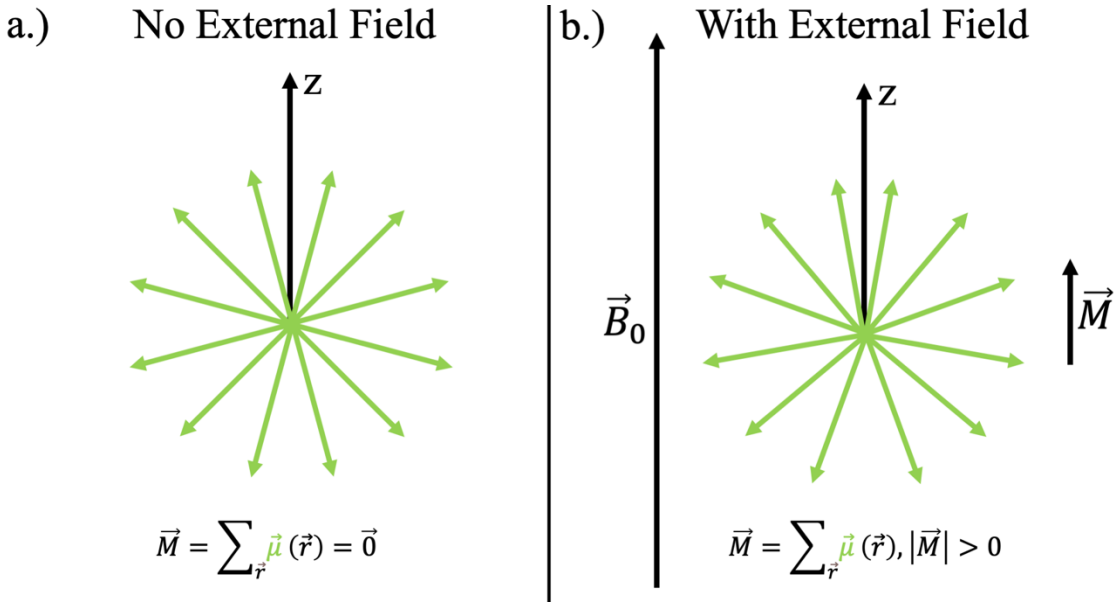

Figure 2.1: Schematic representation of the distribution of magnetic moments with/without application of an external magnetic field. a.) Without external field, no net magnetization is observed, because the direction of magnetic moments is distributed randomly; and b.) In presence of an external field, the spin distribution shows a slight tendency to point along the direction of the main magnetic field, and a macroscopic magnetization vector $\vec{M}$ builds up. Note that the illustrations are two-dimensional, but the actual distribution of magnetic moments rather forms a three-dimensional ball as demonstrated in (29).

2.2 The Rotating Reference Frame

For the analysis of the interaction between macroscopic magnetization and external RF pulses, it is convenient to introduce the so-called rotating reference frame. In contrast to the static laboratory frame, the frame is characterized by an anti-clockwise rotation of its transverse plane around the direction of $\vec{B}_0$ with angular frequency ω_{rot} (28). The relation between rotating and laboratory frame is given by

$$\vec{r}_{\mathrm{rot}} = R \cdot \vec{r}_{\mathrm{lab}} = \begin{pmatrix} \cos(\omega_{\mathrm{rot}} \cdot t) & -\sin(\omega_{\mathrm{rot}} \cdot t) & 0 \\ \sin(\omega_{\mathrm{rot}} \cdot t) & \cos(\omega_{\mathrm{rot}} \cdot t) & 0 \\ 0 & 0 & 1 \end{pmatrix} \cdot \vec{r}_{\mathrm{lab}}. \qquad [2.10]$$

In case of $\omega_{\mathrm{rot}} = \omega_0$, spins remain stationary in the rotating reference frame. Consequently, it applies that $|\vec{B}_{0,\mathrm{rot}}| = 0$ in this case. A schematic representation is given in Figure 2.2. Note that $\omega_{\mathrm{rot}}(t)$ can be time dependent. In general, it therefore applies that

$$\vec{B}_{0,\mathrm{rot}}(t) = B_0 - \frac{\omega_{\mathrm{rot}}(t)}{\gamma}. \qquad [2.11]$$

The spatial axes in the rotated coordinate system will be denoted with x′, y′ and z′.

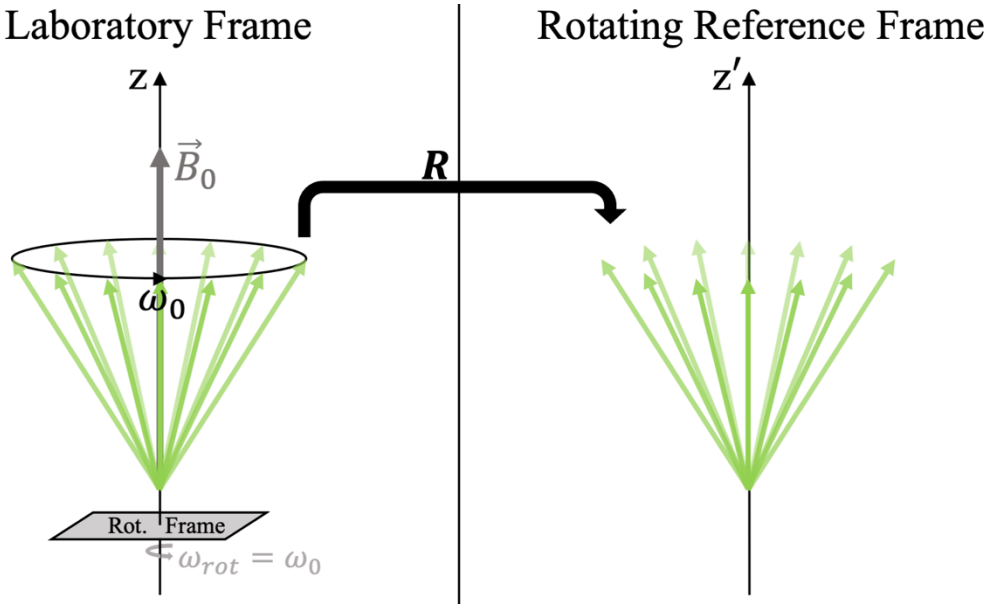

Figure 2.2: Comparison between laboratory and rotating reference frame. In the laboratory frame, spin ensembles (green arrows) precess around the direction of the main magnetic field. Here, the rotating frame precesses around the same axis with the same angular frequency. In the rotating reference frame, spins appear stationary. The matrix R describes the transition between both coordinate systems. Note that only a small subgroup of spins, pointing along the direction of the main magnetic field, is shown here for illustration purposes.

2.3 RF Excitation and Flip Angle

Using the introduced concepts, the interaction between the bulk magnetization vector $\vec{M}$ and an external RF pulse can finally be described (18)(28). An arbitrary external RF pulse in the laboratory frame can be written as

$$\vec{B}_{1,\mathrm{lab}}(t) = \begin{pmatrix} B_{1,\mathrm{x}}(t) \\ B_{1,\mathrm{y}}(t) \\ 0 \end{pmatrix} = B_1(t) \cdot \begin{pmatrix} \cos(\omega_{\mathrm{RF}}(t) \cdot t + \phi_0) \\ -\sin(\omega_{\mathrm{RF}}(t) \cdot t + \phi_0) \\ 0 \end{pmatrix}. \qquad [2.12]$$

Eq. [2.12] shows that the RF pulse is oscillating perpendicular to the main magnetic field. In general, the envelope function $B_1(t)$ as well as the modulation frequency $\omega_{\mathrm{RF}}(t)$ can be time dependent. By applying the concepts of the rotating reference frame from Eq. [2.10], Eq. [2.12] yields:

$$\vec{B}_{1,\mathrm{rot}}(t) = R \cdot \begin{pmatrix} B_{1,\mathrm{x}}(t) \\ B_{1,\mathrm{y}}(t) \\ 0 \end{pmatrix} = B_1(t) \cdot \begin{pmatrix} \cos((\omega_{\mathrm{RF}}(t) - \omega_{\mathrm{rot}}(t)) \cdot t + \phi_0) \\ -\sin((\omega_{\mathrm{RF}}(t) - \omega_{\mathrm{rot}}(t)) \cdot t + \phi_0) \\ 0 \end{pmatrix}. \quad [2.13]$$

Previous analysis showed that the strength of the main magnetic field $\vec{B}_{0,\mathrm{rot}}(t)$ depends on the modulation frequency of the rotating reference frame. Therefore, an effective magnetic field results:

$$\begin{aligned} \vec{B}_{\mathrm{eff}}(t) &= \vec{B}_{1,\mathrm{rot}}(t) + \vec{B}_{0,\mathrm{rot}}(t) \\ &= B_1(t) \cdot \begin{pmatrix} \cos((\omega_{\mathrm{RF}}(t) - \omega_{\mathrm{rot}}(t)) \cdot t + \phi_0) \\ -\sin((\omega_{\mathrm{RF}}(t) - \omega_{\mathrm{rot}}(t)) \cdot t + \phi_0) \\ 0 \end{pmatrix} + \begin{pmatrix} 0 \\ 0 \\ B_0 - \dfrac{\omega_{\mathrm{rot}}(t)}{\gamma} \end{pmatrix}. \end{aligned} \quad [2.14]$$

In case of $\omega_0 = \omega_{\mathrm{RF}} = \omega_{\mathrm{rot}}$ and $\phi_0 = 0$, it follows that

$$\vec{B}_{\mathrm{eff}}(t) = B_1(t) \cdot \begin{pmatrix} 1 \\ 0 \\ 0 \end{pmatrix}. \quad [2.15]$$

Eq. [2.15] describes a time dependent field along the x′-axis in the rotating reference frame, which is applied at the resonance frequency of the spin system. Note that the time dependency only refers to the amplitude of the field, since the frequency of the RF pulse is kept fix. The effect on the bulk magnetization vector $\vec{M}_{\mathrm{rot}}$ can be described by utilizing Eq. [2.6]:

$$\frac{d\vec{M}_{\mathrm{rot}}}{dt} = \gamma \vec{M}_{\mathrm{rot}} \times \vec{B}_{\mathrm{eff}}, \quad [2.16]$$

which is solved by

$$\begin{aligned} M_{\mathrm{x,rot}}(t) &= 0, \\ M_{\mathrm{y,rot}}(t) &= M_{\mathrm{z}}^0 \sin\left(\int_0^T \gamma B_1(t)dt\right) = M_{\mathrm{z}}^0 \sin\left(\int_0^T \omega_1(t)dt\right), \\ M_{\mathrm{z,rot}}(t) &= M_{\mathrm{z}}^0 \cos\left(\int_0^T \gamma B_1(t)dt\right) = M_{\mathrm{z}}^0 \cos\left(\int_0^T \omega_1(t)dt\right), \end{aligned} \quad [2.17]$$

describing a rotation around the x-axis with the time depended angular frequency $\omega_1(t)$. Here, the field $B_1(t)$ is applied for a total duration T. The term $\alpha = \int_0^T \omega_1(t)dt$ is interpreted as the so-called flip angle. According to Eq. [2.17], the flip angle α depends on the area under the $B_1(t)$ envelope function as well as the duration of exposure T (cf. Figure 2.3 for a schematic demonstration of this relation).

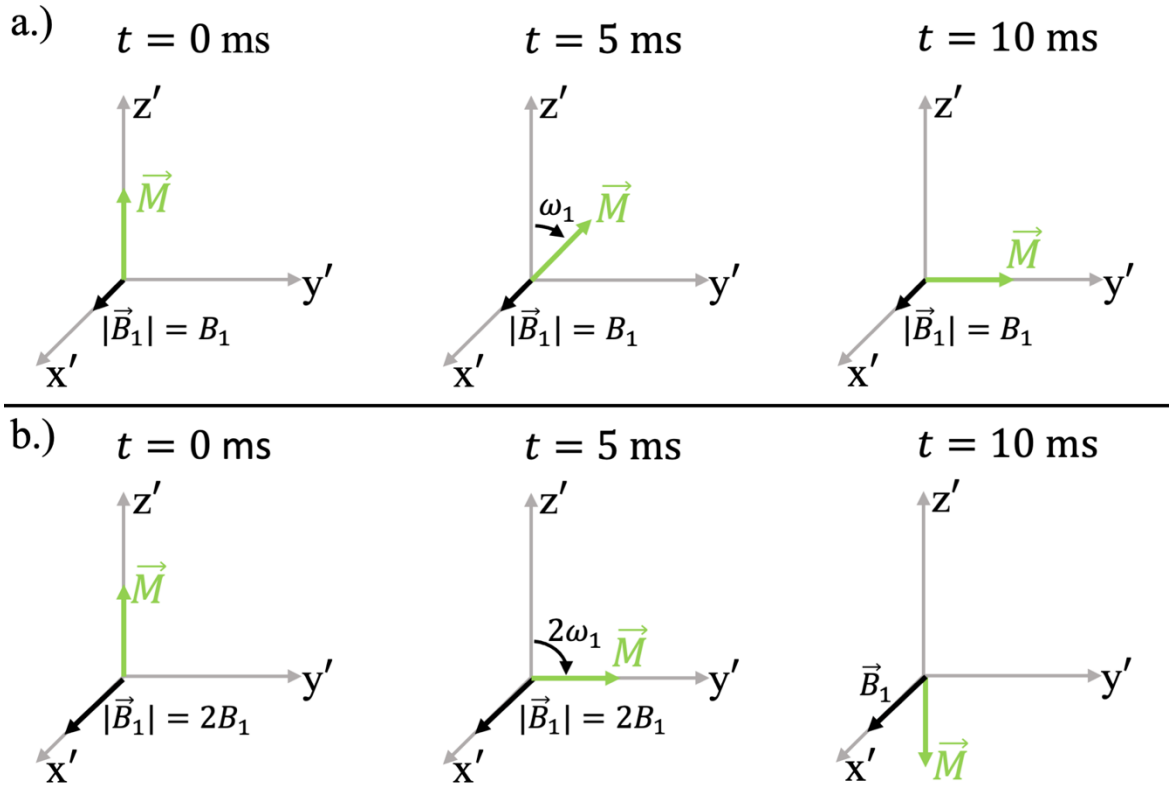

Figure 2.3: Schematic representation of the relation given by Eq. [2.17] with a.) A rectangular pulse with constant RF field along the x′-axis in the rotated reference frame with amplitude B_1 and a duration of 10 ms results in a 90° flip angle of the magnetization vector $\vec{M}$. The relation only holds for a specific strength of the field $|\vec{B}_1| = B_1$; and b.) The same pulse but the amplitude is doubled to $2B_1$. The same flip angle is achieved after half the pulse duration, corresponding to the same area under the envelope of $B_1(t)$ as in a.). After the same pulse duration, a 180° flip is achieved.

2.4 Relaxation Processes

After application of the RF pulse, the spin system will not stay excited, but slowly returns to the equilibrium state, which is related to variation of microscopic magnetic fields in the

surroundings of each nuclei (28). This results in two distinct processes of decay, namely T_1 and T_2 relaxation. T_1 relaxation describes the increase of longitudinal magnetization with time, also referred to as spin-lattice relaxation. T_2 relaxation describes an on-going loss of phase coherence between spin ensembles in the x-y-plane, also known as spin-spin-relaxation. In the laboratory frame, both processes result in a damped free precession of the macroscopic magnetization vector $\vec{M}$ back to its equilibrium state. In the rotating reference frame, relaxation can be phenomenologically described by

$$\frac{dM_{\mathrm{z,rot}}}{dt} = -\frac{M_{\mathrm{z,rot}} - M^0_{\mathrm{z,rot}}}{T_1}, \qquad [2.18]$$

and

$$\frac{dM_{\mathrm{xy,rot}}}{dt} = -\frac{M_{\mathrm{xy,rot}}}{T_2}. \qquad [2.19]$$

T_1 and T_2 are the characteristic decay constants of the respective process. The process of T_1 decay, described by Eq. [2.18], is solved by

$$M_{\mathrm{z,rot}}(t) = M^0_{\mathrm{z,rot}} + c \cdot \exp\left(-\frac{t}{T_1}\right). \qquad [2.20]$$

Using the initial condition $M_{\mathrm{z,rot}}(0) = 0$, corresponding to perfect 90° excitation, it follows that

$$M_{\mathrm{z,rot}}(t) = M^0_{\mathrm{z,rot}}\left(1 - \exp\left(-\frac{t}{T_1}\right)\right), \qquad [2.21]$$

describing a saturation recovery process. After inversion, $M_{\mathrm{z,rot}}(0) = -M^0_{\mathrm{z,rot}}$, which yields

$$M_{\mathrm{z,rot}}(t) = M^0_{\mathrm{z,rot}}\left(1 - 2 \cdot \exp\left(-\frac{t}{T_1}\right)\right), \qquad [2.22]$$

describing an inversion recovery process. The solution of Eq. [2.19] is given by

$$M_{\mathrm{xy,rot}}(t) = M_{\mathrm{xy,rot}}(0) \cdot \exp\left(-\frac{t}{T_2}\right). \qquad [2.23]$$

After initial saturation, the longitudinal magnetization has recovered to a fraction of $\left(1 - \frac{1}{e}\right)$ of its initial $M^0_{\mathrm{z,rot}}$ value after the specific time T_1. The transversal magnetization

in contrast has decayed to a fraction of $\frac{1}{e}$ of its initial $M_{\mathrm{xy,rot}}(0)$ value after the characteristic time T_2. A visualization of both relaxation processes after initial saturation are given in Figure 2.4.

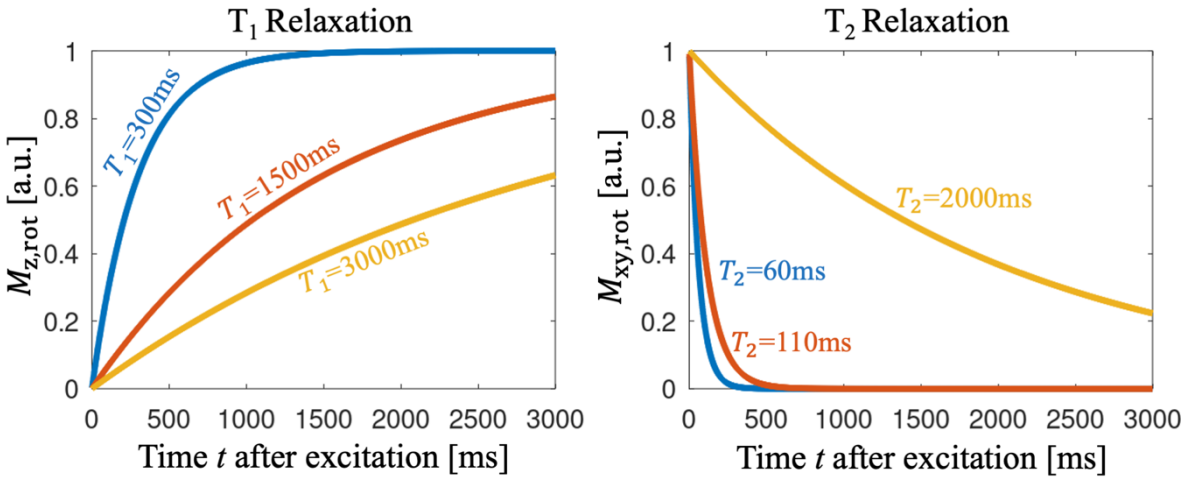

Figure 2.4: Comparison of T_1 and T_2 relaxation processes after initial saturation according to Eq. [2.21] and [2.23]. Given values roughly correspond to subcutaneous fat (blue), gray matter (red) and cerebrospinal fluid (CSF, yellow) at a field strength of 3T.

As shown, different types of tissue show differences in their longitudinal and transversal relaxation behavior. This lays the foundation for generating different image contrasts using different repetition times TR between individual excitations. Tissue with long T_1 relaxation times only recovered a small fraction of its $M^0_{\mathrm{z,rot}}$ magnetization at the time of the next excitation, while tissue with short T_1 components recovered more and thus appears brighter (neglecting T_2 decay processes after excitation). Another possibility for generating contrast is to introduce delays in between excitation and image readout. Signal from tissue with short T_2 relaxation times will rapidly decay and appear dark, while long T_2 times ensure that some amount of signal is still available at time of the image readout. Combining these ideas, T_1-, T_2- and proton-density-weighted image contrast are achievable.

In practice, T_2^* relaxation, rather than pure T_2 relaxation, is observed after excitation of the transverse magnetization. T_2^* relaxation describes an additional process of spin dephasing, originating from inhomogeneities of the main magnetic field. The loss of signal is characterized by the T_2^* constant:

$$\frac{1}{T_2^*} = \frac{1}{T_2} + \frac{1}{T_2'}, \qquad [2.24]$$

with $\frac{1}{T_2'} = \gamma \Delta B_{\mathrm{inhom}}(t)$, where $\Delta B_{\mathrm{inhom}}(t)$ describes the inhomogeneity across respective imaging voxels (32). The loss of this additional phase coherence is reversible if the inhomogeneity of the main magnetic field is not time dependent.

Taking the transversal relaxation processes into account, a so-called free induction decay is measured in the laboratory frame after initial excitation. As the name suggests, the measured signal consists of the free precession of the magnetization vector around the main magnetic field. This precession, however, is not of infinite duration but is damped by the T_2^* relaxation process. The rotating magnetization vector induces a current in the receive coils, as predicted by Faraday's law. The corresponding measured signal is then described by

$$S(t) \approx S_0 \exp\left(-\frac{t}{T_2^*}\right) \exp(-i\omega_0 t), \qquad [2.25]$$

assuming spins with a single precession frequency and initial signal intensity S_0. Note that this relaxation is only valid for Lorentzian distributed spectral density functions in the excited region (28). Otherwise, the decay is only approximated by the corresponding exponential decay process.

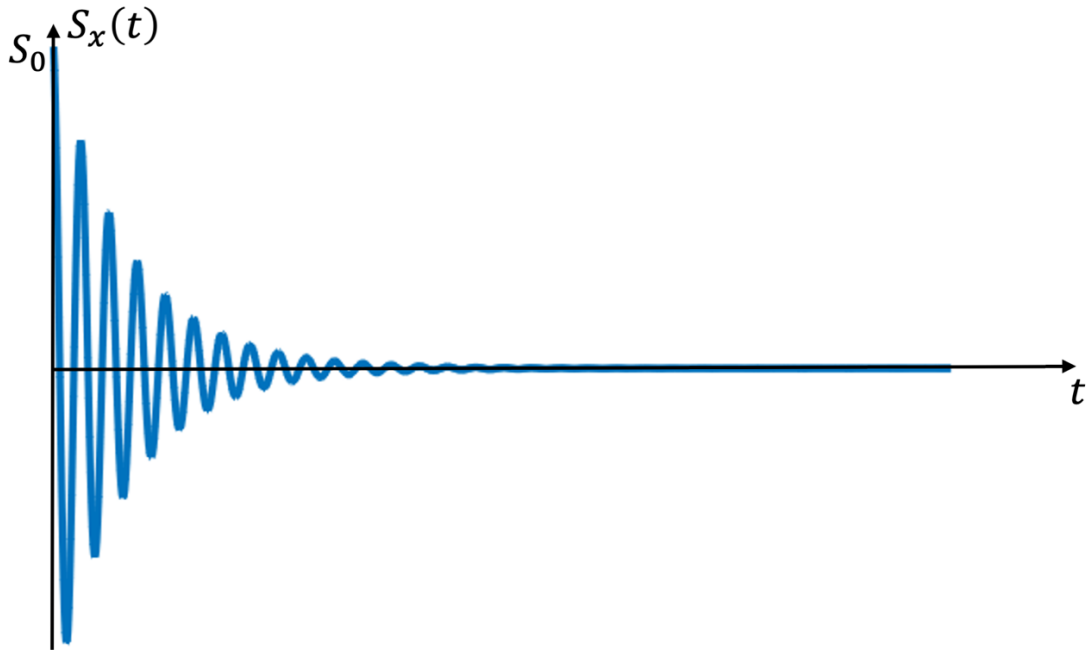

Figure 2.5: Example for free induction decay after excitation according to Eq. [2.25]. Only the projection of the complex signal on the x-axis is shown here.

2.5 Spin Echoes

The T_2^* relaxation results in a rapid loss of phase coherence between spin ensembles. From a signal perspective, this corresponds to a rapid damping of the induced currents in the receive coils and thus a limitation of the maximum duration of suitable data acquisition windows. 180° refocusing pulses can be applied to reverse the portion of temporally constant spin dephasing, resulting from temporally constant local magnetic field inhomogeneities $\Delta B_{\mathrm{inhom}}(\vec{r})$. The basic concept of spin echo formation is demonstrated in Figure 2.6.

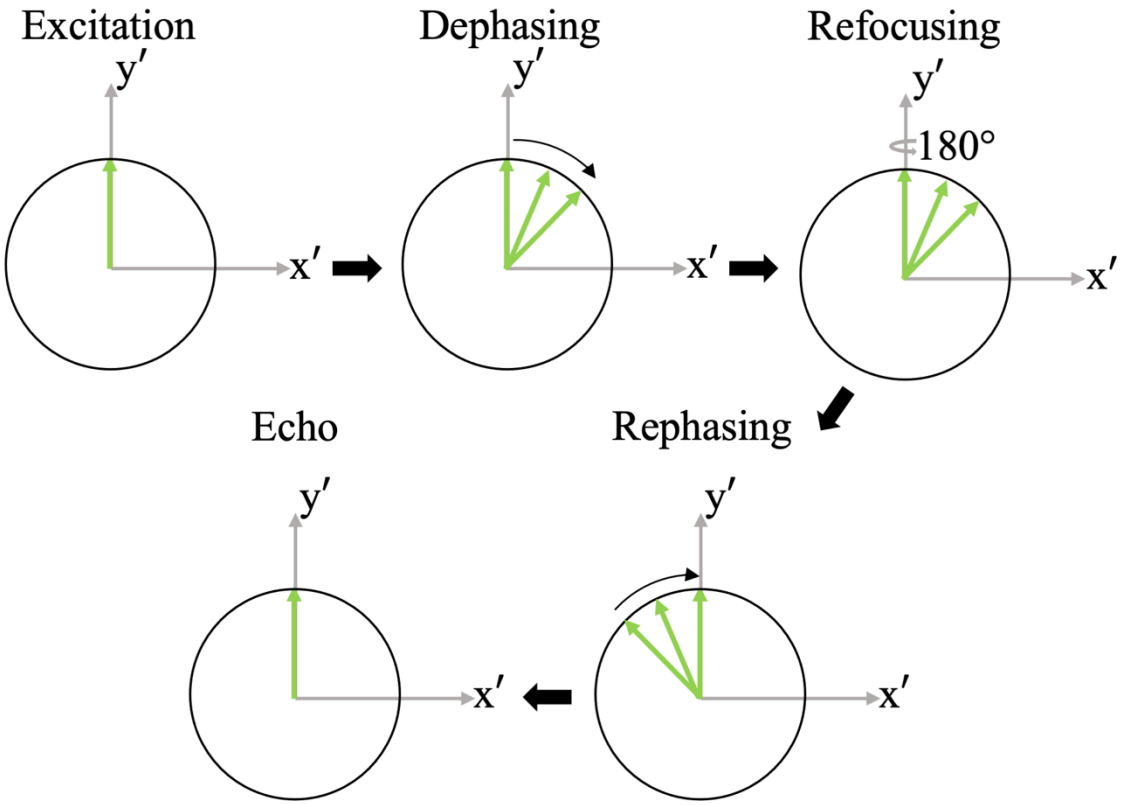

Figure 2.6: Concept of spin echo formation as viewed from the rotating frame of reference. Note that constant local field variation is assumed here, and no additional dephasing processes resulting in non-reversable loss of phase coherence were included.

After application of the initial 90° excitation pulse, the magnetization vectors of different spins lie in the transverse plane. Due to the local variation of the main magnetic field, spins accumulate different amounts of additional phase, which results in dephasing. Application of a 180° refocusing pulse rotates the spins around the y'-axis. Afterwards, spins accumulate phase again, which results in formation of a spin echo. The amplitude of the echo is determined by the T_2 relaxation constant of respective tissue. Since the T_2 decay is related to stochastic dephasing processes, the corresponding loss of phase coherence is not reversed by the refocusing pulse. The spin echo is formed after double the temporal distance between excitation and refocusing pulse. This time is known as the echo time TE. Application of multiple refocusing pulses allows the generation of multiple spin echoes, which is commonly exploited in many MR pulse sequences.

2.6 Bloch Equations

Combining the effects of the static magnetic field, an external RF pulse as well as T_1 and T_2 relaxation, the behavior of the bulk magnetization $\vec{M}_{\mathrm{rot}}$ in the rotating reference frame can be described in a more generalized form, known as the Bloch equations:

$$\frac{d\vec{M}_{\mathrm{rot}}}{dt} = \gamma\, \vec{M}_{\mathrm{rot}} \times \vec{B}_{\mathrm{eff}} - \begin{pmatrix} \frac{M_{\mathrm{x,rot}}}{T_2} \cdot \cos\big((\omega_0 - \omega_{\mathrm{rot}})t\big) \\ -\frac{M_{\mathrm{y,rot}}}{T_2} \cdot \sin\big((\omega_0 - \omega_{\mathrm{rot}})t\big) \\ \frac{M_{\mathrm{z,rot}} - M^0_{\mathrm{z,rot}}}{T_1} \end{pmatrix}. \quad [2.26]$$

In case of $\omega_0 = \omega_{\mathrm{rot}}$, the relation simplifies to

$$\frac{d\vec{M}_{\mathrm{rot}}}{dt} = \gamma\, \vec{M}_{\mathrm{rot}} \times \vec{B}_1 - \begin{pmatrix} \frac{M_{\mathrm{x,rot}}}{T_2} \\ \frac{M_{\mathrm{y,rot}}}{T_2} \\ \frac{M_{\mathrm{z,rot}} - M^0_{\mathrm{z,rot}}}{T_1} \end{pmatrix}. \quad [2.27]$$

Eq. [2.26] and [2.27] yield a general framework which allows to describe and analyze the interaction of the bulk magnetization vector $\vec{M}$ with different external fields.

2.7 Slice-Selection Gradients

So far, it has been discussed how the magnetization of a whole object inside the scanner can be excited using RF pulses. In most cases, it is desired to only excite the magnetization in a single slice or volume, while leaving the magnetization in the rest of the object unaffected. In MRI, this is achieved by introducing a gradient in the magnetic field during the application of the RF pulse (28). A magnetic field gradient has the general form

$$\vec{G} = \begin{pmatrix} G_x \\ G_y \\ G_z \end{pmatrix} = \begin{pmatrix} \frac{dB_z}{dx} \\ \frac{dB_z}{dy} \\ \frac{dB_z}{dz} \end{pmatrix}, \quad [2.28]$$

which describes a variation of the main magnetic field $B_z = B_0(z)$ along the three spatial axes. A linear variation of the magnetic field now enables selective excitation of magnetization in a specific slice profile. Assuming a linear gradient $\vec{G} = \begin{pmatrix} 0 \\ 0 \\ G_z \end{pmatrix}$ along the z-axis, the Larmor frequency of a spin ensemble is then related to

$$\omega_0 = \gamma(B_0 + G_z \cdot z), \quad [2.29]$$

with z the spatial position along the direction of the main magnetic field. Eq. [2.29] describes a position dependent Larmor frequency. In order to excite only those spins, which reside inside a defined region Δz around the isocenter of the scanner, an RF pulse must be applied which shows an uniform flip angle within the corresponding range of resonance frequencies. This region is linked to the frequency spectrum of the RF pulse, decomposing the temporal pulse into its spectral components, which act on spin ensembles with corresponding resonance frequencies. Given a spectral bandwidth $\Delta\omega$ of the pulse, only those ensembles are excited for which the equation

$$\Delta z = \frac{\Delta\omega}{\gamma G_z} \quad [2.30]$$

holds (18). A graphical depiction of this relation is shown in Figure 2.7.

The linear gradient can be created using a pair of coils which show contrary directions of electric current, resulting in a linear variation of the main magnetic field. In practice, additional magnetic field terms B_x and B_y arise, as predicted by Maxwell's equations for the magnetic field ($\nabla \cdot \vec{B} = 0$ and $\nabla \times \vec{B} = 0$). This limits the practical region, which can be used for imaging, because accumulation of additional unwanted phase during gradient application might occur in outer regions.

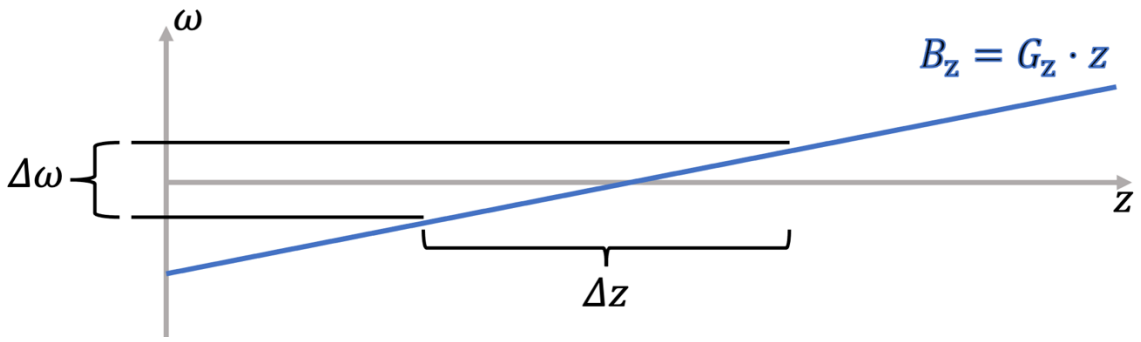

Figure 2.7: Graphical demonstration of the relation between spatial and spectral selectivity in presence of a linear magnetic field gradient G_z. The gradient G_z introduces a linear modulation of the resonance frequency ω. Depending on the bandwidth of the RF pulse, only those spins with precession frequencies in the range $\Delta\omega$ are excited, which corresponds to spatial positions in the range of Δz.

Finally, the application of a slice-selection gradient during application of a RF pulse leads to position dependent phase accrual of spin ensembles throughout the excitation pulse. Depending on pulse shape and applied gradient strength, intravoxel phase dispersion can then lead to signal loss (18). In practice, a rephasing gradient with opposite direction is therefore often applied after slice-selective excitation, which counteracts the accumulated phase.

2.8 Adiabatic Excitation and Inversion

So far, the phenomenon of on-resonance excitation has been covered. However, on-resonance is often not achieved under realistic scenarios, because each object which is placed in the scanner will perturbate the main magnetic field to some extent, mainly related to changes in the magnetic susceptibility between different types of tissue and/or air in the object. Spin ensembles will then precess with a modulated precession frequency according to Eq. [2.9]. Therefore, these ensembles see an effective magnetic field with non-zero $B_{z,\mathrm{rot}}$ component in the rotating frame of reference, which impacts the achieved flip angle. In addition, the distribution of the B_1 field is sometimes not perfectly homogeneous throughout the desired imaging region, being related to the geometry of the transmit coil (18). The concept of adiabatic excitation and inversion allows to achieve highly accurate flip angles under these situations. The following description is based on (18).

Recalling Eq. [2.12], an arbitrary RF pulse was defined with a time dependent modulation frequency $\omega_{\mathrm{RF}}(t)$. The equation for the laboratory frame is repeated here in complex notation:

$$B_1(t) = A(t)\exp(-i\omega_{\mathrm{RF}}(t)\cdot t). \qquad [2.31]$$

The rotating frame of reference is now locked with the time dependent modulation frequency of the RF pulse such that $\omega_{\mathrm{RF}} = \omega_{\mathrm{rot}}$. It follows that, according to Eq. [2.14], spins experience an effective magnetic field in the rotating frame of reference. The transverse component of the RF pulse simply reduces to

$$B_{\mathrm{x,rot}}(t) = A(t). \qquad [2.32]$$

The longitudinal component depends on ω_{RF}:

$$B_{\mathrm{z,rot}}(t) = \frac{1}{\gamma}(\omega_0 - \omega_{\mathrm{RF}}). \qquad [2.33]$$

For the amplitude and direction of the effective field, it follows that:

$$\left|\vec{B}_{\mathrm{eff}}\right| = \sqrt{B^2_{\mathrm{x,rot}}(t) + B^2_{\mathrm{z,rot}}(t)}, \qquad [2.34]$$

and

$$\psi = \arctan\left(\frac{B_{\mathrm{x,rot}}(t)}{B_{\mathrm{z,rot}}(t)}\right). \qquad [2.35]$$

The principle of adiabatic passage now states that the magnetization vector of a spin system will follow the direction of the effective magnetic field if the direction of the former does not change too much during one period of precession. This is mathematically described in terms of the adiabatic condition

$$\left|\frac{d\psi}{dt}\right| \ll \gamma\left|\vec{B}_{\mathrm{eff}}\right|. \qquad [2.36]$$

The basic principle of an adiabatic 90° excitation is shown in Figure 2.8. The extension to a 180° inversion follows the same principle.

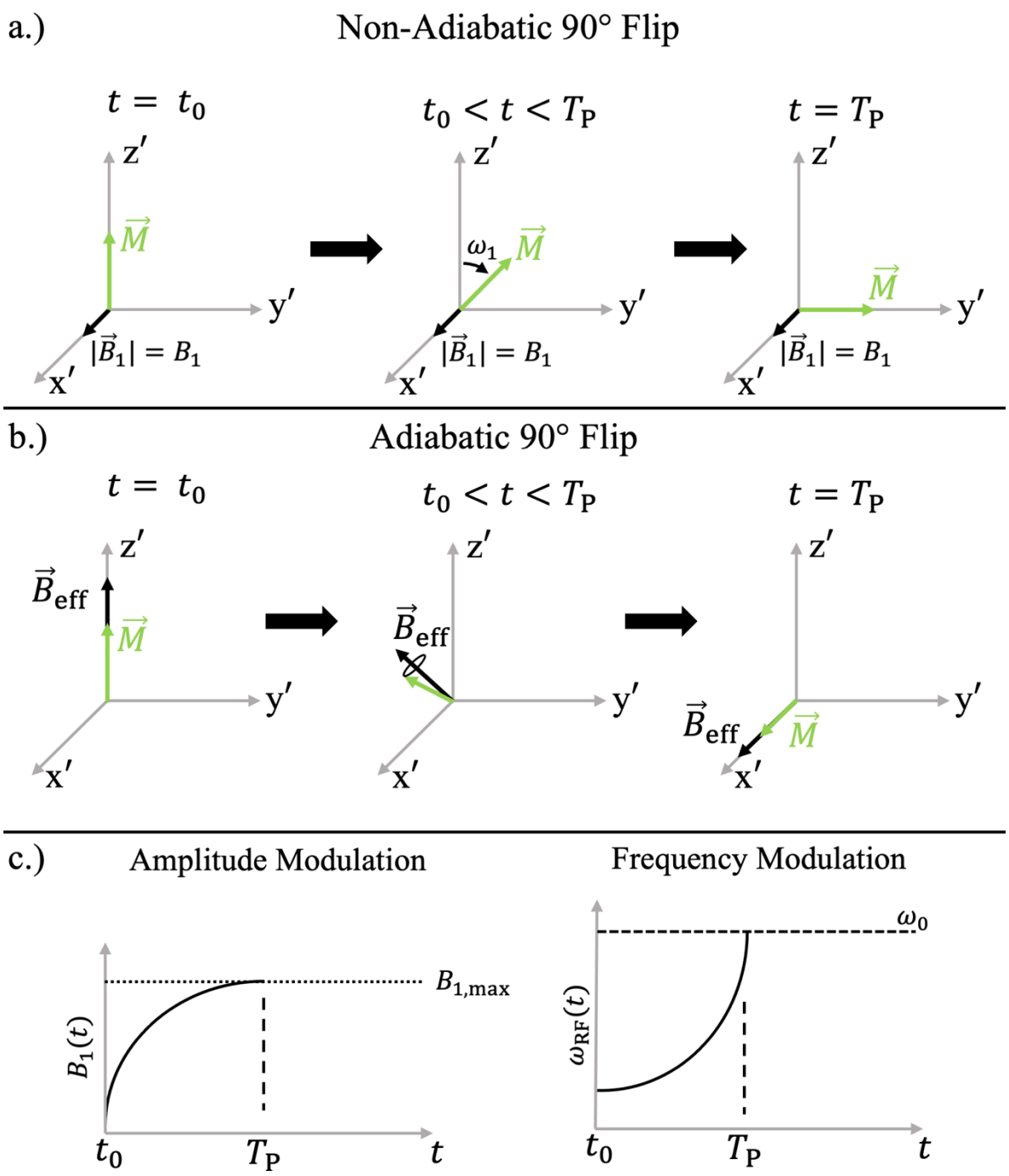

Figure 2.8: Comparison of a non-adiabatic and an adiabatic flip with sine/cosine modulation functions of amplitude and frequency. a.) In the non-adiabatic case, the RF pulse is applied on-resonance e.g., does not change its modulation frequency $\omega_{RF} = \omega_0$; b.) In the adiabatic case, the modulation frequency and amplitude are adjusted, such that the effective magnetic field rotates from an initially aligned state with the z′-axis towards the x′-axis; and c.) The exemplary sine/cosine modulation functions of amplitude and frequency, resulting in an adiabatic excitation.

2.8.1 Frequency Offset Corrected Inversion Pulses (FOCI)

FOCI pulses are a special class of adiabatic inversion pulses, which yield high inversion efficiency together with a sharp slice profile (33). A FOCI pulse is based on a hyperbolic secant (HS) pulse, which is modulated with a modulation function $A(t)$. The HS pulse is defined as follows (18)(33):

$$B_{1,\mathrm{HS}}(t) = \Omega_0 \mathrm{Sech}(\beta t), \quad [2.37]$$

$$\Delta\omega_{\mathrm{HS}}(t) = -\mu\beta \cdot \tanh(\beta t), \quad [2.38]$$

$$G_{\max} = \frac{\beta \cdot \mu}{\pi \cdot \gamma \cdot \Delta z}, \quad [2.39]$$

with the gradient strength $G_{\max}$ of the accompanying slice selection gradient, which is needed for the desired slice thickness Δz. Eq. [2.37] and [2.38] fulfill the adiabatic condition if the relation

$$\Omega_0 \gg \frac{\sqrt{\mu}\beta}{\gamma} \quad [2.40]$$

holds (18). Parameters μ and β define the shape of amplitude and frequency functions. It can be shown that a modulation of the amplitude and frequency definitions of the HS pulse by

$$A(t) = \begin{cases} \mathrm{Sech}(\beta t)^{-1}, & \mathrm{Sech}(\beta t) > 1/A^{\max} \\ A^{\max}, & \text{else} \end{cases} \quad [2.41]$$

still satisfies the adiabatic condition, while simultaneously delivering a sharper slice profile (33)(34)(35). The result is a so-called C-shape FOCI pulse, which is defined according to

$$B_{1,\mathrm{FOCI}}(t) = A(t) \cdot \Omega_0 \mathrm{Sech}(\beta t), \quad [2.42]$$

$$\Delta\omega_{\mathrm{FOCI}}(t) = -A(t) \cdot \mu\beta \cdot \tanh(\beta t), \quad [2.43]$$

and

$$G_{\mathrm{FOCI}}(t) = A(t) \cdot G_{\mathrm{HS}}(t), \quad [2.44]$$

with $G_{\mathrm{HS}}(t)$ the gradient strength of the hyperbolic secant pulse for a desired slice thickness. A comparison of both the HS and C-shape FOCI pulse shapes is given in Figure 2.9.

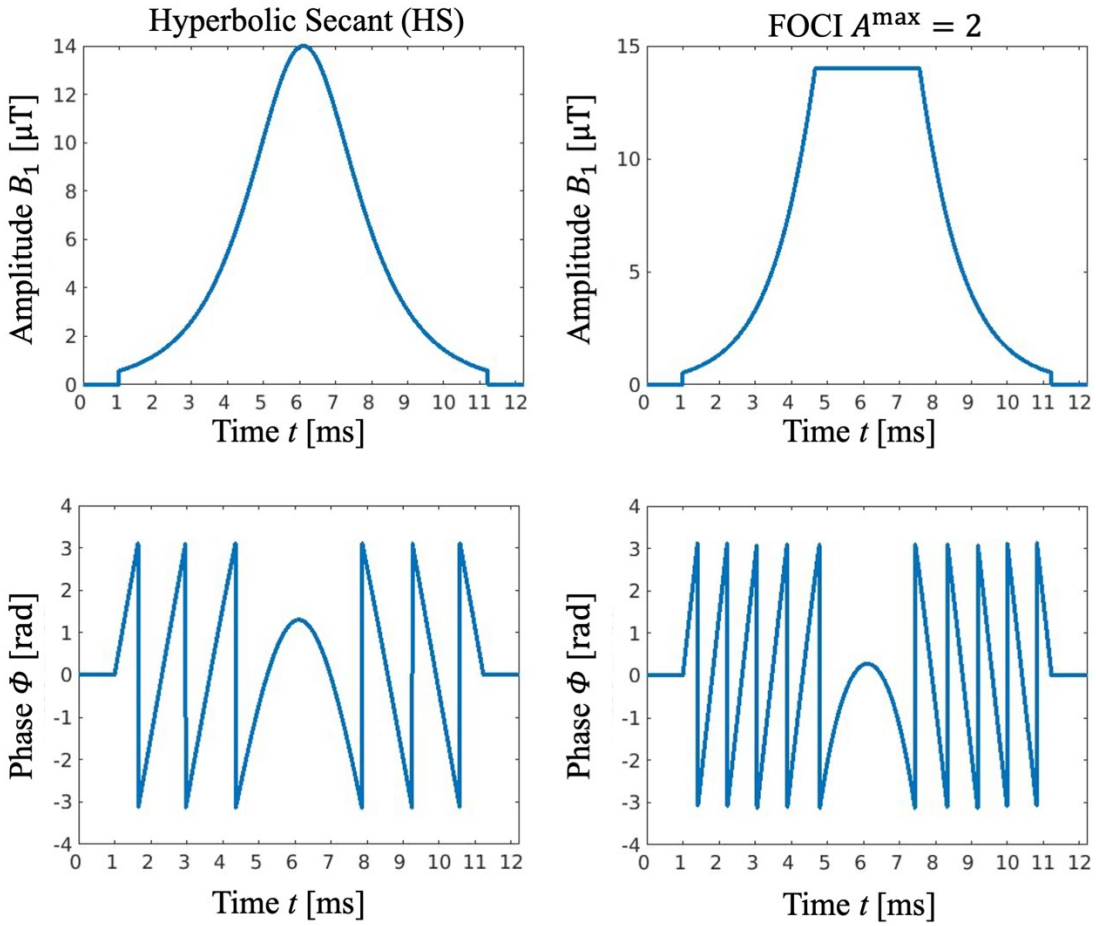

Figure 2.9: Comparison of amplitude and phase evolution of a hyperbolic secant and FOCI pulse. The phase evolution is given as the integral over the modulation frequency, which is a common approach for the implementation of pulses for MRI systems.

The sharper slice profile of a FOCI pulse when compared to the standard HS pulse arises from the increased gradient strength at the beginning and end of the pulse as given by Eq. [2.44]. During the application of the FOCI/HS pulse in combination with a linear magnetic field gradient, the outer edge of the slice profile is inverted first, due to the shift of the off-resonance frequency from Eq. [2.43] (cf. Figure 2.10). If a stronger gradient is applied at this time, the spatial adiabatic region is sharper, resulting in a sharper edge of the slice profile. From the edge, the inversion region extends over the desired slice profile. Finally, the other edge of the profile gets inverted at the end of the pulse application.

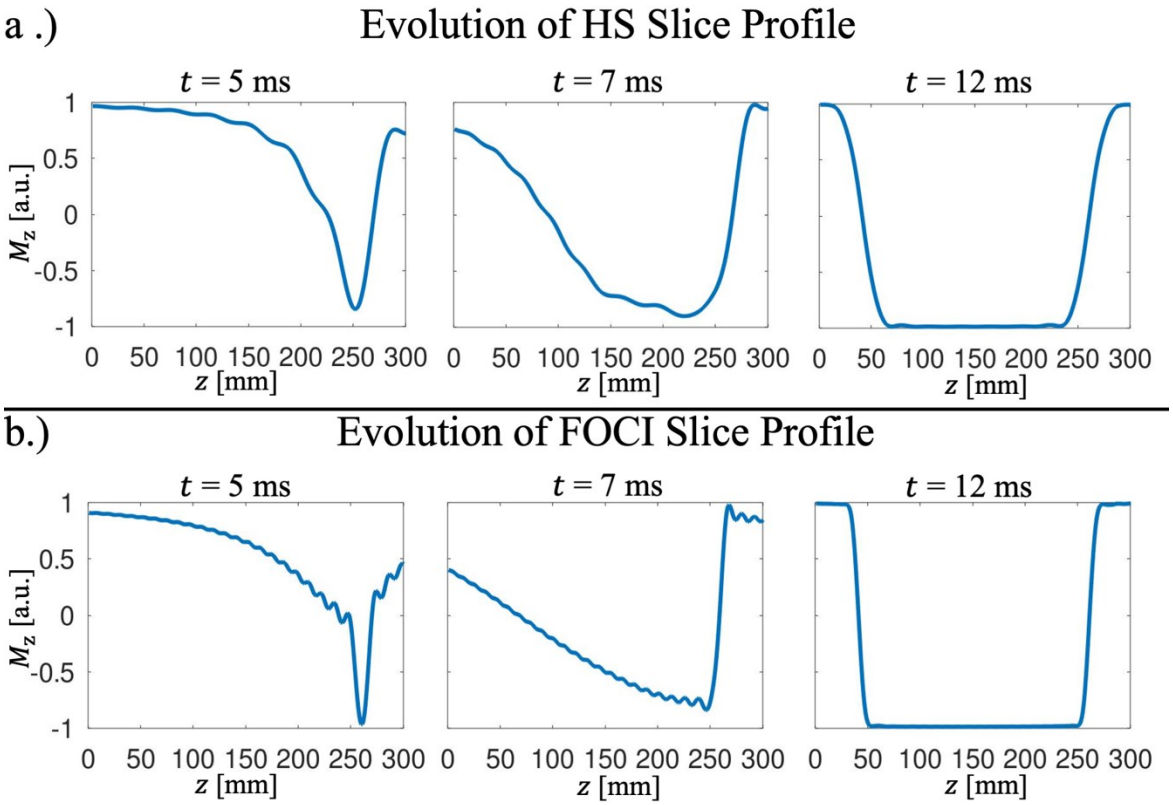

Figure 2.10: Evolution of the Slice Profile of a.) HS and b.) FOCI pulses with a total duration of 12.24 ms. Outer areas of the slice profile are inverted at the beginning and end of the pulse. The strength of the gradient at these times defines the sharpness of the slice profile, due to broader or sharper profiles of the adiabatic region of the respective pulse.

2.9 Adiabatic Fast Passage

Besides the basic principle of adiabatic excitations and inversion, another concept for achieving adiabatic inversion exists, which is of special importance for the arterial spin labeling techniques, discussed later in this work. Returning to Eq. [2.29], spins at different locations experience a variation in their Larmor frequency while exposed to a magnetic field gradient. Assuming a gradient along the z-axis of the laboratory frame, an effective magnetic field results, according to

$$\vec{B}_{\mathrm{eff}} = \vec{B}_1 + G_{\mathrm{z}} \cdot z \cdot \vec{e}_{\mathrm{z}}, \qquad [2.45]$$

with $\vec{e}_{\mathrm{z}}$ a unity vector along the z direction. Without loss of generality, it is assumed that $\vec{B}_1$ is linear polarized along the y′ direction. If a spin moves along the direction of $\vec{e}_{\mathrm{z}}$, the Larmor frequency changes with the position of the spin. If the spin is far away from the isocenter of the gradient, the effective field becomes

$$\vec{B}_{\mathrm{eff}}(z \ll 0) \approx -G_{\mathrm{z}} \cdot z \cdot \vec{e}_{\mathrm{z}} \qquad [2.46]$$

and is initially aligned with the z-axis in opposite direction of $\vec{e}_{\mathrm{z}}$ in case of a positive gradient amplitude. If spins move forward, they eventually reach the isocenter position, where

$$\vec{B}_{\mathrm{eff}}(z = 0) \approx \vec{B}_1, \qquad [2.47]$$

corresponding to an on-resonance application of the RF pulse. Afterwards, the spins will leave the isocenter again, and the effective magnetic field becomes

$$\vec{B}_{\mathrm{eff}}(z \gg 0) \approx G_{\mathrm{z}} \cdot z \cdot \vec{e}_{\mathrm{z}}, \qquad [2.48]$$

such that the effective field is again aligned with the z-axis. The whole procedure resembles a sweep of the effective magnetic field from $-\vec{e}_{\mathrm{z}}$ to $\vec{e}_{\mathrm{z}}$. The reverse sweep occurs if $G_{\mathrm{z}} < 0$. Therefore, if the adiabatic condition from Eq. [2.36] is fulfilled, the described process results in an inversion of moving spins. As can be easily understood from the previous description, the adiabatic condition is now linked to the angle between direction of the magnetic field gradient and the moving spins. In addition, the velocity $\vec{v}$

of the spins is important, because relaxation processes might occur. Together, these considerations result in a reformulation of the adiabatic condition, according to

$$\frac{1}{T_1}, \frac{1}{T_2} \ll \frac{\left|\vec{G} \cdot \vec{v}\right|}{\left|\vec{B}_{\text{eff}}\right|} \ll \gamma \cdot \left|\vec{B}_{\text{eff}}\right|. \qquad [2.49]$$

Further details of the concept and application of adiabatic fast passage can be found in (36). A schematic representation is given in Figure 2.11.

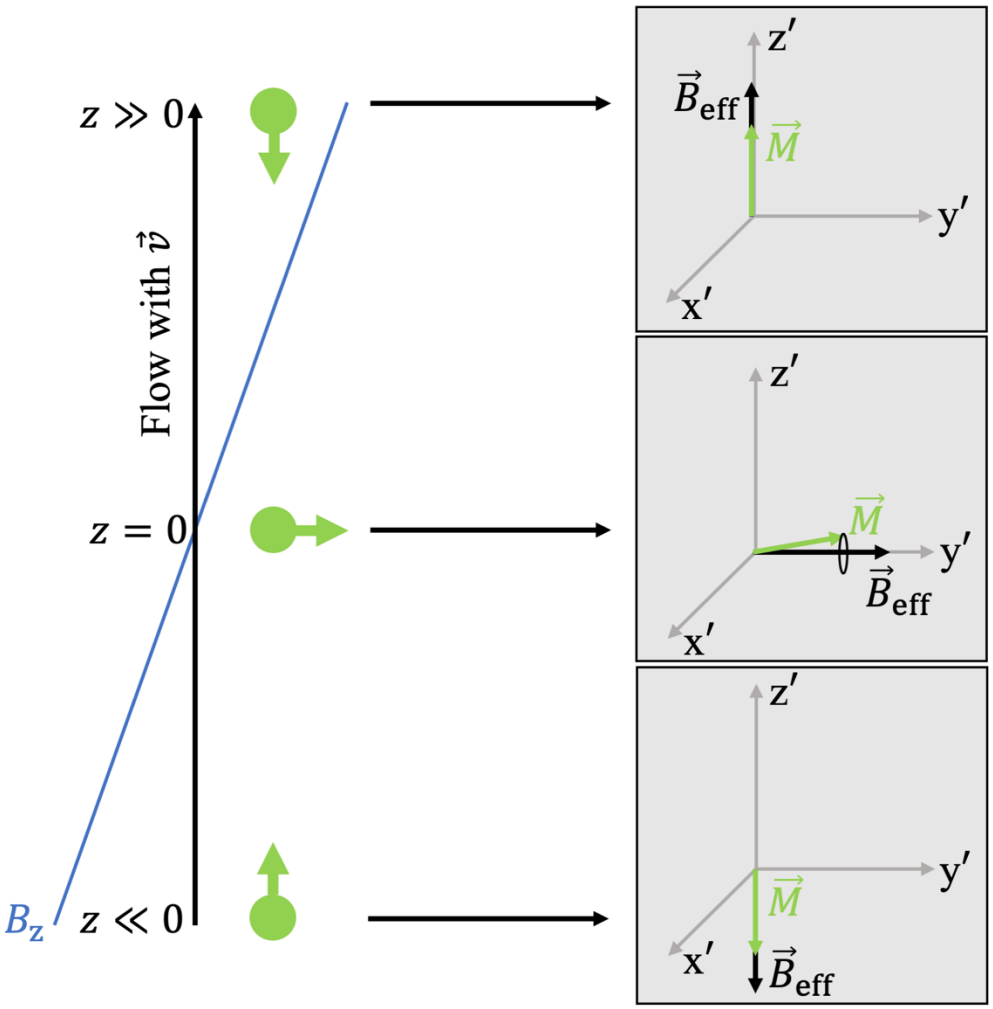

Figure 2.11: Principle of adiabatic fast passage. Spins are flowing along the direction of a linear magnetic field gradient B_z (bottom to top), while being exposed to an external RF pulse. According to the principles of the effective magnetic field, the flow of the spins results in a sweep of $\vec{B}_{\text{eff}}$, if the adiabatic condition from Eq. [2.49] is fulfilled.

2.10 Imaging Gradients

Using the concepts of excitation and relaxation, a FID signal, as depicted in Figure 2.5, can be generated. The measured signal is created by the sum of precessing spin ensembles in the excited region, which does not allow to draw conclusions about the spatial distribution of the spin density. In the following, the concepts of frequency, phase encoding and the k-space formalism are introduced, which allow to recover the spatial information from the measured MRI signals.

2.10.1 Frequency Encoding

Frequency encoding is achieved by a linear magnetic field gradient $\vec{G}_{\mathrm{freq}.} = \left(G_{\mathrm{x}}, G_{\mathrm{y}}, G_{\mathrm{z}}\right)$ during the readout of the signal. $\vec{G}_{\mathrm{freq}.}$ results in a linear variation of the precession frequency of excited spin ensembles (28). Without loss of generality, it is now assumed that $\vec{G}_{\mathrm{freq}.} = (G_{\mathrm{x}}, 0, 0)$. The resonance frequency then becomes a function of the x-coordinate:

$$\omega(x) = \omega_0 + \gamma G_{\mathrm{x}} x. \qquad [2.50]$$

Neglecting decay processes, the measured signal over time can be written as

$$S(t) = \int_{-\infty}^{\infty} \rho(x) \exp(-i\omega_0 t - i\gamma G_{\mathrm{x}} x t)\, dx. \qquad [2.51]$$

After demodulation using the carrier frequency $\exp(-i\omega_0 t)$, it follows that:

$$S(t) = \int_{-\infty}^{\infty} \rho(x) \exp(-i\gamma G_{\mathrm{x}} x t)\, dx. \qquad [2.52]$$

Eq. [2.52] is well known from the field of Fourier analysis. Here, the spatial signal distribution $\rho(x)$ of an object is directly linked to its frequency content, according to

$$S(k_{\mathrm{x}}) = \int_{-\infty}^{\infty} \rho(x) \exp(-i2\pi k_{\mathrm{x}} x) dx. \qquad [2.53]$$

A direct comparison now yields

$$k_{\mathrm{x}} = \frac{\gamma G_{\mathrm{x}} t}{2\pi}. \qquad [2.54]$$

The frequency encoding mechanism therefore enables a one-dimensional Fourier analysis of the object. Using the inverse one-dimensional Fourier transform, the projection of the object along the direction of the frequency encoding gradient can be recovered this way. Note that frequency encoding gradients are also often referred to as readout gradients.

2.10.2 Phase Encoding

Using frequency encoding, a one-dimensional projection of the object can be recovered. However, images are usually multidimensional, and thus another encoding mechanism is needed. The concept of phase encoding is quite similar to the previous description of frequency encoding. The idea is to introduce spatial phase variations across the spin ensembles in the region of interest prior to the acquisition of data (28). Let us assume a linear phase encoding gradient $\vec{G}_{\mathrm{phase}} = (0, G_{\mathrm{y}}, 0)$. During application of the gradient, the resonance frequencies of spin ensembles are again modulated:

$$\omega(y) = \omega_0 + \gamma G_{\mathrm{y}} y. \qquad [2.55]$$

Let us further assume that the phase encoding gradient is switched on for a time T_{PE}. After application of the phase encoding gradient, a position dependent phase shift

$$\Phi(y) = \int_0^{T_{\mathrm{PE}}} (\omega_0 + \gamma G_{\mathrm{y}} y) dt = \omega_0 T_{\mathrm{PE}} + \gamma G_{\mathrm{y}} y T_{\mathrm{PE}}. \qquad [2.56]$$

is then observed. The measured signal after application of the phase encoding gradient then becomes

$$S(t) = \int_{-\infty}^{\infty} \rho(y) \exp(-i\omega_0 t - i\omega_0 T_{\mathrm{PE}} - i G_{\mathrm{y}} y T_{\mathrm{PE}})\, dy. \qquad [2.57]$$

After demodulation and neglection of the constant phase term, we see that

$$S(k_y) = \int_{-\infty}^{\infty} \rho(y) \exp(-i2\pi k_{\mathrm{y}} y) dy, \qquad [2.58]$$

with

$$k_{\mathrm{y}} = \frac{\gamma G_{\mathrm{y}} T_{\mathrm{PE}}}{2\pi}. \qquad [2.59]$$

It follows that it is possible to spatially encode the measured MRI signal by phase encoding gradients in between different readout periods. Note that the subsequent combination of spatial gradients along the same axis with opposite polarities allows the formation of so-called gradient echoes. Here, a prephasing gradient is applied to dephase the generated transverse magnetization first. Afterwards, the magnetization is rephased, and the gradient echo is formed. Combining frequency and phase encoding along different spatial axes, the multi-dimensional encoding in terms of k-space can finally be described.

2.10.3 K-space Formalism

Using the concepts of frequency and phase encoding, the so-called k-space can be filled in a Cartesian fashion. A multi-dimensional inverse Fourier transform then allows straight forward recovery of the spatial spin distribution, and thus the generation of an image. So far, the concepts of frequency and phase encoding have been described for continuous signals. In practice, discrete signals are sampled in MRI. Eq. [2.53] and [2.58] are therefore expressed for discrete signals yielding the following combined formula:

$$S(k_{\mathrm{x}}, k_{\mathrm{y}}) = \sum_{-\frac{N_{\mathrm{x}}}{2}}^{\frac{N_{\mathrm{x}}}{2}-1} \sum_{-\frac{N_{\mathrm{y}}}{2}}^{\frac{N_{\mathrm{y}}}{2}-1} \rho(x,y) \exp\left(-i\frac{2\pi}{N_{\mathrm{x}}} k_{\mathrm{x}} x\right) \exp\left(-i\frac{2\pi}{N_{\mathrm{y}}} k_{\mathrm{y}} y\right). \qquad [2.60]$$

with N_{x}, N_{y} the number of discrete data points. Now, k_{x} and k_{y} describe discretely sampled points in two-dimensional k-space and x as well as y correspond to the position of discrete image pixels. The discretization of the k-space signal can be seen as a multiplication of the continuous signal with a comb-function, and from Fourier theory it follows that $\Delta k_{\mathrm{x}} = \frac{1}{N_{\mathrm{x}}}$ and $\Delta k_{\mathrm{y}} = \frac{1}{N_{\mathrm{y}}}$ need to be fulfilled to avoid aliasing in the image domain. In real world units, this corresponds to

$$\Delta k_{\mathrm{x}} = \frac{1}{\mathrm{FOV_x}}, \qquad [2.61]$$
$$\Delta k_{\mathrm{y}} = \frac{1}{\mathrm{FOV_y}},$$

which in combination with Eq. [2.54] and [2.59] defines how duration and amplitude of frequency and phase encoding gradients need to be selected in order to sample a specific point in k-space. For minimum and maximum spatial frequencies, it follows that

$$-k_{\mathrm{x,max}} = -\frac{1}{2}N_{\mathrm{x}}\Delta k_{\mathrm{x}}, \qquad k_{\mathrm{x,max}} = \frac{1}{2}(N_{\mathrm{x}} - 1)\Delta k_{\mathrm{x}}, \tag{2.62}$$

and

$$-k_{\mathrm{y,max}} = -\frac{1}{2}N_{\mathrm{y}}\Delta k_{\mathrm{y}}, \qquad k_{\mathrm{y,max}} = \frac{1}{2}(N_{\mathrm{y}} - 1)\Delta k_{\mathrm{y}}. \tag{2.63}$$

To sample k-space data in the given ranges, frequency and phase encoding gradients are typically combined. The combination with a distinct excitation pattern using RF pulses is generally known and referred to as MR pulse sequence. The basic concept for a simple pulse sequence to acquire 2D k-space using multiple excitations is demonstrated in Figure 2.12.

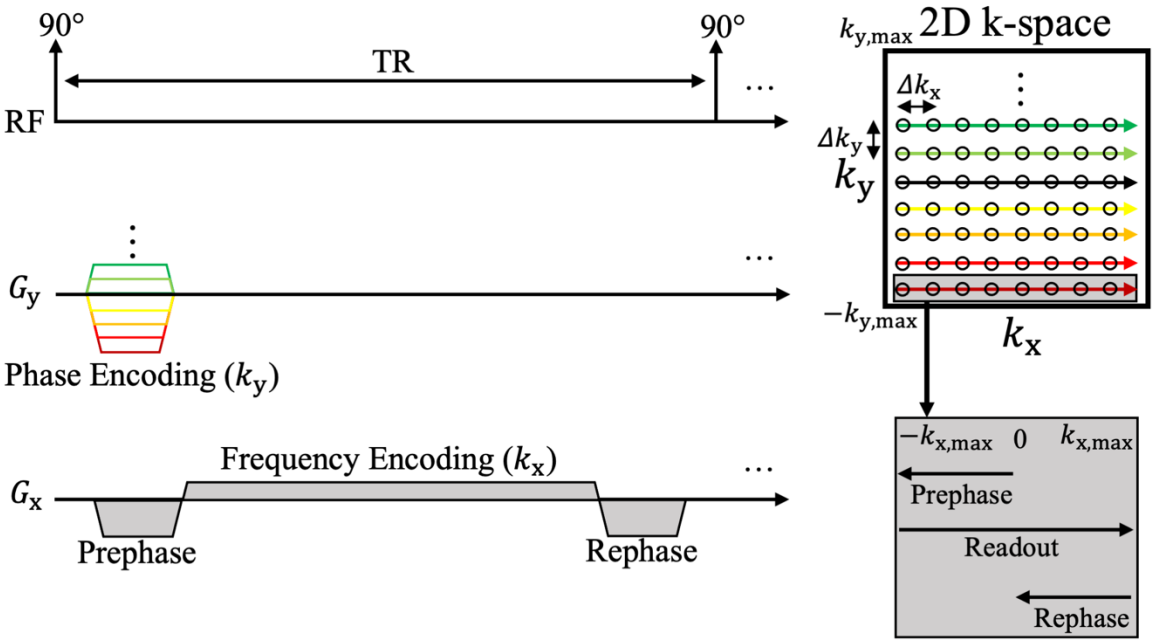

Figure 2.12: Basic pulse sequence using frequency and phase encoding to fill two-dimensional k-space. After 90° excitation, a prephasing gradient is applied on the frequency encoding axis, which starts the data readout at $-k_{\mathrm{x,max}}$. In addition, a phase encoding gradient on the G_{y}-axis encodes a specific k_{y} value. After the readout, a rephasing gradient along the frequency encoded axis removes the k_{x} momentum. Successive application of the scheme with the so-called repetition time TR and varying phase encoding gradient strengths results in sampling of the 2D discrete k-space data.

As initially mentioned, frequency and phase encoding can be applied along arbitrary linear combinations of the three spatial axes. Therefore, three-dimensional as well as non-Cartesian encoding schemes are also possible (cf. Figure 2.13). The latter might require sophisticated reconstruction algorithms however, since the inverse Fourier transform is not directly applicable to non-Cartesian data. In addition, the Nyquist criterion might be violated, and image artifacts can occur. A more detailed description of the pulse sequences applied in this work can be found in section 3.4.

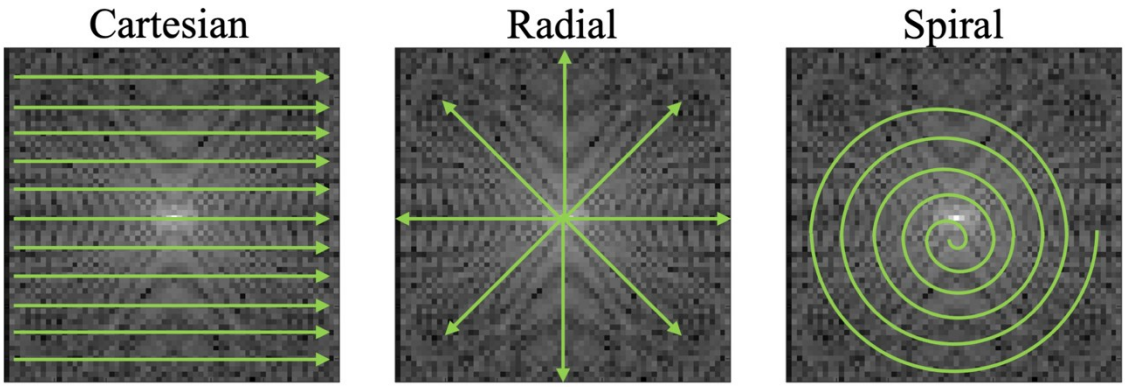

Figure 2.13: Exemplary concepts of different k-space trajectories. The standard Cartesian readout allows direct application of the inverse Fourier transform to recover the spatial image content. Other readout schemes, such as radial or spiral, require more sophisticated image reconstruction algorithms.

3 Arterial Spin Labeling

Keeping the basic concepts of signal generation and adiabaticity in mind, the idea of arterial spin labeling (ASL) will be further described next. The basic concept of ASL was first described almost thirty years ago (9) and has seen many developments and improvements over time. ASL relies on the inversion (labeling) of blood which flows into the organ of interest. After waiting for a certain delay time, which allows the labeled blood to reach the region of interest and to perfuse from macrovascular to microvascular compartments, a so-called label image is acquired using a 2D or 3D imaging sequence. Afterwards, the experiment is repeated, but the inflowing blood is not inverted, resulting in a control image. A perfusion-weighted image is calculated by subtracting both images, such that residual static tissue cancels out and the difference signal, introduced by the perfused blood, remains (cf. Figure 3.1).

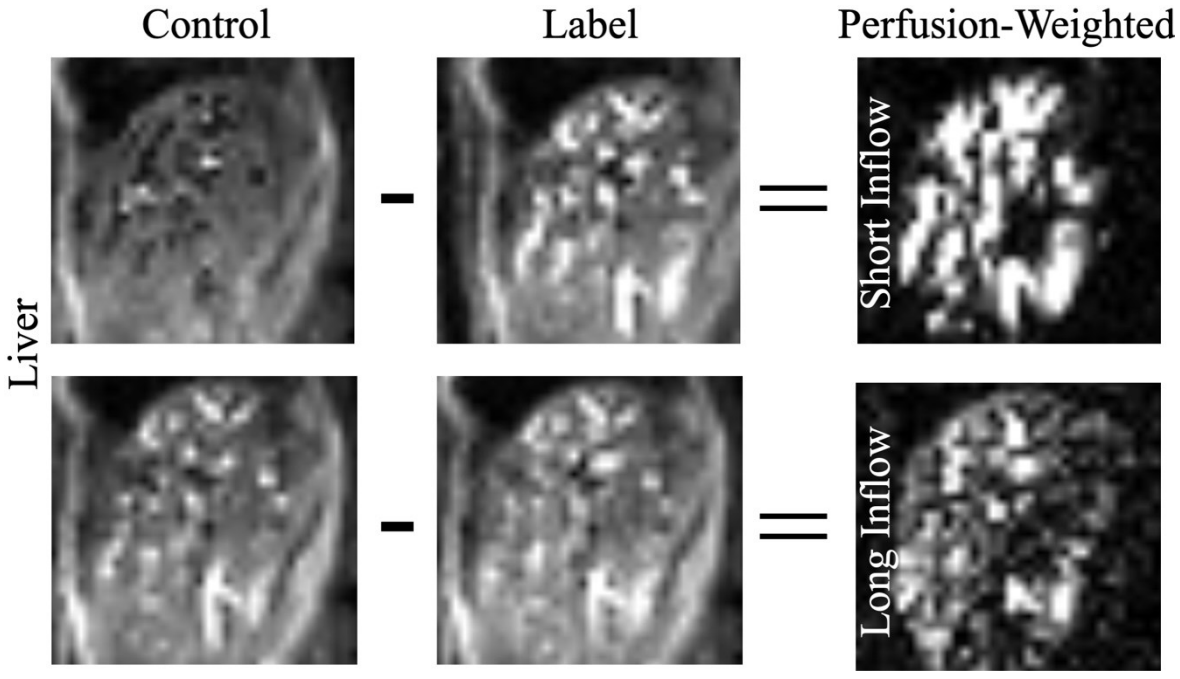

Figure 3.1: Basic ASL experiment in the liver. Label and control images with/without inversion of the inflowing blood are acquired. Between inversion and data acquisition, a delay is introduced, allowing the inverted blood to perfuse into microvascular tissue (cf. short and long inflow times). Subtraction of both images cancels the static tissue signal, resulting in a perfusion-weighted image.

Arterial spin labeling can be subdivided into different categories, which differ in the way, the labeled bolus of blood is generated. Pulsed techniques apply a single adiabatic inversion pulse to generate the label, while continuous techniques exploit the principle of adiabatic fast passage (cf. section 2.9), inverting all blood which flows through the so-called labeling plane (18)(37). Both techniques will be briefly described in this section.

3.1 Pulsed Arterial Spin Labeling (PASL)

Pulsed arterial spin labeling (PASL) describes a family of pulse sequences, which have in common that a bolus of labeled magnetization is created using a single adiabatic RF inversion pulse (18). Different PASL techniques can be distinguished by the way the inversion pulse is applied to generate label and control images.

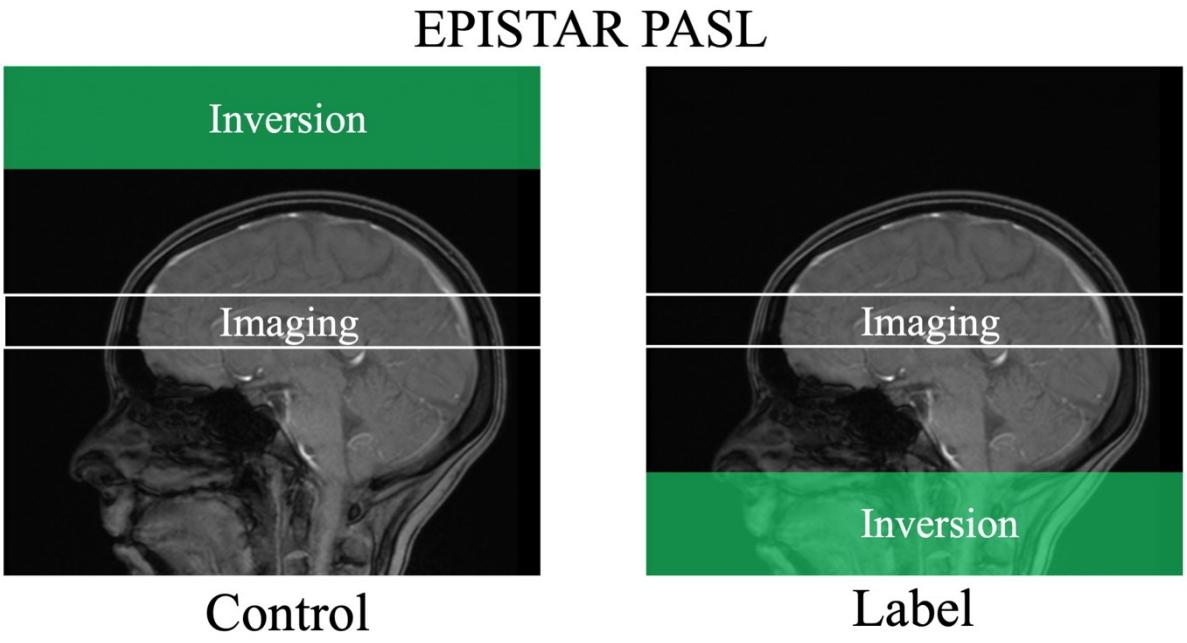

Figure 3.2: Concept of EPISTAR PASL.

In EPISTAR (**e**cho-**p**lanar **i**maging and **s**ignal **t**argeting with **a**lternating **r**adiofrequency), inflowing blood is inverted within a thick slab of multiple centimeters during the label experiment (38) (cf. Figure 3.2). Inverted blood travels to the region of interest and induces a change in the local magnetization. The control experiment is performed by mirroring the inversion region, such that the inflowing blood from the feeding vessels remains

unaffected. Mirroring of the inversion region is needed due to magnetization transfer (MT) effects, resulting from the off-resonant inversion pulse with respect to the imaging region. If the control experiment would be performed without application of the inversion pulse, the MT effects would result in additional saturation differences between label and control images, which could easily overlay the magnetization change, induced by the perfused blood. In both cases, the imaging region is usually saturated after application of the inversion pulse to further reduce MT-related signal deviations. Note that, as the name suggests, EPISTAR was initially combined with an EPI imaging readout (see section 3.4.1). However, the general concept can be applied in combination with arbitrary imaging sequences.

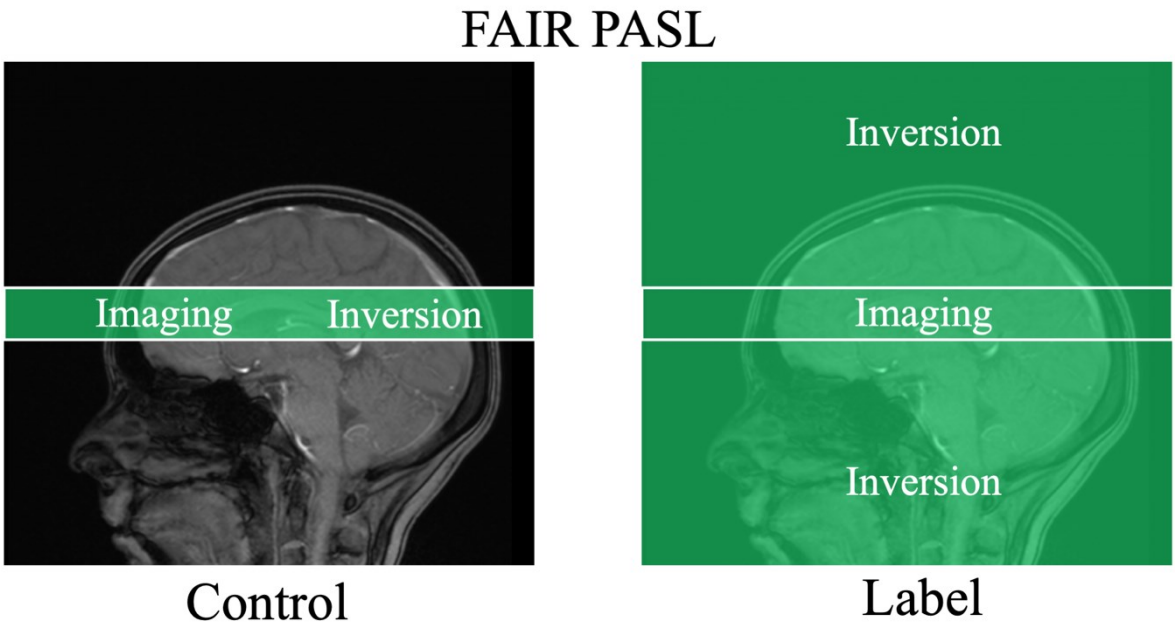

Figure 3.3: Concept of FAIR PASL.

Another concept for PASL is the FAIR scheme (**f**low-sensitive **a**lternating **i**nversion **r**ecovery). Using FAIR, an inversion pulse is applied with (control) and without (label) accompanying slice-selection gradient. Afterwards, the imaging region is saturated. In contrast to EPISTAR, the non-spatial-selective inversion results in labeling of all blood outside the imaging volume, which subsequently flows into the imaging region. In case of the control experiment, the spatial extend of the inversion pulse is reduced to the imaging region and thus inflowing blood is not affected. Note that the naming convention for the label and control case is sometimes applied vice versa in the literature (18).

FAIR shows advantages over the EPISTAR labeling approach, because the inversion pulses are applied on-resonance, which reduces magnetization transfer effects (18)(39). In addition, the global labeling of FAIR is especially helpful in organs like liver, where the exact position of arterial and portal-venous blood supplies might be unknown. A potential drawback of FAIR labeling is the need for an increased TR, due to the global labeling approach. If the time between label and control acquisition is too short, inverted blood has not yet fully recovered to its equilibrium value. The signal difference between label and control is then decreased when compared to the fully relaxed case.

3.2 Continuous and pseudo-continuous Arterial Spin Labeling

Historically, continuous arterial spin labeling (CASL) was the first ASL perfusion technique, which was shown to yield perfusion-weighted contrast and quantitative perfusion values in the rat brain by applying multiple slice-selective saturation pulses to the region in the neck (9). Further studies have demonstrated the application to human brain (40). Note that higher image SNR in perfusion-weighted images can be achieved by inverting inflowing spins, rather than saturating them, which is achieved using the principle of fast adiabatic inversion as discussed in section 2.9 (18). Here, the labeling plane is placed perpendicular to the feeding vessel of the organ of interest, such that all through-flowing blood gets inverted when leaving the labeling region. Although being quite effective, the application of a continuous RF pulse of several seconds often leads to SAR (specific absorption rate) limitations, or exceeds the capabilities of the RF amplifier (18). In addition, strong MT effects due to the off-resonant labeling pulse with respect to

the imaging region are expected. Pseudo-continuous ASL (pCASL) addresses these problems by subsampling the long continuous labeling pulse with many slice-selective, low-amplitude RF pulses, which are applied in rapid succession (cf. Figure 3.4). The basic principle was first described in (41) and will be briefly summarized here.

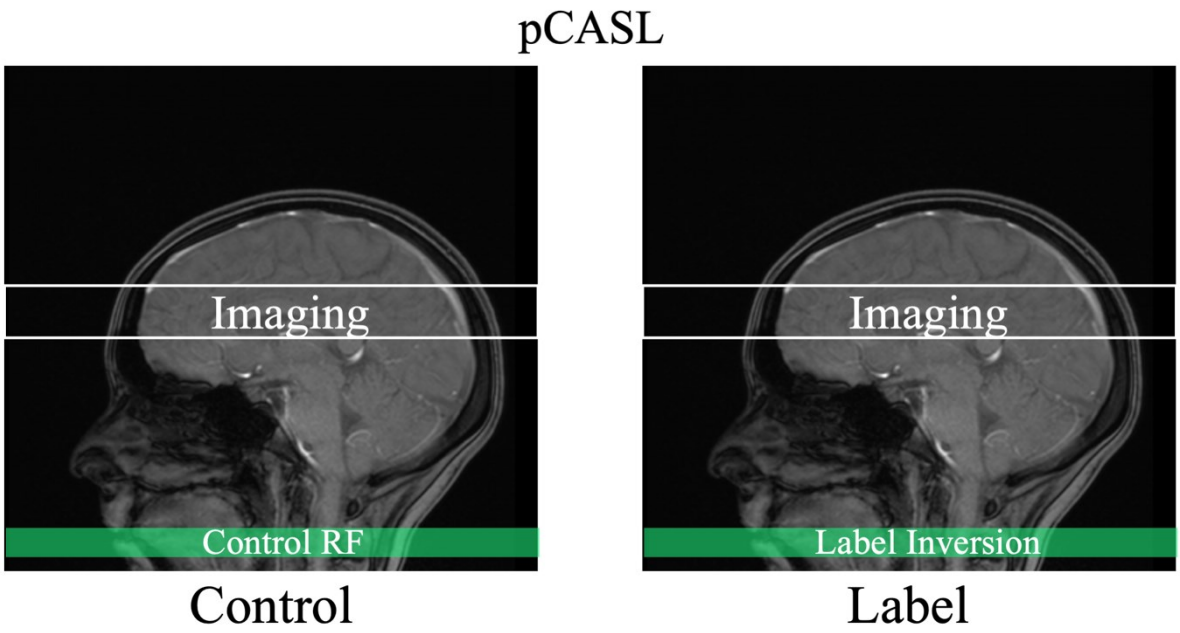

Figure 3.4: Concept of pCASL imaging. A constant RF pulse, needed for fast adiabatic inversion in the neck region, is subsampled using many low-flip angle RF pulses in the label case. For the control experiment, alternating phase shifts are introduced to the RF pulses such that no net inversion occurs but the MT effects are the same.

To decrease the load of the RF amplifier, an obvious approach is to subsample the long rectangular RF pulse by multiple short rectangular pulses (cf. Figure 3.5b) (41). The subsampled train of RF pulses can be written as a convolution of the well-known comb function with a rectangular RF pulse of duration δ, according to

$$RF_{\mathrm{Sub}} = \frac{1}{\Delta t} \cdot \mathrm{comb}\left(\frac{1}{\Delta t}\right) * \mathrm{rect}\left(\frac{1}{\delta}\right), \qquad [3.1]$$

where * denotes the convolution. Here, Δt depicts the center-to-center time of two subsequent pulses. The comb-function is defined as $\mathrm{comb}(t) = \sum_{-\infty}^{\infty} \delta\,(t - n)$, which represents a train of delta functions.

The rectangular function is defined as

$$\mathrm{rect}(t) = \begin{cases} 1, & |t| > \frac{1}{2} \\ 0, & \text{otherwise} \end{cases}. \quad [3.2]$$

The resulting slice profile is obtained by application of the Fourier transform:

$$F\{RF_{\mathrm{Sub}}(t)\} = \mathrm{comb}(f\Delta t) \cdot \delta\mathrm{sinc}(\pi\delta f). \quad [3.3]$$

Eq. [3.3] shows that replicas of the labeling plane appear at positions $f = \frac{n}{\gamma G \Delta t}$ if a gradient of strength G is applied. The replicas are modulated by the sinc function. Unfortunately, the sinc function does not decay fast enough to cancel aliasing planes. However, faster decay of the modulation can be obtained by selecting more sophisticated shapes for the subsampling pulses. An appropriate choice is a so-called Hanning pulse

$$H(t) = \begin{cases} 0.5 + 0.5\cos(2\pi t), & |t| < \frac{1}{2} \\ 0 & , \text{ otherwise} \end{cases}, \quad [3.4]$$

such that

$$RF_{\mathrm{Sub,Hanning}} = \frac{1}{\Delta t} \cdot \mathrm{comb}\left(\frac{1}{\Delta t}\right) * \mathrm{H}\left(\frac{1}{\delta}\right), \quad [3.5]$$

and

$$F\left\{RF_{\mathrm{Sub,Hanning}}(t)\right\} = \mathrm{comb}(f\Delta t) \cdot \delta \cdot \mathrm{sinc}(\pi\delta f)\frac{1}{2(1-\delta^2 f^2)}. \quad [3.6]$$

Eq. [3.6] shows that the drop of the frequency response is increased by a factor $\frac{1}{2(1-\delta^2 f^2)}$. The gradient amplitude G_{max} of a single Hanning pulse relative to the average gradient G_{ave} between concurrent pulses can be increased to further raise the spatial selectivity (cf. Figure 3.5d). Hence, aliased labeling planes will be effectively suppressed, if the condition

$$\frac{G_{\mathrm{max}}}{G_{\mathrm{ave}}} \gg \frac{\Delta t}{\delta} \quad [3.7]$$

is fulfilled (41). The average gradient over time $G_{\mathrm{ave}} \neq 0$ is added to introduce a position dependent phase shift for the labeling case and should correspond to the values selected for CASL experiments. The same holds for the average B_1 amplitude over the same time interval. For the control case, the average B_1 is set to zero by alternating the sign of subsequent RF pulses or by introducing a 180° phase shift from pulse to pulse, effectively suppressing subtraction errors due to MT effects. Note that these MT effects are generally lower than in CASL experiments, due to the increased slice selectivity of the Hanning pulses (39). In addition, pCASL labeling efficiency exceeds CASL labeling efficiency. Therefore, pCASL is the recommended continuous labeling approach in modern ASL applications (37). Pseudo-continuous ASL has potential benefits over PASL in terms of SNR; the reason being that the duration of the labeled bolus is typically longer than for PASL, where the extend is limited by the spatial coverage of the transmit coil. Another drawback of PASL is that the complete bolus is inverted at a singular timepoint during the sequence and thus experiences a global T_1 decay until arriving at the imaging plane. In pCASL, spins which were inverted at the end of the labeling phase experienced less T_1 decay, when compared to earlier inverted spins. Thus, a higher SNR can be achieved. Finally, the choice for the appropriate labeling approach heavily depends on the organ of interest.

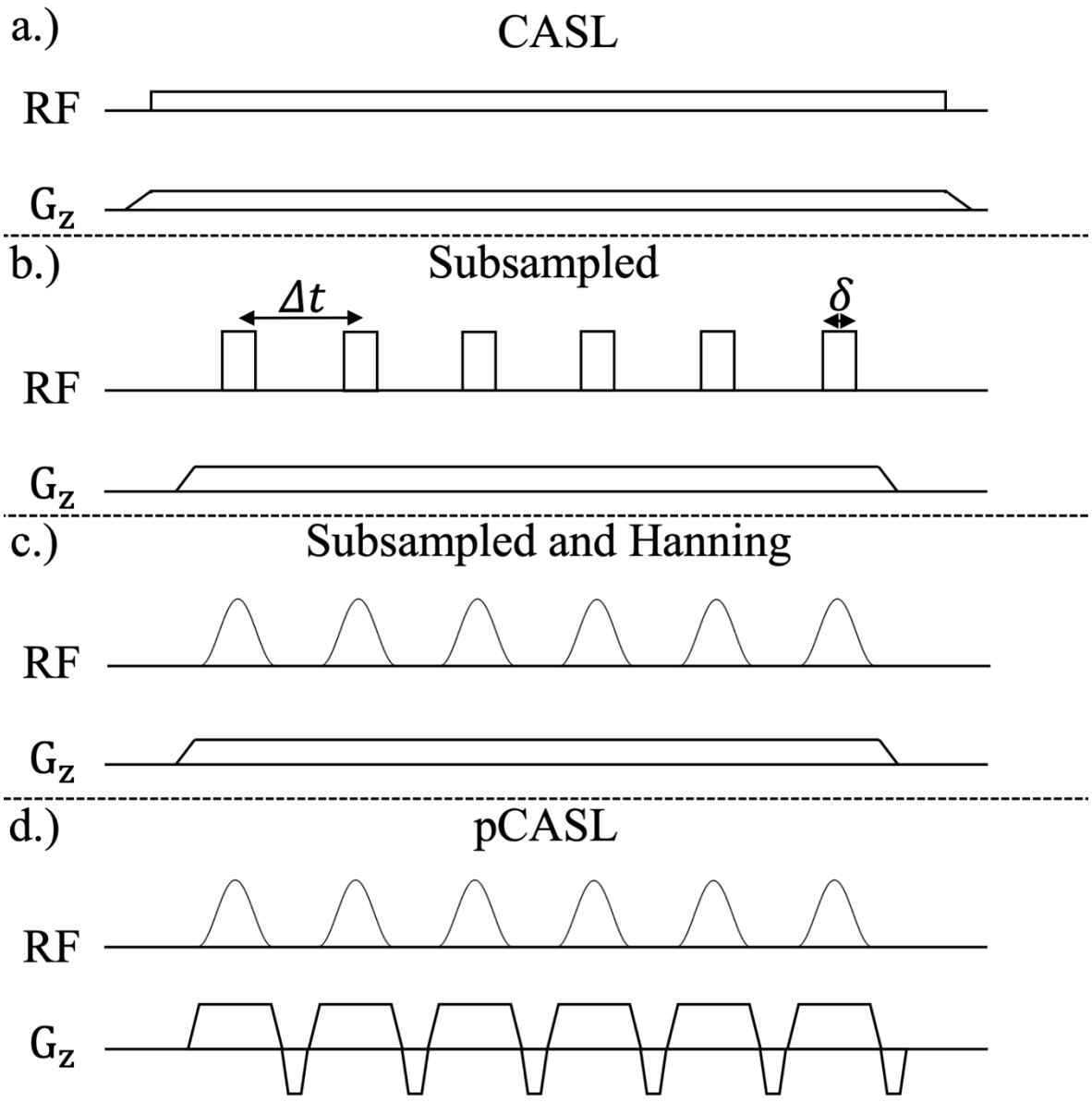

Figure 3.5: From CASL to pCASL. The continuous RF pulse is subsampled using a train of short Hanning-shaped RF pulses.

3.3 Background Suppression (BS)

PASL and pCASL techniques both rely on the subtraction of label and control images to reveal the underlying perfusion-weighted signal. Unfortunately, the difference signal is in the order of only a few percent of the static tissue signal. Therefore, subtraction errors, due to signal fluctuations and motion during the scan, are likely to overlay the desired perfusion information (36) (cf. Figure 3.6). Background suppression (BS) allows a reduction of these effects by suppressing static tissue signal using multiple inversion

recovery processes after an initial saturation (42). In addition, a spectral fat saturation module is usually applied immediately before image excitation, which excites and dephases the off-resonant fat magnetization. The schematic concept of background suppressed ASL sequences is shown in Figure 3.7a and b.

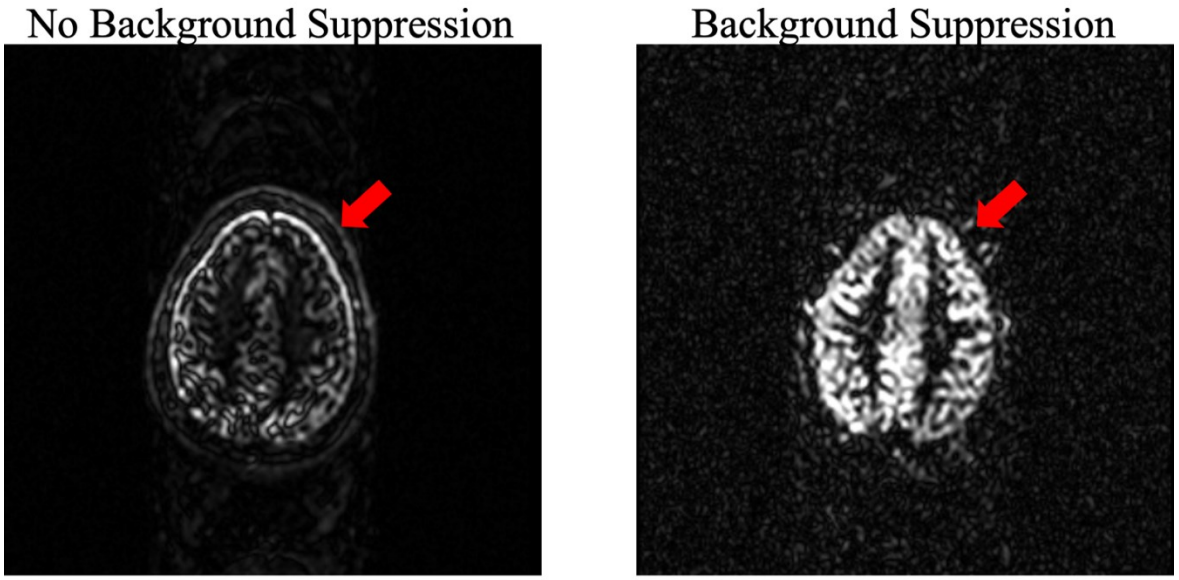

Figure 3.6: pCASL experiment with/without background suppression during the ASL preparation. Note, that different image scaling factors were applied during the online reconstruction process. Typical subtraction errors due to signal fluctuation are observed in non-perfused regions and near air-tissue interfaces if no BS is applied. Using BS, a drastic reduction of these effects is achieved.

Different methods have been proposed to calculate optimal timings of inversion pulses for a suppression of certain T_1 values at excitation (43)(44)(45). Here, the method described in (43) is briefly summarized, which allows fast analytical calculation of inversion timings for two components with relaxation times T_1 and $2 \cdot T_1$. Optimal timings after an inflow time TI are obtained by solving

$$\tau_{1,2}(TI) = TI + \frac{2}{R_1} \cdot \ln\left(\left(\frac{1}{2} \pm \frac{1}{4}\right) + \left(\frac{1}{2} \mp \frac{1}{4}\right) \cdot \exp(-1/2 \cdot T_1 \cdot R_1)\right), \qquad [3.8]$$

with $R_1 = \frac{1}{T_1}$. In typical ASL experiments, TI is either chosen to correspond to the time between saturation and excitation of the imaging pulse sequence or a short delay is introduced, nulling the static tissue signal prior to the imaging module. This is usually

beneficial, because perfect nulling of certain tissue results in opposite phase of the perfused blood in these regions, which in turn results in errors in the magnitude subtraction of label and control images (43). An example for the signal evolution with/without nulling delay is given in Figure 3.7c.

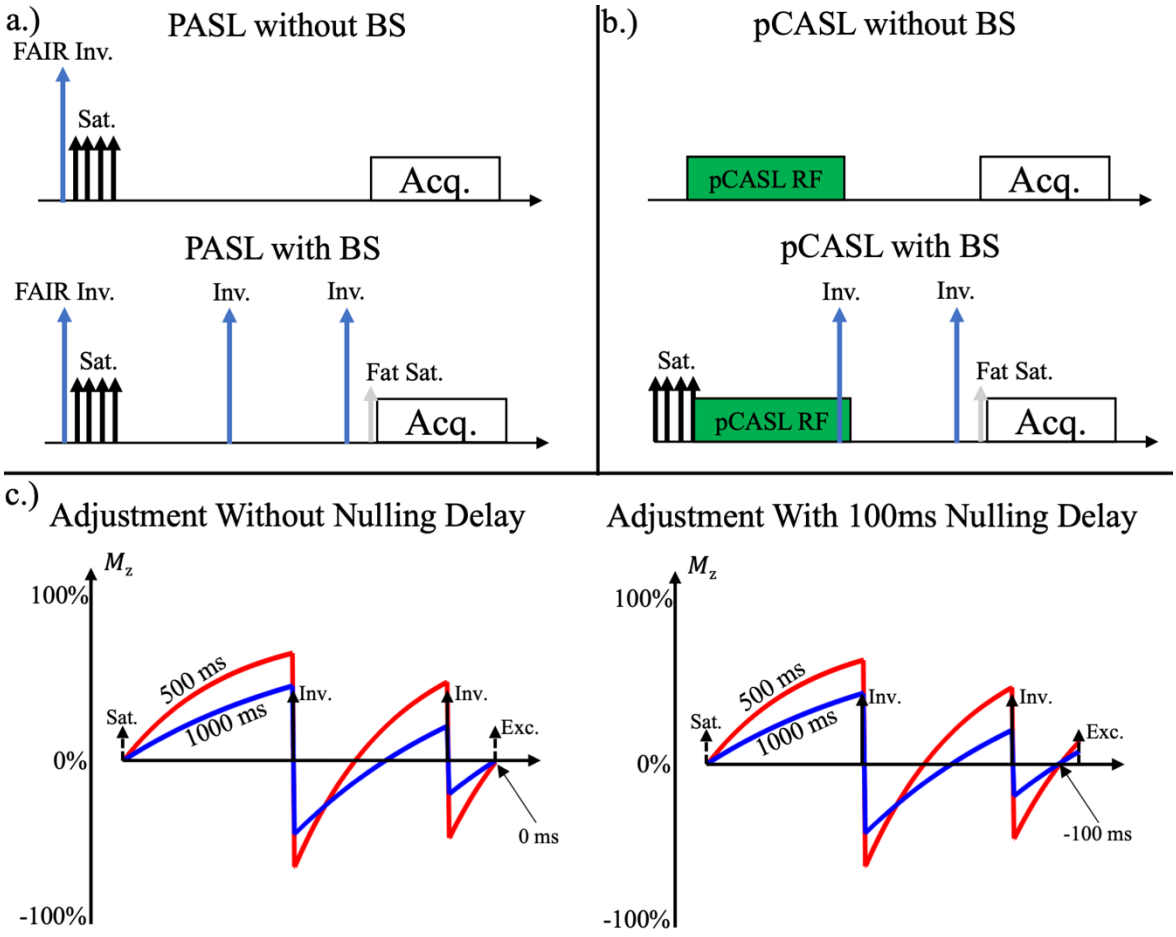

Figure 3.7: a.) PASL sequence with and without background suppression using saturation and multiple inversion pulses; b.) pCASL sequence with and without background suppression using saturation and multiple inversion pulses; and c.) Background suppression example using Eq. [3.8] for $T_1 = 500$ ms and $TI = 1000$ ms. Signal is nulled at TI and at $TI - 100$ ms. By introducing the delay, the static tissue has an overall positive sign such that subtraction errors are prevented.

If BS is applied during an ASL experiment, the initially inverted/non-inverted blood experiences multiple additional inversions during the ASL preparation phase. If an even number of BS inversion pulses is used, the initial label/control condition is restored at time of excitation (cf. Figure 3.8a). For uneven numbers, label and control conditions exchange, resulting in signal increase in case of label and decrease in case of control (cf. Figure 3.8b).

This fact must be considered when subtracting magnitude images to reveal the perfusion information.

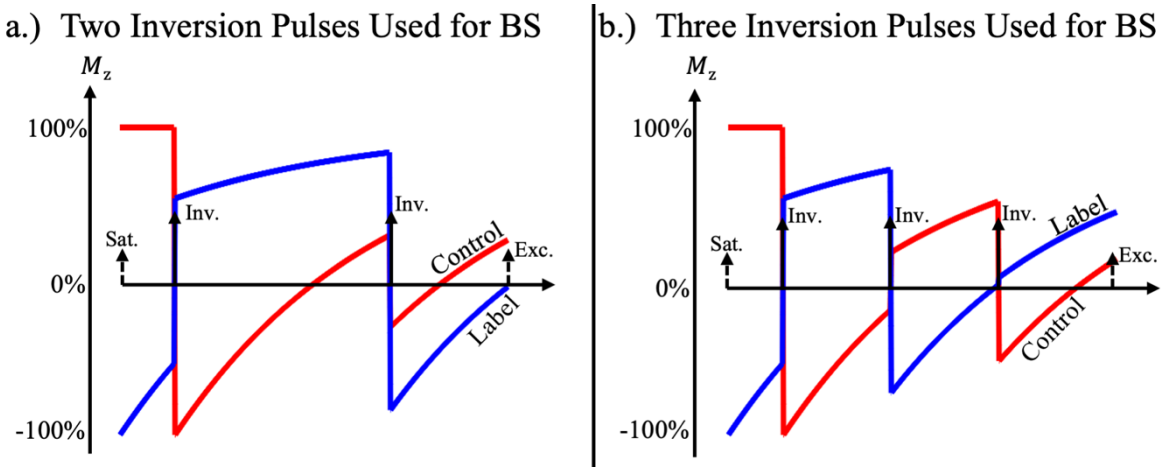

Figure 3.8: Effect of a.) even and b.) uneven numbers of inversion pulses during the BS preparation. The label/control state is interchanged with each BS inversion. If an uneven number of BS inversions is applied, the order of subtraction needs to be changed or the magnitude value must be taken.

The easiest method which generates a perfusion-weighted image subtracts magnitude label and control images and takes the magnitude of the resulting perfusion-weighted image:

$$I_{\text{perf}} = \big||C| - |L|\big|. \qquad [3.9]$$

This way, the order of subtraction does not matter, and the perfusion-weighted signal is recovered independently of the number of applied inversions (cf. Figure 3.9). The mode from Eq. [3.9] is also beneficial in those cases where the static signal is almost completely suppressed. In this scenario, the correct order of subtraction strongly depends on local distributions of residual signal. Eq. [3.9] guarantees a positive sign for the difference signal between label and control images. Another option is to take the number of inversion pulses into account and adjust the subtraction accordingly such that

$$I_{\text{perf}} = |C| - |L| \qquad [3.10]$$

in case of an even number of inversion pulses and

$$I_{\text{perf}} = |L| - |C| \qquad [3.11]$$

in case of odd numbers. If the correct order of subtraction is not applied, the perfusion-weighted signal becomes negative. Usually, perfusion-weighted images are directly reconstructed at the MRI system, which writes out DICOM images. Here, the range of gray values is adopted to the range of the desired DICOM format (usually 0 to 4095), and all values below zero are clipped. This could result in images as shown in Figure 3.9. It is also possible to perform the image subtraction using complex label and control images, according to

$$I_{\mathrm{perf}} = |C - L|. \qquad [3.12]$$

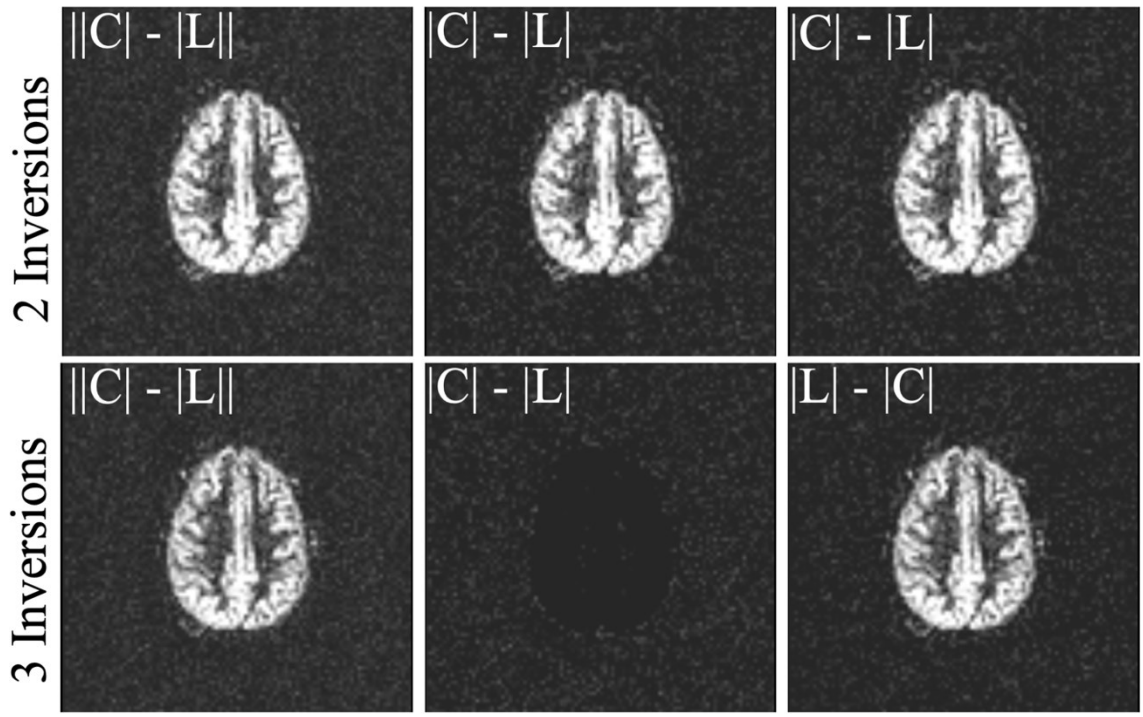

Figure 3.9: Comparison of DICOM subtraction images from a pCASL experiment using even/odd numbers of BS inversion pulses. If the magnitude of the magnitude subtraction is taken, the order of label and control subtraction does not matter. Otherwise, negative values are cut during the conversion to DICOM number ranges, and the order of subtraction must be adjusted, depending on the number of applied inversion pulses.

The perfusion-weighted image is recovered by taking the magnitude of the complex subtraction image. Note that this approach might be helpful in case of almost perfect suppression of static tissue signal, but sophisticated phase-correction schemes might be

needed if many measurements are acquired, and image data is averaged prior to the subtraction step, which is common practice in ASL imaging. It must be mentioned that the actual subtraction scheme has a direct effect on the underlying noise distribution (cf. Figure 3.10). This might be relevant for e.g., SNR analysis of perfusion-weighted images, which often assumes gaussian or Rayleigh distributions (46). While subtraction of two magnitude images results in a gaussian-like noise distribution, the conversion to positive values clearly creates a non-gaussian, non-Rayleigh distribution.

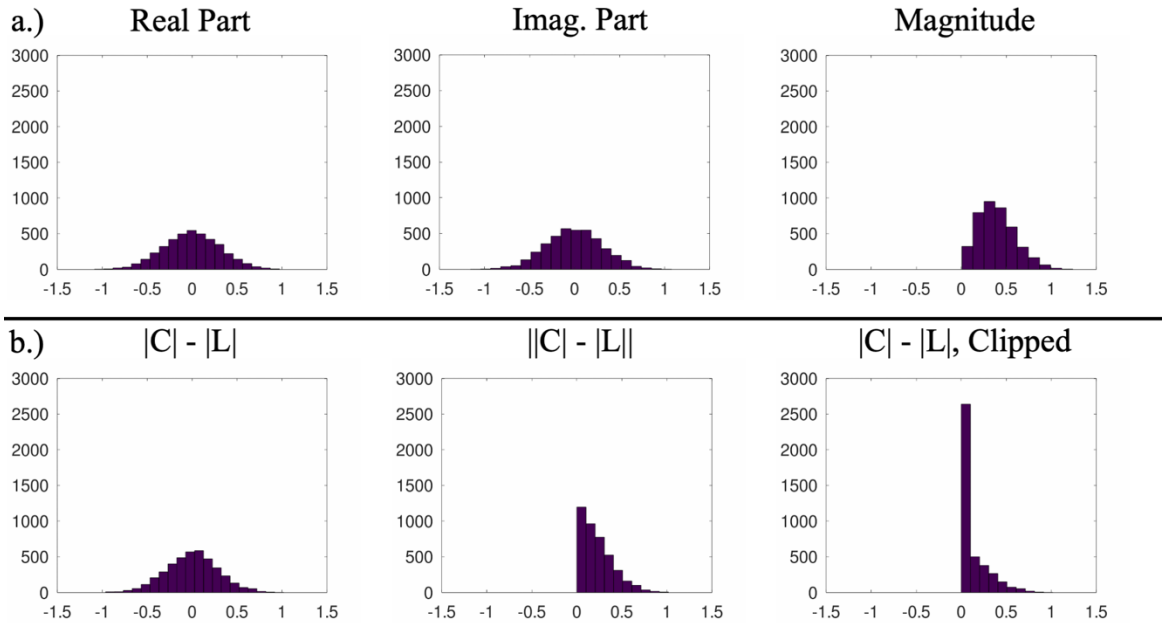

Figure 3.10: Effect of the ASL subtraction scheme on the underlying noise distribution in perfusion-weighted images. a.) Real and imaginary part of measured label/control signals show gaussian distributed noise. Magnitude calculation transforms the noise to a Rayleigh distribution; and b.) The noise distribution in calculated perfusion-weighted images heavily depends on the subtraction scheme and additional signal manipulation. SNR calculation based on DICOM images is therefore not recommended due to non-gaussian/non-Rayleigh distributed noise, which is often assumed in SNR estimation methods (46).

3.4 Selected Imaging Techniques

In principle, all MRI imaging techniques are suitable for ASL imaging, because the preparation phase is independent from the actual image acquisition. Previously, 2D imaging techniques, like multi slice single shot 2D echo-planar imaging (EPI), were recommended for use with ASL due to the rapid image readout, which makes them somewhat insensitive to motion (18). In addition, these techniques are available on all major MRI systems (37). However, 3D readouts have some major advantages over 2D readouts. First, they provide higher SNR than 2D multi slice techniques, which is a critical point in ASL imaging. In 3D imaging, a whole slab rather than a thin slice is excited during each TR. This way, more spins contribute to the measured signal during the readout window. Second, 3D techniques are better suited for optimal BS. Using 3D readouts, multiple k-space partitions are acquired after a single excitation, allowing to align the suppression or reduction of static tissue signal with the application of the excitation pulse. Using multi slice 2D sequences, multiple excitation pulses are played out, which makes BS timing less accurate for some of the later slices (37). 3D readouts can utilize many different k-space trajectories to encode the image data. Due to the simple image reconstruction, 3D GRASE is the imaging modality of choice in this work. Since 3D GRASE is based on an EPI readout strategy, both techniques are discussed in brief.

3.4.1 Echo Planar Imaging (EPI)

Echo planar imaging is a fast imaging technique, being able to generate a two-dimensional image in a couple of milliseconds (18). The technique was proposed in the late 1970s and allows sampling of complete k-space after a single excitation (47). In EPI, a series of bipolar frequency encoded readout gradients is applied. In combination with a corresponding prephasing gradient, multiple gradient echoes are generated this way. In between different gradient echoes, a phase encoding gradient is applied, which steps through the second k-space dimension resulting in a two-dimensional set of k-space samples. The corresponding sequence diagram is shown in Figure 3.11.

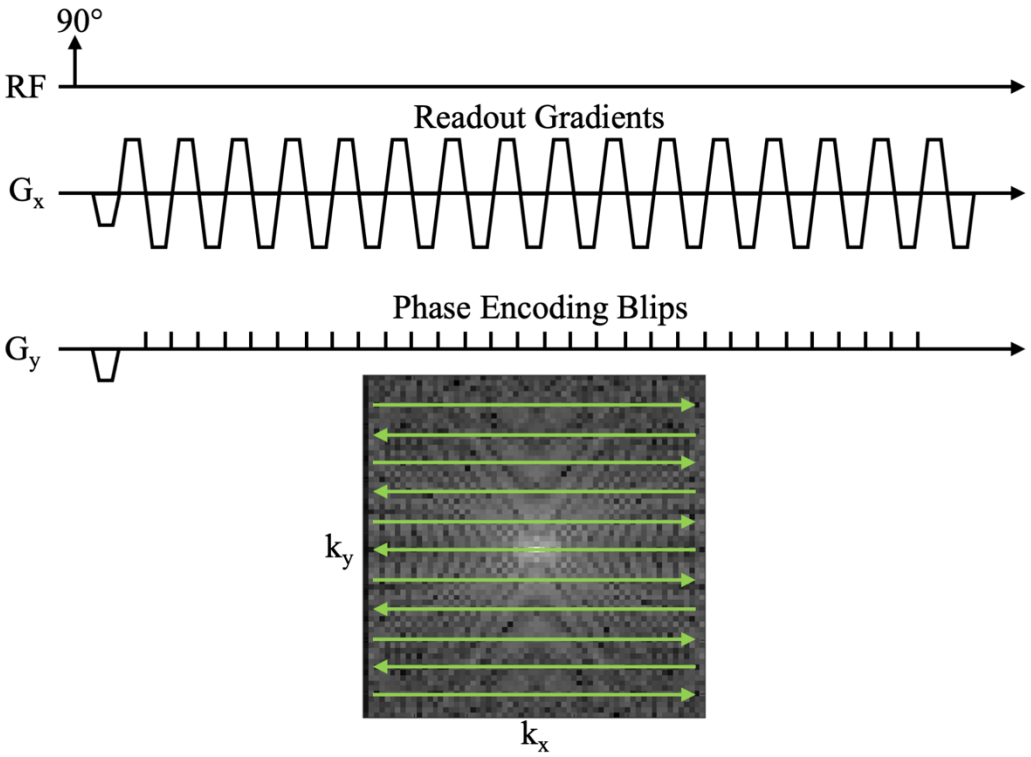

Figure 3.11: Basic concept of EPI image formation. After application of prephasing gradients, multiple frequency encoded readout gradients are played out to generate multiple gradient echoes. So-called phase encoding blips are played out in between to encode the second k-space dimension. In addition, three-dimensional EPI image acquisition is possible by another phase encoding gradient.

The number of acquired gradient echoes after the excitation pulse is referred to as echo train length. The echo spacing describes the time interval between the acquisition of two neighboring points in the k_y direction.

3.4.1.1 EPI Image Artifacts

The fast EPI image acquisition comes with some major drawbacks concerning artifacts in resulting images, as shown in Figure 3.12.

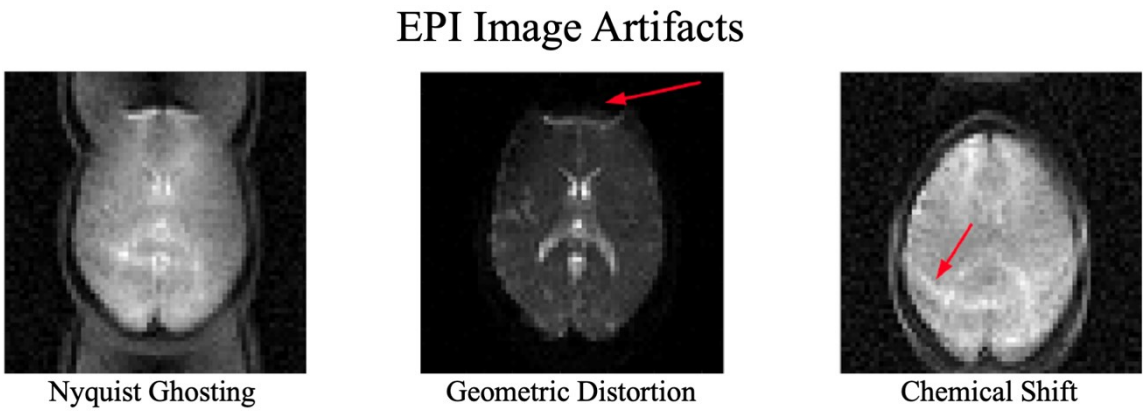

Figure 3.12: Common EPI image artifacts. While Nyquist ghosting can be a result of phase errors induced by eddy currents, geometric distortion and chemical shift artifacts are the result of additional phase accumulation due to local or tissue dependent off-resonance.

The most common artifact is so-called Nyquist Ghosting. Ghosting artifacts arise if phase errors are introduced between even and odd lines in k-space. In EPI imaging, these lines are acquired with opposite readout gradient lobes, resulting in delays and inconsistent phase errors. The latter are the result of eddy currents. If these phase errors are not corrected, ghosting artifacts occur. Most common, a reference scan, sampling the k-space origin with both readout polarities, is therefore integrated into the EPI sequence. From the acquired data, phase errors can be estimated and corrected in the subsequent image data. In most applications, this approach is sufficient for adequate ghost removal. If needed, more sophisticated techniques exists (48)(49).

Geometric distortion arises from inhomogeneities in the main magnetic field. This can be easily understood when recalling the image encoding process as described by the k-space formalism in Eq. [2.60]. The EPI encoding scheme creates measurable k-space signal according to

$$S(k_x, k_y) = \sum_{-\frac{N_x}{2}}^{\frac{N_x}{2}-1} \sum_{-\frac{N_y}{2}}^{\frac{N_y}{2}-1} \rho(x,y) \exp\left(-i\frac{2\pi}{N_x}k_x x\right) \exp\left(-i\frac{2\pi}{N_y}k_y y\right). \quad [3.13]$$

Let us further recall Eq. [2.9], which states that the precession frequency of a spin ensemble is directly linked to the strength of the local magnetic field B_0. Assuming local magnetic field variations ΔB_0, ensembles will experience an additional phase accumulation throughout the EPI pulse train according to

$$\Delta\Phi_{\mathrm{RO}} = \frac{\Delta B_0}{\gamma} \cdot \Delta t_{\mathrm{RO}}, \qquad [3.14]$$

and

$$\Delta\Phi_{\mathrm{PE}} = \frac{\Delta B_0}{\gamma} \cdot \Delta t_{\mathrm{PE}}, \qquad [3.15]$$

with Δt_{RO} and Δt_{PE} the temporal spacing between the acquisition of neighboring k-space samples in readout and phase encoding directions. In EPI, Δt_{RO} is usually short (in the order of microseconds), because the readout bandwidth is high to avoid signal loss arising from T_2^* decay (see section 2.4). Therefore, the corresponding phase accumulation can be neglected. In the phase encoding direction, however, Δt_{PE} is in the order of milliseconds and a non-neglectable phase accumulation occurs. It is now assumed that the k_{y} direction is phase encoded. Inserting Eq. [3.15] into [3.13], the phase encoding process can be written as

$$\begin{aligned} \Phi\left(k_{\mathrm{y}}, \Delta t_{\mathrm{PE}}\right) &= \exp\left(-i\frac{2\pi}{N_{\mathrm{y}}}k_{\mathrm{y}}y\right)\exp\left(-ik_{\mathrm{y}}\Delta\Phi_{\mathrm{PE}}(y)\right) \\ &= \exp\left(-i\frac{2\pi}{N_{\mathrm{y}}}k_{\mathrm{y}}\left(y + \frac{N_y\Delta\Phi_{\mathrm{PE}}(y)}{2\pi}\right)\right) \\ &= \exp\left(-i\frac{2\pi}{N_{\mathrm{y}}}k_{\mathrm{y}}(y + \Delta y)\right). \end{aligned} \qquad [3.16]$$

It follows that the additional phase accumulation translates into an artificial position offset. This results in geometric image distortion, as demonstrated in Figure 3.12. Different techniques exist to correct for geometric distortion. One of the most widespread techniques is Topup (50). Here, two images are acquired with alternated phase encoding directions. The unique distortion in each of the images allows estimation of the underlying field map.

Finally, chemical shift artifacts are closely related to geometric distortion. In contrast to water protons, fat shows a shift in the resonance frequency of about 440 Hz at a field strength of 3T. This again results in a spatial displacement of corresponding signals. In contrast to geometric distortion, chemical shift artifacts are difficult to correct retrospectively, due to the large spatial offsets. It is therefore common to apply spectral fat saturation pulse before image excitation and acquisition.

3.4.2 3D GRASE

The term GRASE stands for gradient and spin echo and describes the basic idea behind the technique: A train of RF refocusing pulses is played out together with alternating gradient lobes, which form a gradient and spin echo, respectively. A schematic representation of the pulse diagram is given in Figure 3.13. After the initial excitation pulse, multiple refocusing pulses are played out, forming spin echoes at the center between consecutive pulses. Each refocusing pulse is accompanied by a slice-selection gradient and a pair of so-called crusher gradients. Crusher gradients are needed, because multiple signal pathways are created after application of the RF pulse (51). By applying the same gradient lobe before and after the refocusing pulse, the wanted signal is first dephased and then rephased, while additional signal is effectively spoiled. Different gradients follow, encoding the current k-space partition (G_z) as well as the in-plane phase (G_y) and readout (G_x). The in-plane readout is based on the EPI sequence (cf. section 3.4.1), which acquires k-space data of the current partition, followed by a gradient (G_z) which reverses the partition moment. In single-shot acquisitions, the procedure is repeated until the data of all partitions is collected.

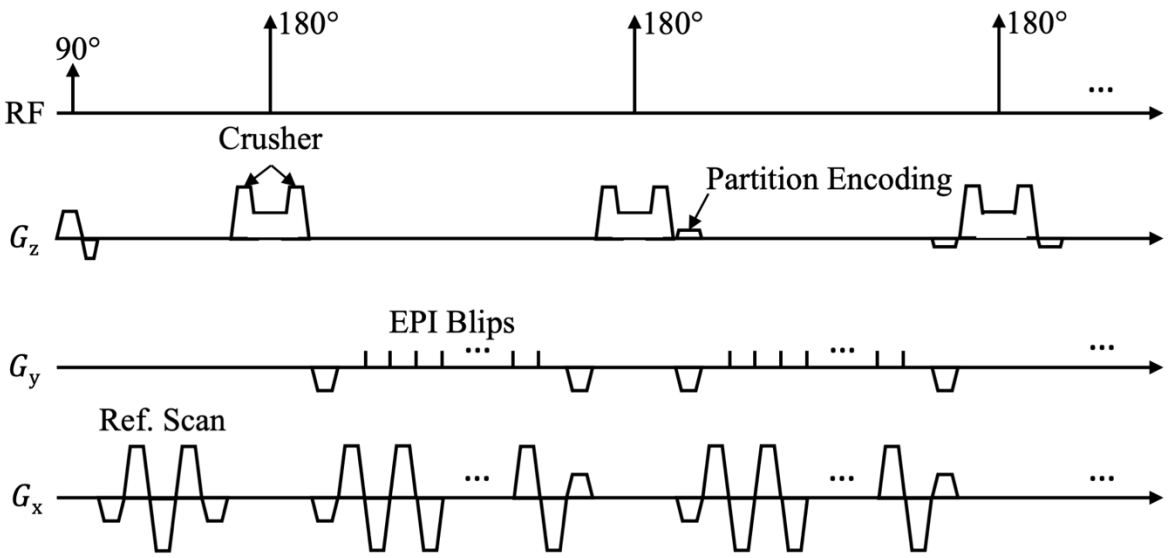

Figure 3.13: Schematic representation of the 3D GRASE pulse diagram. In this implementation, the central k-space partition is acquired first. Subsequently, remaining partitions are acquired in a center-out fashion.

Images acquired using 3D GRASE combine properties from EPI readouts and spin echo readouts like RARE (18). First, T_2 decay occurs after the initial excitation pulse. Since different partitions are acquired after each refocusing pulse, the T_2 decay majorly shows in a decrease of signal along the partition direction, which limits the number of partitions which can be acquired after a single excitation. However, no continuous phase accrual appears along the partition encoding direction, due to the refocusing pulses, making the partition dimension of 3D GRASE rather insensitive to off-resonance effects. Note that this does not hold for the in-plane direction. Here, the EPI-like readout is affected by off-resonance effects, which lead to image distortion. In addition, the typical EPI ghosting artifacts can occur (cf. 3.4.1.1). Finally, some amount of T_2^* weighting is observed in the in-plane direction (18). In order to decrease T_2 and T_2^* related effects, it is common to apply a segmentation in the phase or partition encoding direction. Using segmentation, not all k-space data is acquired after a single shot. Instead, k-space is divided into different segments, which are acquired after subsequent excitations. A segmentation of the in-plane phase encoded direction comes with the additional benefit of reduced geometric distortion, because additional phase which is accumulated in between the acquisition of subsequent k-space lines is reduced. However, segmentation of the partition encoding direction is also possible. As a potential drawback, Cartesian segmentation of the 3D GRASE readout comes with the disadvantage of increased sensitivity to subject motion during the scan, because multiple ASL preparation phases and excitations are needed to completely fill the 3D k-space. Subject motion is a common problem in clinical reality (52). If e.g., rotational motion occurs in between the acquisition of two Cartesian segments, correction of motion and recombination of the data becomes difficult, since different parts of k-space are sampled, resulting in a random distribution of missing k-space samples. In addition, retrospective estimation of subject motion from single segments is not straight forward, requiring reconstruction of whole k-space data using parallel imaging algorithms, such as ESPIRIT (53). In 2011, Tan et al. therefore demonstrated 3D GRASE PROPELLER as an alternative segmentation approach (54).

3.4.3 3D GRASE PROPELLER

3D GRASE PROPELLER (3DGP) is an in-plane segmentation approach of 3D GRASE readouts, based on the famous PROPELLER (**P**eriodically **R**otated **O**verlapping **P**aral**EL** **L**ines with **E**nhanced **R**econstruction) trajectory (55). Using 3DGP, multiple rectangular

three-dimensional bricks are rotated around the origin of k-space (cf. Figure 3.14) with each shot. Each brick samples a unique part of higher k-space frequencies. The central k-space region is sampled by each brick and allows the reconstruction of a low-resolution navigator image as indicated by the red circle in Figure 3.14.

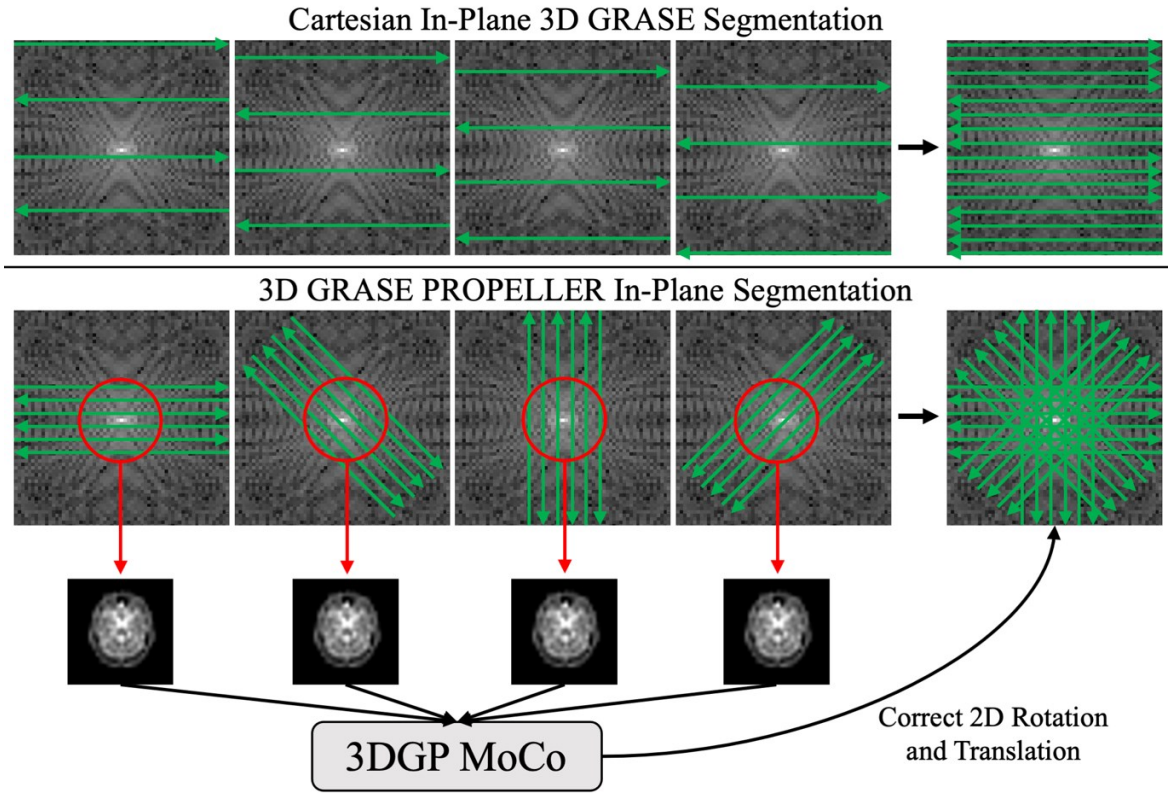

Figure 3.14: Comparison between in-plane Cartesian and PROPELLER segmentation using 3D GRASE readouts. While Cartesian-segmented 3D GRASE acquires different three-dimensional sets of Cartesian lines with each shot, the PROPELLER trajectory rotates so-called bricks around the origin of k-space. Since low-resolution information is encoded within the central part of each brick, multiple navigators can be reconstructed and registered. Using estimated motion, the angles and linear phase ramps of acquired data can be corrected, and a motion corrected image is reconstructed after combination of individual bricks.

If motion occurred in between the acquisition of two 3D GRASE bricks, in-plane rotational and translational estimates can be found by maximizing the cross-correlation between the central navigator regions. Motion is then corrected by applying corresponding adjustments of the acquisition angle in k-space as well as linear phase modulations to remove translational motion (55). A two-dimensional example of the PROPELLER motion correction pipeline is given in Figure 3.15.

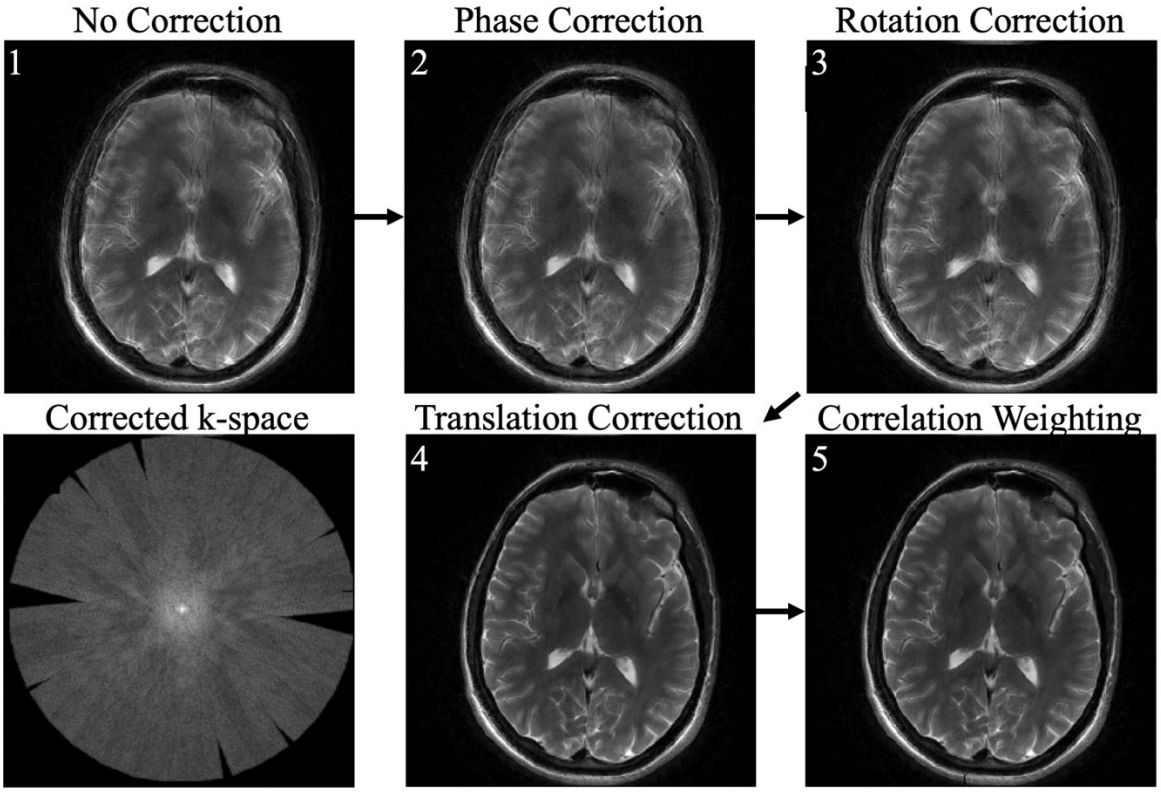

Figure 3.15: Example for the retrospective motion correction as described in (55) using a 2D PROPELLER segmentation of a turbo spin echo readout with intentional subject motion during the scan: 1) Reconstructed data without any correction algorithm; 2) Reconstructed data with additional phase correction. Although not present in this example, signal loss due to phase incoherence might occur in PROPELLER imaging; 3) Additional rotation correction. Note, how the fanning out of structures in the frontal area is visibly reduced; 4) Additional correction of translational motion by removal of linear phases. Motion artifacts are now visibly reduced; and 5) Additional correlation weighting. If strong through-plane motion occurred, this step would further improve the image quality.

Besides the capability for motion correction, a PROPELLER segmentation of the 3D GRASE readout comes with some drawbacks when compared to a Cartesian segmentation. First, the oversampling of the k-space center comes at the cost of additional scan time, because more shots are needed to fully sample k-space. If the same scan time for Cartesian-segmented and 3DGP acquisitions is desired, more phase-encoded lines per segment need to be measured with each 3DGP shot as demonstrated in Figure 3.14. This however increases the in-plane T_2^* blurring and prolongs the acquisition window, which also results in increased through-plane blurring when compared to the Cartesian segmentation. In addition, geometric distortion appears different when comparing a 3DGP

segmentation with its Cartesian counterpart. Using 3DGP, individual bricks are acquired with the same temporal spacing between phase encoded lines as done in single-shot acquisitions. Therefore, reconstructed navigators from the k-space origin can contain a severe amount of image distortion. The direction of distortion in individual navigators is rotated in accordance with the phase-encoding direction. The different directions of distortion add up during the final k-space combination of individual bricks, resulting in smearing of signal in affected regions (cf. Figure 3.16).

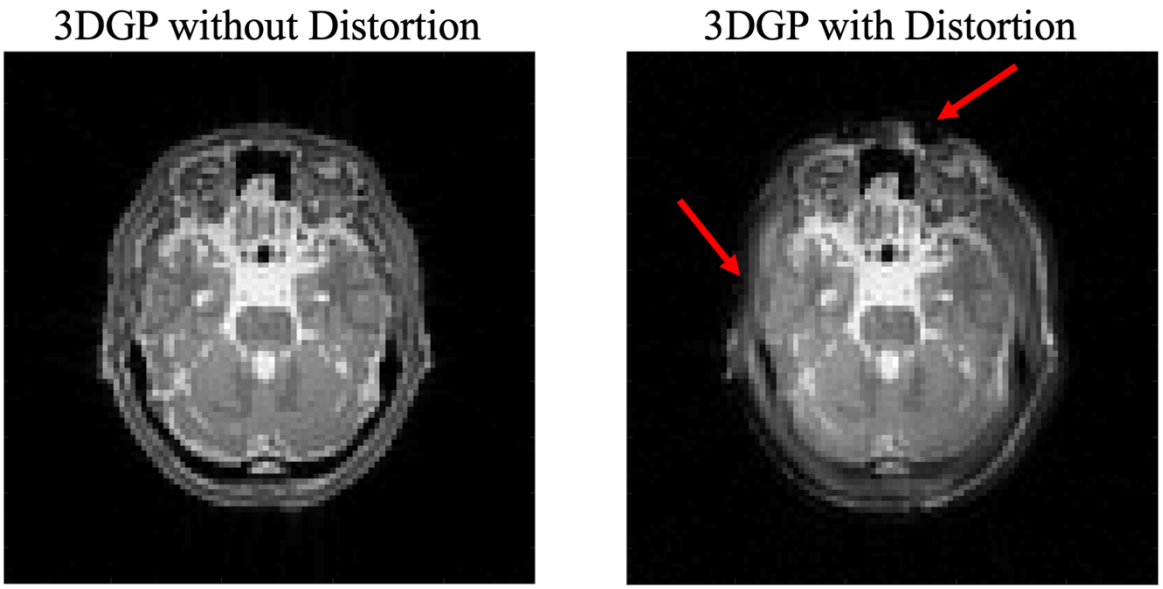

Figure 3.16: Simulation of 3DGP acquisitions with and without additional off-resonance fields. The smearing of signal is indicated by the red arrows. Simulations were carried out using the Jemris simulation framework (56).

Part II

New Methodology

Introduction to Part II

The basic concepts of ASL were described decades ago. Further improvements, in terms of pCASL labeling and 3D image acquisition with additional background suppression, greatly improved the SNR when compared to the early methods. However, to date, ASL never found wide application outside the scientific community. The major remaining challenge of ASL is the sensitivity to motion during the scan, which, unfortunately, is common in clinical practice (52). In most ASL experiments, multiple averages are acquired for each label/control preparation, resulting in typical measurement times of several minutes. All collected data is finally used to calculate a single perfusion-weighted subtraction image, which is the reason for the high motion sensitivity (cf. Figure 3.17).

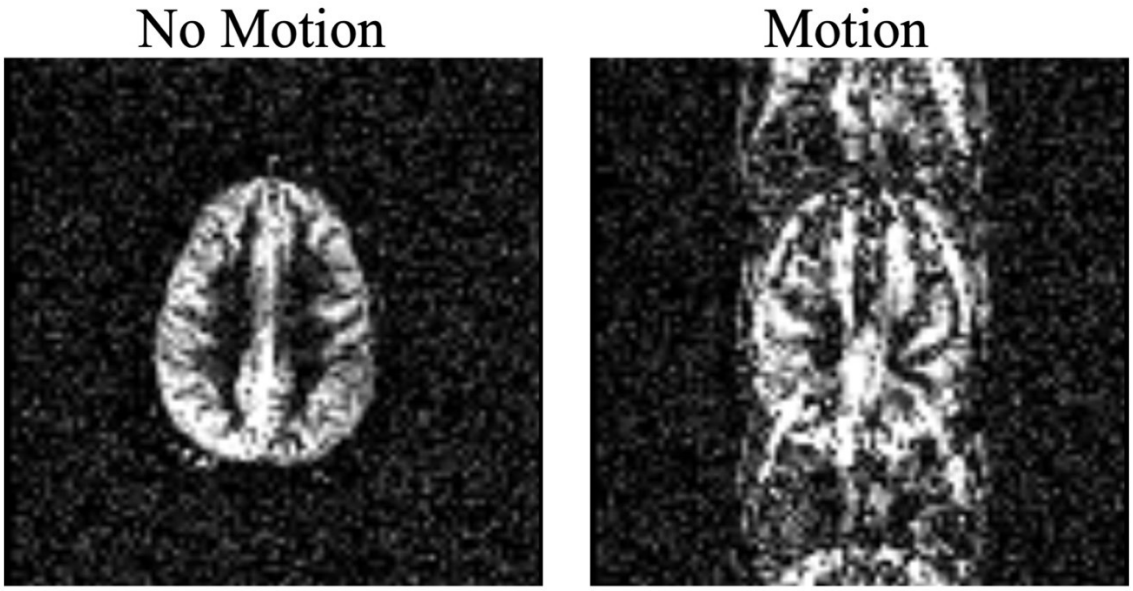

Figure 3.17: Comparison of brain ASL imaging without/with subject motion during the scan. As shown, the perfusion information is overlayed by static tissue subtraction errors as well as ghosting artifacts.

Motion during ASL examinations can occur in different forms. During brain scans, the likelihood of slow drifts or random changes in position increases with scan time (57). This type of motion can be modeled using two- or three-dimensional rigid body models, and it was shown that retrospective in-plane rigid body motion correction can be achieved using a PROPELLER readout (54)(55). In combination with ASL imaging, the application of 3D GRASE PROPELLER (3DGP) was demonstrated, but potential effects of inhomogeneities

of the main magnetic field on the accuracy of estimated motion trajectories were neglected. In addition, the feasibility of three-dimensional rigid body motion correction using 3DGP was not investigated so far.

Another common source of motion, which is almost unavoidable during ASL scans, is respiration. Respiratory motion is especially problematic in liver ASL scans, due to the proximity of the liver to the lungs, resulting in severe displacements of the organ throughout the breathing cycle. Retrospective correction of the high frequent breathing motion is challenging. Therefore, respiratory motion is typically compensated using long breathholds or timed-breathing protocols, which were demonstrated to be quite effective in liver ASL examinations (58). However, for untrained subjects or patients, the strict breathing patterns might be difficult to follow. In addition, scan times are prolonged, due to phases of respiration without data acquisition. A robust technique for free-breathing liver ASL imaging is therefore of high clinical interest.

Irrespective of the origin of motion, background suppression was shown to be an important technique for reduction of motion related artifacts in ASL imaging. Many techniques have been proposed (42)(43)(45), but no recommendation for application in combination with additional motion correction techniques was given so far. In addition, the proper selection of background suppression related parameters prior to the scan is often complex and might result in imperfect setups, affecting the quality of perfusion-weighted images.

Section 4 introduces novel methodologies which were especially designed for motion compensation in ASL imaging, addressing the potential inadequacies of current approaches. In section 5, developed techniques were evaluated in brain and liver ASL imaging using healthy volunteers and additional phantom scans. A general discussion and conclusion about the future developments in the field of motion robust ASL imaging is given in section 6.

4 Novel Strategies for Motion Compensation in ASL Imaging

4.1 Reduction of Motion Sensitivity using Background Suppression

4.1.1 Introduction

Background suppression (BS) is an important aspect of most modern ASL pulse sequences to reduce the sensitivity to motion. The basic idea is to decrease the amount of static tissue signal at excitation. This way, subtraction errors, arising from minor displacements or static signal fluctuation, are prevented (also cf. section 3.3). Typically, the suppression or reduction of the static tissue signal is achieved by an initial saturation of the imaging volume followed by multiple inversion pulses. The timing of the inversion pulses heavily depends on the total inflow time and the T_1 values to be suppressed. Therefore, different BS approaches have been proposed, which provide a calculation of suitable inversion timings (42)(43)(45). All of these have in common that the magnetization of a fixed range of T_1 values is cancelled at a specific timepoint, which either coincides with the imaging excitation or is placed a few milliseconds before the excitation. This delay prevents subtraction errors arising from phase variations of the static tissue signal. Unfortunately, off-resonant fat signal shows short T_1 times and recovers a large amount of its longitudinal magnetization during the temporal gap between nulling and image excitation. Therefore, a spectral-selective fat saturation pulse is often applied immediately before the image excitation to cancel chemical shift artifacts. The spectral saturation efficiency might however be decreased, due to inhomogeneities in the main magnetic field. Severe inhomogeneities are typically present in abdominal imaging (59). Residual fat signal in acquired label and control images is a major problem if motion occurs, and the on-resonant static tissue signal is subsequently aligned using motion correction algorithms. This can be easily understood from Figure 4.1a. Using a 3D GRASE readout, the shift of fat occurs in

the in-plane phase encoded direction. If motion occurs during the scan and is corrected retrospectively by registering the on-resonant residual static tissue signal in both images, mismatches of the shifted fat occur. The signal of the latter will then not cancel out during the subtraction procedure as exemplarily demonstrated for the 3D GRASE PROPELLER experiment in Figure 4.1b.

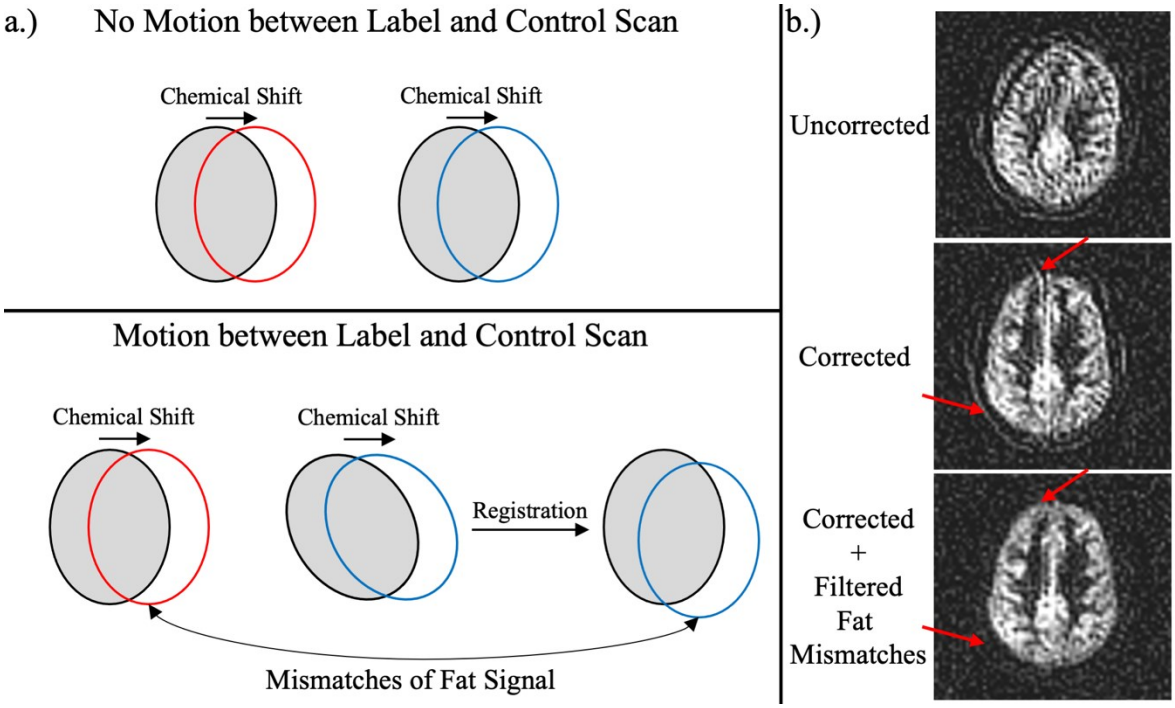

Figure 4.1: a.) Effects of chemical shift artifacts in ASL imaging. If no motion occurs, shifted fat signal is at the same position in subsequent label and control images and is canceled out after image subtraction. If motion occurs, and the phase encoding direction remains the same, fat shows slight offsets after registration of the on-resonant static tissue signal. Thus, subtraction errors might be introduced in the perfusion-weighted image; and b.) Example of this effect in an ASL experiment with motion and a 3D GRASE PROPELLER readout. After motion correction, the perfusion-weighted image clearly shows non-zero subtractions in non-perfused areas. After filtering all data which showed mismatches of fat signal residual errors are removed.

It can be easily followed that almost perfect nulling of fat is mandatory if robust motion correction in ASL imaging is desired. Therefore, a novel BS approach, which combines a spectral fat saturation pulse with selective nulling of specific T_1 components (off-resonant fat with short T_1), while reducing others to positive residual offsets (on-resonant static tissue of the organ of interest), is developed in this work. The algorithm is described in section 4.1.2 and referred to as optimized fixed BS scheme. The optimized fixed BS scheme is verified in combination with different motion compensation techniques in brain

and liver PASL and pCASL experiments using healthy volunteers. The experimental setups, results and discussion of experiments are given in sections 5.2.1, 5.3.1 and 5.3.2. The algorithm has been published as parts of abstracts, which were presented at the 29th Annual Meeting of the ISMRM (60)(61). In addition, the algorithm is part of work which was published in Magnetic Resonance in Medicine (62). The presented description and evaluations are extensions of these publications.

Besides the special importance of optimal fat suppression for the application of motion correction, another common problem with all BS algorithms is that an assumption about the underlying T_1 distribution in the region of interest is needed. The T_1 distribution heavily depends on the organ of interest and might even vary between subjects (cf. e.g., the range of reported values by Garry et al. (63)). A suitable selection of BS related parameters is therefore a complex task, especially if the operator is not familiar with the underlying BS algorithm or organ of interest. As a result, subtraction errors, arising from insufficiently suppressed static tissue signal, might occur, which can easily mislead the operator or clinician. Maleki et al. (45) proposed to suppress the full range of reasonable T_1 values at excitation such that specific T_1 distributions of individual organs are always covered. This, however, comes at the cost of many inversion pulses, which increase energy deposition and could result in a loss of SNR in perfusion-weighted images, due to non-ideal inversion efficiency. In this work, a novel adaptive BS technique is therefore proposed to tackle the problem of complex BS related setups. Instead of incorporating assumptions about the underlying T_1 distribution, the actual distribution is measured and used for optimization of inversion timings. The reduction of static tissue signal is then automatically adapted to the region of interest. The technical implementation is described in section 4.1.3, and the algorithm is evaluated in phantom as well as brain pCASL experiments with two healthy volunteers (cf. section 5.1.2). The description and analysis is an extension of work which was submitted and presented at the 29th Annual Meeting of the ISMRM (64) and the 37th Annual Meeting of the ESMRMB (65).

Finally, BS algorithms usually assume perfect inversions during their optimization routines and therefore require a high experimental efficiency of inversion pulses. The optimization of FOCI pulses for application in BS is therefore described and evaluated in section 5.1.1.

4.1.2 Optimized Fixed Background Suppression Scheme

The optimized fixed scheme for background suppression is proposed for application in combination with motion correction strategies. Therefore, selective cancellation of fat with short T_1 components and simultaneous reduction of on-resonant tissue to small positive offsets needs to be achieved. Hence, optimal timings $\vec{t}$ of n inversion pulses are calculated by minimizing the following functional:

$$e(\vec{t}) = \left(\sum_{T_1} \left[M_z(T_1, TI, \vec{t}) - M_{res} \right] \cdot w(T_1) \right) + \lambda f(\vec{t}). \quad [4.1]$$

Here $M_z(T_1, TI, \vec{t})$ depicts the longitudinal magnetization after the inflow time TI for tissue with a relaxation time T_1, $M_{res}(T_1)$ is the desired level of residual magnetization in percent and $w(T_1)$ is a weighting factor. Note that $M_z(T_1, TI, \vec{t})$ ranges between [-1; 1] and thus represents the relative amount of the actual M_0 value. The weighting factor allows a certain prioritization of some tissue components during the minimization process. Prioritization can be relevant in cases where the number of inversions n is restricted, due to e.g., SAR constraints. The minimization procedure requires the evaluation of $M_z(T_1, TI, \vec{t})$. This is accomplished in an iterative fashion. Assuming n total inversion pulses, the final magnetization level after the last inversion pulse can be calculated using

$$M_z(T_1, TI, \vec{t}) = 1 + M_{1,n} \cdot \exp\left(\frac{-(TI - \vec{t}[n])}{T_1} \right). \quad [4.2]$$

The value of $M_{1,n}$ needs to be evaluated based on the timing of previous inversions. It applies that

$$M_{1,n} = -1 - \left(1 + M_{1,n-1} \cdot \exp\left(\frac{-(\vec{t}[n] - \vec{t}[n-1])}{T_1} \right) \right). \quad [4.3]$$

Before application of the first inversion pulse, the signal starts to recover from its initial saturation. In that case:

$$M_{1,0} = -1.$$

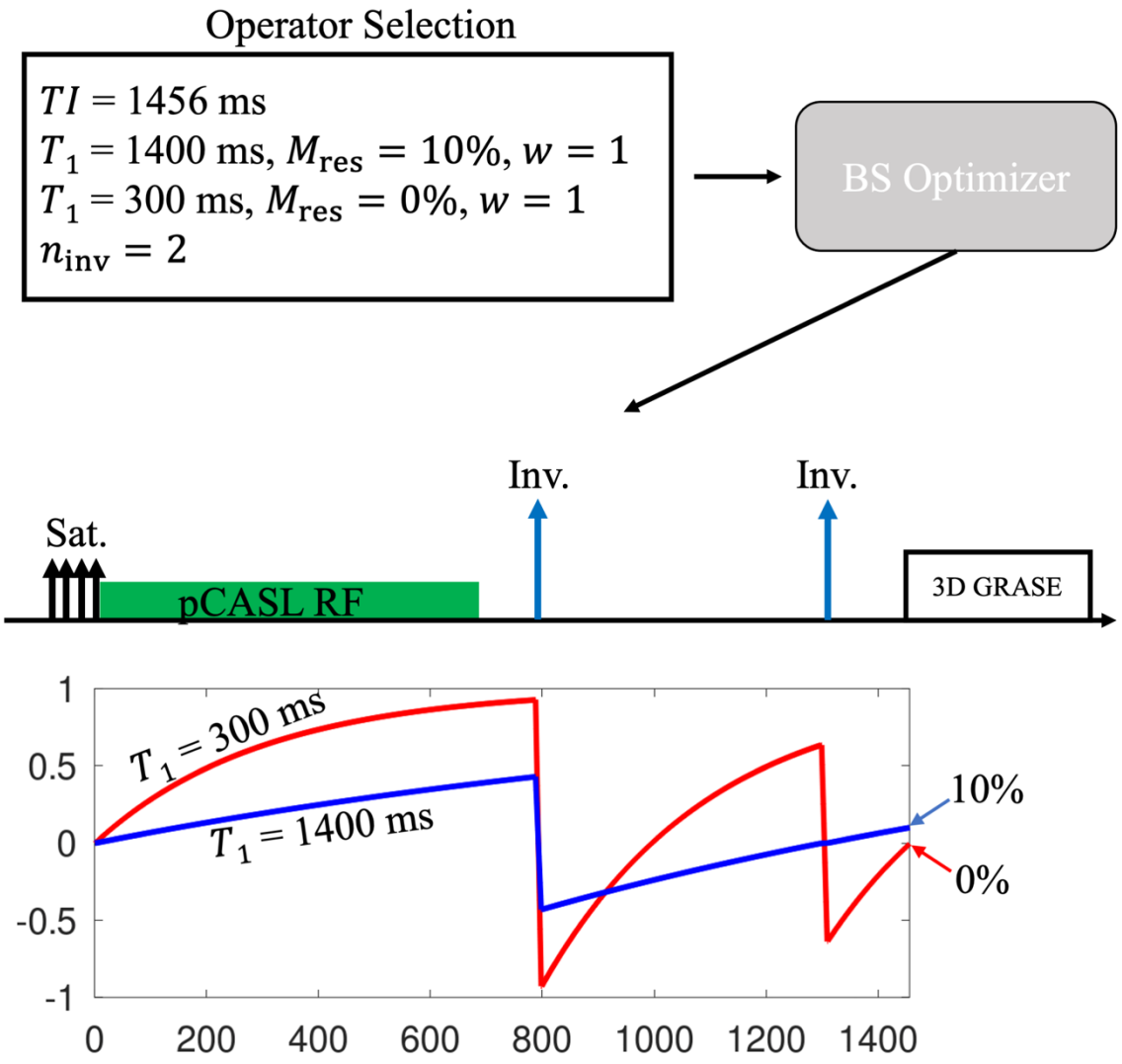

Figure 4.2: Concept of optimized fixed BS. In this case, fat signal is nulled at excitation, while gray matter signal is reduced to a small positive offset to prevent errors during magnitude image subtraction. T_1 values correspond to estimates for field strengths of 3T. The optimization routine from Eq. [4.1] calculates inversion timings which achieve the desired signal distribution at excitation.

In practice, some constraints must be considered during the minimization of Eq. [4.1]. First, some blocked time at the beginning and the end of the inflow time TI must be respected due to e.g., the application of a spectral fat saturation pulse and/or dephasing gradients after initial saturation. In addition, BS inversion pulses should not overlap. These constraints are reflected by the penalty function $\lambda f(\vec{t})$. $\lambda f(\vec{t})$ is zero, if none of the previously mentioned constraints is true and returns a penalty value as soon as the algorithm converges to non-applicable solutions. In order to further improve the quality of the optimization, the fitting procedure is repeated using different random initializations for pulse timings $\vec{t}$ and the configuration which yields the lowest error e is finally selected.

The duration of a BS inversion pulse is also considered. The proposed optimization routine is implemented in the Siemens ICE framework (Siemens Healthineers, Erlangen), based on a Levenberg-Marquardt optimization from the Eigen library (66). The concept of individual suppression of fat while keeping on-resonant tissue at a small residual offset is exemplarily demonstrated for a pCASL sequence in Figure 4.2.

4.1.3 Adaptive Background Suppression Scheme

In this work, a novel adaptive background suppression scheme is proposed to automatically calculate suitable inversion timings for the T_1 distribution in the region of interest. This way, no a-priori assumptions about the underlying T_1 distribution are needed, reducing the complexity of setting up the ASL sequence. In addition, the number of inversion pulses can be kept low when compared to the approach by Maleki et al. (45). Therefore, a T_1 histogram is calculated based on a preceding saturation recovery scan, commonly known and referred to as M_0 scan (67). M_0 scans are part of routine ASL imaging when quantification of images is desired (68). The calculated T_1 histogram is used to suppress encountered static tissue to a desired level of residual magnetization using an updated version of the optimization routine as described in Eq. [4.1].

4.1.3.1 Calculation of the T_1 Spectrum

In order to adaptively suppress static tissue in the region of interest, the spectrum of encountered T_1 values must be estimated from the preceding M_0 scan. Therefore, M_0, M_1 and T_1 are fitted for each voxel of a three-dimensional 3D GRASE volume using multiple saturation times T_S according to

$$s(T_S) = M_0 \left(1 + M_1 \cdot \exp\left(-\frac{T_S}{T_1}\right)\right). \quad [4.4]$$

Here, $s(T_S)$ depicts the signal measured after saturation time T_S. The magnetization immediately after saturation can be calculated according to

$$M_{z,sat} = M_1 + 1. \quad [4.5]$$

It is further helpful to introduce a saturation efficiency

$$SE = -M_1 \cdot 100. \quad [4.6]$$

If the saturation pulse perfectly flips the magnetization by 90°, the fitting yields $M_1 = -1$ and thus $SE = 100\%$. Note that the saturation efficiency can be higher than 100% if the resulting flip angle is above 90°. Voxel containing majorly noise signal are excluded from

the fitting procedure by calculating a signal mask, based on the average signal intensity from the last saturation time.

In principle, fitted parameter maps can be directly used to calculate optimal BS inversion timings, aiming to suppress the signal in each voxel in the selected imaging region. However, assuming a resolution of 64x64x8 pixels in a typical single-shot 3D GRASE experiment, this would result in 32768 equations, which need to be optimized simultaneously, being computationally demanding. Fortunately, signal in neighboring voxels often originates from the same type of tissue. In addition, rather slow spatial variation of saturation efficiency is expected. Therefore, redundant information can be discarded by calculating a 2D histogram from estimated parameter maps. The first histogram dimension is formed by T_1. Here, a bin size of $\Delta T_1 = 100$ ms is selected, which is expected to be a good compromise between data reduction and representation of the true T_1 distribution. The second dimension consists of estimated saturation efficiencies SE with a bin size of $\Delta SE = 2.5\%$. This way, the local changes in saturation efficiency are not completely lost, but are still considered during the optimization routine. Assuming e.g., two voxels containing signal from gray matter tissue, both may share a T_1 value of $\approx$ 1400 ms at 3T. However, one voxel may be located near exterior regions of the brain, while the other is in central brain regions. It is quite common that the saturation efficiency decreases near air-tissue interfaces, due to changes in susceptibility. This is reflected by individual entries in the two-dimensional histogram. Note that the M_0 map is not integrated into the optimization routine. This way, resulting levels of suppression correspond to fractions of M_0 rather than absolute signal levels. The histogram is filled by processing parameter maps from all voxels in the central $N_z - 2$ slices of the acquired volume, with N_z the total number of slices. The first and last slice of the volume are neglected due to potential aliasing artifacts. In addition, voxels containing signal are first thresholded in each slice based masks which are calculated from the 3D GRASE volume with the longest saturation time. Finally, outlier information from the histogram is removed by filtering 10% of the entries corresponding to the lowest counts. The two-dimensional histogram is stored on the hard disk for further processing of the MRI system. A schematic representation of the procedure is given in Figure 4.3.

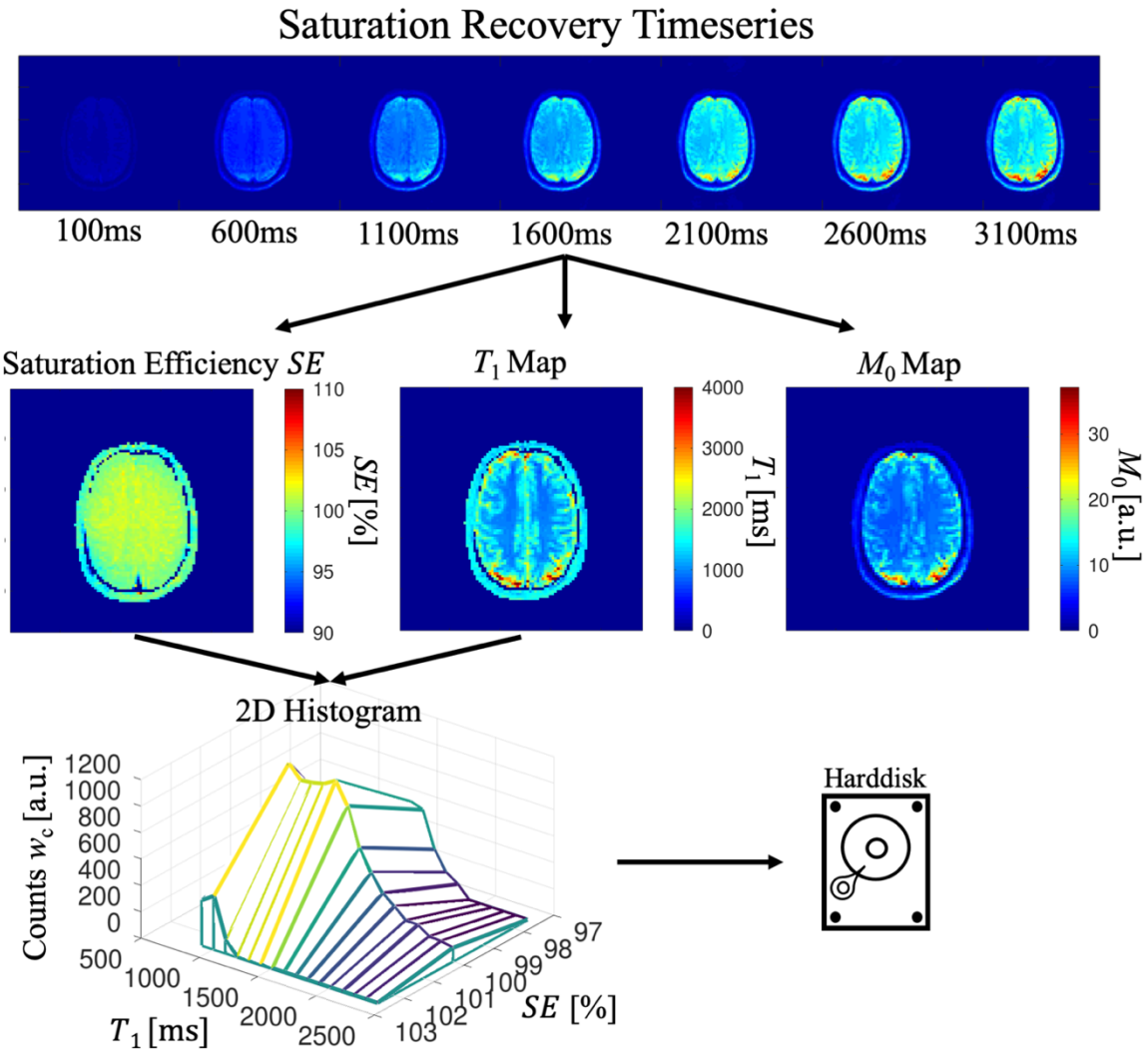

Figure 4.3: Generation of 2D histogram. Saturation recovery data are first fitted to a mono-exponential as given by Eq. [4.4], yielding SE, T_1 and M_0 maps. Many neighboring voxels share quite identical information with regards to all three parameters. Therefore, redundant information is discarded by calculating a two-dimensional histogram, which is stored on the MRI system's hard disk for further processing by the MR sequence.

4.1.3.2 Optimization of BS Inversion Timings

The adaptive BS algorithm aims to focus the measured spectrum at a certain user defined percentage of the nominal M_0 value at excitation of the 3D GRASE imaging module as described in section 4.1.2. The mathematical formulation of the optimization process is therefore almost identical to Eq. [4.1], which was introduced for the fixed optimized BS scheme:

$$e(\vec{t}) = \left(\sum_{T_1,SE} \left[M_z(T_1, SE, TI, \vec{t}) - M_{res} \right] \cdot w(T_1, SE) \right) + \lambda f(\vec{t}). \quad [4.7]$$

Again, $M_z(T_1, SE, TI, \vec{t})$ depicts the longitudinal magnetization after the inflow time TI for tissue with a relaxation time T_1 and initial saturation with saturation efficiency SE. The n-dimensional vector $\vec{t}$ contains the timings of n inversion pulses. M_{res} depicts the desired level of residual magnetization, which is specified by the operator. In section 4.2.2, the weighting factor w was fixed for the selected range of T_1 values based on a-priori assumptions about the need for prioritization of a certain value. Now, the weighting corresponds to the number of counts in the histogram of the calculated T_1 distribution. In order to find optimal timings, the term $M_z(T_1, SE, TI, \vec{t})$ again needs to be evaluated in each iteration of the optimization procedure for a current set of inversion timings $\vec{t}$. After application of the n-th BS inversion pulse, the longitudinal magnetization again recovers according to

$$M_z(T_1, SE, TI, \vec{t}) = 1 + M_{1,n} \cdot \exp\left(\frac{-(TI - \vec{t}[n])}{T_1} \right). \quad [4.8]$$

The magnetization levels $M_{1,n}$ at the time immediately after inversion pulse n are again calculated as described by Eq. [4.3]. In contrast, however, before the first inversion pulse $n = 1$, the signal starts to recover from the estimated saturation level:

$$M_{1,0} = M_{z,sat} - 1. \quad [4.9]$$

Note that the same penalty term $\lambda f(\vec{t})$ as used for the optimized fixed BS scheme is introduced to prevent impossible pulse configurations. The proposed adaptive BS optimization routine is again implemented in the Siemens ICE framework (Siemens Healthineers, Erlangen), using a Levenberg-Marquardt optimization from the Eigen library (66). An overview is depicted in Figure 4.4.

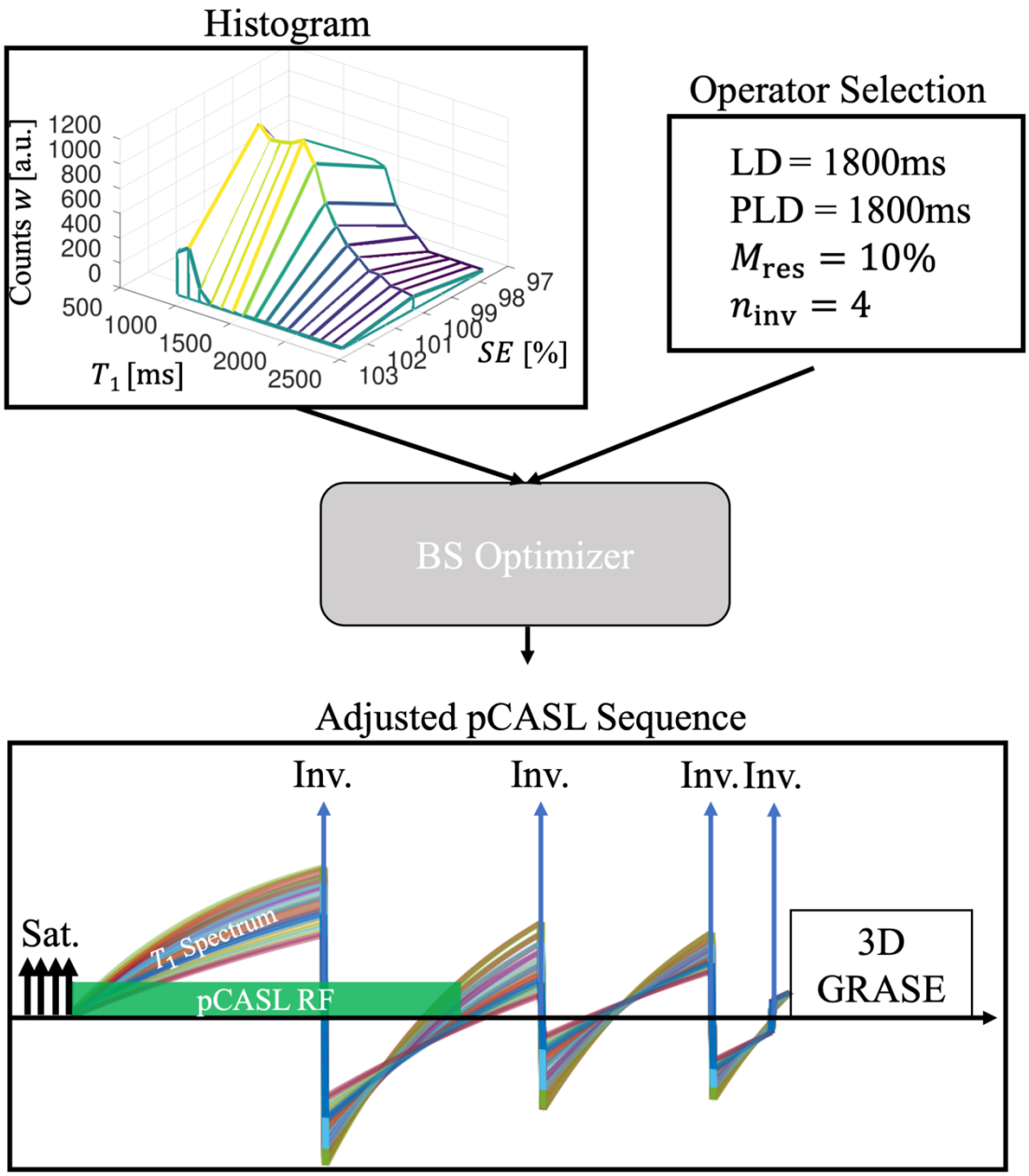

Figure 4.4: Adaptive adjustment of BS timings, shown for a pCASL sequence. The calculated two-dimensional histogram as well as the desired target magnetization M_{res}, the number of inversion pulses to be applied during the preparation phase n_{inv} and label duration as well as the post labeling delay are used as input for the BS optimizer. Optimal timings of BS inversions are then calculated, and the sequence starts. Note how the spectrum of measured T_1 values fans out after the initial saturation and is refocused at the desired level at time of the 3D GRASE excitation.

4.2 Novel Approaches for Motion Compensation using 3D GRASE PROPELLER

4.2.1 Introduction

Occasionally, sophisticated BS only is not sufficient to suppress subtraction errors in perfusion-weighted images, because movements of the organ were too large. In these cases, retrospective correction of motion artifacts is attractive, because no additional implementation on the sequence side is needed, and retrospective methods can almost always be applied to the acquired label/control 3D GRASE data after the scan. This makes retrospective techniques a versatile approach for tackling motion in ASL imaging, as demonstrated e.g., in work from Wang et. al (69). In practice, in-plane segmentation of the 3D GRASE readouts is often applied to shorten the echo-train length and thus reduce through-plane blurring as well as geometric distortion. Unfortunately, the applicability of retrospective image registration methods to segmented 3D GRASE acquisitions is rather limited. Let us assume that a rotation occurs in between the acquisition of multiple 3D GRASE segments. In that case, the rotation needs to be estimated from individual segments first, which requires sophisticated methods to fill the missing k-space lines such as ESPIRiT (53). But even if the rotation is correctly identified, a direct retrospective correction is difficult. This follows from the rotation theorem of the Fourier transform, which states that the rotation in image space leads to the same rotation in k-space. Even if the rotation of the acquired segment is corrected, e.g., by gridding the acquired data (70), missing k-space samples might result in residual artifacts.

An elegant way which enables self-navigated retrospective motion correction in combination with a multi-shot GRASE readout is achieved by using the well-known PROPELLER trajectory for data acquisition, resulting in a 3D GRASE PROPELLER (3DGP) readout (54)(55). The basic concept was introduced in section 3.4.3. However, in ASL, 3DGP never found wide application. This is potentially related to the following reasons.

First, the original publication by Tan et al. (54) did not validate the effectiveness of motion compensation in ASL imaging using 3DGP. Consequently, it remained unclear if the accuracy of motion estimates is affected by different levels of residual static tissue magnetization, which depend on the respective BS algorithm and the individual setup.

Moreover, the rotated phase encoded direction results in a variation of the direction of geometric distortion in individual 3DGP navigators, which can affect the accuracy of motion estimates (71). To this aim, a novel 3DGP reconstruction algorithm is presented in this work, which allows a **J**oint **E**stimation and correc**T**ion of in-plane rigid body motion and geometric distortion (3DGP-JET) from the central k-space data of individual bricks with subsequent correction of both types of artifacts. Details about the implementation are given in section 4.2.2. Evaluation in combination with the optimized fixed BS scheme in form of a pCASL study with five healthy volunteers is given in section 5.2.1. The work is based on abstracts which were submitted and presented at the 27th Annual Meeting of the ISMRM (71) as well as the 29th Annual Meeting of the ISMRM (ISMRM Magna Cum Laude award) (61) and a paper which was published in Magnetic Resonance in Medicine (62).

Second, although three-dimensional data using 3DGP is acquired, motion compensation was restricted to in-plane rigid body corrections so far. Therefore, it shall be investigated whether estimation and correction of 3D rigid body motion is possible using the low-resolution image space information from 3DGP navigators. Details concerning the reconstruction algorithm are given in section 4.2.3. The feasibility of three-dimension motion estimation and correction using the proposed algorithm is initially validated in brain pCASL imaging using a healthy volunteer (cf. section 5.2.2). Both chapters are based on work which was submitted and presented at the 36th Annual Meeting of the ESMRMB (72).

4.2.2 3DGP-JET: Joint Estimation and Correction of Motion and Geometric Distortion

It was demonstrated that geometric distortion can affect the accuracy of 3DGP motion estimates (71). A straight-forward solution is the correction of distortion prior to the motion estimation step using e.g., TOPUP (50) or adapted tools designed for EPI-based PROPELLER trajectories (73). However, the application of these techniques in case of motion is difficult. Usually, the distortion correction assumes the same positioning of the object in image space, which does not necessarily hold in case of motion during the scan. On the other hand, motion cannot be accurately corrected before the distortion correction step since the motion estimation is affected by the latter. Therefore, both phenomena need to be jointly estimated. Consequently, this work presents a novel 3DGP reconstruction algorithm, which allows a **J**oint **E**stimation and correc**T**ion of motion and geometric distortion (3DGP-JET) from the brick's central k-space data. The general idea is inspired by the TOPUP algorithm (50) and work from (74).

4.2.2.1 3DGP-JET Theory

The signal of the n-th complex 3D navigator after an inverse Fourier transform along the z-direction, complex coil combination and gridding with deconvolution can be written as

$$s_n(\vec{k}, z) = \sum_{x,y} \rho(\vec{r}, z) \exp\left[-i \frac{2\,\pi}{N_\mathrm{x}} k_\mathrm{x}\, x\right] \exp\left[-i \frac{2\,\pi}{N_\mathrm{y}} k_\mathrm{y}\, y\right], \qquad [4.10]$$

with $\vec{r} = (x, y)^\mathrm{T}$ the spatial position in image space, N_x, N_y the number of pixels of the low-resolution navigator and k_x, k_y the position in 2D discrete k-space, respectively. As in all EPI-based MR imaging techniques, local displacements $d(\vec{r})$ in the in-plane phase-encoded direction $\mathrm{PE}_{\mathrm{x,y}}$, due to inhomogeneity of the main magnetic field, must be considered such that:

$$s_n(\vec{k}, z) = \sum_{x,y} \rho(\vec{r}, z) \exp\left[-i \frac{2\,\pi}{N_\mathrm{x}} k_\mathrm{x} \left(x + \vec{D}_{n,\mathrm{x}}\right)\right] \exp\left[-i \frac{2\,\pi}{N_\mathrm{y}} k_\mathrm{y} \left(y + \vec{D}_{n,\mathrm{y}}\right)\right], \qquad [4.11]$$

with

$$\vec{D}_n = [\sin(\alpha_n), \quad -\cos(\alpha_n), \quad 0]^T \cdot d(\vec{r}). \tag{4.12}$$

Here, α_n depicts the angle of acquisition of the associated brick in k-space, rotating $\mathrm{PE_{x,y}}$ and hence the direction of geometric distortion with each shot. It is explicitly assumed that no phase accrual along the second phase encoding along k_z occurs. This is true for 3D GRASE readouts if perfect 180° refocusing pulses are applied. In case of lower refocusing flip angles, additional phase accrual between different partition encoding steps might, however, occur. Modeling of these phase errors is not trivial. However, the effect should be comparable for different bricks, because the direction of partition encoding does not change. Therefore, these phase errors are neglected at this point. Eq. [4.11] is now extended by deviations induced by translational motion:

$$\begin{aligned} \mathrm{s}_n(\vec{k}, z) = \sum_{x,y} \rho(\vec{r}, z) \cdot &\exp\left[-i\frac{2\,\pi}{N_\mathrm{x}} k_\mathrm{x}\left(x + \vec{D}_{n,\mathrm{x}} + \vec{t}_{n,\mathrm{x}}\right)\right] \\ \cdot &\exp\left[-i\frac{2\,\pi}{N_\mathrm{y}} k_\mathrm{y}\left(y + \vec{D}_{n,\mathrm{y}} + \vec{t}_{n,\mathrm{y}}\right)\right]. \end{aligned} \tag{4.13}$$

In contrast to the local shifts introduced by $\vec{D}_n(\vec{r})$, $\vec{t}_n$ describes a global displacement of $\rho(\vec{r}, z)$ and thus a global, navigator dependent translation. Rotational motion can be added by rotating the undistorted magnetization prior to applying the distorted and translated Fourier operation:

$$\begin{aligned} s_n(\vec{k}, z) = \sum_{x,y} &\rho\left(\underline{R}_{n,+}(\Delta\alpha_n) \cdot \ \vec{r}, z\right) \\ &\cdot \exp\left[-i\frac{2\,\pi}{N_\mathrm{x}} k_\mathrm{x}\left(x + \vec{D}_{n,\Delta\alpha_n,\mathrm{x}} + \vec{t}_{n,\mathrm{x}}\right)\right] \\ &\cdot \exp\left[-i\frac{2\,\pi}{N_\mathrm{y}} k_\mathrm{y}\left(y + \vec{D}_{n,\Delta\alpha_n,\mathrm{y}} + \vec{t}_{n,\mathrm{y}}\right)\right], \end{aligned} \tag{4.14}$$

with $\underline{R}_{n,+} = \underline{R}_z(\Delta\alpha_n)$ the 2D rotational matrix. Note that

$$\vec{D}_{n,\Delta\alpha_n} = [\sin(\alpha_n), \quad -\cos(\alpha_n), \quad 0]^\mathrm{T} \cdot d(\vec{r}, \Delta\alpha_n) \tag{4.15}$$

is now dependent on the rotational estimate, too. If the undistorted magnetization is rotated by $\Delta\alpha_n$, the estimated distortion field needs to be rotated and interpolated to the same rotational motion state to accurately reflect the local displacements. This explicitly assumes that the distortion field does not change in case of motion. This is obviously not

perfectly true. The shimming procedure at the beginning of the MRI experiment will adapt the local magnetic field to the changes introduced by the object inside the scanner. If the object moves during the acquisition, the shim is not as accurate as before and the distortion field might change. It is however justifiable to assume a constant field if movements are expected to be small, as it is the case during brain examinations, where large motion is restricted by the imaging coils and headphones during the experiment. Eq. [4.14] is already directly applicable to a minimization approach. However, it is somewhat impractical since calculation of $d(\vec{r}, \Delta\alpha_n)$ and $\rho\left(\underline{R}_{n,+}(\Delta\alpha_n) \cdot \vec{r}, z\right)$ requires interpolation algorithms, which are problematic for calculation of analytical gradients. In this case, the exact implementation of the interpolator must be known, which is often not the case if external libraries are used. It is therefore beneficial to further exploit the rotational theorem of the Fourier transform, which states that a rotation in image space yields an identical rotation of k-space:

$$
\begin{aligned}
s_n(\vec{k}, z) &= A_n[\rho](\vec{k}, z) \\
&= \sum_{x,y} \rho(\vec{r}, z) \\
&\quad \cdot \exp\left[-i \frac{2\,\pi}{N_\mathrm{x}} (\underline{R}_{n,+} \cdot \vec{k})_\mathrm{x} \left(x + (\underline{R}_{n,-} \cdot \vec{D}_n)_\mathrm{x} + \vec{t}_{n,\mathrm{x}}\right)\right] \\
&\quad \cdot \exp\left[-i \frac{2\,\pi}{N_\mathrm{y}} (\underline{R}_{n,+} \cdot \vec{k})_\mathrm{y} \left(y + (\underline{R}_{n,-} \cdot \vec{D}_n)_\mathrm{y} + \vec{t}_{n,\mathrm{y}}\right)\right].
\end{aligned}
\qquad [4.16]
$$

The rotational operation is now integrated into the encoding procedure, rotating the k-space samples instead of the object in image space. This skips the explicit interpolation step and allows calculation of analytical gradients. Note that this also includes an opposite rotation of the direction of geometric distortion, as indicated by $\underline{R}_{n,-} \cdot \vec{D}_n$. This is needed, due to the interpolation of the distortion field, taking care of the fact that a rotation does not change the direction of phase-encoding, but the direction in which the signal is shifted. If e.g., the true magnetization would be rotated by 180° due to physical rotation and the distortion field is constant, all local displacements would alternate their direction if the in-plane phase encoding is kept constant. This is considered by counter rotating the direction of geometric distortion with $\underline{R}_{n,-} = \underline{R}_z(-\Delta\alpha)$. As already mentioned, Eq. [4.16] now enables minimization using analytical gradients.

A suitable choice as a loss function is the L2-norm of measured and expected signals in k-space:

$$e = 0.5 \cdot \sum_{n} \sum_{z} \sum_{\vec{k}} |s_n(\vec{k}, z) - A_n[\rho](\vec{k}, z)|^2. \quad [4.17]$$

Eq. [4.17] can be directly minimized using e.g., a gradient descent approach, which is done in this work. The estimated field map is finally smoothed using a gaussian filter. Enforcing smooth distortion fields can also be directly integrated into Eq. [4.17]. This is accomplished by adding regularization terms concerning the L1 norm of the first and second derivative $\Delta d(\vec{r})$ and $\nabla d(\vec{r})$ of the distortion field such that:

$$e = 0.5 \cdot \sum_{n} \sum_{z} \sum_{\vec{k}} |s_n(\vec{k}, z) - A_n[\rho](\vec{k}, z)|^2 + \lambda_1 \cdot \mathrm{L1}\big(\Delta d(\vec{r})\big) + \lambda_2 \cdot \mathrm{L1}\big(\nabla d(\vec{r})\big). \quad [4.18]$$

A proper choice of the regularization parameters is however not straight forward in ASL experiments, where the actual level of error heavily depends on the level of measured static tissue signal. Therefore, the smoothing approach is preferred over the alternative from Eq. [4.18] in this work.

Eq. [4.16] reveals that a pseudo-inverse of the operator A_n can be calculated which maps the distorted k-space data back to the undistorted image space. By interpolating $d(\vec{r})$ to the size of full bricks $I_n(x, y)$ with respect to estimated motion parameters, the unwarping operation is written as

$$I_n(x, y) = A_n^{-1}\big[S_n(k_x, k_y)\big]. \quad [4.19]$$

4.2.2.2 Implementation of Image Reconstruction

Perfusion-weighted images are reconstructed using the 3DGP-JET algorithm, as depicted in Figure 4.5. After complex coil combination (75), the brick with highest normalized cross-correlation χ_{ref} with all other bricks is selected as the reference. Using 3DGP-JET, bricks with $\chi_{n,\,ref} < 0.5$ are filtered prior to the JET routine. Motion and the underlying distortion field are estimated from all non-filtered control and label bricks. After distortion correction, pairs of label/control bricks with the same acquisition angle are filtered if

$|\Delta\alpha_c - \Delta\alpha_l| > 10°$ or $|\Delta t_{x,c} - \Delta t_{x,l}| > 10\,\text{mm}$ or $|\Delta t_{y,c} - \Delta t_{y,l}| > 10$ mm, due to potential subtraction errors from shifted fat. The fat filtering step is only applied if the number of detected bricks is less than 30% of the whole dataset. The unwarping operation from Eq. [4.19] is performed by first interpolating the distortion field to the estimated motion state of individual bricks. Afterwards, corrected data is recovered by finding the least-squares solution of Eq. [4.19] using algorithms from the Eigen library (66). In addition to the 3DGP-JET algorithm, the standard 3DGP-STD algorithm is implemented as an interchangeable module to enable direct comparison of both methods. A small modification for the standard procedure is introduced with regards to the method described in (54). Here, a single 2D motion estimate is assigned to each three-dimensional brick: In terms of bulk rotation estimation, the cross-correlation of the whole stack-of-slices with the reference stack is calculated for different angles, followed by parabolic fitting. In translation estimation, the procedure as described by Pipe (55) is performed for each slice, and mean estimates are assigned as the brick's translational parameters. For both 3DGP-JET and 3DGP-STD, the correlation weighting procedure was adjusted such that a brick n is only removed from the dataset if the correlation $\chi_{n,\text{ref}} < 0.8$ after motion correction to prevent excessive filtering of data. All image reconstruction steps were implemented in C++ within the Siemens ICE framework (Siemens Healthineers, Erlangen).

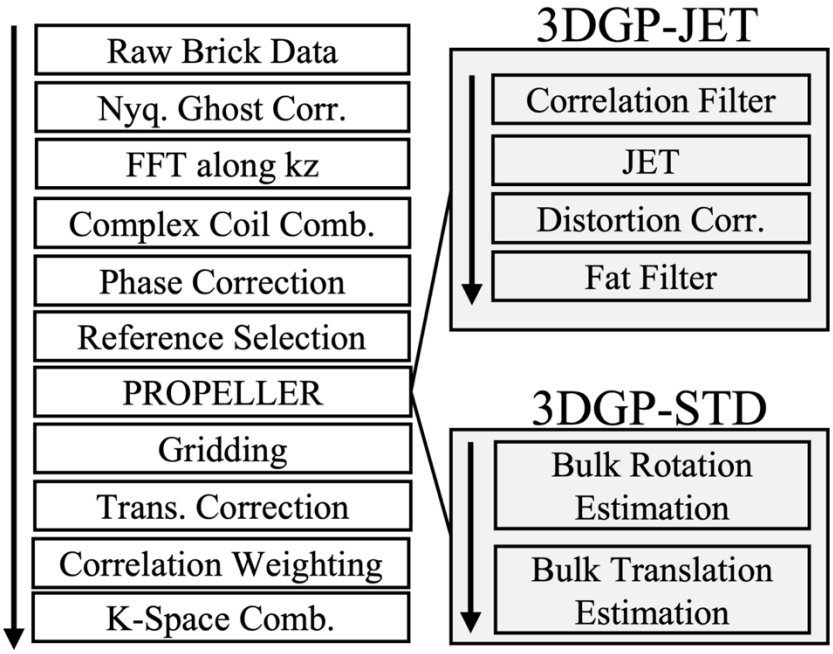

Figure 4.5: Reconstruction of acquired data with the 3DGP-JET or standard 3DGP-STD algorithm as implemented in the Siemens ICE framework.

4.2.3 3D Rigid Body Motion Correction using 3DGP

Using the 3DGP readout in ASL imaging, a whole three-dimensional k-space brick is acquired after a single excitation. The standard 3DGP reconstruction as well the proposed 3DGP-JET reconstruction, however, only apply in-plane motion estimation and correction. Through-plane motion is handled by filtering affected bricks. If the motion state of these bricks would be corrected instead, this could have a positive impact on the SNR in reconstructed perfusion-weighted images. Although it would be possible to extend the 3DGP-JET routine to incorporate three-dimensional rigid body motion, the corresponding theory would get quite complicated, due to different step sizes along the three k-space axes. In addition, it is not clear if low-resolution 3DGP navigators provide enough information to accurately estimate through-plane motion. To this aim, it should be initially clarified, whether estimation and correction of three-dimensional rigid body motion using 3DGP is feasible. Instead of complex extension of the 3DGP-JET routine, a straight-forward image space-based approach is applied for this purpose. Details concerning the implementation are subsequently provided.

4.2.3.1 Implementation of Image Reconstruction

The proposed image reconstruction pipeline is depicted in Figure 4.6. After the standard 3DGP preprocessing steps, which were already described in the previous section, three-dimensional low-resolution navigators are extracted from each brick. Using a 3D rigid body image registration algorithm from the Insight Toolkit (76), six motion parameters $\Delta\alpha_{\mathrm{x}}, \Delta\alpha_{y}, \Delta\alpha_{\mathrm{z}}, \Delta t_{\mathrm{x}}, \Delta t_{\mathrm{y}}, \Delta t_{\mathrm{z}}$ are obtained for each brick by using the first acquired volume as a reference. Subsequently, the motion correction step is performed in k-space. Here, it must be considered that spacings Δk_{x}, Δk_{y}, Δk_{z} are not equal due to the different extensions of the field of view. In 3DGP imaging, the field of view is typically lowest in the partition direction, which shows a higher Δk_{z} than the in-plane directions. This can either be respected during the resampling part or is compensated by zero filling in the slice direction, according to

$$N_{\mathrm{z,interpol}} = \frac{\Delta k_{\mathrm{z}}}{\Delta k_{\mathrm{x}}} \cdot N_{\mathrm{z}}, \qquad [4.20]$$

where N_z depicts the number of acquired partitions and $N_{z,interpol}$ depicts the number of slices after zero filling. Note that it is explicitly assumed that $\Delta k_x = \Delta k_y$, which is the usual case for 3DGP acquisitions. Estimated rotational motion is then compensated during a 3D gridding procedure. Afterwards, 3D translational shifts are removed from the image data by applying corresponding linear phases in k-space. Corrected k-space data is combined using the standard k-space combination procedure (55). Finally, the interpolation introduced by zero filling is reverted, and the ASL subtraction is performed. The 3DGP-3D image reconstruction pipeline is implemented in the Gadgetron framework as C++ modules (77).

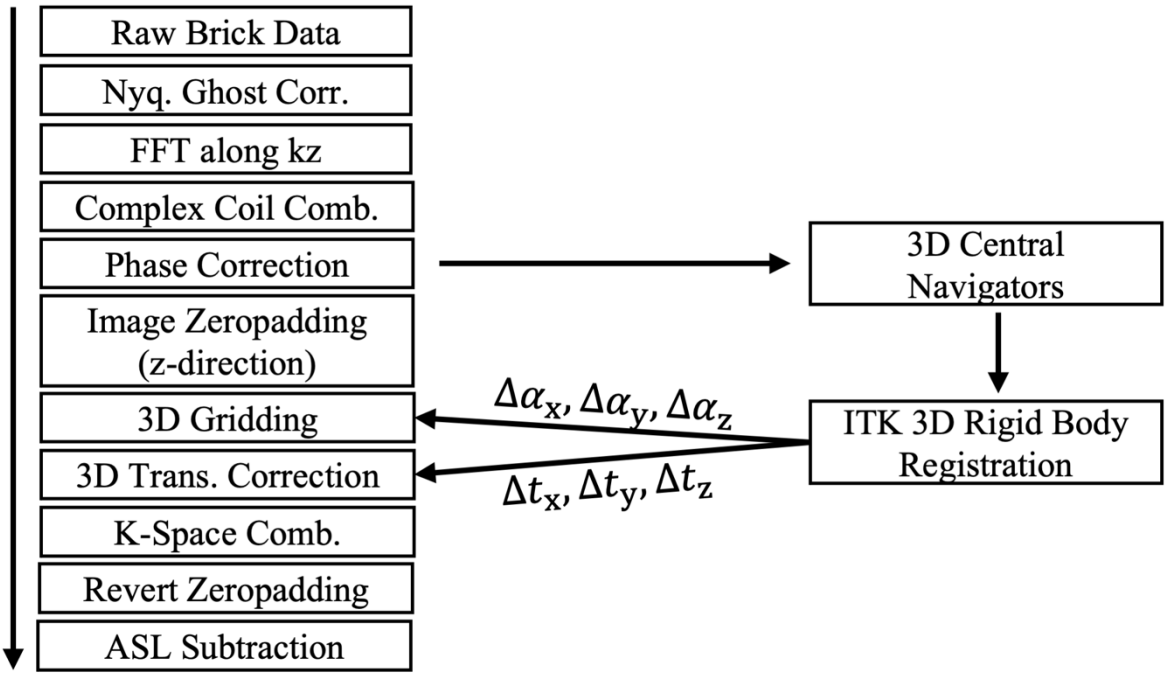

Figure 4.6: Proposed 3DGP-3D reconstruction pipeline. Estimated rotations are corrected during the gridding procedure, while subject translations are transferred to linear phase ramps which are removed from each brick afterwards.

4.3 Compensation of Respiratory Motion Artifacts

4.3.1 Introduction

A combination of sophisticated background suppression with retrospective motion correction techniques such as 3DGP could be effective for compensating slow drifts or low-frequent in-plane motion during ASL examinations. Some extend of through-plane motion compensation might also be achieved by either filtering or correcting affected data using appropriate three-dimensional motion models. The capability for retrospective correction of through-plane motion, however, is limited by the extend of the field of view in the through-plane direction, which is usually much smaller than in the in-plane direction using 3D GRASE readouts. This especially holds for single-shot experiments, where the number of acquired k-space partitions is restricted due to the T_2 decay of the signal. It is clear that large through-plane movements result in sampling of different regions, which cannot be aligned retrospectively, because sampled data are different. Another potential problem can arise from mismatches between the initial saturation region and the image volume, which is excited after the ASL preparation phase. If these regions are not aligned, signal fluctuation from spin history artifacts might be introduced in label and control images (78), which could easily overlay the perfusion information. A retrospective correction of high frequent motion with large displacements in the through plane direction is therefore a challenging task in ASL examinations. Unfortunately, respiration can be a potential source of such motion. Exhaling and inhaling results in volume variation of the lungs, which in turn results in shifts and deformations of abdominal organs. The resulting respiratory motion is most severe in liver, which is located close to the lungs (cf. Figure 4.7).

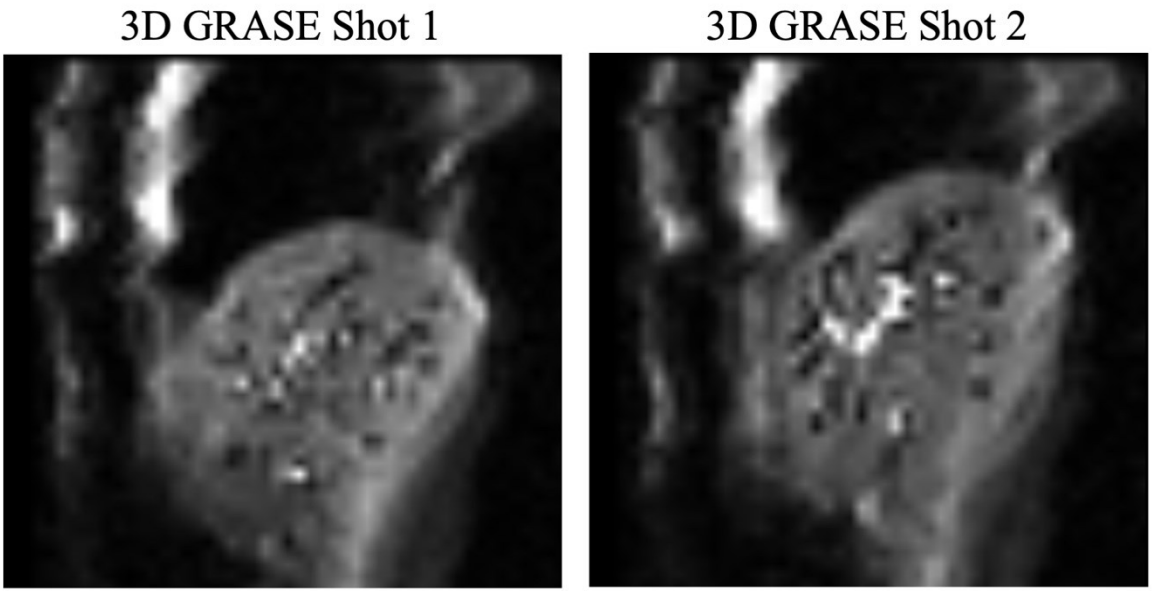

Figure 4.7: Central slice of two 3D GRASE measurements with control preparation, acquired under free-breathing conditions. The liver shows a large displacement in the cranial-caudal direction with additional elastic deformations, due to inhaled/exhaled states during the image readout.

These large shifts might be problematic for retrospective correction routines depending on the selected positioning. In addition, the duration of the breathing cycle typically lies in regions of multiple seconds, which is the same timescale as the delay between initial saturation and image readout of background suppressed ASL sequences. Mismatches between spatial saturation and image excitation are therefore likely in free-breathing liver ASL imaging. Although respiration was also shown to potentially affect EPI examinations of the brain (79), the severity of resulting motion in brain ASL experiments using a 3D GRASE readout is tolerable. This can be seen from the fact that no recommendations for avoidance or correction of respiratory motion is given in the ASL whitepaper by Alsop et al. (37). The following sections will therefore focus on the compensation of respiratory motion in liver ASL imaging, where the effects are most severe.

Straight-forward solutions for respiratory motion compensation are timed-breathing protocols (58) and long breathholds (80). These protocols ensure that the breathing state during data acquisition and ASL preparation stays the same throughout the examination. However, the strict breathing pattern might be difficult to follow for untrained subjects and requires a careful briefing prior to the scan. In addition, long scan times when compared to free-breathing examinations are typically required. Therefore, two novel techniques for compensation of respiratory motion in liver ASL imaging are introduced in this work.

First, an alternative to timed-breathing is proposed, which automatically triggers the application of the ASL preparation and image acquisition if a breathhold is detected. This way, the subject can personally decide about the duration of breathing and breathhold phases throughout the ASL scan, which potentially increases the comfort. The technique will be referred to as multi-breathhold detection and details concerning the implementation are described in section 4.3.2. The feasibility of the technique is initially demonstrated in liver FAIR PASL imaging in a healthy volunteer in combination with the optimized fixed BS scheme. A description of the experiment as well as results and discussion are given in section 5.3.1. This work is an extension of the abstract which was presented at the 29th Annual Meeting of the ISMRM (60).

In addition, a novel technique for prospective compensation of respiratory induced motion during liver ASL scans is presented to overcome the need for timed-breathing protocols. This way, the time needed for the total exam can be potentially decreased when compared to timed-breathing protocols and the comfort of the subject is further increased since no breathholds are required. The prospective method exploits the fact that respiratory motion shows a repetitive pattern, due to the repetitive breathing cycle. The positions of the initial saturation and 3D GRASE imaging regions are updated throughout the scan to compensate for respiratory induced displacements. The technique is described in section 4.3.3 and validation in liver pCASL imaging using eight healthy volunteers is performed in section 5.3.2. The described methods and analysis are based on initial work which was demonstrated at the 37th Annual Meeting of the ESMRMB (81) and a revised manuscript which was submitted to Magnetic Resonance in Medicine and is currently under review again. In addition, this work was accepted as an oral presentation for the ISMRM Perfusion Workshop in 2022.

4.3.2 Sequence Triggering using Multi-Breathhold Detection

Sequence triggering by automatic detection of breathholds is proposed as an alternative to timed-breathing protocols for compensation of respiratory motion. Therefore, a trigger module is inserted into the ASL sequence immediately before PASL/pCASL preparation. The trigger module calculates the variance of the last two seconds of the respiratory signal, obtained from an external respiratory cushion, which is attached to the subject prior to the scan. The next preparation and acquisition phase is only triggered, if the variance falls below a user-defined threshold. Otherwise, a delay of 100 ms is inserted, and the variance is analyzed again. The basic implementation of a PASL and pCASL variant of the sequence is given in Figure 4.8. The determination of an optimal threshold for separation of breathing and breathhold states depends on the positioning and procurement of the respiratory cushion. Therefore, a-priori selection of thresholds is difficult. In this work, a subject-specific threshold is therefore determined, based on a preceding saturation recovery M_0 scan, acquired in a single breathhold with a 3D GRASE readout. For each saturation time T_S, the variance of the last two seconds of the respiratory signal is recorded, representing expected values in breathholds. A threshold is selected for the subsequent ASL experiment which lies above observed values.

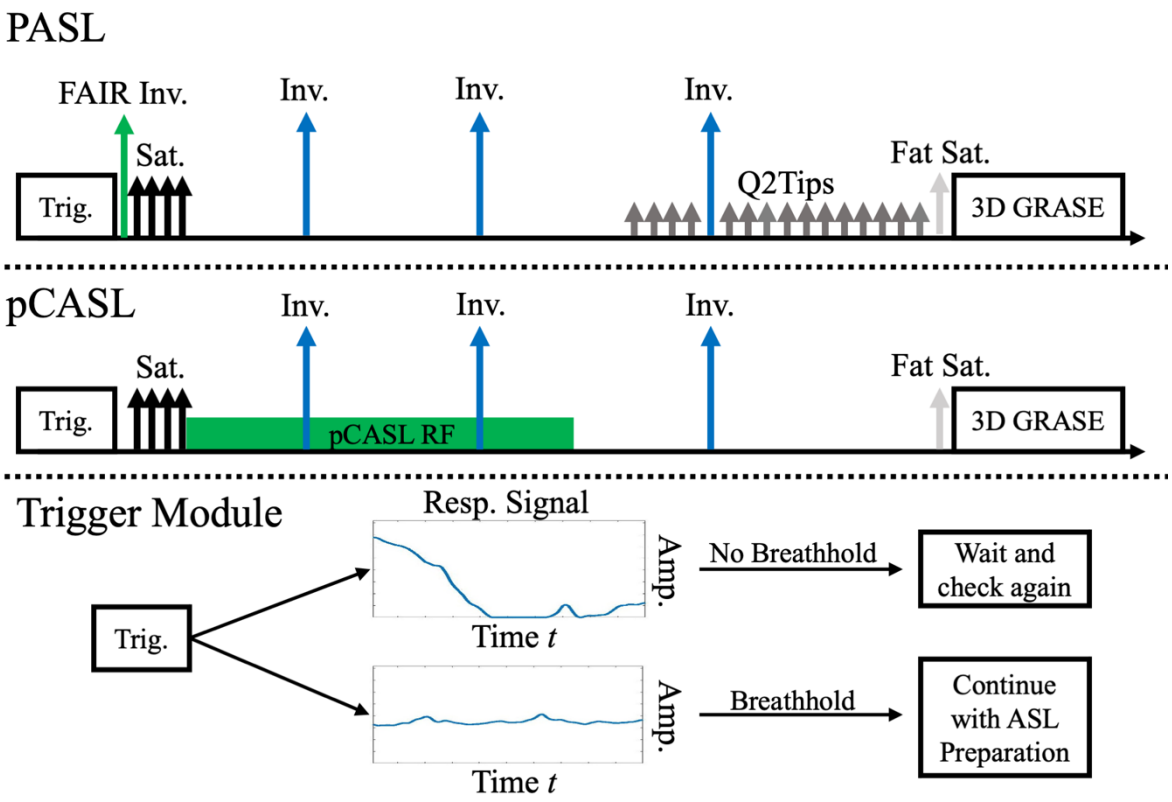

Figure 4.8: Schematic representation of PASL and pCASL sequences with automatic breathhold detection, as applied in this work. In both sequences, an initial saturation is followed by multiple inversion pulses for suppression of static tissue. The trigger module checks the last two seconds of the respiratory signal and only plays out the whole ASL preparation and signal readout, if the variance of the signal falls below a certain threshold.

4.3.3 Prospective Correction of Respiratory Motion using Navigator Matching

Free-breathing ASL experiments of the liver have been accomplished by using navigator echoes of the diaphragm to identify the phase of the breathing cycle, while acquired data is only accepted in the exhaled phase. This procedure was then followed by nonrigid image registration (11). However, in that work, background suppression was only achieved by presaturation of the imaging plane, without additional inversion pulses, which results in higher static tissue signal for later inflow times. This can potentially lead to increased subtraction errors. In addition, only a single coronal slice was acquired. Using a 3D GRASE readout, acquisition of full three-dimensional label/control volumes is performed after pCASL preparation, and filtering of data not corresponding to the exhaled state would become highly inefficient. In addition, respiratory triggering in ASL becomes somewhat difficult. Usually, a fixed delay between labeling and image readout is desired to visualize and quantify the temporal perfusion pattern.

It is well known that by far the major amount of liver motion during the breathing cycle appears as translational shifts in the cranial-caudal direction (82) (also cf. Figure 4.7). In the following, a prospective cranial-caudal motion compensation technique is therefore proposed, which is compatible with the low signal levels arising in background suppressed 3D GRASE pCASL imaging. All associated image reconstruction steps were implemented in C++ within the Siemens ICE framework (Siemens Healthineers, Erlangen).

4.3.3.1 Prospective motion correction by matching 2D EPI navigators to EPI reference data

The correction of cranial-caudal liver shifts during pCASL experiments with a single-shot 3D GRASE readout should benefit from a prospective solution. This can easily be motivated by the high spatial selectivity of the initial saturation and 3D GRASE excitation regions as depicted in Figure 4.9.

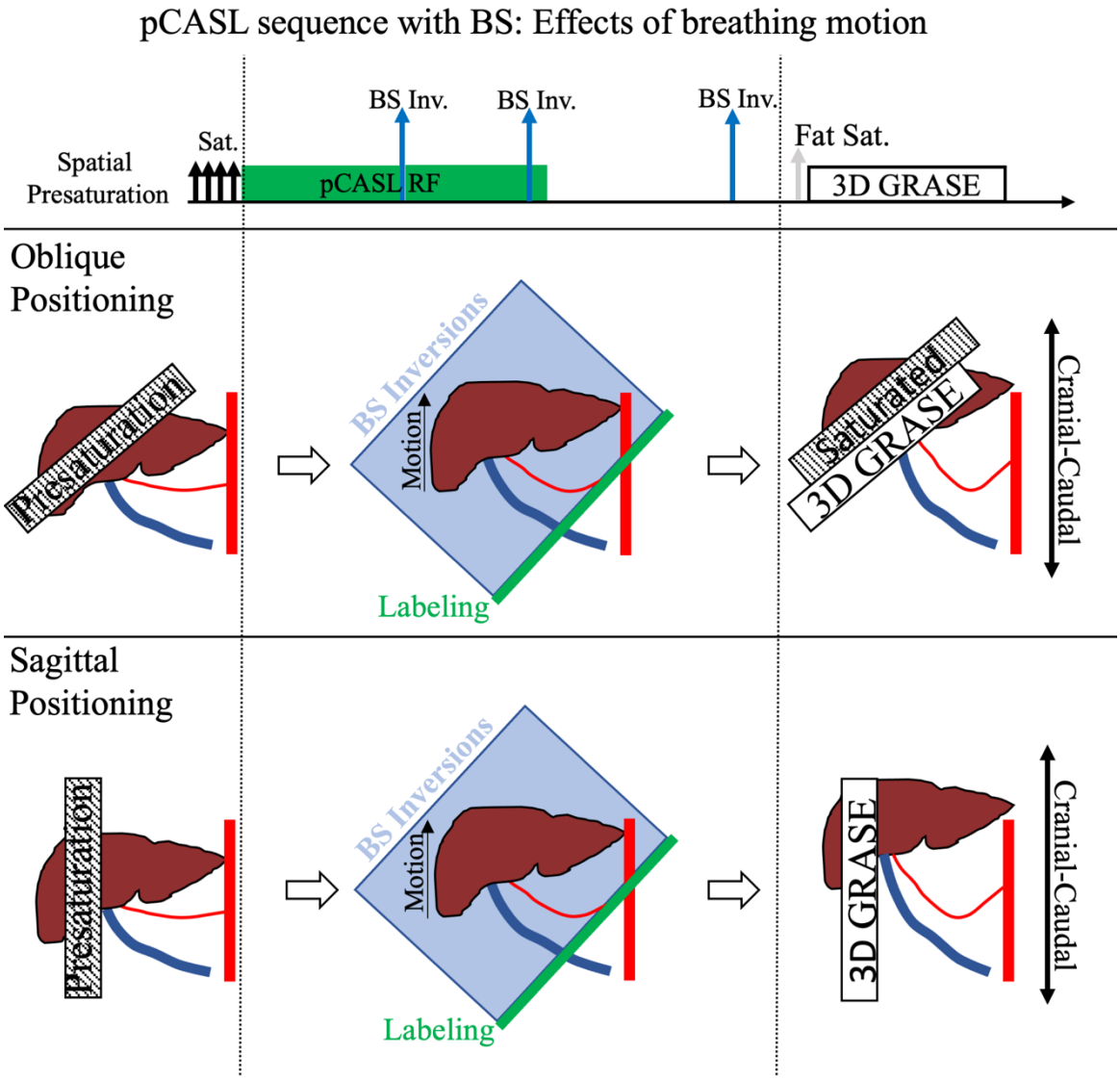

Figure 4.9: Application of a pCASL sequence to liver during free-breathing. The sequence consists of presaturation of the image region, followed by the labeling phase with additional application of inversion pulses, reducing the static tissue signal at excitation. Finally, label/control image data is acquired using a 3D GRASE readout. As shown, saturation and 3D GRASE excitation regions are not aligned using oblique positioning, leading to substantial signal fluctuation and potential spin-history artifacts in acquired images. Using a sagittal positioning, presaturation and image readout are aligned, but large amounts of translational in-plane motion are expected.

As visualized, cranial-caudal liver motion appears through-plane in subsequent image acquisitions using oblique positioning. Mismatches of saturation/imaging regions could result in serious spin-history artifacts (78), which cannot be corrected retrospectively, but could be tackled by prospective adaption. In addition, the image content in subsequent 3D GRASE volumes might differ in subsequent label/control acquisitions. In sagittal/coronal positioning, large in-plane shifts of the liver are expected. Note that the BS inversion

region usually covers a large area, beginning at the labeling plane and extending over the imaging region, which makes it less affected by movements of the liver (cf. Figure 4.9). Thus, prospective correction of the inversion region is not coercively needed. The position of the labeling plane is also kept fix throughout the scan, because analysis of the effects of breathing motion with respect to labeling efficiency is beyond the scope of this work. The following paragraphs therefore describe the general implementation of a prospective pCASL sequence which updates the saturation and 3D GRASE modules to the current motion state of the liver.

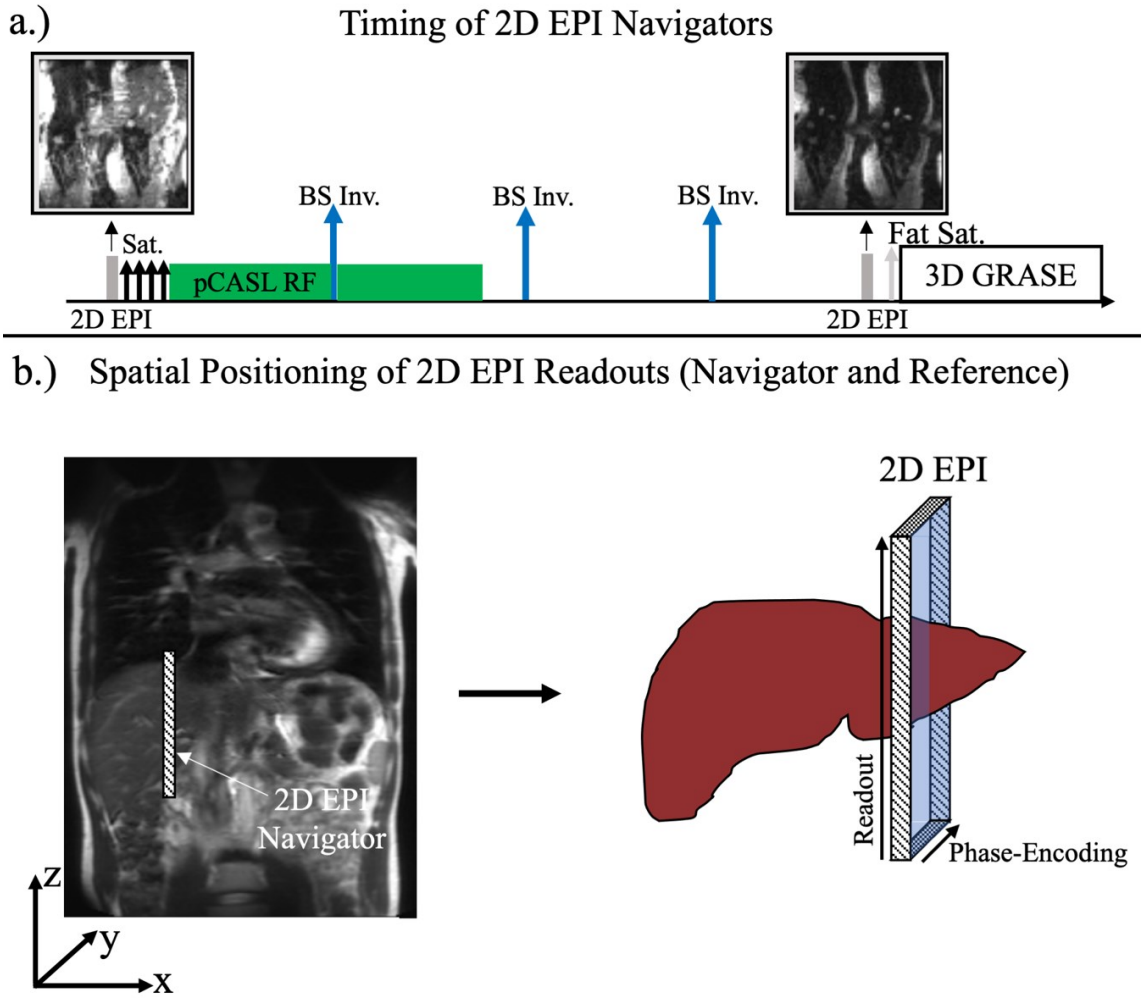

Figure 4.10: a.) Timing of navigator readouts during the pCASL scan. Two navigators are inserted immediately before the initial saturation of the imaging slab as well as the 3D GRASE image readout module; and b.) Schematic representation of the sagittal positioning of the 2D EPI readouts. The readout direction of the navigator corresponds to the cranial-caudal direction, where major translational shifts are expected. The phase-encoding direction corresponds to the anterior-posterior direction. According to the indicated coordinate system, the 2D EPI readout lies in the z-y-plane. Note that the navigator positioning is always sagittal, irrespective of the actual 3D GRASE positioning.

Sagittal 2D EPI navigator readouts are inserted into the background suppressed pCASL sequence immediately before saturation and 3D GRASE excitation to estimate the position of the liver (cf. Figure 4.10a). Sagittal positioning of the navigator is selected such that the cranial-caudal shift appears in-plane (cf. Figure 4.10b). As shown, the application of the BS inversion pulses results in a lack of liver signal immediately before the 3D GRASE module, making direct image registration difficult (cf. Figure 4.10a). However, residual signal, mainly arising from abdominal fat, can be used to estimate the current liver position, based on a matching algorithm with an EPI reference series.

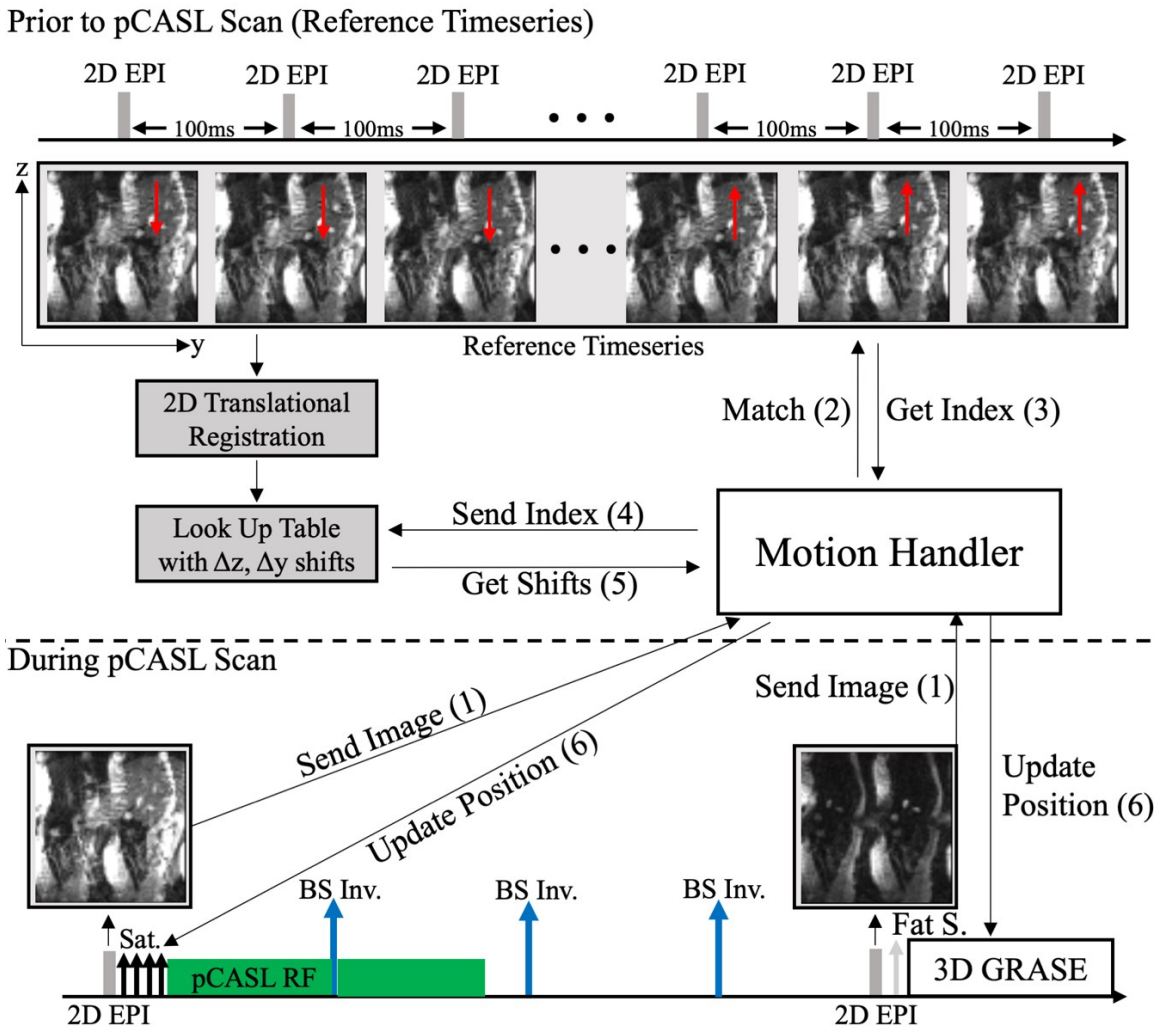

Figure 4.11: Schematic presentation of the prospective compensation of cranial-caudal liver shifts during the pCASL experiment. A 2D EPI reference timeseries is acquired prior to the pCASL experiment, and liver shifts are calculated and stored in a lookup table. During the pCASL scan, 2D EPI navigators are matched to the reference timeseries (see (1)(2)(3)). The highest correlation indicates the current state of the liver during the breathing cycle and a corresponding 2D shift from the look up table is sent back to the sequence in real-time, which is used to update the position of the saturation/3D GRASE module (see (4)(5)(6)).

The series of EPI reference images is acquired over a period of multiple seconds prior to the actual pCASL scan under free-breathing conditions. During this time, the range of respiratory induced liver displacements is sampled and can be calculated from the EPI reference series (cf. Figure 4.11, “Prior to pCASL Scan”) (83). Reference EPI images show contributions from both abdominal fat and liver tissue. For each image of the reference series, a lookup table entry is stored with the current position of the liver.

After acquiring the EPI reference series and filling the lookup table, the actual pCASL experiment is run with the previously described EPI navigator acquisition (cf. Figure 4.11, “During pCASL Scan”). Immediately after each navigator acquisition, the index of the best matching image from the reference series is obtained by finding the maximum normalized cross-correlation (cf. Figure 4.11, (1),(2),(3)). Using the index, a corresponding shift from the lookup table is obtained (cf. Figure 4.11, (4), (5)) and a position update is sent back to the saturation/3D GRASE module of the pCASL sequence, compensating the respiratory induced liver motion.

4.3.3.2 Registration of the 2D EPI reference series

Registration of the EPI reference series is not trivial, because estimates are likely to be guided by the high intensity signal of abdominal tissue and fat (cf. Figure 4.11). We therefore propose an algorithm which aims to identify a spatial region in the reference series, most likely corresponding to the desired liver movements, based on two properties: First, the liver forms a contiguous region in acquired images, while fat covers locally distributed bands with limited extend in the phase-encoding direction. Therefore, if the phase-encoding direction is subdivided into different spatial segments, many segments containing signal from liver should share comparable motion trajectories. Second, it can be assumed that the difference

$$\Delta z_{\mathrm{diff}} = |\Delta z_{\mathrm{max}} - \Delta z_{\mathrm{min}}|, \qquad [4.21]$$

with Δz_{max}, Δz_{min} the maximum and minimum estimated cranial-caudal shifts, should be large in liver regions. Combining both ideas, we propose the algorithm in Figure 4.12. Let $N_{\mathrm{x}}, N_{\mathrm{y}}$ be the number of readout and phase encoding samples in the EPI reference images, respectively. A sliding window of size N_{x} x $N_{\mathrm{y,w}}$ with $N_{\mathrm{y,w}} < N_{\mathrm{y}}$ is defined which is shifted in the phase-encoding direction of the timeseries in a pixel-by-pixel fashion. For each

window position y_w, an image registration with the windowed data is performed, yielding motion estimates $\Delta z(t, y_w)$, $\Delta y(t, y_w)$ (cf. Figure 4.12, (1) and (2)). The Δz estimate covers the cranial-caudal direction and will be used for the following classification (cf. Figure 4.12, (2)):

1. From the pool of estimated trajectories $\Delta z(t, y_w)$ select the one with largest difference $\max(\Delta z_{diff}(y_w))$. The chosen trajectory $\Delta z_i(t)$ defines a new group i. Store the deflection $\Delta z_{diff,i}$
2. Process all remaining trajectories $\Delta z(t, y_w)$ which were not yet classified and calculate the mean squared error $\mathrm{MSE}\big(\Delta z(t, y_w), \Delta z_i(t)\big)$. If MSE < 2, increase the number of counts $N_c(i)$ of the group by 1 and remove $\Delta z(t, y_w)$ from the pool.
3. Go to 1 if not all trajectories are sorted into groups.

The utilized threshold of $\mathrm{MSE} < 2$ was found to yield adequate results during initial tests. Finally, groups are assigned a score

$$S_i = N_c(i) \cdot \Delta z_{diff}(i). \qquad [4.22]$$

The group of segments with highest score $\max(S_i)$ is finally selected, and the largest coherent region of spatial segments in that group is used for the final registration (cf. Figure 4.12, (3)). Note that the final $\Delta y(t)$ component is discarded if

$$\Delta y_{diff} = |\Delta y_{max} - \Delta y_{min}| > 8\ \mathrm{mm}, \qquad [4.23]$$

due to potentially misguided $\Delta y(t)$ estimates from truncated liver vessels. For the first acquired navigator image, no feedback is sent to the sequence. Instead, the lookup table is recalculated to yield relative position updates with respect to the first navigator. The registration of the reference time series as well as the matching procedure are implemented in the vendor-specific image reconstruction framework ICE (Siemens Healthineers, Erlangen, Germany). Note that the identified liver region is only used for filling the lookup table with correct shifts. During the pCASL experiment, the whole image content of acquired navigators is used for calculation of cross-correlation, exploiting a maximum of the position variation of different signals in acquired images.

4.3.3.3 Application of prospective $\Delta z(t)$, $\Delta y(t)$ updates

Motion estimates from the lookup table describe shifts in the cranial-caudal and anterior-posterior anatomical direction due to the sagittal positioning of the EPI reference series. The implemented algorithm therefore takes care on the correct application of these shifts depending on the actual positioning of saturation plane and 3D GRASE volume during the pCASL scan. Using an oblique positioning, as demonstrated in Figure 4.9, updates need to be applied as a linear combination of different Cartesian directions. Note that for some positionings such as sagittal, the technical updating of the saturation plane has no physical effect, due to the infinite extend of the in-plane saturation region.

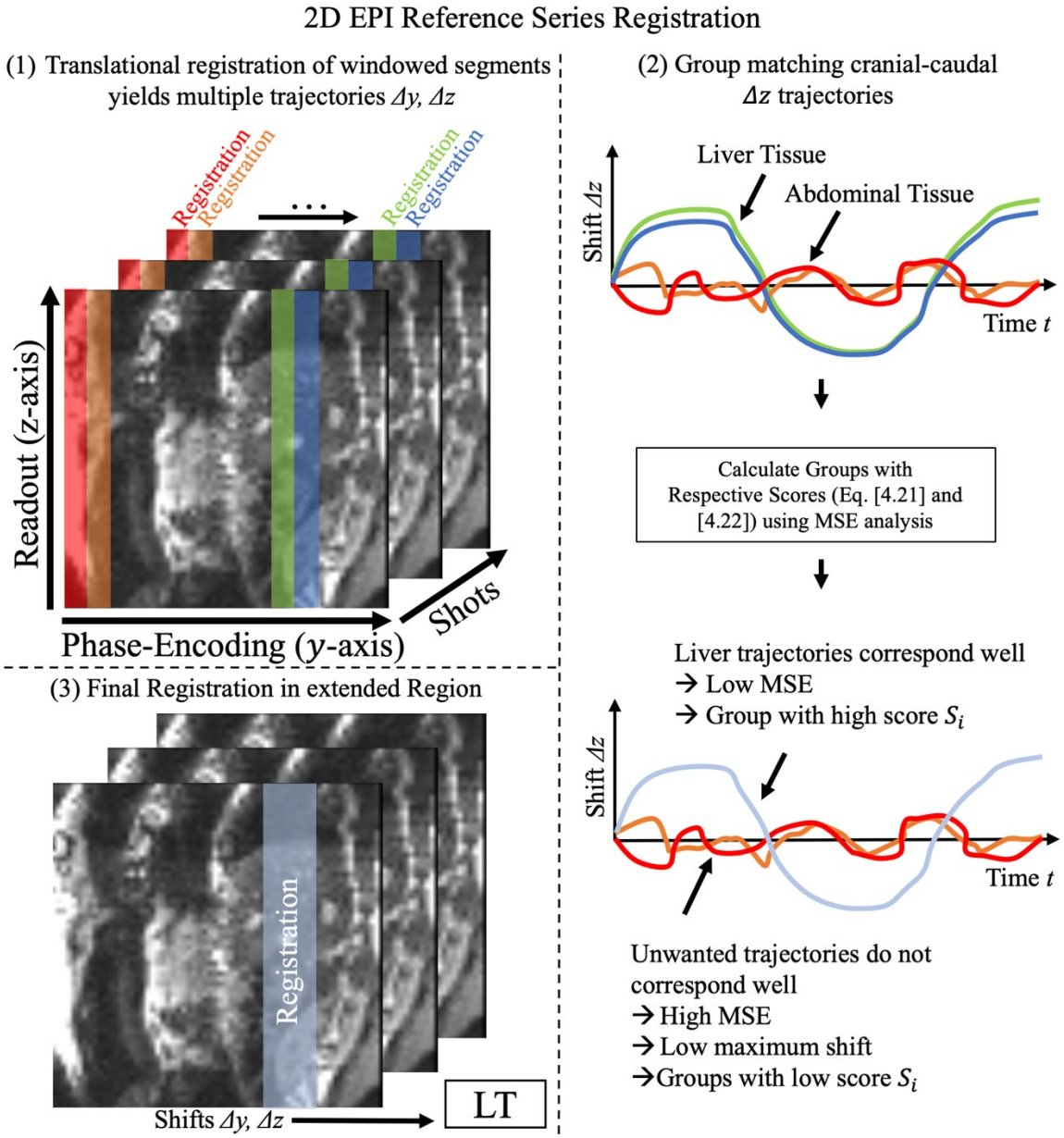

Figure 4.12: Schematic representation of the image registration method applied to the EPI reference series. Numbers indicate the temporal succession of the processing steps as described in section 4.3.3.2.

5 Evaluation of Novel Approaches

5.1 Reduction of Motion Sensitivity using Background Suppression

5.1.1 Optimization of BS Inversion Pulses

This section describes the optimization of FOCI pulses, which can be used for background suppression (BS) in brain as well as abdominal ASL experiments. The goal is to derive pulse parameters which achieve inversion efficiencies close to 100%, being mandatory for accurate static tissue reduction and thus motion insensitivity. In addition, if multiple BS inversion pulses with imperfect efficiency are played out during ASL experiments, a decrease in perfusion SNR might result (44), as exemplarily illustrated in Figure 5.1.

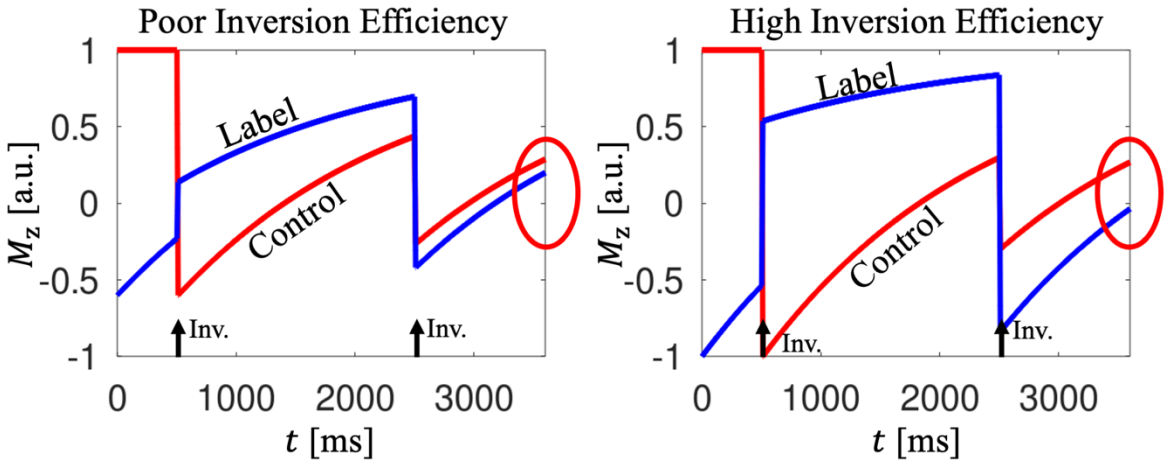

Figure 5.1: Demonstration of the effect of imperfect inversion efficiency in a background suppressed PASL experiment. In case of low inversion efficiency, the initial labeling pulse does not achieve complete inversion of the inflowing blood. In addition, the difference between inverted/non-inverted blood is decreased with each additional inversion pulse. Finally, after the inflow time, the difference between label and control state is drastically decreased, resulting in a loss of SNR.

The basic concept of adiabatic excitation and inversion has been discussed in section 2.8. Of high interest for the following analysis is the so-called inversion efficiency, which is defined as

$$IE = \frac{\left(M_z(0) - M_z(T_P)\right)}{2M_z(0)} \cdot 100, \qquad [5.1]$$

with the duration of the adiabatic pulse T_P, the longitudinal magnetization $M_z(T_P)$ after application of the inversion pulse and the longitudinal magnetization $M_z(0)$ before application of the inversion pulse.

5.1.1.1 Methods

In order to obtain optimal parameters μ and β of FOCI pulses to be used for BS inversion in brain and abdominal ASL sequences, Bloch simulations were carried out. In this work, the C-shape FOCI pulses (cf. section 2.8.1) with modulation functions $A(t)^{\max} = 1, 2, 5, 10$ and a duration of $T_p = 10.24$ ms were investigated. The achievable maximum amplitude of RF pulses in abdominal imaging is usually restricted. In case of the 3T Siemens Skyra Magnetom (Siemens Healthineers, Erlangen) system, which was used for all measurements in this work, a typical maximum amplitude of 14 µT was observed during initial liver ASL examinations. Accordingly, maximum amplitudes of $B_{1,\max} = 14$ µT were allowed in the simulation process to ensure that pulses are played out as intended. Relaxation times were set to $T_1 = 1920$ ms and $T_2 = 275$ ms, which corresponds to expected values for blood at 3T (84). Simulations were performed for FOCI parameter ranges of $\beta = (200 - 1800)\frac{1}{s}$ and $\mu = 0 - 12$. For each pair of values, the mean longitudinal magnetization $\overline{M_z}(T_p)$ was calculated over a region of $\Delta\omega = \pm 400$ Hz and $\Delta B_{1,\max} = \pm 20\%$ without application of a slice selection gradient (44). In addition, the area under the RF envelope of the pulses $\int_0^{T_p} B_1(t)dt$ was calculated. Although the mathematics for accurate calculation of the SAR (specific absorption rate) contribution of a RF pulse are quite complex (cf. e.g., (85)), comparison of amplitude integrals allows a relative statement about the total energy of investigated pulses. For this purpose, the amplitude $B_{1,\max} = 14$ µT was assumed here. Using theoretical results from the Bloch simulation, suitable combinations of β and μ were identified based on a compromise between mean inversion efficiency, the relative pulse energy and the product $\beta \cdot \mu$. Higher

values of the latter increase the sharpness of the slice profile, due to an increased gradient strength according to Eq. [2.39]. A high inversion efficiency $\overline{IE}_{\mathrm{Theo}}$ close to 100% was the main focus during the manual selection of suitable value pairs. Finally, the minimum possible slab thickness using selected parameters was identified according to (33). A maximum gradient strength of $G_{\max} = 40\,\frac{\mathrm{mT}}{\mathrm{m}}$ was assumed here, corresponding to the hardware limits of the system.

Additional simulations using determined optimal values were carried out with a slice-selective gradient and a desired slab thickness of $\Delta z_{\mathrm{slab}} = 220$ mm and $\Delta\omega = \pm 400$ Hz to investigate the slice profiles in dependence of different off-resonance frequencies. For the purpose of this analysis, the pulse amplitude was kept fixed to $B_{1,\max} = 14$ µT.

The C-shape FOCI pulses with selected parameters were finally implemented on the 3T Siemens Skyra Magnetom System (Siemens Healthineers, Erlangen). The inversion efficiency was experimentally determined by performing an inversion recovery experiment using a 3D GRASE readout with ten inversion times, ranging from $TI = 100$ ms to $TI = 2800$ ms with a step size of $\Delta TI = 300$ ms. Parameters of the inversion recovery experiment were: TR/TE = 15000 ms/31.1 ms, matrix size = 96 x 96 x 8 with two-fold Cartesian segmentation in the in-plane phase encoding direction, FoV = (300 x 300 x 32) mm^3, voxel size = (3.125 x 3.125 x 4) mm^3. Scans were performed using a geometric phantom with given relaxation times of $T_1 = (290 \pm 20)$ ms and $T_2 = (260 \pm 30)$ ms. Acquired magnitude image data was fitted voxel wise to an inversion recovery model according to

$$s(TI) = \left| M_{\mathrm{z},0}\left(1 + M_1 \cdot \exp\left(-\frac{TI}{T_1}\right)\right)\right|. \qquad [5.2]$$

The longitudinal magnetization immediately after inversion $M_{\mathrm{z}}(T_{\mathrm{p}})$ is obtained by the relation

$$M_{\mathrm{z}}(T_{\mathrm{p}}) = M_1 + 1. \qquad [5.3]$$

Experimental inversion efficiencies $IE_{\mathrm{exp}}(x, y, z)$ were calculated voxel wise using Eq. [5.1] assuming $M_{\mathrm{z}}(0) = 1$. The averaged experimental inversion efficiency $\overline{IE}_{\mathrm{exp}}$ is then obtained by averaging $IE_{\mathrm{exp}}(x, y, z)$ over the four central slices of the acquired 3D GRASE volume. Note that relevant non-noise voxels are first thresholded based on the

average signal in the volume of the last measured timepoint $TI = 2800$ ms. Finally, theoretical and experimental inversion efficiencies were qualitatively compared.

5.1.1.2 Results

Figure 5.2 and Figure 5.3 show calculated mean inversion efficiencies $\overline{IE}_{\mathrm{Theo}}$ as well as the amplitude integral $\int_0^{T_\mathrm{p}} B_1(t)dt$ for different combinations of parameters β and μ. The region for which the adiabatic condition holds clearly shows as a deep red band. Outside of this region imperfect inversion occurs. The amplitude integral depends on the parameter β and visibly decreases for higher values of β. In general, the amplitude integral takes higher values for higher modulation functions $A(t)^{\max}$. Selected compromises in terms of values for β and μ are indicated by a white dot.

The corresponding pulse properties are summarized in Table 5.1. As shown, theoretical mean inversion efficiencies are comparable high for all values of $A(t)^{\max}$, ranging between 98% and 99%. The amplitude integral increases with higher values for $A(t)^{\max}$. The same trend is observed for the minimum slab thickness, due to amplified gradient strengths.

Figure 5.4 shows simulated slice profiles at $\Delta\omega = 0$ using $A(t)^{\max} = 1, 2, 5, 10$ and optimal parameters μ and β from Table 5.1. As shown, the transition between desired non-inverted/inverted regions gets steeper for higher modulation functions, and the desired slice profile is more accurately resampled. In addition, slight fluctuation of $M_\mathrm{z}(T_\mathrm{p})$ is observed in the inverted region for $A(t)^{\max} = 1$. For higher modulation factors, $M_\mathrm{z}(T_\mathrm{p})$ in inverted regions is steadier.

Figure 5.5 shows a comparison of slice profiles for different off-resonance frequencies $\Delta\omega = \pm 400$ Hz. Sharper and steadier slice profiles are achieved with higher modulation functions. $A(t)^{\max} = 10$ yields the sharpest profile with the highest robustness against variation in off-resonance.

Finally, Figure 5.6 shows a comparison of theoretical mean inversion efficiencies and fitted mean inversion efficiencies from the inversion recovery experiment. Average theoretical efficiency is slightly higher than the measured value for $A(t)^{\max} = 1, 2, 5$. The inverse observation is made for $A(t)^{\max} = 10$, which yielded the highest measured

experimental inversion efficiency. The spatial distribution of inversion efficiencies, calculated from individual slices, shows lower inversion efficiencies for low modulation functions in outer areas, when compared to higher modulations. However, in general, all implemented FOCI pulses yielded high experimental inversion efficiencies between 97% and 98%.

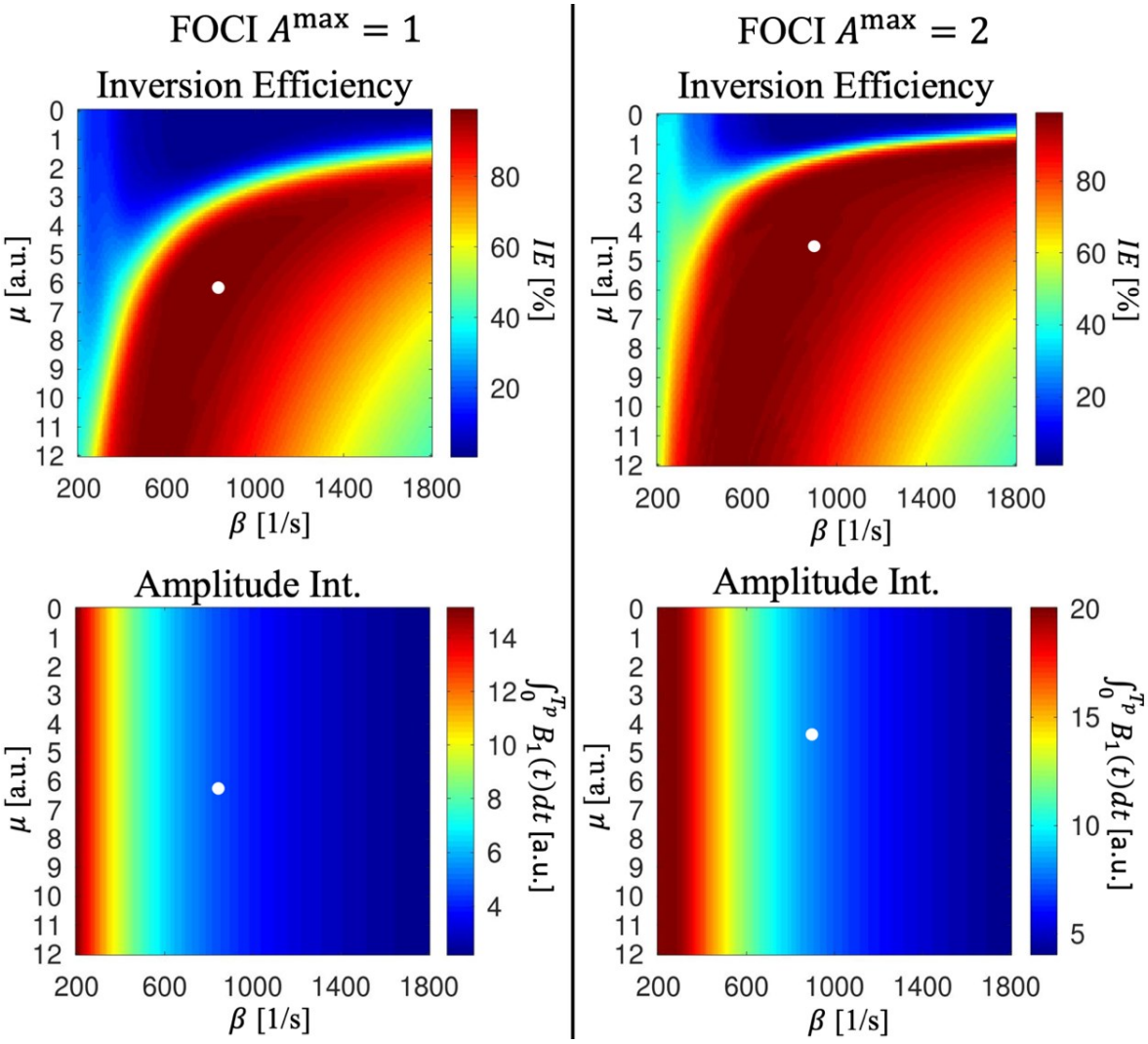

Figure 5.2: Calculated mean inversion efficiencies $\overline{IE}_{\mathrm{Theo}}$ for different combinations of μ and β (upper row) as well as the amplitude integral $\int_0^{T_p} B_1(t)dt$ (lower row) for modulation functions $A(t)^{\max} = 1{,}2$. White dots indicate the selected pair of values.

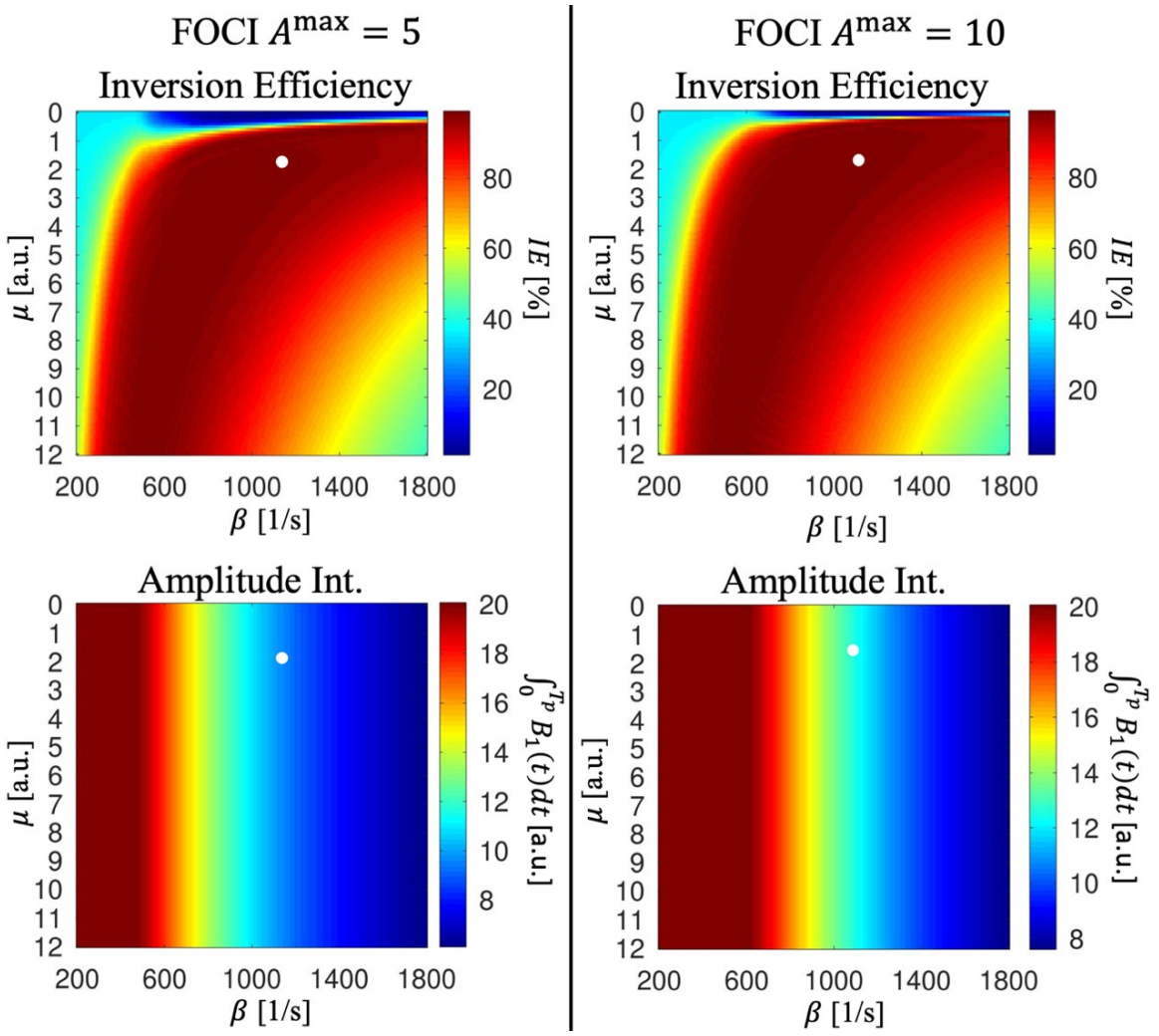

Figure 5.3: Calculated mean inversion efficiencies $\overline{IE}_{\mathrm{Theo}}$ for different combinations of μ and β (upper row) as well as the amplitude integral $\int_0^{T_p} B_1(t)dt$ (lower row) for modulation functions $A(t)^{\max} = 5{,}10$. White dots indicate the selected pair of values.

$A(t)^{\max}$ [a.u.]	1	2	5	10
β [1/s]	760	910	1150	1100
μ [a.u.]	6.3	4.2	1.9	1.8
$\overline{IE}_{\mathrm{Theo}}$ [%]	99	98	98.5	98
$\int_0^{T_p} B_1(t)dt$ [a.u.]	5.15	7.98	9.53	12.44
$\Delta z_{\mathrm{min,slab}}$ [mm]	0.9	1.4	2	3.7

Table 5.1: Selected values μ and β and corresponding theoretical mean inversion efficiencies $\overline{IE}_{\mathrm{Theo}}$ as well as calculated energy contribution $\int_0^{T_p} B_1(t)dt$ and minimum slab thickness $\Delta z_{\mathrm{min,slab}}$. The minimum slab thickness was calculated according to (33).

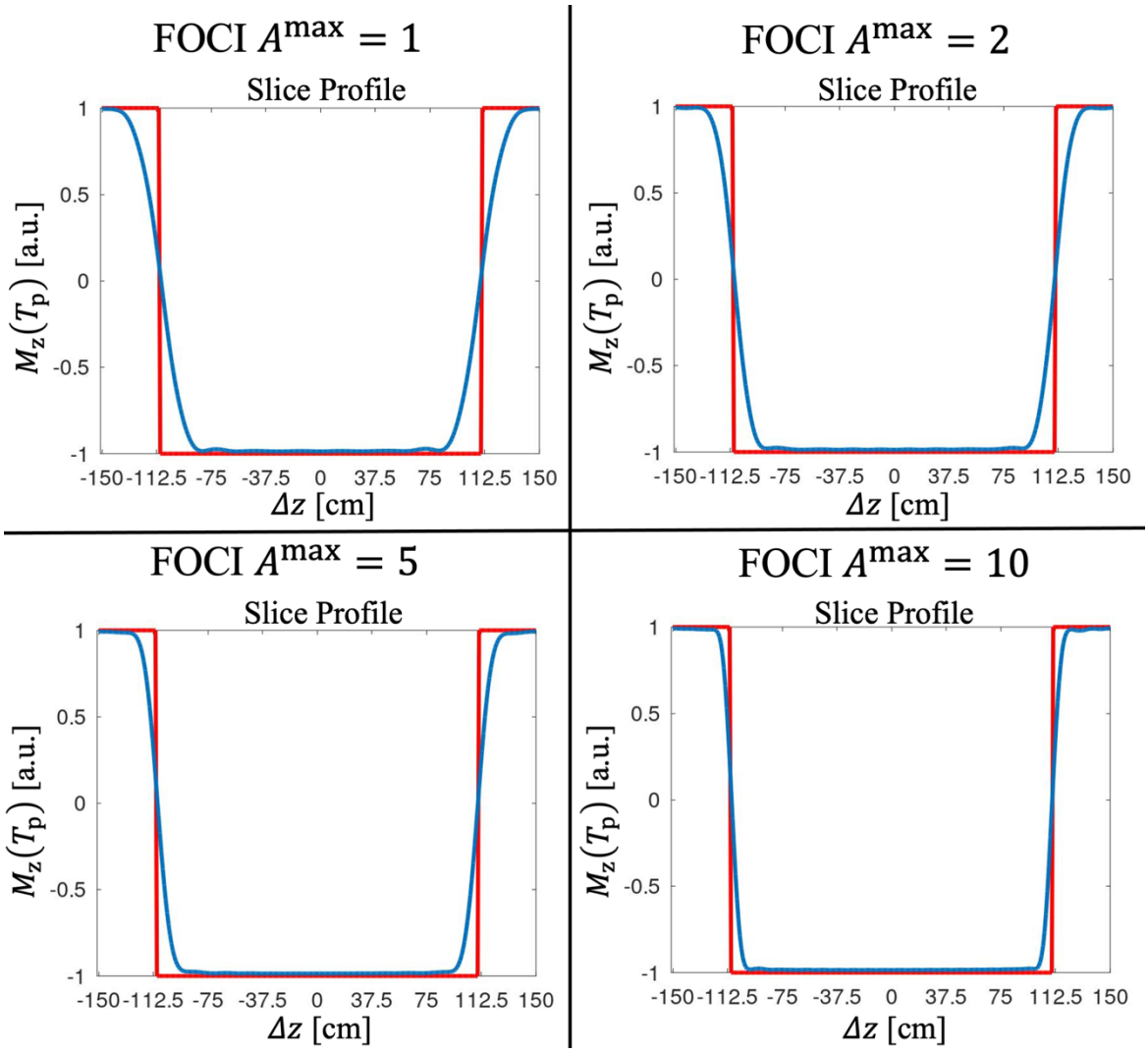

Figure 5.4: Slice profiles (Δω = 0Hz) of FOCI pulses using the optimal parameters from Table 5.1 for a targeted slab thickness of 220 mm. As visualized, a higher modulation function results in sharper slice profiles and less modulation in the inverted region.

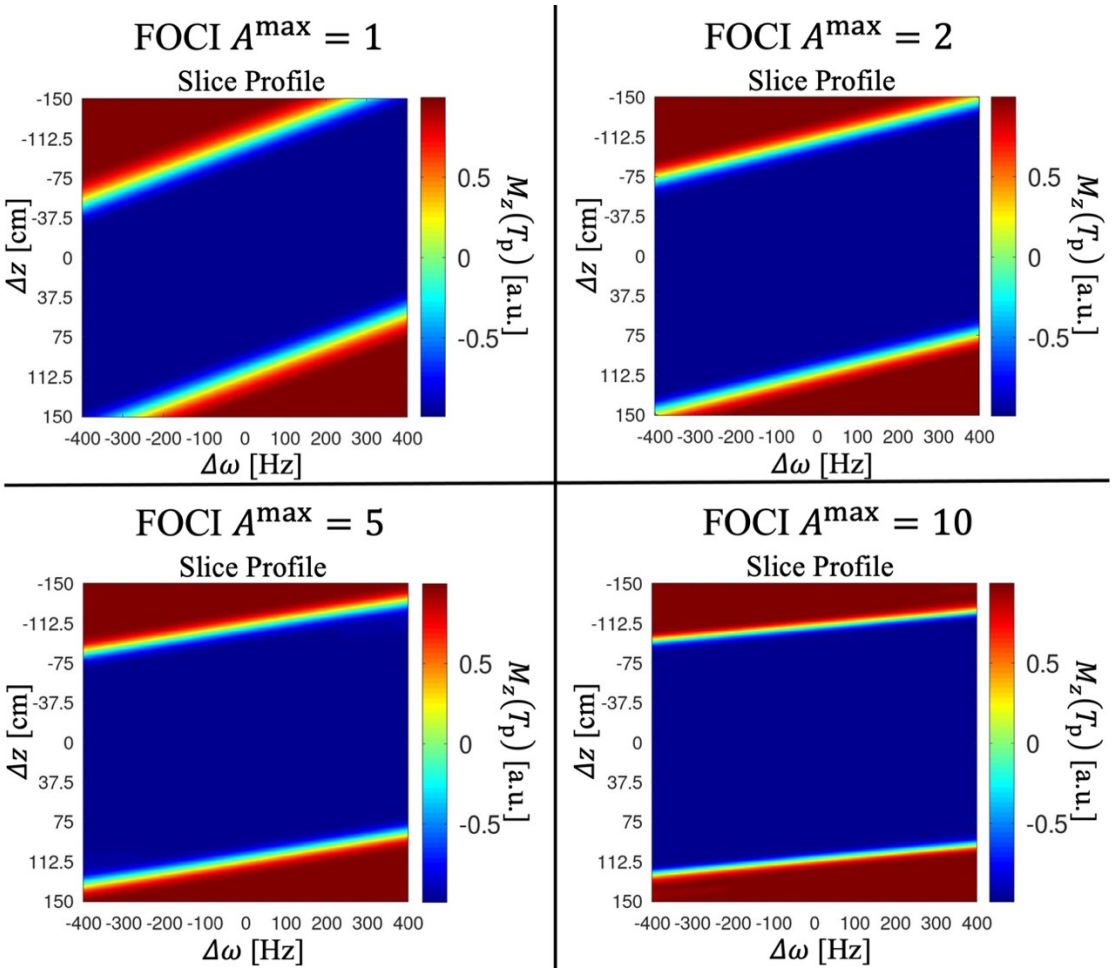

Figure 5.5: Simulated slice profiles of FOCI pulses for off-resonances $\Delta\omega = \pm 400$ Hz using optimal parameters from Table 5.1 and a slab thickness of 220 mm.

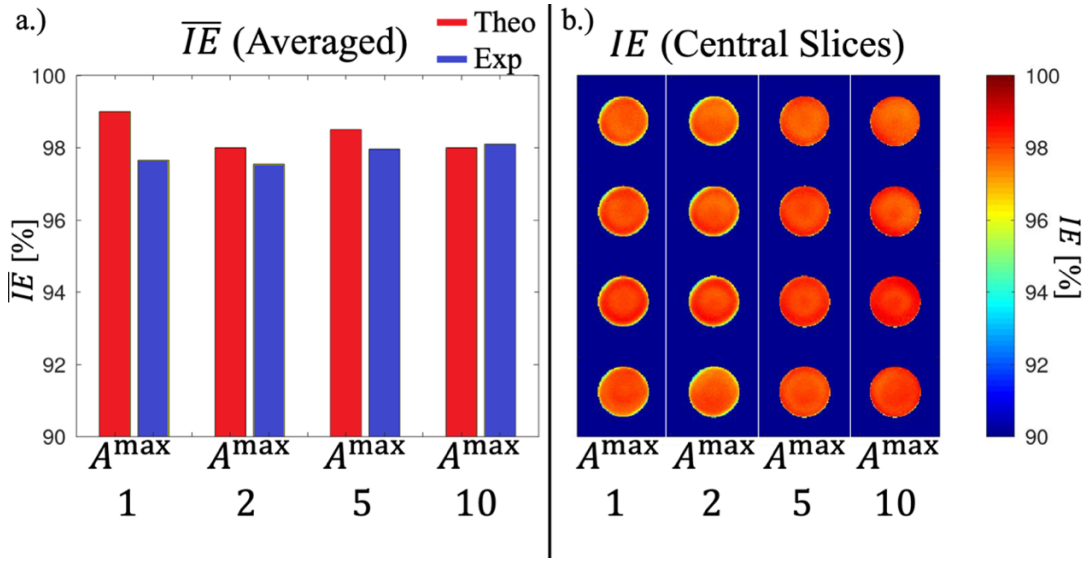

Figure 5.6: a.) Comparison of mean inversion efficiencies obtained from the theoretical and experimental setups for the FOCI pulses using parameters from Table 5.1 with different modulation functions; and b.) Local inversion efficiencies in the geometric phantom achieved with different FOCI pulses.

5.1.1.3 Discussion

The theoretical analysis using Bloch simulations allowed clear identification of value pairs of β and μ which satisfy the adiabatic condition for all modulation functions $A(t)^{\max}$ which were investigated in this work. Chosen value pairs from Table 5.1 lie inside the respective adiabatic regions and were primary selected based on the mean inversion efficiency with respect to reasonably low amplitude integrals. Note that, if SAR limitations are the primary concern, even stricter compromises exist which show further reduced SAR contribution while still achieving high inversion efficiencies (cf. the extend of the adiabatic regions in Figure 5.2 and Figure 5.3) with potential minor impacts on the sharpness of the slice profile. Since robust inversion was the focus in this work, the less stringent non-analytical compromises are suitable choices, as indicated by high theoretical inversion efficiencies. A distinct advantage of higher modulation functions is the sharper slice profile (cf. Figure 5.4 and Figure 5.5). A sharp slice profile is of high importance in pCASL imaging to ensure complete inversion of the labeled blood bolus with each BS pulse. In FAIR PASL imaging, the slice profile defines how much of the blood outside the image volume is perturbated in the control case. Ideally, the effect of the inversion outside the imaging region should be neglectable. From this point of view, $A(t)^{\max} = 10$ is clearly the recommended choice. However, this comes at the cost of increased amplitude integrals and thus again increased SAR load. In addition, the modulation of the gradients increases the minimum achievable slice thickness. (cf. Table 5.1). In practice, SAR limitations of the system were not met using four FOCI pulses with $A(t)^{\max} = 10$ and a TR of 4500 ms in abdominal imaging. Therefore, SAR is not found to be a limiting factor for most reasonable pCASL/PASL setups in this work. The increased minimum slice thickness is also not problematic for ASL imaging using a 3D GRASE readout, where inversion regions are usually much larger than 3.7 mm. Therefore, the benefits of a sharp slice profile and highest measured inversion efficiency using $A(t)^{\max} = 10$ predominate the minor drawbacks.

Measured experimental mean inversion efficiencies are above 97% for each of the implemented FOCI configurations and thus suitable for ASL imaging (cf. Figure 5.6a). Slightly higher mean inversion efficiency for higher modulation functions arises from the increased inversion efficiency in outer areas of the phantom (cf. Figure 5.6b). It is often encountered that the B_1 field strength decreases and the off-resonance frequency increases due to poorer shimming near interfaces of different types of chemical substances (86). A

higher modulation function seems to ensure increased inversion efficiency, here. Note, however, that the decrease in inversion efficiency for lower modulations is in the region of $\approx 1-2\%$ in these areas and thus not found to be severe.

Last, it should be mentioned that a direct comparison between mean theoretical and experimental inversion efficiencies from Figure 5.6a is difficult. While the range of B_1 and $\Delta\omega$ variation is known in the theoretical case, the distribution remains unknown in the phantom during the experiments. The recreation of the theoretical scenario in experiments is not straight forward since increased off-resonance also affects the 3D GRASE imaging module in terms of geometric distortion and potential signal loss. Due to the previous discussion, it can however be assumed that higher modulation functions are beneficial for increased robustness against variation in B_1 and $\Delta\omega$ if SAR limitations and hardware capability are not met.

5.1.1.4 Conclusion

Achieved inversion efficiencies of FOCI pulses with a maximum amplitude of $\left|B_{1,\max}\right| = 14\,\mu\mathrm{T}$ using modulation functions $A(t)^{\max} = 1, 2, 5, 10$ were theoretically and experimentally assessed. Optimal parameters were found for each FOCI setup, yielding a set of FOCI configurations for abdominal ASL imaging, which can be applied for different SAR and hardware limitations. If both constraints are not met, a FOCI pulse with $T_\mathrm{p} = 10.24\,\mathrm{ms}$, $\mu = 1.8$, $\beta = 1100\,\frac{1}{\mathrm{s}}$ and $A(t)^{\max} = 10$ is recommended, yielding nearly optimal inversion efficiency in combination with a sharp slice profile.

5.1.2 Application of Adaptive Background Suppression to Brain pCASL Imaging

In the following section, the feasibility of the adaptive BS technique from section 4.1.3 is evaluated in phantom and brain pCASL measurements. The goal is to derive a recommendation about the needed number of BS inversions and the optimal target level of residual magnetization for application in brain ASL imaging, which allows reconstruction of high-resolution perfusion-weighted images, which could then be used as a setup for automized adjustment of BS in future studies.

5.1.2.1 Methods

Experiments

To investigate the accuracy of the implemented adaptive BS technique as well as the quality of reconstructed perfusion-weighted images, a watermelon as well as the brain of two healthy volunteers (1m, 1w) were scanned using a pCASL sequence at 3T on a Siemens MAGNETOM Skyra (Siemens Healthineers, Erlangen) with axial positioning. For all scans, a M_0 scan was acquired first and the two-dimensional histogram was automatically calculated. Then, multiple pCASL experiments were performed with targeted BS levels of $M_{\mathrm{res}} = 0\%,\ 4\%,\ 8\%,\ 12\%$. The sequence was adjusted using $n_{\mathrm{inv}} = 1, 2, 3, 4$ inversion pulses during the labeling and post-labeling period for each of the given BS levels, resulting in a total number of sixteen pCASL scans per subject. Both subjects provided written informed consent prior to scanning and the study was run under a general protocol for pulse-sequence development approved by the local ethics committee.

For both, the M_0 scan and the pCASL imaging scan, a 3D GRASE readout module with a total matrix size of 96 x 96 x 8 and three segments of size 96 x 32 x 8 each, yielding a nominal resolution of (3.1 x 3.1 x 5) mm^3, was used. Other imaging parameters were TR/TE = 4500 ms/23.9 ms, Bandwidth = 2264 HZ/Px, FoV = (300 x 300 x 40) mm^3. In both cases, two magnetization preparation scans were applied. In addition, three Q2Tips pulses followed by a spectral fat saturation pulse were played out immediately before the 3D GRASE excitation. For the M_0 scan, six different saturation times, starting at T_S = 200 ms with an increment of 400 ms, were acquired. For the pCASL 3D GRASE acquisition, a labeling duration/post-labeling delay of 1800 ms/1800 ms was applied, according to ASL

whitepaper recommendations (37), and five measurements were averaged to increase the SNR in perfusion-weighted images, resulting in a total measurement time of 54 s per ASL scan.

Analysis of acquired data

To evaluate the accuracy of the proposed adaptive BS approach, a quantitative comparison of targeted and measured mean signal levels was performed. Therefore, a spatial percentual suppression level was calculated according to

$$M_{\mathrm{z},\%}(x,y,z) = \frac{M_{\mathrm{z,meas}}(x,y,z)}{M_0(x,y,z)}. \quad [5.4]$$

Here, $M_{\mathrm{z,meas}}(x,y,z)$ depicts the measured averaged magnitude signal of each voxel. In pCASL experiments, measured label and control data both do not perfectly correspond to the static tissue signal due to the inflowing inverted/non-inverted blood. Depending on the timing of inversion pulses, the measured signal can then be described as

$$M_{\mathrm{z,c}}(x,y,z) = M_{\mathrm{z}}(x,y,z) + M_{\mathrm{b,c}}(x,y,z), \quad [5.5]$$

and

$$M_{\mathrm{z,l}}(x,y,z) = M_{\mathrm{z}}(x,y,z) + M_{\mathrm{b,l}}(x,y,z), \quad [5.6]$$

with $M_{\mathrm{b,l}}$, $M_{\mathrm{b,c}}$ the respective magnetization levels of the inflowing blood in dependence of the inversion timings and initial inversion state (also cf. Figure 3.8). Therefore, label and control data were combined to partially compensate the effect of the inflowing blood according to

$$\begin{aligned} M_{\mathrm{z,meas}}(x,y,z) &= \frac{M_{\mathrm{z,c}}(x,y,z) + M_{\mathrm{z,l}}(x,y,z)}{2} \\ &= M_{\mathrm{z}}(x,y,z) + \frac{M_{\mathrm{b,c}}(x,y,z) + M_{\mathrm{b,l}}(x,y,z)}{2}. \end{aligned} \quad [5.7]$$

In cases where $M_{\mathrm{b,c}}$ and $M_{\mathrm{b,l}}$ have opposite signs the additional term is completely or partially cancelled. Otherwise, a small residual error in perfused regions might persist. Note that the phase of each acquired volume is phase-corrected using an algorithm as

described in (55). The term $M_0(x,y,z)$ is obtained from the previous M_0 scan. A mean suppression level is then calculated for each combination of parameters according to

$$\bar{M}_{\mathrm{z,\%}}(n_{\mathrm{inv}}, M_{\mathrm{res}}) = \frac{1}{n}\sum_{x,y,z} M_{\mathrm{z,\%}}(x,y,z). \quad [5.8]$$

with n the total number of voxels considered. Again, the outer two slices were excluded from the analysis here. In addition, noise voxels were excluded by only considering those voxels which were not thresholded during the M_0 scan fitting routine.

A percentual mean model error was further calculated by averaging the difference between predicted and measured signal:

$$\bar{e}_{\mathrm{model}}(n_{\mathrm{inv}}) = \frac{1}{n}\sum_{x,y,z}\sum_{M_{\mathrm{res}}} |(M_{\mathrm{z,meas}}(x,y,z) - M_{\mathrm{z,predict}}(x,y,z))/M_0(x,y,z)| \quad [5.9]$$

Voxel wise calculation of $M_{\mathrm{z,predict}}(x,y,z)$ was performed using Eq. [4.8]. Finally, a qualitative comparison of measured and predicted signal contrasts was performed and the visual quality of perfusion-weighted images was compared for both volunteers with respect to different combinations of n_{inv} and M_{res}.

5.1.2.2 Results

Estimated parameter maps from the saturation recovery scan for both in-vivo subjects and the watermelon are given in Figure 5.7. High T_1 values of about 2000 ms were encountered in the watermelon since the tissue predominantly consists of water. T_1 values were decreased in regions corresponding to the peel and seeds. The estimated saturation efficiency was close to 100% in the whole region of interest, which corresponds to a flip angle of 90°. However, in the first slice shown, saturation efficiency appeared to be slightly decreased.

Similar effects were found for both in-vivo subjects. Calculated T_1 maps clearly show a separation of gray and white matter regions. CSF from outer brain regions showed higher T_1 values when compared to white and gray matter regions. Estimated saturation efficiency maps showed a slight decrease in outer brain regions.

Reconstructed perfusion-weighted images using different numbers of inversion pulses and target magnetization levels are shown in Figure 5.8. Perfusion-weighted images showed good visual agreement for two – four inversion pulses and BS levels between 4% and 12%. Image quality visible decreased if suppression levels close to 0% were selected and/or only one inversion pulse was played out during the ASL preparation phase. On closer inspection, it is noticeable that the perfusion-weighted signal slightly decreased with an increased number of inversion pulses.

Figure 5.9 shows calculated mean levels of suppression in the watermelon. Measured signal and targeted magnetization agreed well for two to four inversion pulses. Slightly decreased accuracy was observed if one inversion pulse was applied. In addition, the standard deviation decreased with increased number of inversion pulses, as indicated by the error bars. The mean error between predicted and measured signal levels was below 1% for all configurations of targeted levels and numbers of inversion pulses.

The previous findings did not hold for the in-vivo data. Best correspondence between the mean measured and targeted signal was achieved for two and three inversions and the accuracy was found to be decreased if one or four inversion pulses were applied (cf. Figure 5.10a and Figure 5.11a). In addition, large errors between the model prediction and the measured signal were observed, which were significantly higher when using one or four inversions compared to two or three inversions (cf. Figure 5.10b and Figure 5.11b).

These quantitative findings correspond to visual comparison of predicted and measured image contrasts (cf. Figure 5.12 - Figure 5.14). Starting with the watermelon, the predicted and measured contrast showed high visual accordance for all levels of suppression and numbers of inversions pulses. Increased deviations were observed for the in-vivo data, especially in case of one or four inversions. However, a stepwise increase of residual signal levels using two – four inversions was observed for both subjects, regardless.

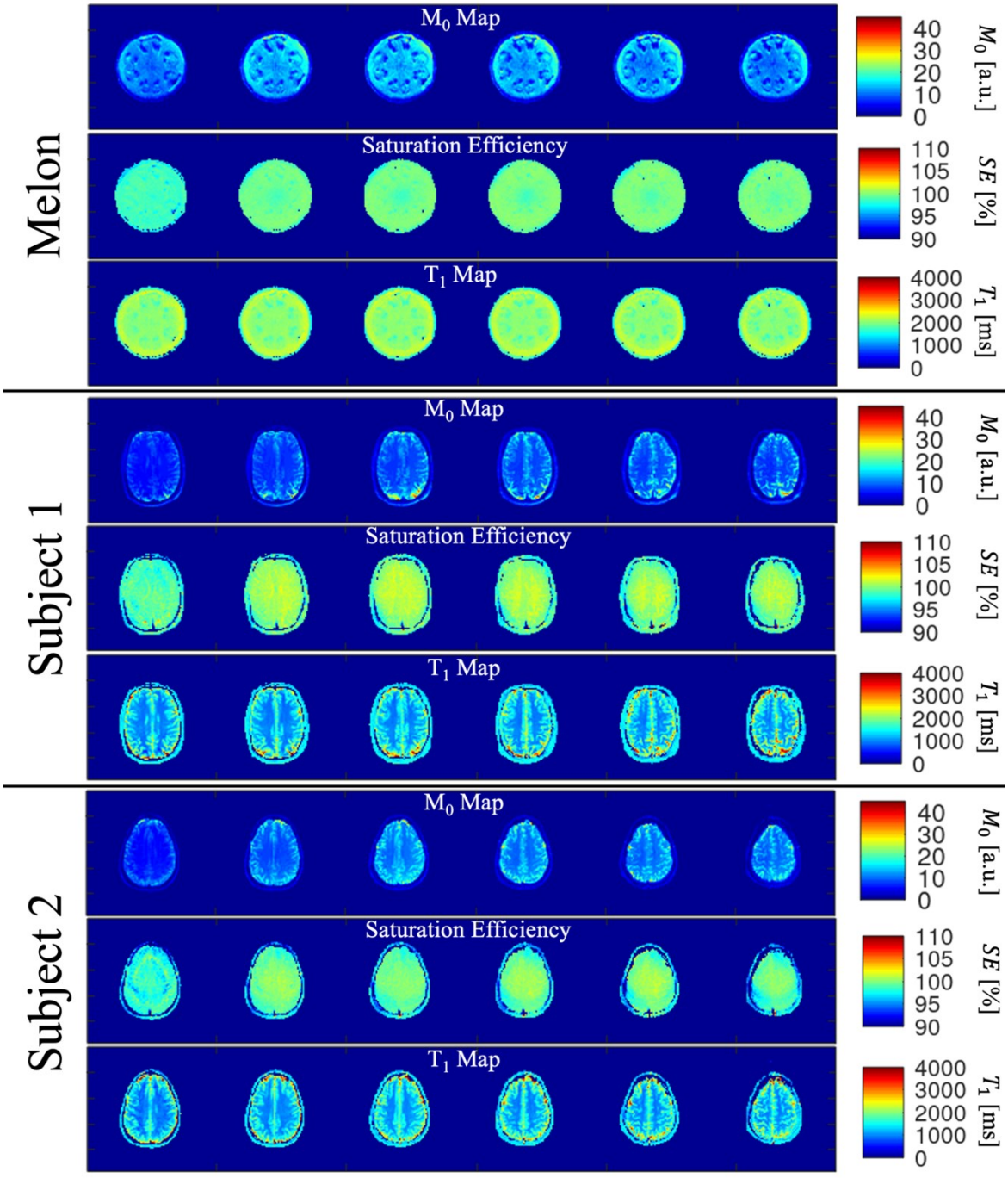

Figure 5.7: Calculated parameter maps from M_0 scans. Maps are shown for the watermelon as well as both in-vivo subjects. Columns show the six central slices of the 3D GRASE volume.

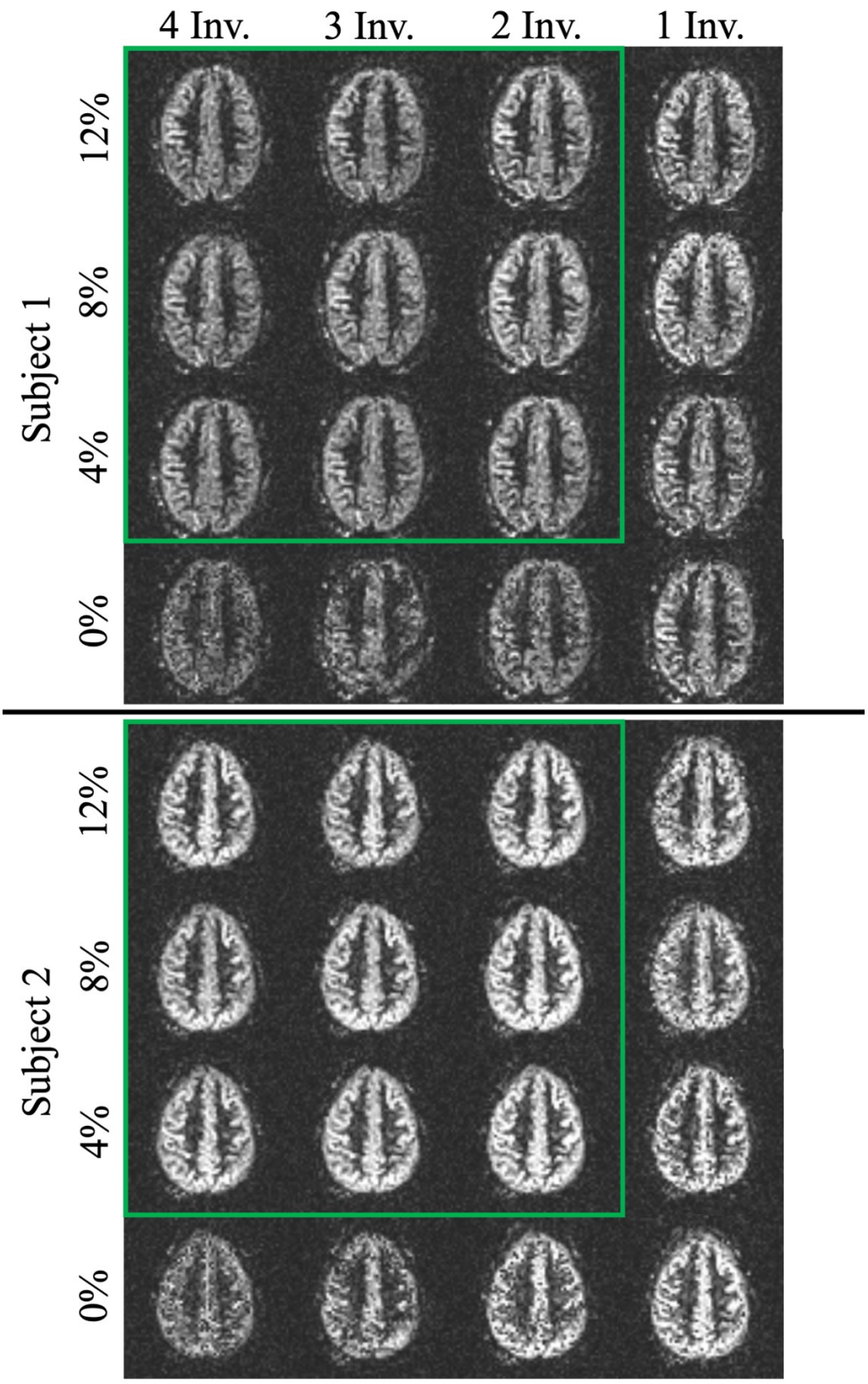

Figure 5.8: Perfusion-weighted images from a central slice of the acquired 3D volumes. Columns show images acquired using different numbers of inversion pulses, while rows show the respective targeted BS level. The green box indicates suitable combinations of settings for high quality perfusion-weighted images.

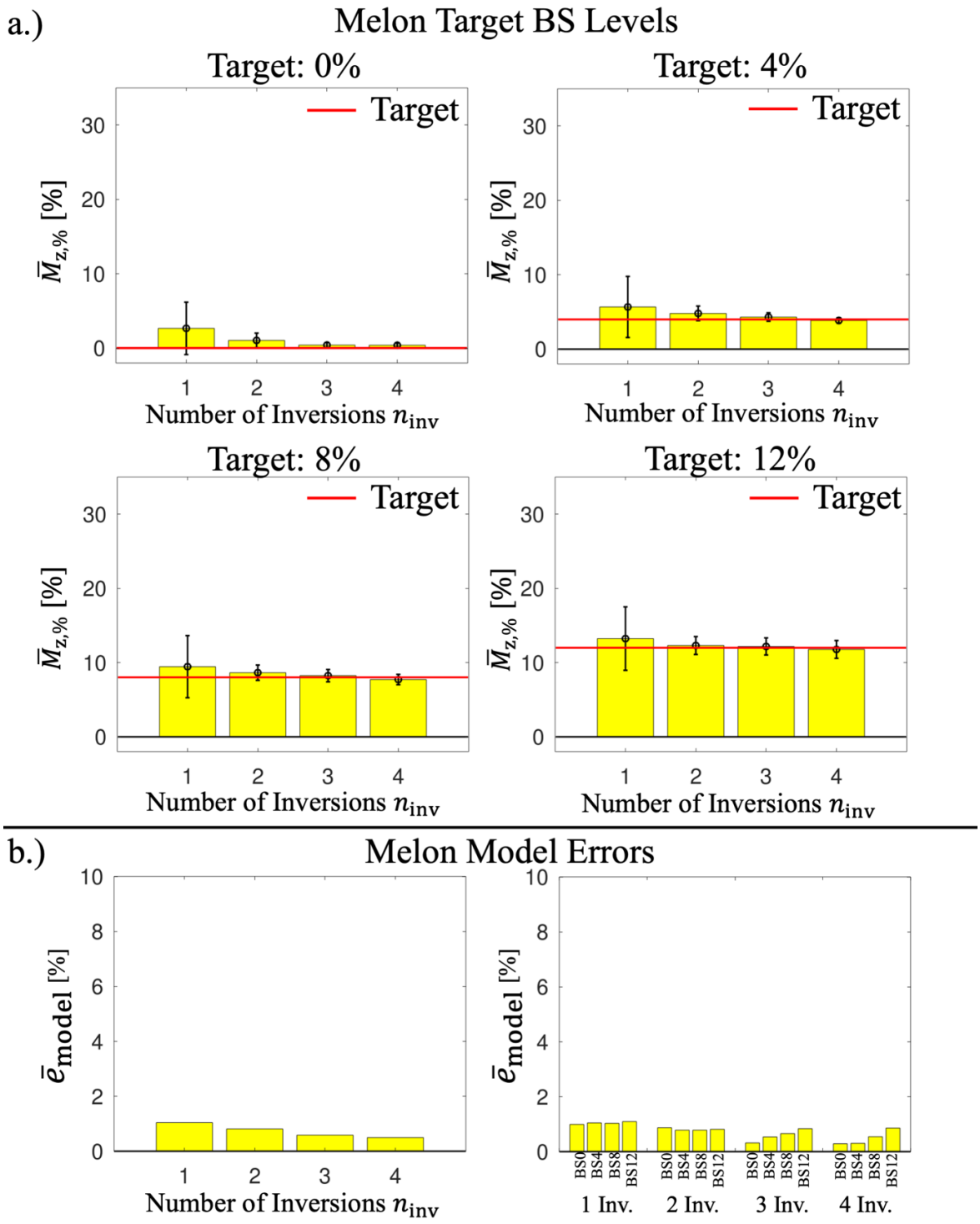

Figure 5.9: a.) Calculated mean residual levels of magnetization in the central six slices of the watermelon for different target levels and numbers of inversion pulses. The red line indicates the desired level of magnetization; and b.) Left: Calculated error between predicted and measured magnetization (Eq. [5.9]). Right: Mean model error without averaging over different target magnetization levels.

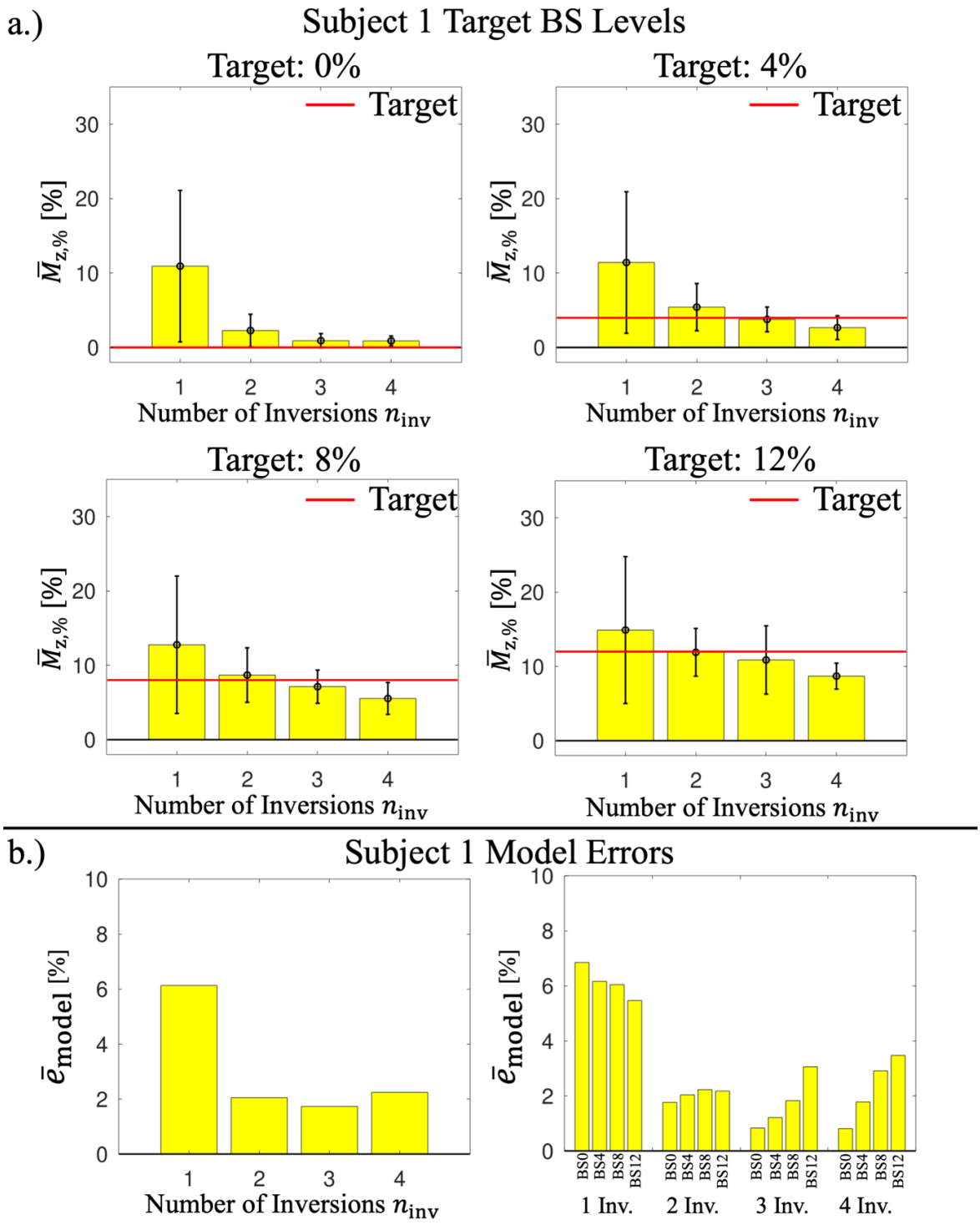

Figure 5.10: a.) Calculated mean residual levels of magnetization in the central six slices of subject 1 for different target levels and numbers of inversion pulses. The red line indicates the desired level of magnetization; and b.) Left: Calculated error between predicted and measured magnetization (Eq. [5.9]). Right: Mean model error without averaging over different target magnetization levels.

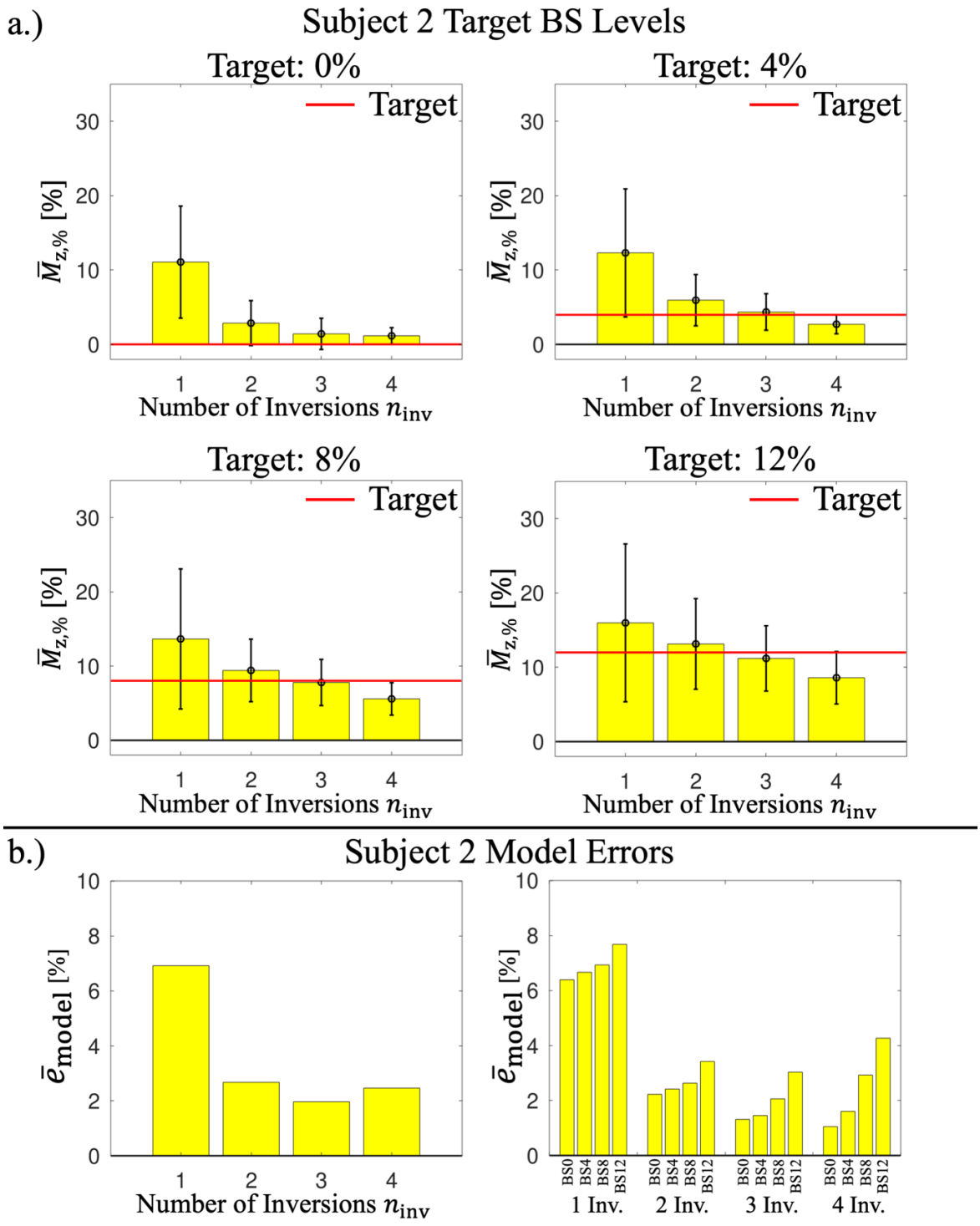

Figure 5.11: a.) Calculated mean residual levels of magnetization in the central six slices of subject 2 for different target levels and numbers of inversion pulses. The red line indicates the desired level of magnetization; and b.) Left: Calculated error between predicted and measured magnetization (Eq. [5.9]). Right: Mean model error without averaging over different target magnetization levels.

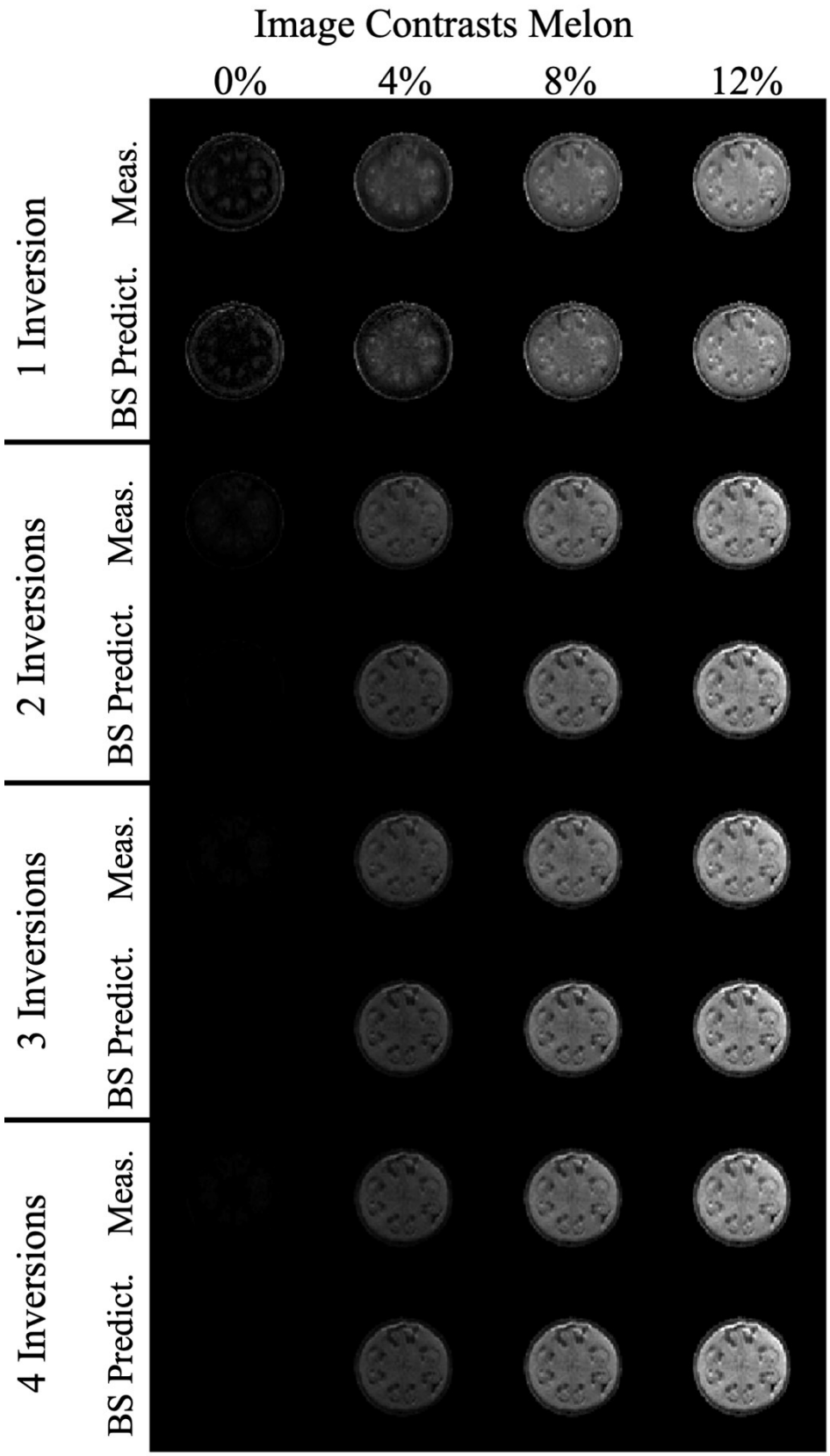

Figure 5.12: Comparison of predicted and measured image contrasts for the melon phantom. Different columns depict different levels of targeted magnetization. Rows show different numbers of inversion pulses used during the ASL preparation phase.

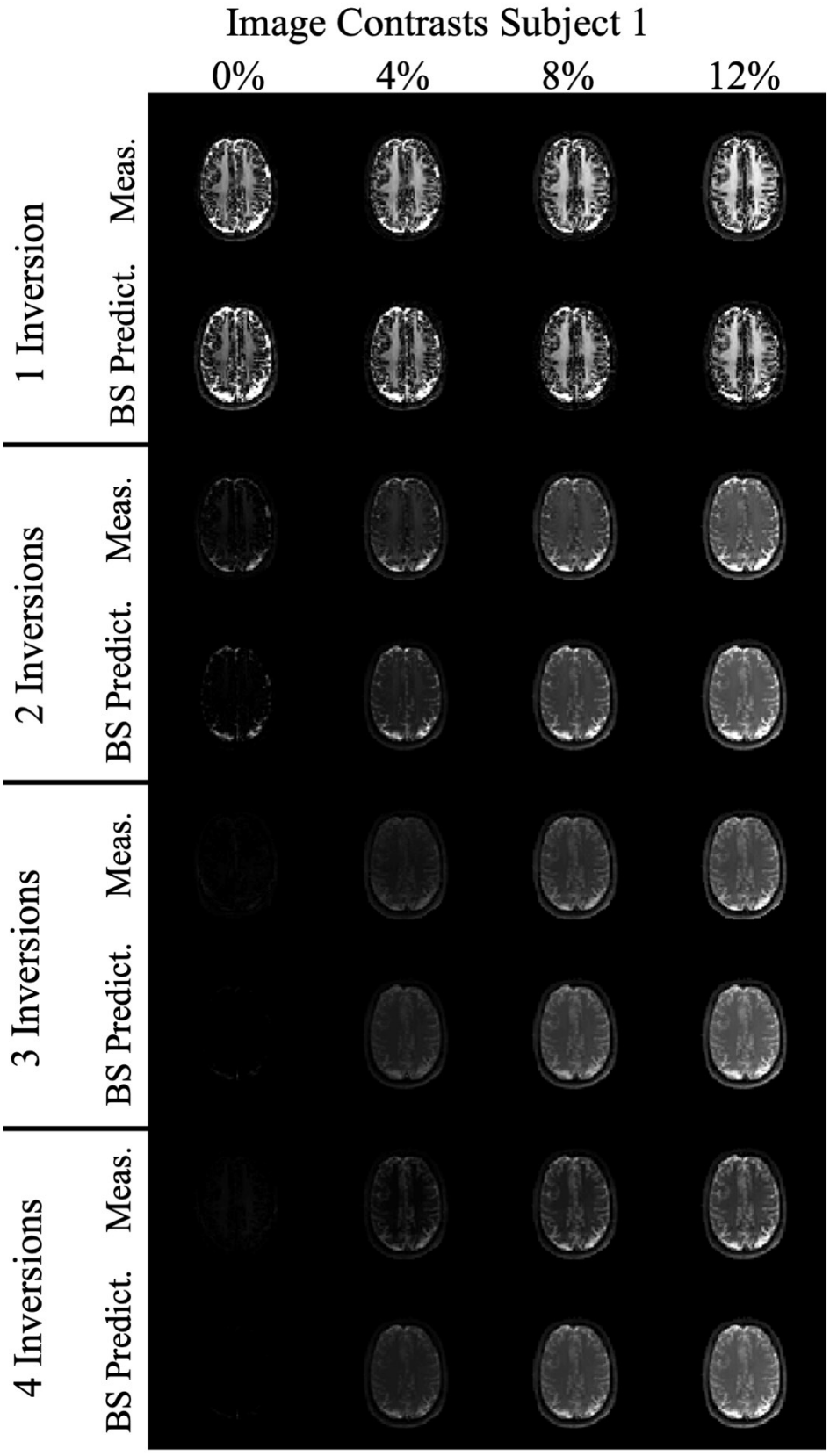

Figure 5.13: Comparison of predicted and measured image contrasts for subject 1. Different columns depict different levels of targeted magnetization. Rows show different numbers of inversion pulses used during the ASL preparation phase.

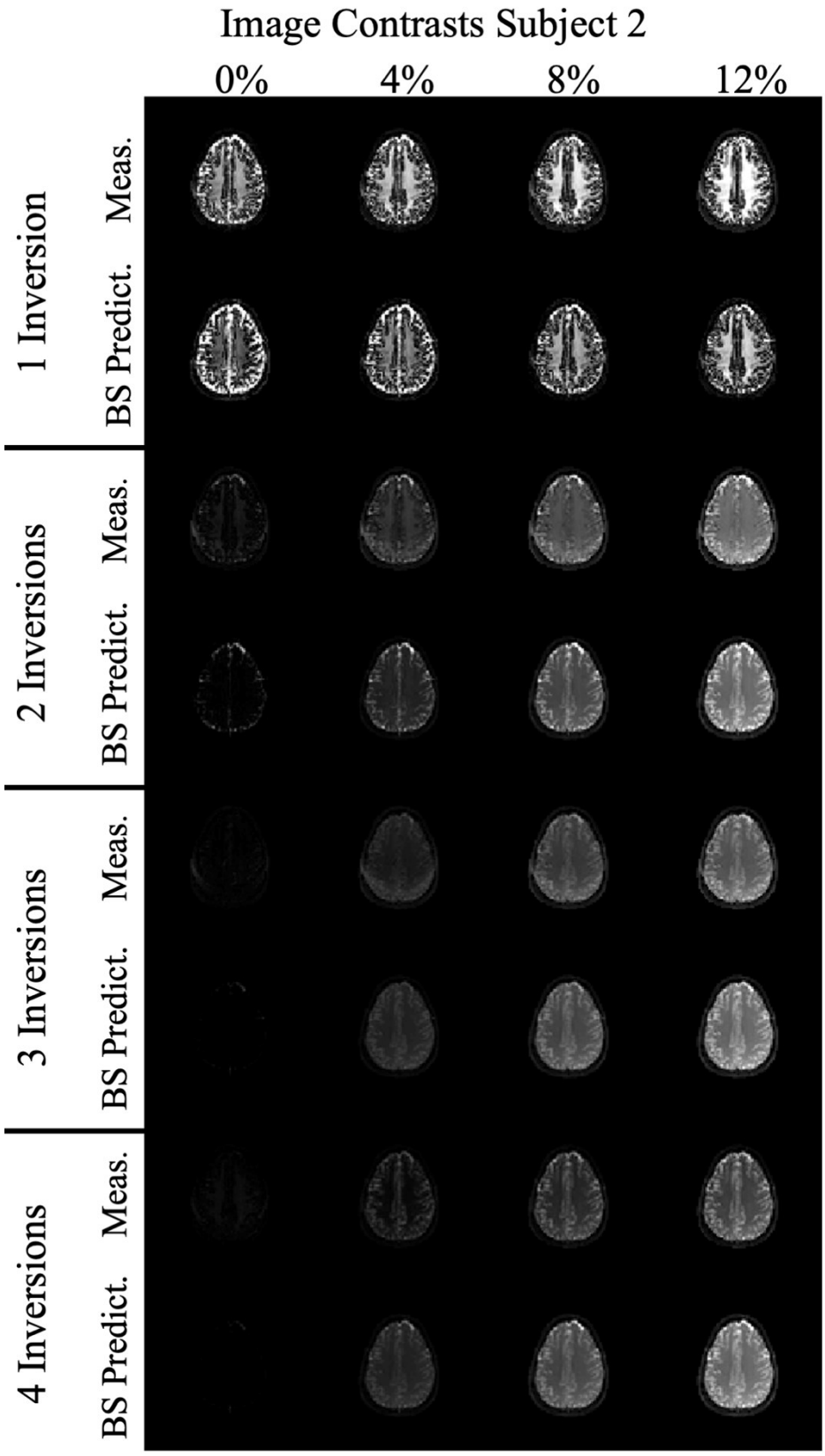

Figure 5.14: Comparison of predicted and measured image contrasts for subject 2. Different columns depict different levels of targeted magnetization. Rows show different numbers of inversion pulses used during the ASL preparation phase.

5.1.2.3 Discussion

Saturation recovery fitting

The implemented fitting routine of the saturation recovery image series yielded realistic parameter maps with saturation efficiency levels near 100% and T_1 values, corresponding to literature reports for gray and white matter (87)(88) as well as fruits (89). Estimated parameter maps were therefore found to be suitable for further processing and usage in the BS optimization routine.

Quality of perfusion-weighted images

The quality of perfusion-weighted images heavily depended on the selected combination of numbers of inversion pulses and residual magnetization (cf. Figure 5.8). Using only one inversion, it might happen that static tissue magnetization in perfused regions recovers too much such that artifacts due to signal fluctuations arise. On the other hand, it is also conceivable that relevant signal is suppressed to values close to zero, which might also yield poor quality in the case of magnitude image subtraction (cf. low signal in gray matter region in Figure 5.13 and Figure 5.14). Therefore, background suppressed pCASL experiments using the proposed method with only one inversion pulse are not further recommended. Image quality increased if some residual magnetization levels were preserved at excitation (cf. Figure 5.8, 4% - 12%). Each of these levels in combination with two to four inversion pulses is therefore found to be a suitable setup from an image quality perspective. A minor drawback of increased numbers of inversion pulses might be reduced SNR in perfusion-weighted images, which was observed by visual inspection (cf. Figure 5.8). If more inversion pulses are played out during the ASL preparation phase, it becomes more likely that the optimization routine yields timings which fall inside the pCASL labeling duration. The labeling RF is then shortly interrupted and resumed after inversion, which results in a small unlabeled gap in the tagged bolus. This can potentially decrease the SNR in perfusion-weighted images. In addition, inversion efficiency for moving blood was found to be restricted for a wide range of different classes of inversion pulses in a previous study (44). It can be expected that this effect, although not as significant as reported in that study, might also reduce the image SNR here. From this point of view, the number of inversion pulses used for BS should be kept to the minimum level, which yields the desired suppression of tissue. Here, the combination of two

inversion pulses and a targeted signal level of 4% or 8% was found to be sufficient for application of the presented method to brain imaging, which could be used for automized setups of the sequence in future experiments.

Model accuracy using the saturation recovery scan parameters

Besides the quality of perfusion-weighted images, the accuracy of the underlying BS model using parameter maps from the M_0 scan is of relevance to make sure that the targeted levels of magnetization are closely resembled. Residual levels of magnetization in the watermelon almost perfectly fitted the targeted levels, indicating that the theoretical considerations were valid here (cf. Figure 5.9a). As shown, the error between targeted and measured levels decreased with increased numbers of inversion pulses, because more pulses allow a more accurate reduction of the measured T_1 spectrum. Using a single pulse, a compromise was found by the algorithm, which prefers a suppression of T_1 values which show the highest numbers of occurrence. Here, the melon's pulp covered the largest region and was therefore nearly optimally suppressed in case of one inversion and target levels of 0% (cf. Figure 5.12). Low averaged model errors also indicate that the calculated set of parameters is suitable to describe the observed signal levels in the watermelon (cf. Figure 5.9b). This might also be related to the fact that no inflow occurred, and the averaging method from Eq. [5.7] yielded the unaffected M_z component.

In the in-vivo case, stronger deviation between targeted and observed signal levels occured when only one inversion pulse was used (cf. Figure 5.10a and Figure 5.11a). Here, the spectrum of T_1 values was broader than in the watermelon. Therefore, one inversion only resulted in a poor compromise which could not adequately reduce the whole T_1 spectrum. However, the trend of increased accuracy with increased numbers of inversions was not completely reproduced in-vivo, indicating that the model might not sufficiently explain the observed signal levels here. This is also backed up by strong fluctuation of the model's error, which was highest for one and four inversions (cf. Figure 5.10b and Figure 5.11b). Since this showed for both subjects, it is most likely not related to random effects such as subject motion during the experiments. One potential reason was already addressed in terms of residual unsaturated signal contributions related to inflowing blood (cf. Eq. [5.7]). Figure 5.13 and Figure 5.14 (cf. Four Inversions) however show that a major mismatch between prediction and measurement also arised in the white matter region, where

perfusion is way lower than in the gray matter regions. Additional effects which could explain the discrepancy should therefore be quickly discussed.

First, the inversion efficiency of BS pulses was neglected in the signal prediction model. As initially demonstrated (cf. Figure 5.1), imperfect inversion efficiencies might readily explain offsets from anticipated signal levels. In this work, the optimized FOCI pulse from section 5.1 with $A(t)^{\max} = 10$ was used, which showed a high level of efficiency in phantom experiments. However, reports showed that the efficiency of a range of adiabatic inversion pulses can be restricted in in-vivo scans (44). Therefore, future work should cover additional experiments with accompanying inversion recovery scans in the in-vivo case to estimate the local inversion efficiency, which is then integrated into the adaptive BS signal model. However, imperfect inversion efficiency should result in a somewhat linear decrease of the model accuracy with increased number of inversion pulses, which was not observed in this experiment. Model errors were found to be lowest for two and three BS inversions and higher for one and four inversions. Therefore, a combination of signal offsets due to a minor restriction in inversion efficiency as well as other effects is likely.

Another potential explanation could be the additional saturation of the static tissue in the region of interest, which occurs in in-vivo scans but not in the phantom scans using the watermelon phantom. Such saturation might result from magnetization transfer (MT) effects (39)(90). In the present experiment, the Q2Tips pulses as well as the fat saturation pulse appear off-resonant for the on-resonant static tissue in the imaging region, and thus possibly result in MT effects. A direct influence of Q2Tips pulses on on-resonant static tissue was demonstrated in PASL experiments (91). In this work, the same pulses were applied in both, the M_0 scan and the pCASL experiment. Therefore, MT effects should manifest themselves in a comparable manner in both experiments. This was also verified by additional datasets acquired for one of the volunteers, where Q2Tips and fat saturation pulses were switched off during M_0 and pCASL experiments (data not shown here). No significant differences to the previous findings were observed. Another difference between the saturation recovery and pCASL imaging sequences is the application of the pCASL labeling train. The application of the train of labeling pulses appears as another source of off-resonance irradiation in the imaging volume. The control experiment exists to remove the resulting MT induced saturation effect from the perfusion-weighted subtraction image (39). However, when comparing the averaged pCASL image data to the M_0 scan data, the saturation of the image volume might become a relevant source of discrepancy when

predicting the final signal level. An argument against this assumption is that when compared to CASL, MT related effects of pCASL sequences should be greatly reduced (39). However, Petr et al. reported a non-neglectable MT related effect of the pCASL labeling on CBF quantification, depending on the distance between labeling and image volume (92). The quantification error arises from faulty M_0 estimates, which are only valid for scans without the additional saturation effect. The same effect could explain observed discrepancies in this work. It is recommended to further investigate the potential MT effect on the accuracy of BS signal prediction in future studies, e.g., by performing the same experiment with/without application of the labeling pulse train. Note that this might also readily explain, why no comparable mismatches in signal prediction were observed in the watermelon. Watermelons consist almost exclusively of water (~90%) and thus no major pool of solid-like molecules exists here, which could contribute to MT.

Finally, non-coherent differences arising from the image reconstruction procedure might contribute to the observed difference. This e.g., includes filters in the online reconstruction pipeline of the MR system, which introduce minor signal variation depending on the actual signal level in different parts of the image volume. An example is the EPI-related phase correction that is applied to encounter Nyquist ghosting in final images. Imperfect correction not only results in ghosting but also in manipulation of the main signal as described in (18). Although these effects are not expected to be a major factor, further investigation by using a simple offline reconstruction framework, with access to all filtering and preprocessing steps, could lead to further insights here.

Although the targeted levels of magnetization might not be perfectly achieved, the desired increase in residual magnetization with each BS level was very well observed in the reconstructed anatomical images if two or more inversions were applied (cf. Figure 5.13 and Figure 5.14). Since the maximum model error was below a value of 3% (for two or more inversion pulses), configurations with anticipated signal levels of 4% to 12% should be suitable to prevent subtraction errors due to complete cancellation of static tissue components. This assumption is in accordance with the high quality of corresponding perfusion-weighted images (cf. Figure 5.8).

Applicability in combination with additional motion correction algorithms

One benefit of the optimized fixed BS technique over literature methods is the potential for selective nulling of fat while keeping other tissue at residual non-zero offsets, being especially beneficial for motion correction techniques, which usually register the on-resonant static tissue signal. Using the adaptive BS technique, T_1 values corresponding to fat were not recognized due to the fat saturation pulse, which was applied in the M_0 experiment. The adaptive algorithm therefore did not consider short T_1 values arising from fat in this study, which might be a problem if severe motion is present and needs to be corrected. Therefore, one of the following strategies could be applied in future adaptive BS experiments: A hybrid strategy could be applied, consisting of the M_0 scan, which is used to identify the spectrum of on-resonant T_1 values, which is reduced to the desired positive offset. Subsequently, the spectrum is complemented by an artificial fat estimate using $T_1 = 300$ ms and $M_{\mathrm{res}} = 0\%$ together with an a high weighting factor w. As an alternative, a second fat-selective saturation recovery measurement could be performed, applying spatial-spectral excitations as described in (93), which would yield a more accurate subject and region specific estimate of the fat T_1 relaxation, which could subsequently be suppressed to 0%.

Potential improvements for fast adaptive BS preparation

The M_0 scan, which is used for adaptive BS preparation, comes with a non-negligible measurement time. Assuming e.g., a minimum of three saturation times with a TR of 4 s, a total scan time of 12 seconds is needed for acquisition of the adaptive BS preparation data. Although the M_0 scan is usually acquired if quantification is desired, multiple saturation times are not always mandatory, because different options exist which estimate M_0 from a single saturation time (94). Therefore, an updated BS preparation scan would be useful, which also shows a reduced scan time, which in turn also reduces the sensitivity to subject motion. This would be especially helpful in abdominal organs to prevent errors in the T_1 estimation due to respiratory motion. In the future, the saturation recovery M_0 scan could therefore be substituted by a faster technique such as a Look-Locker experiment (95)(96), acquiring many data samples within a few seconds. In addition, instead of applying time intensive readout schemes, a single non-spatially encoded datapoint could be acquired after each excitation, which reflects the sum of signals from the spin ensembles in the excited slab. This drastically increases the SNR of the acquired signal. A proper optimization

algorithm could then fit a model to the acquired data, estimating major T_1 components, which are finally used in the adaptive BS routine. This would also further reduce the number of equations which need to be simultaneously optimized. The experiment could finally be repeated with spectral water saturation to get an accurate estimate about the subject-specific dominant T_1 value corresponding to fat, which will then be targeted to 0% as done in the fixed optimized BS scheme and discussed in the previous paragraph.

5.1.2.4 Conclusion

The proposed adaptive BS technique allowed the reconstruction of high-quality perfusion-weighted images for target magnetization levels of 4% - 12% and two – four inversion pulses. Due to SAR and SNR considerations, usage of two inversion pulses with e.g., 8% residual magnetization is recommended, allowing a complete automated setup of the BS algorithm, thus achieving an operator independent reduction of the motion sensitivity of the ASL sequence. Proposed improvements of the BS preparation scan might further decrease the time needed for BS preparation and would allow subject-specific fat suppression, which could be especially helpful in abdominal ASL imaging. The slight inaccuracies observed in the predicted pCASL signal levels using the M_0 scan parameter maps were not found to be problematic for the given task of acquiring high quality perfusion-weighted images if residual signal is set to values above 4% and two or more inversion pulses were played out.

5.2 Novel Approaches for Motion Compensation using 3D GRASE PROPELLER

5.2.1 Application of Optimized Fixed BS and 3DGP-JET to Brain pCASL Imaging

In the following, the fixed optimized BS scheme (cf. section 4.1.2) in combination with the 3DGP-JET reconstruction (cf. 4.2.2) will be compared to the standard 3DGP-STD reconstruction as well as Cartesian-segmented 3D GRASE readouts in presence of different levels of intentional subject motion and suppression levels of static tissue during brain pCASL scans. The goal is to evaluate the effectiveness of 3DGP-JET pCASL in different motion scenarios and to give a recommendation for a suitable residual static tissue magnetization level in combination with 3DGP for further studies in clinical environments.

5.2.1.1 Methods

Adjustment of optimized fixed BS algorithm

The optimized fixed BS scheme from section 4.1.2 was applied in this study to selectively reduce the on-resonant signal from gray matter and white matter to different positive levels, while simultaneously aiming to suppress signal originating from fat and cerebrospinal fluid (CSF). Pulse timings were optimized for levels of 0%, 5% and 10% of residual magnetization for T_1 values, covering the expected gray and white matter regions. The BS levels are referred to as BS0, BS5 and BS10, respectively. The residual magnetization of unwanted fat and CSF signal was targeted to be 0% at excitation for all configurations accordingly (cf. settings in Table 5.2). Note that a low weighting for CSF was applied such that the optimization algorithm tries to suppress gray/white matter and fat as close as possible to desired levels while allowing residual signal for CSF as a trade-off for situations where no optimal solution for all tissue components can be found. Three C-shape FOCI pulses were applied during the ASL preparation phase (cf. Figure 5.15a).

	CSF	Gray Matter	Whiter Matter	Fat
T_1 [ms]	3500, 4000, 4500	1200, 1300, 1400	700, 800, 900	300, 350, 400
$w(T_1)$	0.016	0.1	0.1	0.116
$M_{\mathrm{res}}(T_1)$	0.0	0.0/0.05/0.1	0.0/0.05/0.1	0.0

Table 5.2: Selected parameters of the optimized fixed BS scheme in this study. Indicated weightings were applied for each of the given T_1 values. The same holds for the residual magnetization levels. The three indicated values for gray and white matter correspond to the BS0, BS5 and BS10 configurations.

3DGP/3D GRASE acquisition and reconstruction

3DGP bricks were acquired using the golden angle scheme depicted in Figure 5.15c. A golden angle scheme shows increased robustness against filtering of bricks in case of corrupted data or through-plane motion. Each brick was acquired using a standard 3D GRASE readout with additional reference lines for Nyquist ghost removal (20). Note that while control/label states are toggled before sampling the next segment in 3DGP the inverse approach is applied for the standard 3D GRASE readout; the reason being that all segments of a single label/control state should be read out as quickly as possible to reduce the likelihood of motion in between them. Details concerning the implementation of reconstruction algorithms of 3DGP-JET and 3DGP-STD data are described in section 4.2.2.2. The Cartesian-segmented 3D GRASE data was reconstructed by exchanging the PROPELLER and all following modules from Figure 4.5 by a 2D rigid body motion estimation using algorithms from the Insight Toolkit (ITK) (21). Motion estimates from single slices were again averaged and applied to the whole 3D volume. 3D GRASE image reconstruction was also implemented in C++ within the Siemens ICE framework (Siemens Healthineers, Erlangen).

Experiments

Axial measurements of five healthy volunteers (3m, 2w, aged 24-40) were acquired at 3T (Siemens MAGNETOM Skyra, Siemens Healthineers, Erlangen) with a total number of eighteen scans per subject: First, three scans were performed without intentional motion using 3DGP with BS10, BS5 and BS0 preparation. The procedure was repeated by

exchanging the 3DGP readout with the Cartesian-segmented 3D GRASE readout. Next, the 3DGP/3D GRASE readout was alternated starting with BS10 and followed by BS5/BS0 preparation and the subject was asked to follow a specific motion protocol (cf. Figure 5.15b), where each rotation occurred after five image readouts during the next labeling period (slow motion). The scans were repeated but this time the rotations occurred during each labeling period (fast motion). All subjects provided written informed consent prior to scanning and the study was run under a general protocol for pulse-sequence development approved by the local ethics committee.

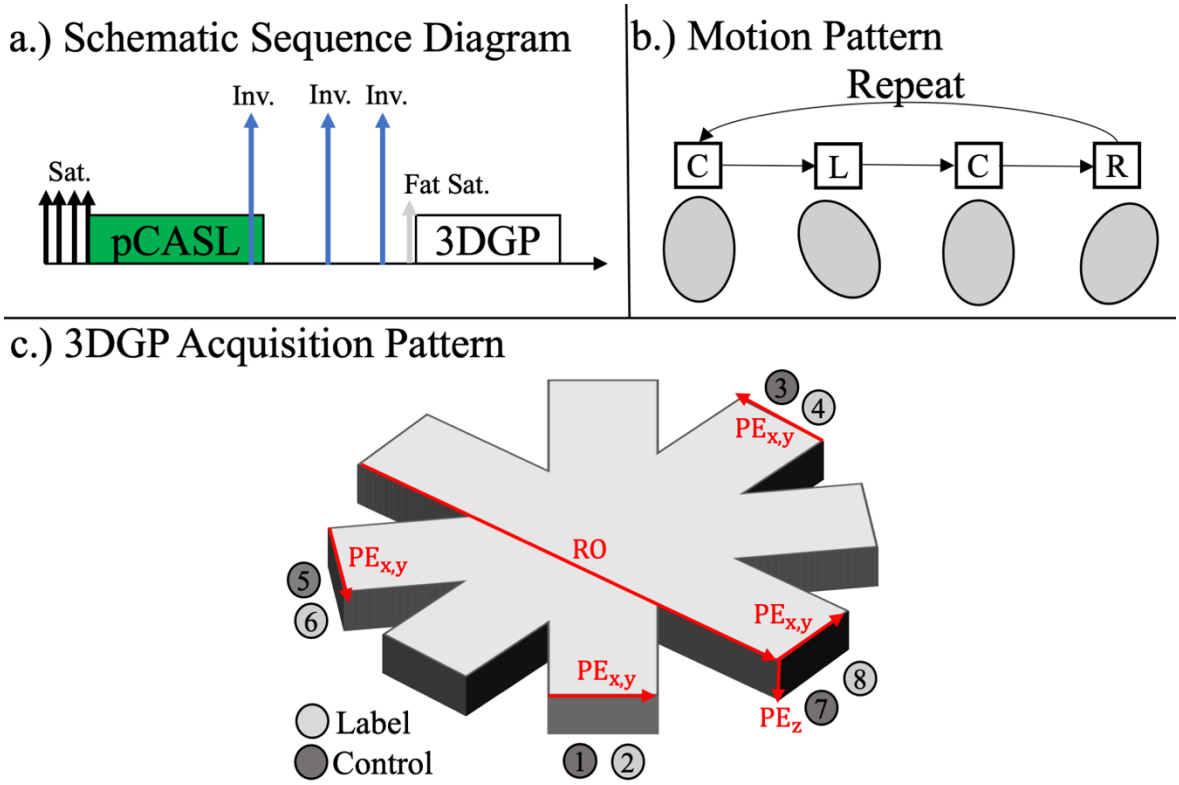

Figure 5.15: a.) Schematic sequence diagram as applied for the experiments in this work. One of the BS inversion pulses was applied during the end of the pCASL labeling train; b.) Motion pattern during slow/fast motion protocols; and c.) Golden angle 3DGP acquisition scheme.

Using 3DGP, a matrix of 96 x 32 x 8 k-space samples was acquired for each brick, resulting in an image resolution of (3.1 x 3.1 x 5) mm^3 with a (9.4 x 9.4 x 5) mm^3 navigator resolution. A total number of sixteen bricks per label/control state, equivalent to four averages/measurements, was acquired using the golden angle scheme, leading to a total

acquisition time of 2:24 minutes. Other imaging parameters were TR/TE = 4500 ms/23.2 ms, readout bandwidth = 2264 Hz/Px, FoV = (300 x 300 x 40) mm^3.

Four 3D GRASE label/control pairs were acquired, with a total matrix size of 96 x 96 x 8 and three Cartesian segments of size 96 x 32 x 8 each, yielding the same nominal resolution (3.1 x 3.1 x 5) mm^3. The total acquisition time was 1:48 minutes. Other imaging parameters were TR/TE = 4500 ms/23.9 ms, bandwidth = 2264 HZ/Px, FoV = (300 x 300 x 40) mm^3. For both 3DGP and 3D GRASE acquisition, a labeling duration/post-labeling delay of 1800 ms/1800 ms was applied (37).

Data analysis

Image quality of perfusion-weighted images was compared for different levels of BS and motion. In addition, the mean SNR per acquisition time was calculated for scans without intentional motion using 3DGP/3D GRASE, following the method described in (46). Therefore, subject-specific gray matter masks were calculated to obtain the average magnitude perfusion signal $|S|$. The noise regions N were selected on left and right image borders to avoid structural artifacts in the phase-encoded direction of 3D GRASE acquisition and edge regions of 3DGP images. SNR was then calculated according to $SNR \propto |S|/\mathrm{std}(N)$. Note that signal and noise regions in subtraction images were selected before conversion to DICOM format to avoid manipulation of the underlying noise distribution (see further explanations in section 3.3). The accuracy of motion detection and correction using 3DGP-JET/3DGP-STD was further investigated by calculating the mean and standard deviation of motion estimates from data without intentional motion across all subjects as well as the mean normalized cross-correlation of central navigators after application of the different reconstruction algorithms. Finally, field maps calculated using 3DGP-JET from data with different BS and different motion patterns were compared.

5.2.1.2 Results

Table 5.3 shows theoretical levels of tissue suppression using the proposed BS algorithm. Levels of white/gray matter are close to the desired suppression level. In case of BS0, fat and CSF show residual offsets from the targeted 0% signal.

Figure 5.16 shows exemplary rotational trajectories for one of the volunteers, estimated using 3DGP-JET and 3DGP-STD.

A visual comparison between different 3D GRASE/3DGP reconstruction modes and levels of BS in case of no intentional motion is shown in Figure 5.17a and b. High quality perfusion-weighted images were obtained using 3D GRASE/3DGP readouts in combination with BS5/BS10. Image quality was found to be slightly reduced in case of magnitude subtraction and BS0. Complex subtraction increased the image quality by some extend. The estimated mean SNR/s using a 3D GRASE/3DGP acquisition is given in Figure 5.17c. Comparable levels were observed for both segmentation strategies. SNR/s levels were slightly reduced for the BS0 case.

Figure 5.18a and b show quantitative parameters in terms of the mean cross-correlation and mean rotational and translational motion estimates. Mean cross-correlation was highest using the proposed 3DGP-JET algorithm for all combinations of BS and motion. Average fluctuation of rotational estimates was lower in case of 3DGP-JET when compared to 3DGP-STD. No significant difference was observed for translational parameters.

Detailed visualization of reconstructed images with the slow motion pattern and different levels of BS are exemplarily shown in Figure 5.19a. Correction of motion related artifacts clearly showed in individual control/label and perfusion-weighted images. Figure 5.19b additionally shows the label/control image contrasts achieved using the optimized fixed BS with different levels of residual magnetization. Correction of motion related artifacts using 3DGP-JET clearly showed for all BS levels in anatomic images. In addition, no major signal from residual shifted fat was visible for all three background suppression levels.

Additional visualization of achieved suppression levels of the static tissue signal are given in Figure 5.20. The achieved signal reduction showed good correspondence with anticipated theoretical levels.

Figure 5.21a shows additional perfusion-weighted images using BS10 and slow/fast motion protocols. Motion artifacts in case of both protocols were drastically reduced using 3DGP-JET/3DGP-STD. In case of slow motion, 3DGP-JET achieved a slightly better suppression of motion related artifacts. In case of fast motion, 3DGP-STD appeared to yield slightly superior image quality. Motion correction with 3D GRASE was not able to reduce motion related artifacts in reconstructed perfusion-weighted images.

Finally, estimated field maps using 3DGP-JET under different levels of BS and motion are shown in Figure 5.22a and b. Estimated field maps appear reasonable and show little influence by the performed motion protocol. The effect of distortion correction on reconstructed images as well as 3DGP navigators is visualized in Figure 5.22c and Figure 5.23.

	CSF	**Gray Matter**	**White Matter**	**Fat**
BS0	6.75%	0.43%	0.82%	1.58%
BS5	3.57%	4.84%	5.40%	0.77%
BS10	0.56%	9.96%	9.95%	0.31%

Table 5.3: Theoretical suppression of static tissue achieved with the proposed BS design. Percentual values were averaged over the T_1 ranges, given in Table 5.2.

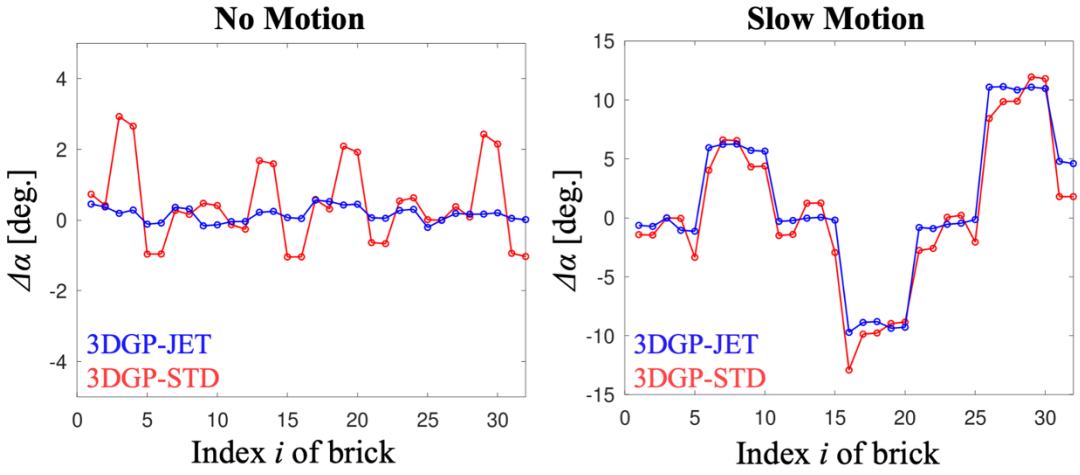

Figure 5.16: Rotational motion trajectories with no/slow motion during the scan, calculated from subject two using BS10. As shown, trajectories are steadier for 3DGP-JET when compared to 3DGP-STD, because effects of off-resonance are included in the motion estimation part. This is the reason for the lower standard deviation from Figure 5.18b.

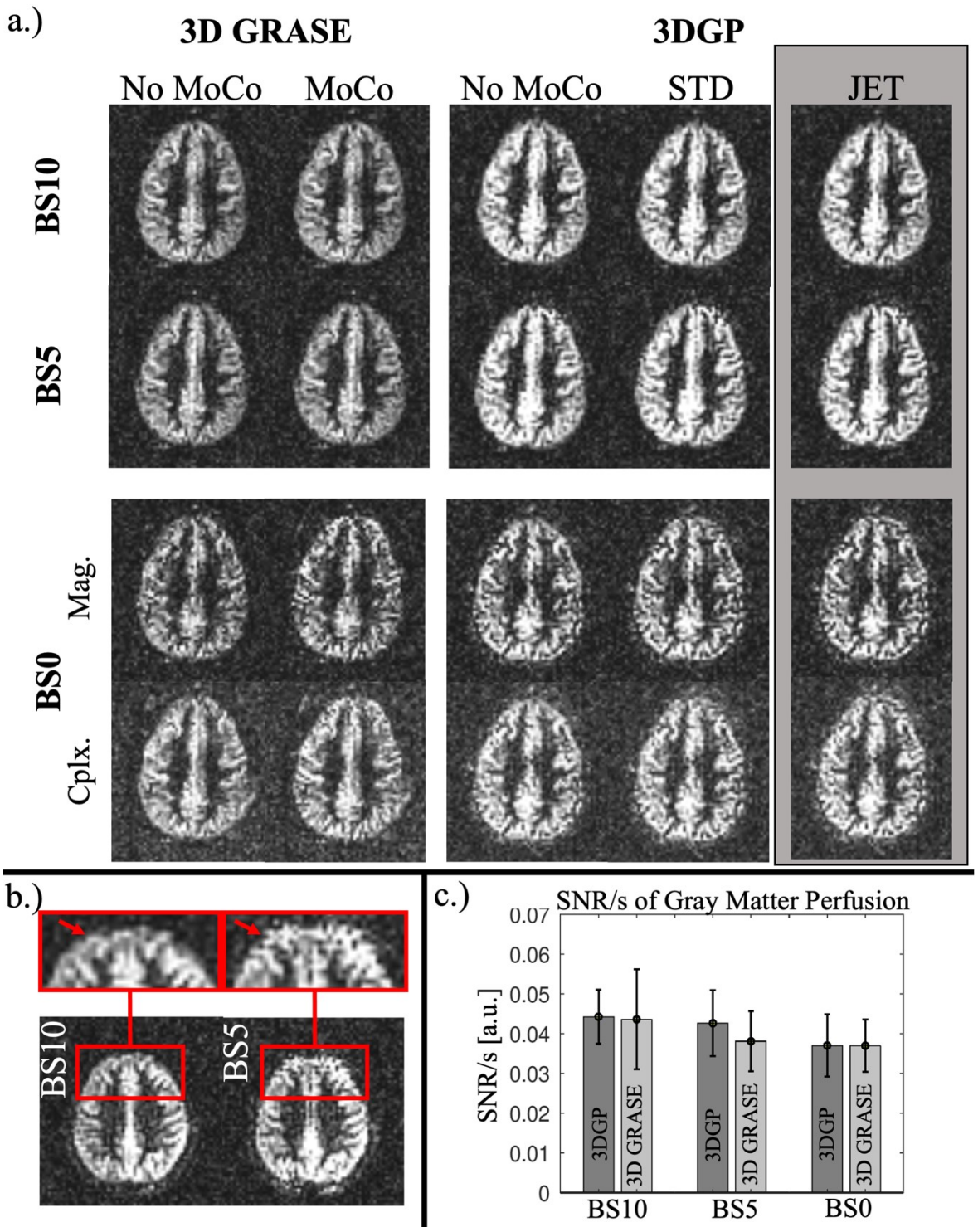

Figure 5.17: a.) Reconstructed perfusion-weighted images of subject five without intentional motion during the scan. Complex subtraction (phase correction not applied in 3D GRASE case) is also shown for BS0; b.) Perfusion-weighted images for subject four using 3DGP and BS10/BS5. Arrows indicate areas where quality in BS5 images is slightly inferior to BS10 images. The same shows for other subjects in this study. Using 3D GRASE, the artifacts are less prominent; c.) Mean SNR/s of gray matter perfusion.

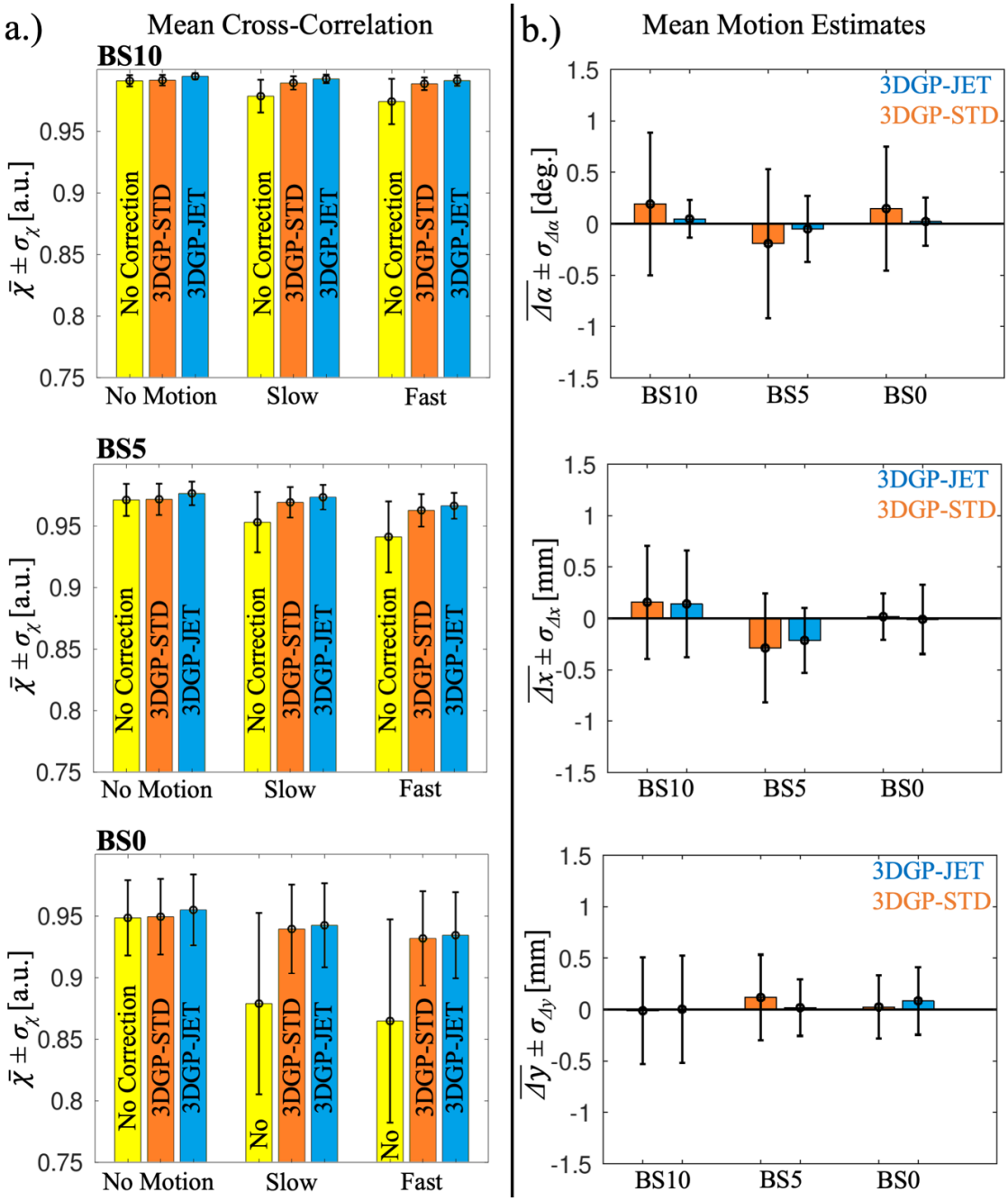

Figure 5.18: a.) Mean cross-correlation of the low-resolution navigator images with their respective reference for different BS modes and reconstruction techniques, averaged over all five volunteers. Different motion patterns during the scan are shown on the x-axis. Errorbars indicate one standard deviation. Comparing BS10, BS5 and BS0 without intentional motion, mean cross-correlation decreases in the given order of BS modes; and b.) Mean rotational and translational motion estimates for data without intentional motion. Estimates were averaged over all five volunteers. Errorbars again indicate one standard deviation. Different BS modes are shown on the x-axis.

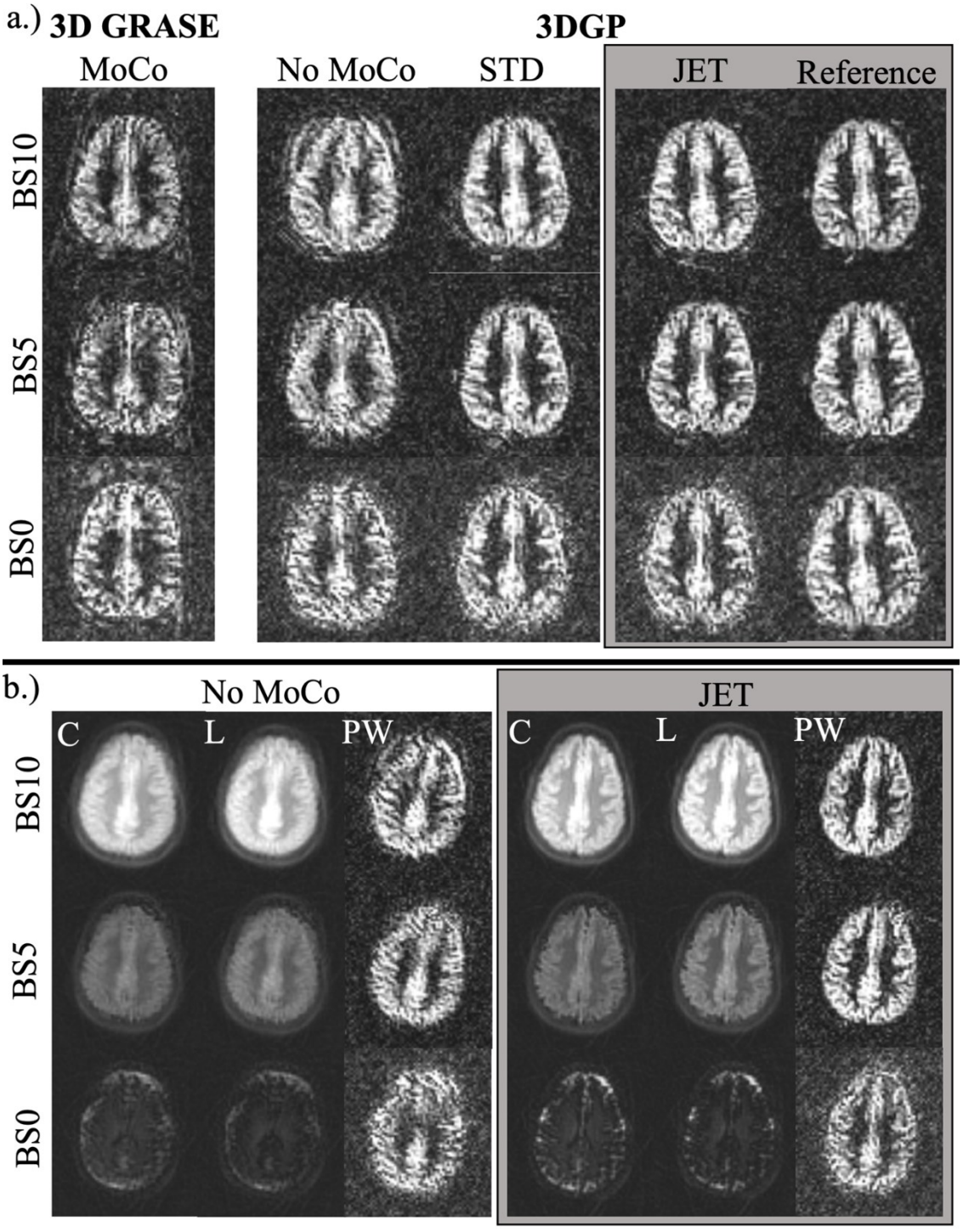

Figure 5.19: a.) Reconstructed perfusion-weighted images of subject two with slow motion during the scan using the indicated acquisition technique and different BS/reconstruction algorithms. Note that the amount of subtraction errors is higher when comparing 3DGP BS10 with 3DGP BS5 (No MoCo), due to the increased suppression of static tissue for BS5. The difference vanishes after application of 3DGP-JET/3DGP-STD since static tissue is correctly aligned and nulled after subtraction. In the BS0 case, complex image subtraction was applied; and b.) Control/label (C/L) and perfusion-weighted images before/after 3DGP-JET correction in the slow motion case for different levels of BS. Again, complex subtraction was applied in the BS0 case.

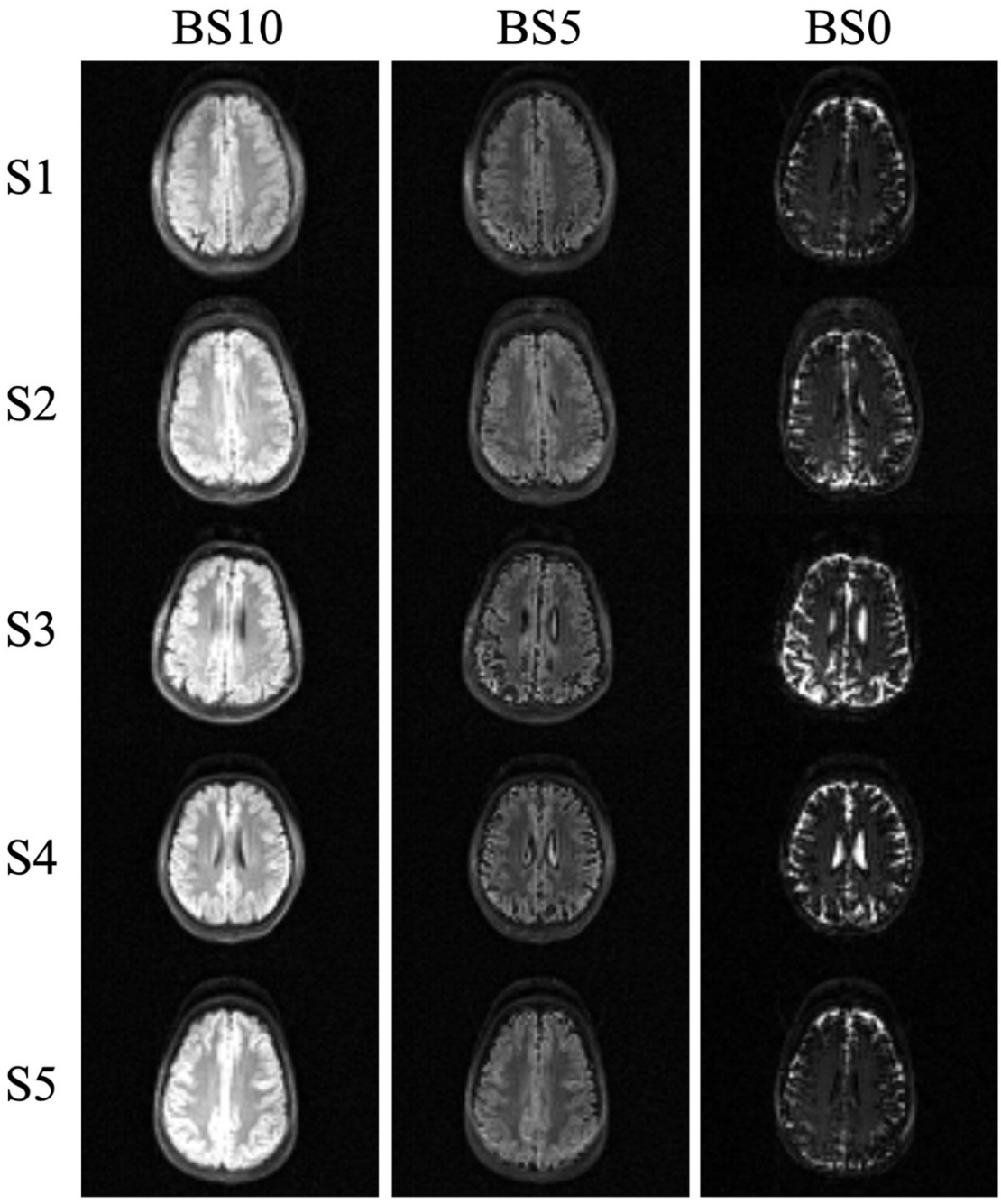

Figure 5.20: Background suppression levels achieved in the five volunteers of this study using BS10, BS5 and BS0 configurations. Shown are reconstructed 3D GRASE control volumes.

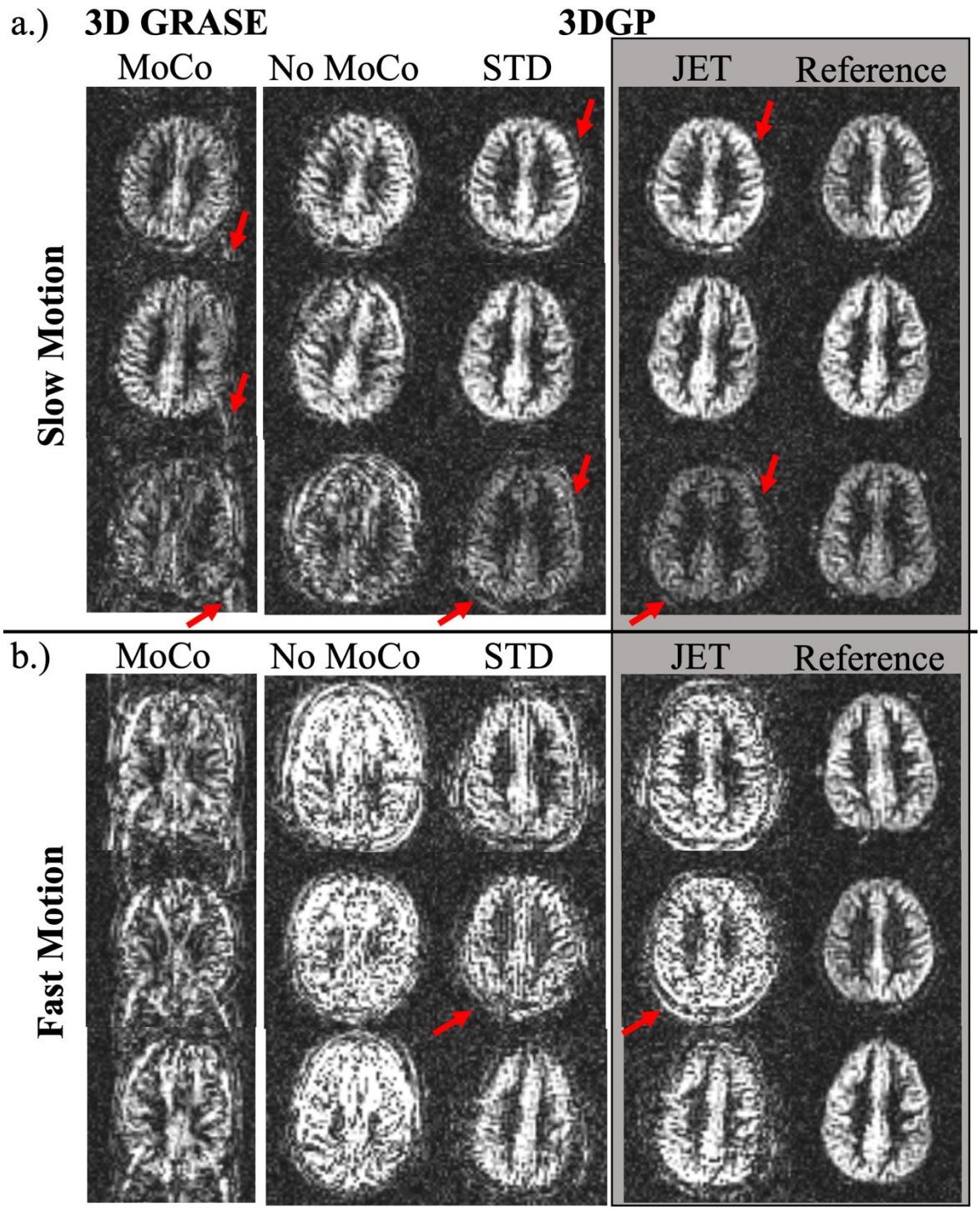

Figure 5.21: Reconstructed perfusion-weighted images using BS10 and different acquisition/reconstruction strategies in case of a.) slow motion and b.) fast motion during the scan. Arrows indicate regions with visible ghosting artifacts in case of 3D GRASE and subtraction errors when comparing 3DGP-STD and 3DGP-JET.

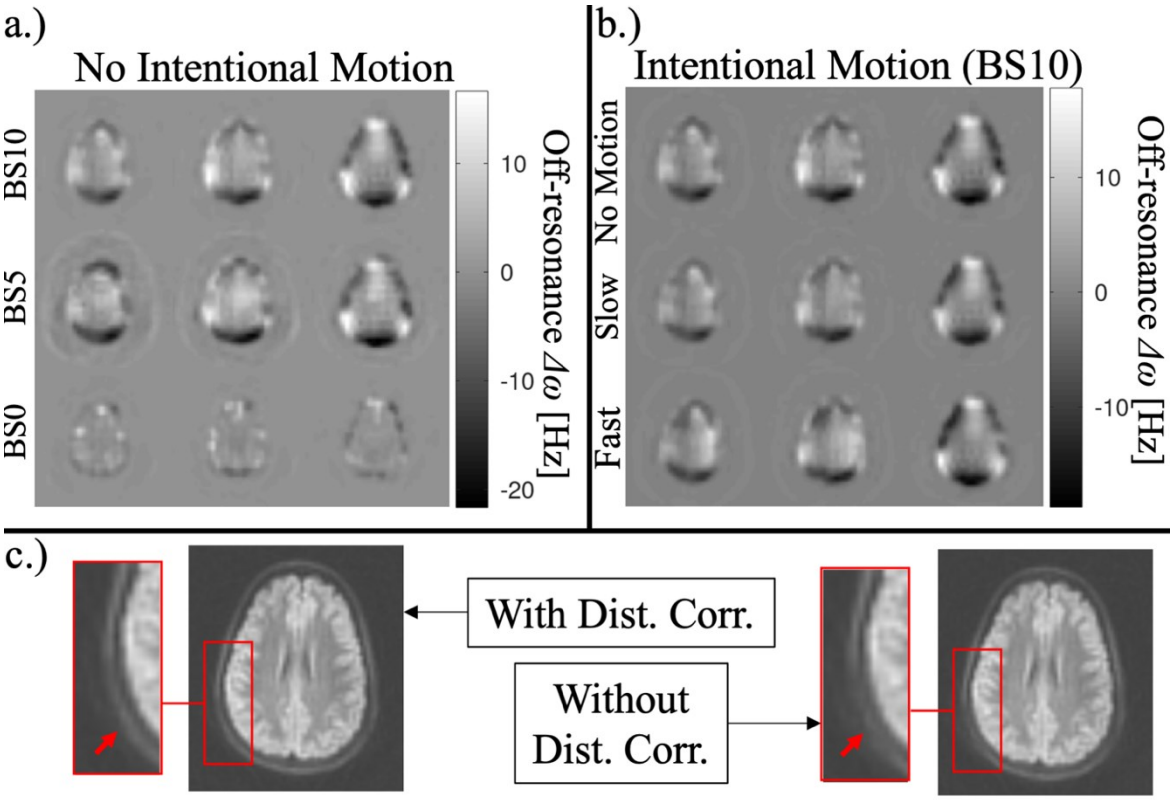

Figure 5.22: a.) Calculated field maps for different background suppression settings without intentional motion of subject five. Field maps, calculated from BS0 data, show reduced amounts of off-resonance due to the stronger suppression of static tissue signal. Columns show different slices of the dataset; b.) Calculated field maps for BS10 and different amounts of motion during the scan. Field maps show comparable results irrespective of the motion pattern during the scan. Columns show different slices of the dataset; and c.) Examples for high-resolution control images, reconstructed from all bricks with/without additional distortion correction. Arrows indicate regions with reduction of smeared signal if distortion correction is applied.

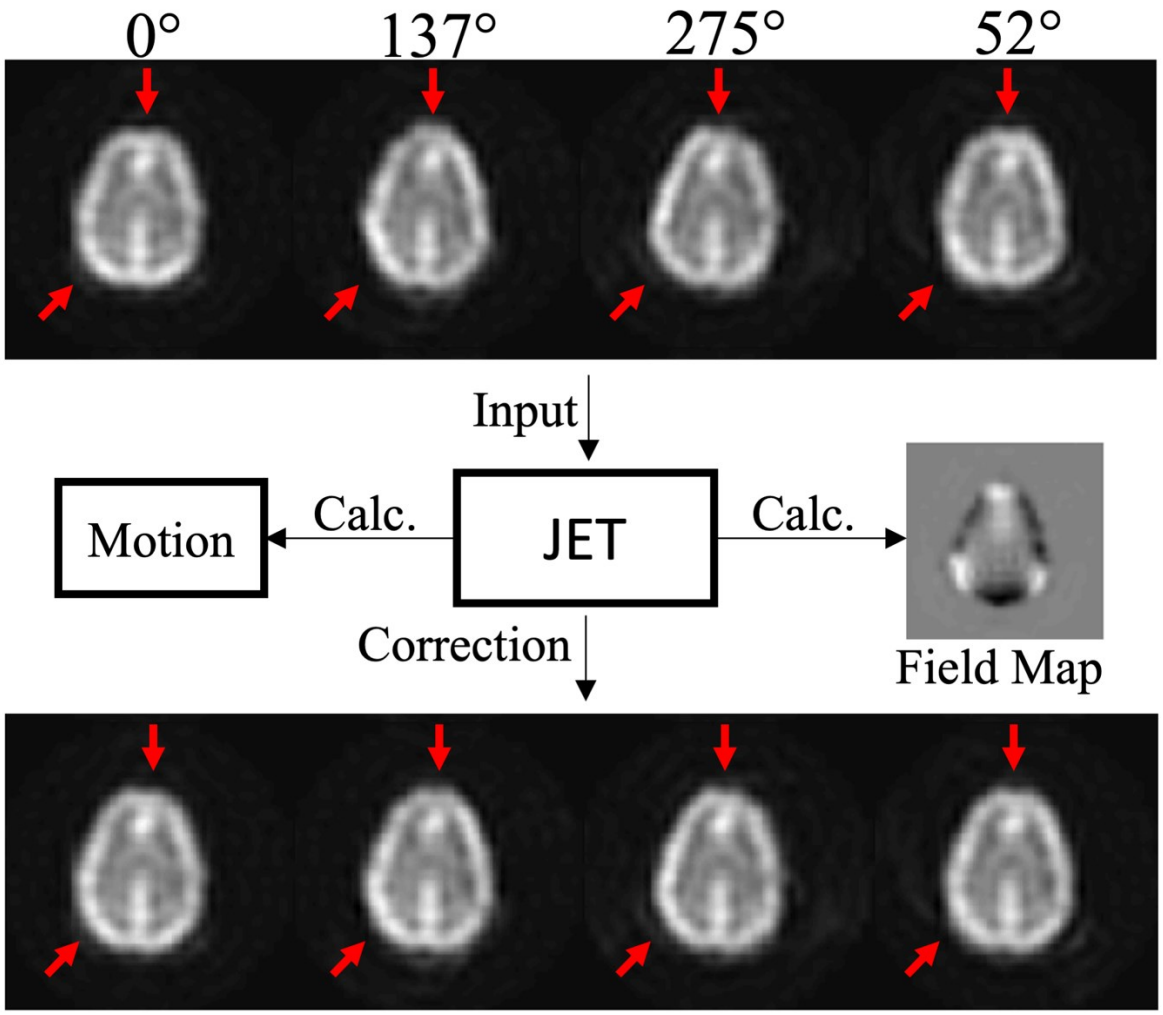

Figure 5.23: Example for distortion correction using the 3DGP-JET algorithm. Arrows indicate areas with visible shifts of static tissue due to the rotated phase-encoded direction in the low-resolution navigator images. Using the estimated field map and the pseudo-inverse correction approach, distortion is visibly reduced.

5.2.1.3 Discussion

Optimized fixed BS in 3DGP pCASL imaging

Targeted residual levels of static tissue signal corresponded well to observed signal contrast in reconstructed label and control images (cf. Figure 5.19b, Figure 5.20 and Table 5.3). Residual CSF signal clearly showed for BS0, resulting from the tradeoff introduced by the lower weighting factor. This was also predicted by theoretical suppression levels. The increased suppression of gray/white matter with lower BS levels was visibly achieved with the proposed algorithm. In addition, no major residual contribution from fat signal was observed in reconstructed 3DGP label/control images, as it was anticipated to prevent

subtraction errors after motion correction (cf. Figure 5.19b). Sufficient suppression of fat can also be concluded from reconstructed perfusion-weighted images using 3DGP-STD, acquired under the slow motion protocol. Here, no severe fat-related subtraction errors were observed, also verifying the applicability of the optimized fixed BS scheme in combination with 3DGP pCASL imaging. Sufficient suppression of fat was also verified in 3D GRASE data control data (cf. Figure 5.20). It appeared, however, that for some subjects the suppression of fat worked better than for others, indicating possible importance of subject and experiment specific variation in e.g., T_1 of fat or the efficiency of the spectral fat saturation pulse.

On the image quality side, 3DGP/3D GRASE in combination with BS0 was found to produce poor image quality using magnitude subtraction (cf. Figure 5.17a). While complex subtraction of label/control images visibly increased image quality in case of 3D GRASE, subtraction errors were still visible for 3DGP. This is most likely related to the PROPELLER phase correction, which might cancel important phase information, which is needed for correct complex image subtraction. In general, BS10 was found to yield better image quality than BS5 using 3DGP in cases without intentional motion (cf. Figure 5.17b). In case of motion, BS10 as well as BS5 showed comparable reduction of motion artifacts in anatomical and perfusion-weighted images using 3DGP-JET, indicating that BS10 was also a suitable choice here (cf. Figure 5.19a and b). Finally, correlation between central navigators was highest for BS10 (cf. Figure 5.18a), because minor amounts of shifted residual fat signal became more apparent for lower BS levels of on-resonant static tissue. This higher fluctuation in correlation might be problematic for the correlation weighting step. Rotation and translation estimation using 3DGP-STD and 3DGP-JET however did not seem to be majorly affected by the level of BS, as indicated by comparable standard deviations (cf. Figure 5.18b).

It is concluded that BS levels of gray and white matter around 10% are a suitable selection for brain 3DGP pCASL imaging. In general, BS levels of tissue of interest close to zero should be avoided due to poorer image quality of 3DGP perfusion-weighted images. The proposed optimized fixed BS technique has proven to be suitable for the application in brain pCASL imaging in combination with 3DGP readouts.

No intentional motion during pCASL scans: comparison of 3D GRASE and 3DGP

In case of no intentional motion during scans, finer structures appeared slightly blurrier in 3DGP images than in 3D GRASE (cf. Figure 5.17a). However, since 3DGP offers the additional robustness against subject movements, this finding is no major drawback. A comparable SNR/s was observed for both acquisition techniques (cf. Figure 5.17c) such that less 3DGP bricks can be acquired without major drawbacks in terms of SNR, when compared to 3D GRASE. A reduction of the number of sampled bricks is possible due to the golden angle acquisition scheme. This way, comparable 3DGP/3D GRASE scan times could be achieved, without major drawbacks concerning the SNR in 3DGP perfusion-weighted images.

No intentional motion during pCASL scans: comparison of 3DGP-STD and 3DGP-JET

Comparing 3DGP-STD and 3DGP-JET, the increased fluctuation of 3DGP-STD rotational estimates (cf. Figure 5.18b) was not surprising, because k-space values are weighted with the squared distance to the origin in bulk rotation correction and thus outer areas of k-space, which are affected most by off-resonance, are emphasized. This clearly shows as artificial rotational motion estimates using 3DGP-STD (cf. Figure 5.16). Pairs of bricks which were acquired with the same angle in k-space share a common direction of geometric distortion and thus share a common artificial rotational estimate. Standard deviations of translational estimates were quite similar for both approaches, because the weighting of k-space values using 3DGP-STD is not applied here. No visible degradation of image quality of reconstructed perfusion-weighted images was seen for 3DGP-STD or 3DGP-JET in case of no intentional motion (cf. Figure 5.17a). However, the fluctuation of 3DGP-STD rotational estimates might be visible as blurring in higher resolutions and the performance of both algorithms for a smaller number of PE steps must be investigated in future work. The correction of off-resonance related geometric distortion using 3DGP-JET is demonstrated by an increase in mean cross-correlation of the central k-space area (cf. Figure 5.18a).

Summing up, comparable image quality and SNR was achieved with both 3DGP reconstructions when compared to 3D GRASE. Hence, 3DGP has proven to be a possible candidate for substitution of Cartesian-segmented 3D GRASE in routine ASL imaging. On

the reconstruction site, 3DGP-JET should be preferred over 3DGP-STD, due to smaller rotational fluctuation and the possibility for distortion correction.

Intentional motion during pCASL scans: comparison of 3D GRASE and 3DGP

Both 3DGP-STD and 3DGP-JET provided superior image quality and great reduction of motion related artifacts in case of slow or fast motion patterns when compared to 3D GRASE (cf. Figure 5.19 and Figure 5.21). This especially holds for the slow motion protocol, where image quality using 3DGP-JET is almost comparable to the reference images. Most prominent, 3DGP images did not suffer from typical ghosting artifacts, which superimposed the 3D GRASE perfusion signal. This is related to the superiority of the 3DGP segmentation, correcting motion before formation of the final k-space data. In case of a Cartesian segmentation, k-space combination is performed prior to further processing, and ghosting cannot be corrected for.

Intentional motion during pCASL scans: comparison of 3DGP-STD and 3DGP-JET

Comparing 3DGP-JET and 3DGP-STD, 3DGP-JET showed superior image quality for the slow motion pattern (cf. Figure 5.21a, arrows); the reason being that rotational estimates using 3DGP-JET are steadier than for 3DGP-STD and that some pairs of label/control bricks are filtered by the fat filtering step. The same shows for the other subjects in this study. Better correction of deviations between individual bricks is also fortified by higher mean correlation estimates for 3DGP-JET (cf. Figure 5.18a).

In case of fast motion, 3DGP-STD showed less subtraction errors than 3DGP-JET (cf. Figure 5.21a). This was somewhat unexpected, due to the better correlation of low-resolution navigators after correction using 3DGP-JET. Investigation of estimated motion trajectories for both modes revealed minor deviations, which might indicate that 3DGP-STD finds more robust estimates here. Optimizations of 3DGP-JET in terms of the minimization procedure are therefore further investigated. In addition, it 3DGP-STD could be integrated into 3DGG-JET as a preprocessing step to calculate initial guesses for the motion estimates.

It must be mentioned that the slow and fast motion patterns were highly artificial. Additional studies with clinical data are therefore recommended to validate the developed 3DGP-JET technique in scenarios with realistic motion.

Finally, 3DGP has proven to be the superior method with robustness against both motion protocols when compared to Cartesian-segmented 3D GRASE in ASL imaging. In future work, we suggest using 3DGP-STD as a preprocessing step for initial 3DGP-JET motion estimates to combine the robustness of both techniques for different motion scenarios in an updated algorithm. In addition, aspects such as a potentially reduced labeling efficiency due to motion should be further investigated.

Estimation of field maps and distortion correction using 3DGP-JET

Realistic field maps were recovered for all BS levels and motion patterns using the proposed 3DGP-JET algorithm (cf. Figure 5.22a and b). This shows that the assumption of constant field maps in case of motion is reasonable for brain ASL imaging. Results from BS0 show that field estimates depend on the level of distortion of residual signal. An example of distortion correction in 3DGP navigator images is given in Figure 5.23. In principle, off-resonance is responsible for both distortion and chemical shift artifacts. Thus, an improved version of the 3DGP-JET algorithm might be able to correct for minor amounts of residual shifted fat in the future. It is mentionable that the correction of distortion did not significantly improve the quality of perfusion images in this work, because estimated off-resonance was rather low in perfused regions. However, for lower brain regions or organs like liver, the additional capability for distortion correction might become more important.

Applicability to other organs

The application of the developed 3DGP-JET algorithm to brain ASL imaging under presence of motion was successfully demonstrated. As already mentioned, future experiments should investigate the application to abdominal organs, such as liver and kidney, due to the increased amount of off-resonance, which is expected in these regions. Larger amounts of off-resonance in combination with large cranial-caudal shifts could potentially violate the underlying assumption of constant distortion fields. Results could

then motivate future variation of the algorithm, estimating multiple field maps for different motion states, which is directly possible if a golden angle acquisition scheme is applied.

5.2.1.4 Conclusion

With 3DGP-JET, a novel reconstruction algorithm for 3D GRASE PROPELLER pCASL imaging was introduced, allowing to recover in-plane motion trajectories as well off-resonance field maps without additional reference scans. 3DGP-JET as well as the standard 3DGP-STD algorithm were compared to Cartesian-segmented 3D GRASE data for different levels of BS and motion patterns during the scan. It was found that a residual offset of static tissue signal of around 10% yielded most robust results in terms of quality of the perfusion-weighted images. The optimized fixed BS scheme achieved adequate suppression of residual fat signal in combination with different levels of residual signal for gray and white matter and is thus the recommended BS approach in combination with 3DGP ASL sequences. In addition, 3DGP-JET showed increased robustness against intentional motion protocols when compared to Cartesian-segmented 3D GRASE and allowed reliable estimation and correction of off-resonance. Comparing 3DGP-STD and 3DGP-JET, the latter showed better results for slow motion patterns, while the first showed increased robustness to fast motion patterns. An updated 3DGP-JET routine will therefore be implemented using 3DGP-STD as a preprocessing step. Future investigation should finally focus on evaluating 3DGP-JET pCASL in realistic scenarios with patients and abdominal organs such as liver.

5.2.2 3D Rigid Motion Correction using 3DGP in Brain pCASL Imaging

The goal of the following experiment is to determine whether retrospective detection and correction of three-dimensional rigid body motion is feasible using 3DGP trajectories. Therefore, the implemented algorithm from section 4.2.3 is applied to brain pCASL scans with different directions of intentional through-plane motion. Based on these results, future implications for a combination of the 3DGP-JET algorithm and the three-dimensional rigid body motion model shall be derived.

5.2.2.1 Methods

Experiments

A healthy volunteer was scanned on a 3T scanner (Siemens MAGNETOM Skyra, Siemens Healthineers, Erlangen). The subject provided written informed consent prior to scanning and the study was run under a general protocol for pulse-sequence development approved by the local ethics committee. Four scans were performed using a standard 3DGP readout pattern, sampling k-space with evenly spaced bricks from 0° to 180°. Background suppression was achieved using presaturation and two additional inversion pulses during the pCASL preparation. Inversion timings were calculated using the algorithm by Günther et al. (43). During the first scan, the subject was told not to move intentionally. Three scans followed, and the subject performed a pre-defined rotation along the x-/y-/z-axis after half the acquisition time (cf. Figure 5.24).

Imaging was performed using a 3DGP pCASL sequence with a label duration of 1.8 s and post-labeling delay of 1.7 s, in combination with four label/control bricks with a 96 x 32 x 24 matrix and axial positioning. Additional parameters were: TR/TE = 4300 ms/21.5 ms, voxel size = (4 x 4 x 4) mm^3, 0.5 ms echo spacing and nine averages, resulting in 5:10 minutes of total measurement time per scan.

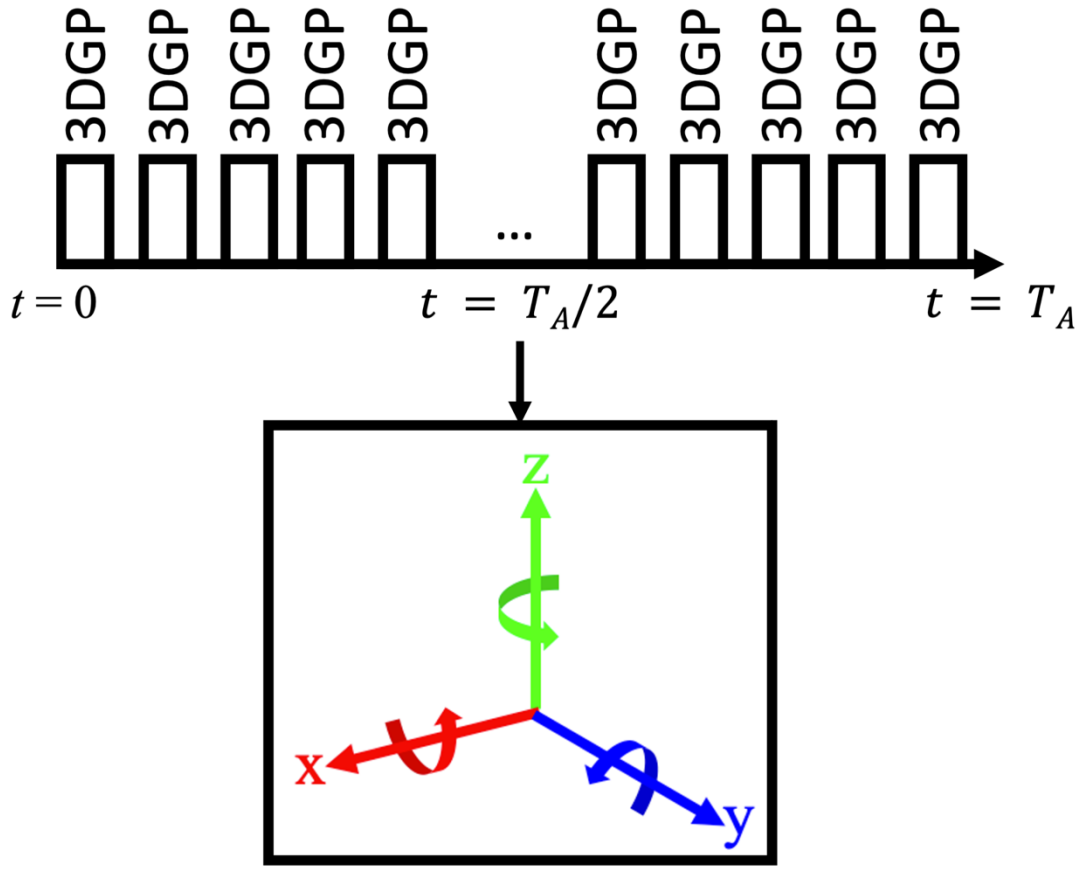

Figure 5.24: Motion Pattern and definition of axes during experiments. The subject performed a head rotation around one of the defined axes after half of the total acquisition time, such that two distinct positions occurred during each experiment. The rotation around the z-axis corresponded to the in-plane rotation.

Data analysis

The implemented algorithm was verified by investigation of estimated motion trajectories. In addition, visual inspection of the quality of reconstructed perfusion-weighted images with regards to the compensation of motion related artifacts was performed.

5.2.2.2 Results

Reconstructed perfusion-weighted images without intentional motion are shown in Figure 5.25. Visual quality of images with/without application of the proposed motion compensation technique was found to be comparable. In both cases, gray matter regions showed higher perfusion-weighting than white matter regions. In addition, visible blurring in the partition-encoded direction showed.

Figure 5.26 to Figure 5.28 show reconstructed perfusion-weighted images if the subject performed the proposed rotation around one of the three spatial axes during the scan. Uncorrected images showed increased blurring in spatial structures when compared to the reference images without motion. Blurring was reduced if the proposed motion correction technique was applied, and the agreement of perfusion-weighted images was more comparable to the reference dataset without motion (cf. arrows).

Corresponding calculated motion trajectories are given in Figure 5.29 and Figure 5.30. Without intentional motion, rotational trajectories showed fluctuation in a region of ± 1°. Translational estimates in a range of ± 2 mm were also observed. In case of rotation around one of the spatial axes, a corresponding rotation was detected by the algorithm after half the acquisition time.

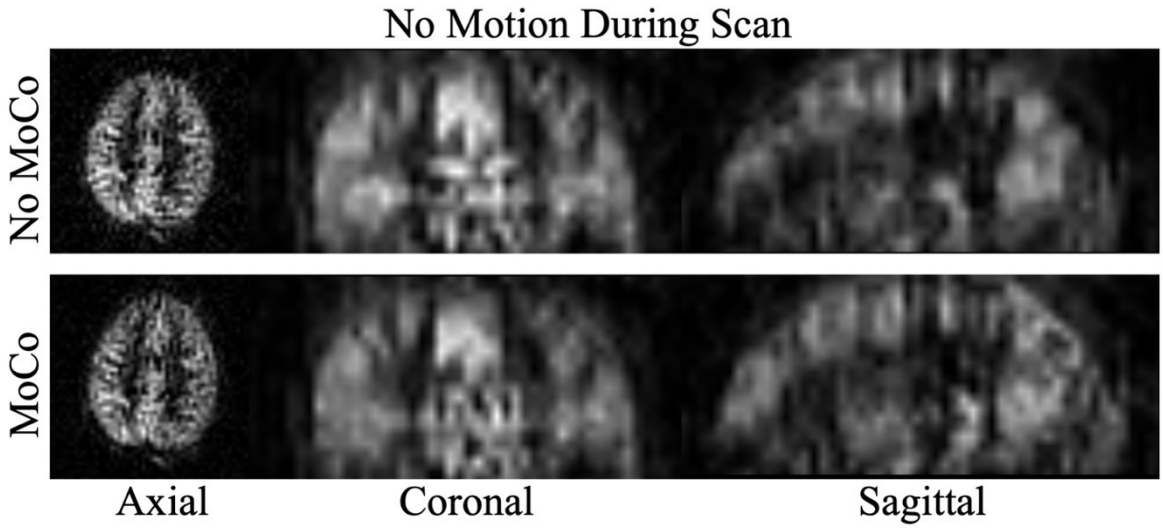

Figure 5.25: Different views of acquired perfusion-weighted images without intentional motion during the scan. The two rows show images with/without application of the motion correction algorithm.

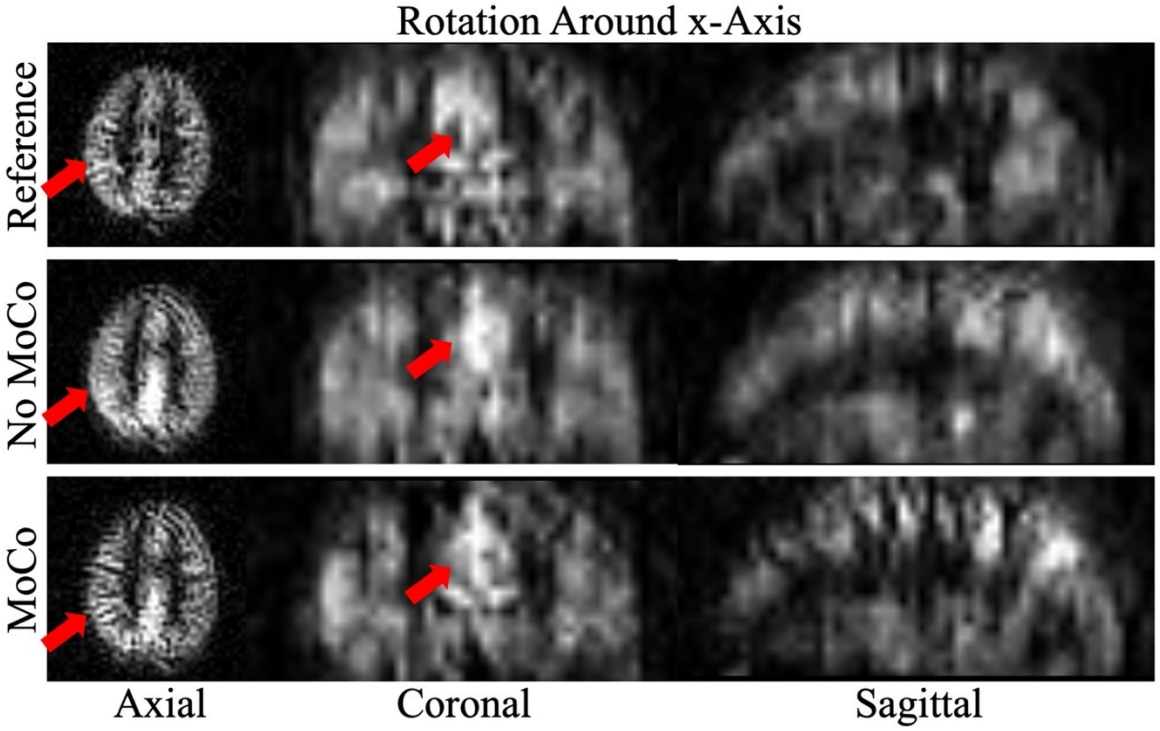

Figure 5.26: Different views of acquired perfusion-weighted images with an intentional rotation around the x-axis after half the acquisition time. The first row shows reference images without intentional motion and without application of motion correction. Additional rows show images with/without application of the motion correction algorithm.

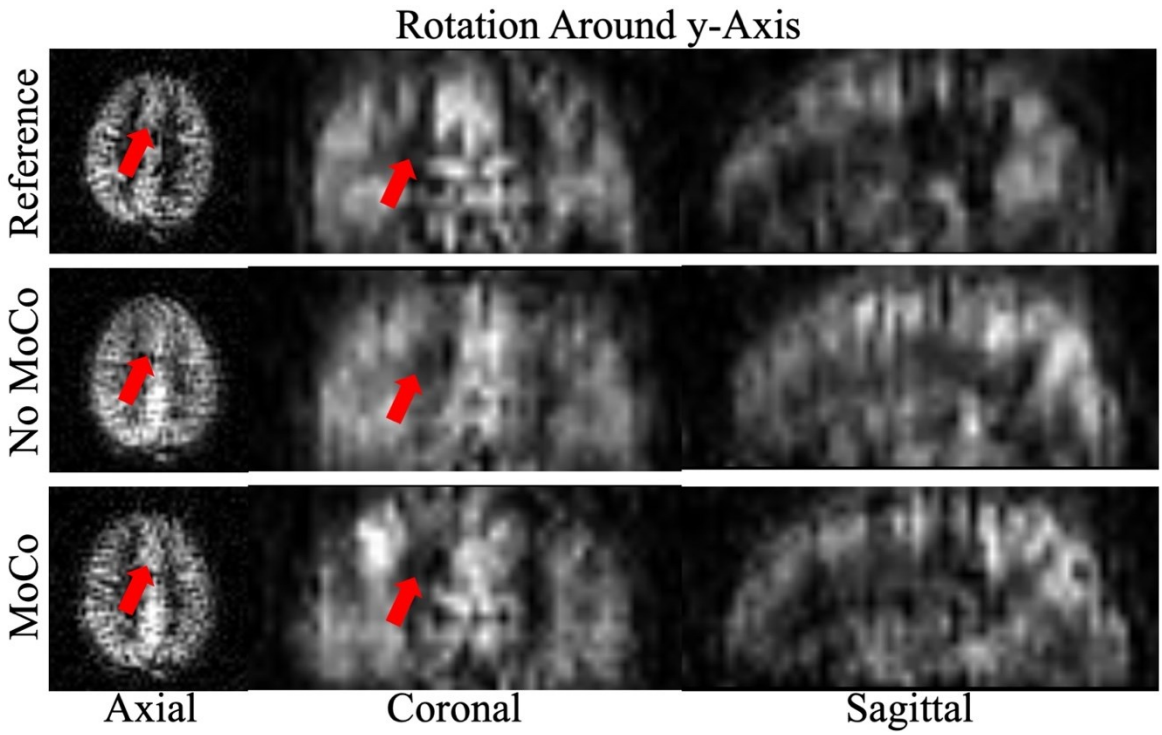

Figure 5.27: Different views of acquired perfusion-weighted images with an intentional rotation around the y-axis after half the acquisition time. The first row shows reference images without intentional motion and without application of motion correction. Additional rows show images with/without application of the motion correction algorithm.

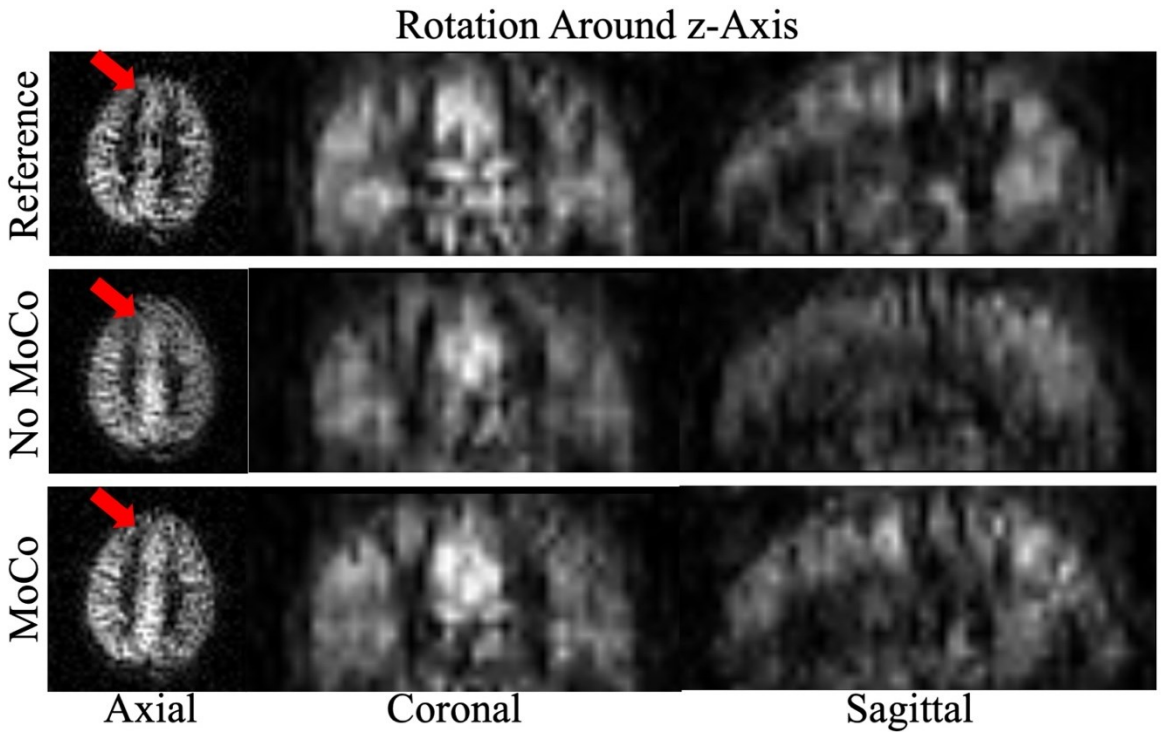

Figure 5.28: Different views of acquired perfusion-weighted images with an intentional rotation around the z-axis after half the acquisition time. The first row shows reference images without intentional motion and without application of motion correction. Additional rows show images with/without application of the motion correction algorithm.

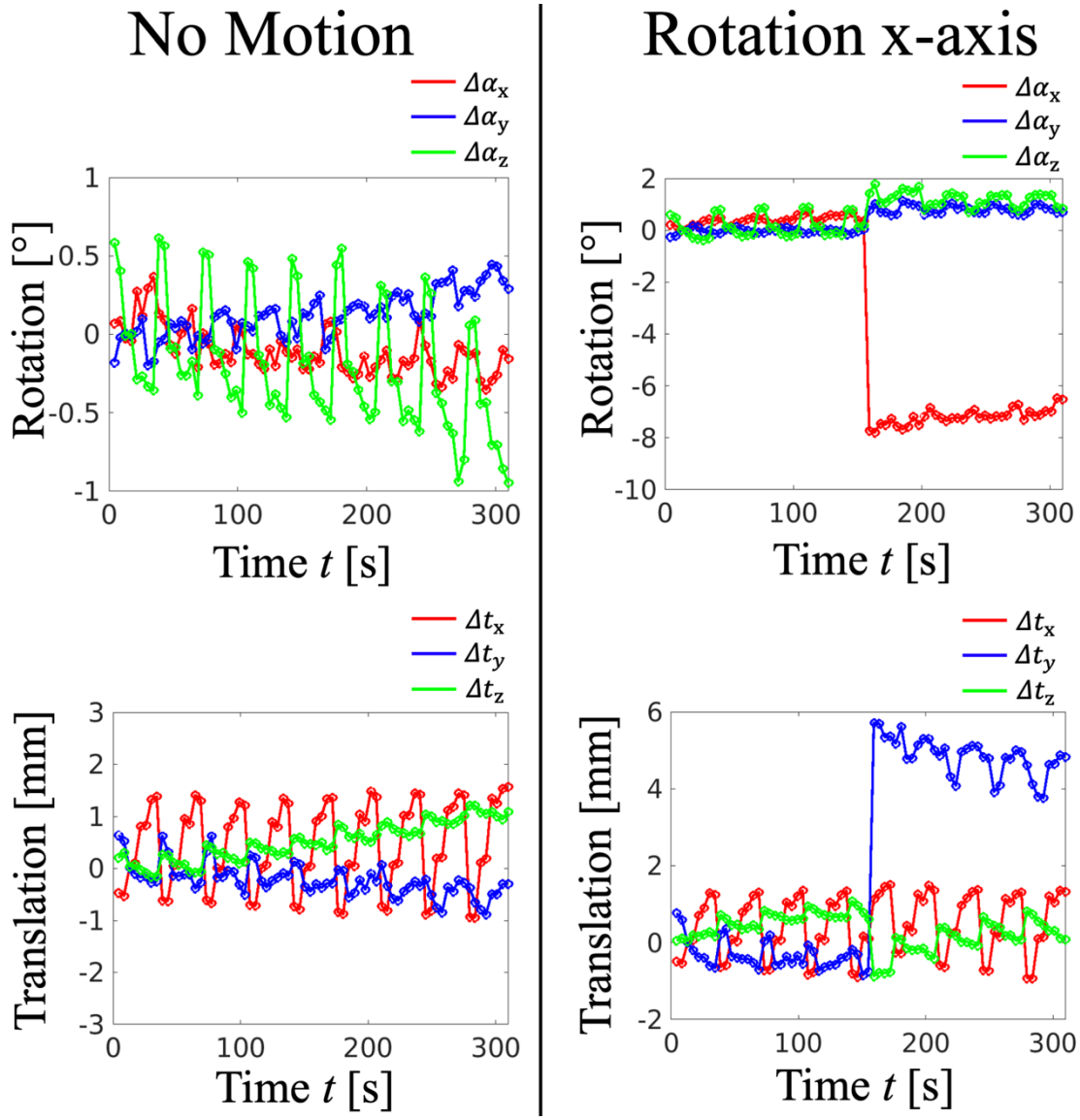

Figure 5.29: Rotation and translation estimates for the indicated motion strategy.

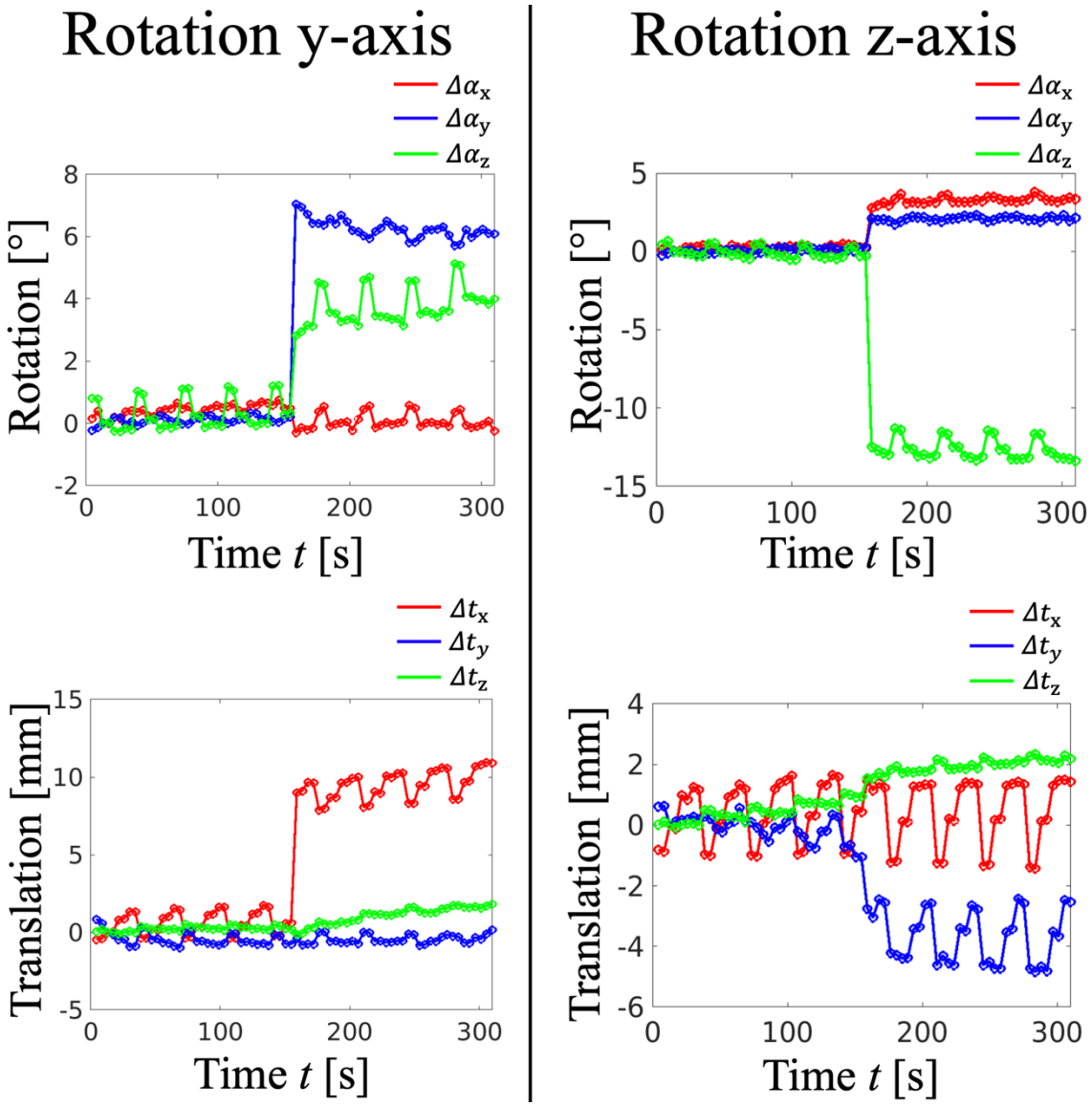

Figure 5.30: Rotation and translation estimates for the indicated motion strategy.

5.2.2.3 Discussion

Estimation of three-dimensional motion trajectories

The image space-based motion estimation technique was able to correctly identify the timepoint and direction of motion during the experiment from the low-resolution navigator images (compare Figure 5.24 with Figure 5.29 and Figure 5.30), indicating that estimation of three-dimensional motion from low-resolution 3DGP navigators was successful. Note that the in-plane resolution of these navigators was relatively high in this experiment (32 phase-encoded steps). Future studies should therefore investigate the accuracy of the estimated trajectories in case of lower numbers of phase encoded steps. Note that estimated trajectories revealed a systematic influence in terms of a repetitive fluctuation, resulting

from uncorrected geometric distortion, which was discussed in the previous section and could be addressed by an updated three-dimensional JET algorithm.

Quality of perfusion-weighted images

The proposed technique achieved improvements of the quality of perfusion-weighted images for all types of intentional motion during the experiments. The residual blurring in the partition encoded direction was not surprising, due to the long acquisition window, which was needed to acquire all 24 partitions. It is, however, not recommended to reduce the number of partitions if three-dimensional motion correction is desired, because through-plane estimates might get more inaccurate and retrospective correction is less effective. Therefore, combination of 3DGP readouts with parallel imaging techniques might be an option to reduce the length of the acquisition window and thus the through-plane blurring.

Potential for future 3DGP developments

Finally, potential future developments in the field of 3DGP ASL imaging are derived from this experiment. As in the previous study, the investigated motion trajectories were highly artificial. As was already mentioned, the applicability of pure retrospective three-dimensional motion correction might be limited under realistic motion scenarios. This is attributed to potential spin-history artifacts and the sampling of different parts of the object in case of high-frequent through-plane motion. A possible future extension of the 3DGP readout could therefore comprise prospective fat-navigation techniques, as described in (97). This would allow to reduce the amount of through-plane motion prior to the image acquisition step. Retrospective three-dimensional correction approaches would then become more efficient. In addition, the six-parameter estimation of rigid body motion should be integrated into the proposed 3DGP-JET algorithm in the future to prevent the observed fluctuation of motion parameters due to geometric distortion.

5.2.2.4 Conclusion

It was shown that estimation and correction of 3D rigid body motion using 3DGP readouts in combination with pCASL imaging is possible. Estimated trajectories, however, revealed the expected influence by geometric distortion, motivating a 3D extension of the previously discussed 3DGP-JET algorithm. In addition, the applicability of purely retrospective 3D rigid body correction to scenarios with high-frequent through-plane motion might be limited and needs to be further investigated. Future work should therefore investigate a combination of a 3D JET algorithm with additional prospective image and saturation alignments.

5.3 Compensation of Respiratory Motion Artifacts

5.3.1 Optimized Fixed BS and Multi-Breathhold Detection in Liver PASL Imaging

The following experiment initially evaluates the developed optimized fixed BS scheme (cf. section 4.1.2) in combination with the multi-breathhold detection (cf. section 4.3.2) in PASL scans of the human liver. The goal is to verify whether the combination of both techniques can compensate for respiratory induced motion artifacts in perfusion-weighted images, which could motivate future studies in clinical scenarios.

5.3.1.1 Methods

Adjustment of optimized fixed BS algorithm

The optimized fixed BS algorithm was used to calculate the timing of three FOCI pulses. The relevant BS parameters are given in Table 5.4. In addition to liver and fat, the reduction of signal from spleen was incorporated, which is also typically present in axial liver ASL images. However, a small weighting factor was introduced here, because reduction/suppression of signal from liver and fat was most relevant.

	Fat	**Liver**	**Spleen**
T_1 [ms]	300/350/400	700/800/900	1200/1300/1400
$w(T_1)$	0.1	0.16	0.03
$M_{\mathrm{res}}(T_1)$	0.0	0.1	0.1

Table 5.4: Selected parameters of the optimized fixed BS scheme in this study. Indicated weightings were applied for each of the given T_1 values. The same holds for the residual magnetization levels.

Experiments

Axial experiments were performed using a healthy volunteer on a 3T Siemens Skyra Magnetom (Siemens Healthineers, Erlangen). The subject provided written informed consent prior to scanning and the study was run under a general protocol for pulse-sequence development approved by the local ethics committee. FAIR PASL was selected as ASL preparation, which ensures high labeling efficiency, because all blood outside the imaging volume is inverted, independently from potential curvatures in portal vein or hepatic artery. Using the multi-breathhold approach, inflow times TI = 2 s, 2.7 s, 3.4 s were acquired to cover the dynamics of inflowing blood from the macrovascular to the microvascular compartment. Further imaging parameters were: Bolus length = 2 s, Bandwidth = 3004 Hz/Px, Matrix = 64 x 48 x 10, FoV = (300 x 240 x 80) mm^3, TE/TR = 23 ms/6000 ms and 15 repetitions, which were finally averaged. A series of Q2Tips pulses was applied after the desired bolus duration to saturate additional inflowing blood. The experiment with TI of 2.7 s was repeated under free-breathing conditions. Prior to the experiment, a M_0 scan during a single breathhold with a TR of 4 s and four saturation times was acquired to manually calibrate the threshold for breathhold detection, as described in section 4.3.2. Other imaging parameters of the M_0 scan were the same as for the PASL experiments. During all experiments, the subject was asked to be in exhaled states during breathholds. Otherwise, the subject could freely decide about the length of breathing and breathhold phases.

Data analysis

Reconstructed label, control and perfusion-weighted data were visually analyzed with regards to the following aspects: First, residual signal levels in control images were qualitatively compared to theoretical signal levels as predicted by the optimized fixed BS routine. Next, perfusion-weighted images obtained under free-breathing and multi-breathhold conditions were qualitatively compared. Finally, the quality of perfusion-weighted images reconstructed from data with different inflow times and acquired using the multi-breathhold technique was assessed.

5.3.1.2 Results

Table 5.5 shows theoretical levels of suppression using the optimized fixed BS algorithm for the different inflow times applied in this experiment. Corresponding measured signal contrast are shown in Figure 5.31. A significant decrease in signal intensity was observed for later inflow times, which is not in accordance with theoretical values.

A comparison of reconstructed perfusion-weighted images acquired using the proposed multi-breathhold and the free-breathing approach for an inflow time of 2.7 s is given in Figure 5.32. Perfusion-weighted images acquired under free-breathing showed increased subtraction errors in areas outside the liver region (cf. red arrows). These artifacts were not present if multi-breathhold triggering was applied, which indicates that reliable detection of the exhaled state was achieved in this study. In addition, perfusion signal from kidney and spleen appeared much higher under free-breathing (cf. green arrows). The same holds for liver perfusion (cf. blue arrows).

Figure 5.33 shows reconstructed perfusion-weighted images using the multi-breathhold approach in combination with different inflow times. While macrovascular signal was high for early inflows, the intensity in microvascular compartments increased with later inflow times. Subtraction errors outside perfused regions were low for all inflow times, which is in accordance with the findings from Figure 5.32 for the multi-breathhold case.

	Liver	**Fat**	**Spleen**
PLD = 2000 ms	9.85%	0.96%	10.6%
PLD = 2700 ms	9.91%	0.73%	9.71%
PLD = 3400 ms	9.96%	0.56%	8.88%

Table 5.5: Theoretical suppression of static tissue achieved with the proposed BS design. Percentual values were averaged over the T_1 ranges, given in Table 5.4.

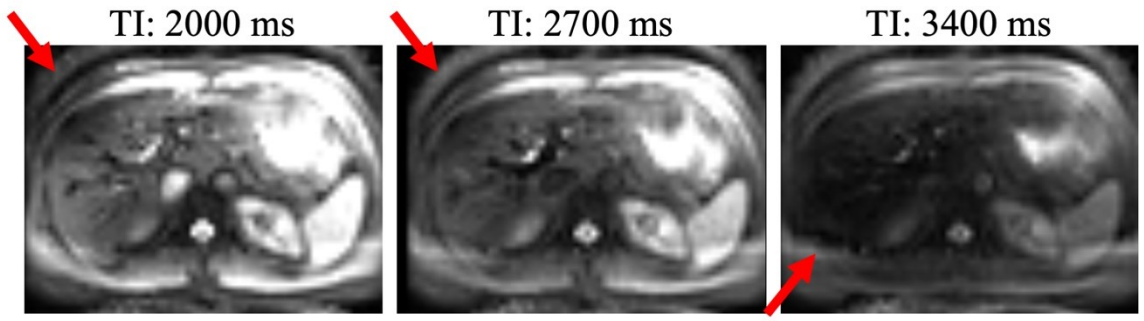

Figure 5.31: Image contrasts achieved in control volumes for different inflow times TI. Arrows indicate residual off-resonant signal from fat.

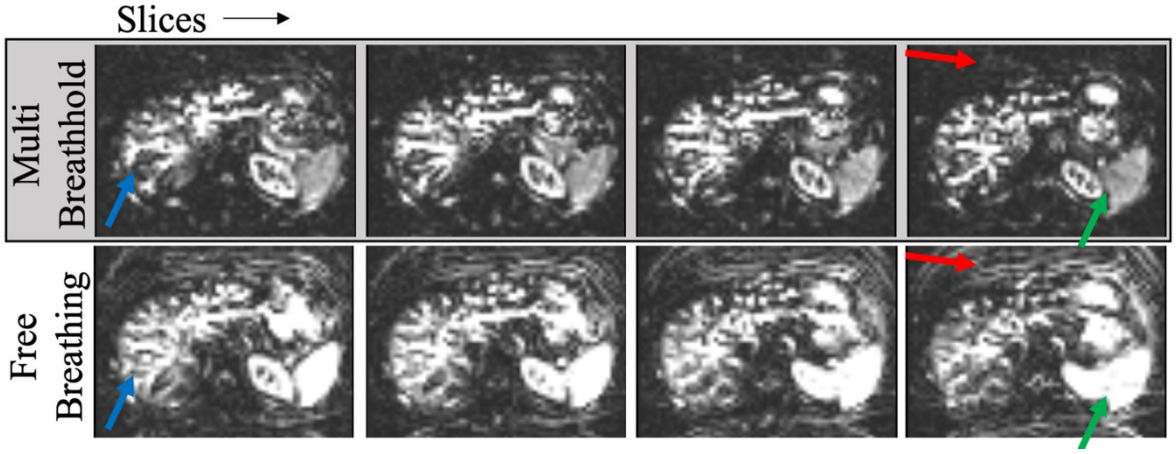

Figure 5.32: Reconstructed perfusion-weighted images using PASL with a bolus duration of 2 s and $TI = 2.7$ s. The top row shows images using the proposed multi-breathhold approach. The bottom row shows images if the subject breathes freely during the scan without further compensation of motion artifacts. Red arrows indicate increased subtraction errors in regions outside the liver under free-breathing. Green arrows show increased artificial perfusion in kidney and spleen. Blue arrows show areas with artificial perfusion in liver if breathing motion is not compensated.

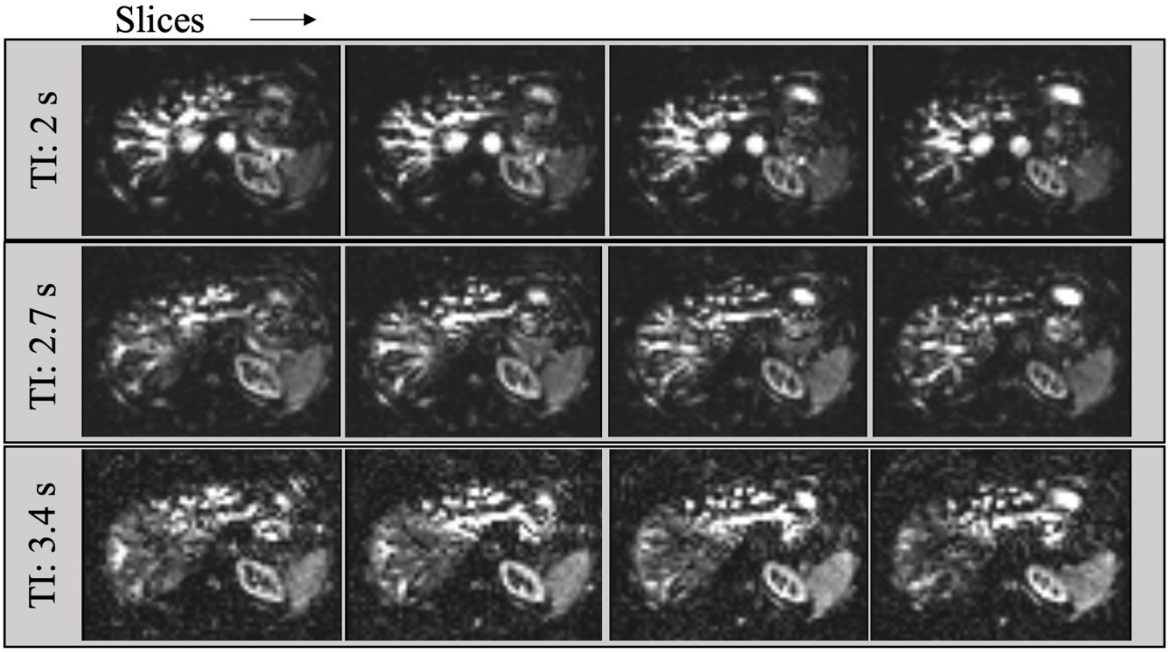

Figure 5.33: Reconstructed perfusion-weighted images in liver using PASL and the proposed multi-breathhold approach for different inflow times. While blood populates macrovascular compartments for early inflow times, microvascular perfusion is clearly visible for later ones. Note that different windowing was applied for different inflow times for visualization purposes.

5.3.1.3 Discussion

Optimized fixed BS in liver FAIR PASL imaging

Theoretical prediction of residual signal of the static tissue was close to anticipated levels, as verified by the results from Table 5.5. Actual measured signals, however, showed a strong additional saturation effect with increased inflow times. It is unlikely that the observed variation in signal levels was related to imperfect inversion efficiencies, because three FOCI pulses were applied for all inflow times in this experiment. The observed saturation of signal for later inflow times was probably related to the application of the train of Q2Tips pulses, which was applied for bolus saturation. The duration of the Q2Tips train increases with the total inflow time if the bolus length is kept constant. Since Q2Tips pulses appear as off-resonant irradiation for the on-resonant static tissue in the imaging plane, additional saturation from MT effects might occur and could potentially explain the observed saturation.

In addition, although, a high level of suppression of off-resonant fat signal was achieved, residual minor chemical shift artifacts were still present in anatomic images (cf. Figure

5.31, arrows). This was unproblematic for this experiment, because the series of label and control images was acquired within multiple exhaled breathholds. This way, the same position of the chemical shift artifacts was ensured, and cancellation was achieved by subtraction. However, the residual fat signal in label and control images indicates that the optimized fixed BS scheme with its theoretical assumptions might have limitations in abdominal imaging. This will be further evaluated in combination with additional motion correction in section 5.3.2.

Quality of perfusion-weighted images: multi-breathhold vs. free-breathing

The proposed multi-breathhold technique allowed reconstruction of axial perfusion-weighted liver images of high quality, making it a suitable technique for mitigation of motion related artifacts in liver ASL imaging. In contrast to previous reports by Martirosian et al. (98), free-breathing liver ASL experiments without motion compensation were highly affected by subtraction errors, especially in the area of the liver (cf. Figure 5.32). The fact that these errors might be misinterpreted as increased perfusion estimates is found problematic for diagnostics or quantification purposes. Although these subtraction errors might be further reduced by further reducing the residual static tissue signal from liver, this will not prevent subtraction of different anatomical regions due to large cranial-caudal shifts under free-breathing, demanding for sophisticated additional motion correction techniques.

A potential drawback of the technique for clinical practice could be increased acquisition time, when compared to a fixed timed-breathing scheme. However, if a subject fails to follow the fixed protocol, scan time could also be prolonged due to repeated experiments. Therefore, the application of the multi-breathhold approach as an alternative to timed-breathing protocols could be applied based on the condition of the subject/patient under investigation. Future experiments are therefore recommended, which compare timed breathing and multi-breathhold detection in scans under clinical conditions.

Applicability to other abdominal organs

As expected, the FAIR PASL approach resulted in high labeling efficiency as indicated by strong macrovascular signal for the early inflow times. The presented technique might therefore also be a promising candidate for other abdominal organs, where accurate

positioning of a pCASL labeling plane is even more challenging than in the liver. This holds for e.g., female breast and prostate, where ASL could be a promising technique to identify tumors (99)(100). Hence, future experiments in these organs are proposed.

5.3.1.4 Conclusion

It can be concluded that the presented multi-breathhold technique in combination with the optimized fixed BS scheme were suitable for mitigation of respiratory related artifacts in liver ASL imaging with the cost of potential additional scan times when compared to fixed timed-breathing protocols. The fact that strong artifacts appear in perfusion-weighted images under free-breathing illustrated the demand for proper respiratory motion compensation techniques in liver ASL imaging. In future work, the technique should be compared to timed breathing protocols with respect to scan times in a larger cohort of subjects or patients.

5.3.2 Optimized Fixed BS and Prospective Navigator Matching in Liver pCASL Imaging

In the following, the optimized fixed BS scheme (cf. section 4.1.2) will be evaluated in combination with the prospective compensation of respiratory motion (cf. 4.3.3) in liver pCASL imaging. The goal is to investigate whether the prospective navigator matching approach can adequately correct the strong cranial-caudal liver shifts during free-breathing. In addition, the effectiveness of additional elastic image registration to compensate for residual local deformations will be investigated. Besides quantitative reduction of liver motion, special attention is paid to the quality of the perfusion-weighted images. Based on these results, the potential and future direction of free-breathing liver ASL imaging is outlined.

5.3.2.1 Methods

Positioning of 3D GRASE readout

The goal of this study was to evaluate the effectiveness of the prospective motion compensation technique during free-breathing liver pCASL experiments. Therefore, a sagittal orientation was selected for the 3D GRASE module (cf. Figure 5.34). This way, the cranial-caudal main component of liver motion lied in the readout direction of acquired 3D GRASE volumes, which allowed straight-forward visual inspection of residual shifts and deformations. In addition, the application of retrospective methods to quantitatively assess remaining displacements of the liver was simplified. Note the side effect that the mismatch between presaturation and readout was minimized using this setup. Therefore, no spin-history related artifacts might be observed in acquired 3D GRASE data and the effectiveness of updating the saturation plane was not directly accessible. However, since the principle of prospective updating the saturation and 3D GRASE position was the same, indirect conclusions about the saturation accuracy, could still be drawn from estimated residual motion in the 3D GRASE image data.

Positioning of the pCASL labeling plane

High SNR in perfusion-weighted images was desired, thus the positioning of the labeling plane was mainly adapted to the portal venous supply. Therefore, the anatomic information from a HASTE localizer scan was used to get a rough idea about the vessel structure in the liver region. After positioning, a single pCASL subtraction experiment (one label, one control acquisition) without any motion correction was performed in breathhold using a TR of four seconds and a PLD of 700 ms (other parameters as described below) for visual verification of suitable labeling efficiency. The background suppression inversion region was adapted to the positioning of the labeling plane, resulting in setups as demonstrate in Figure 5.34.

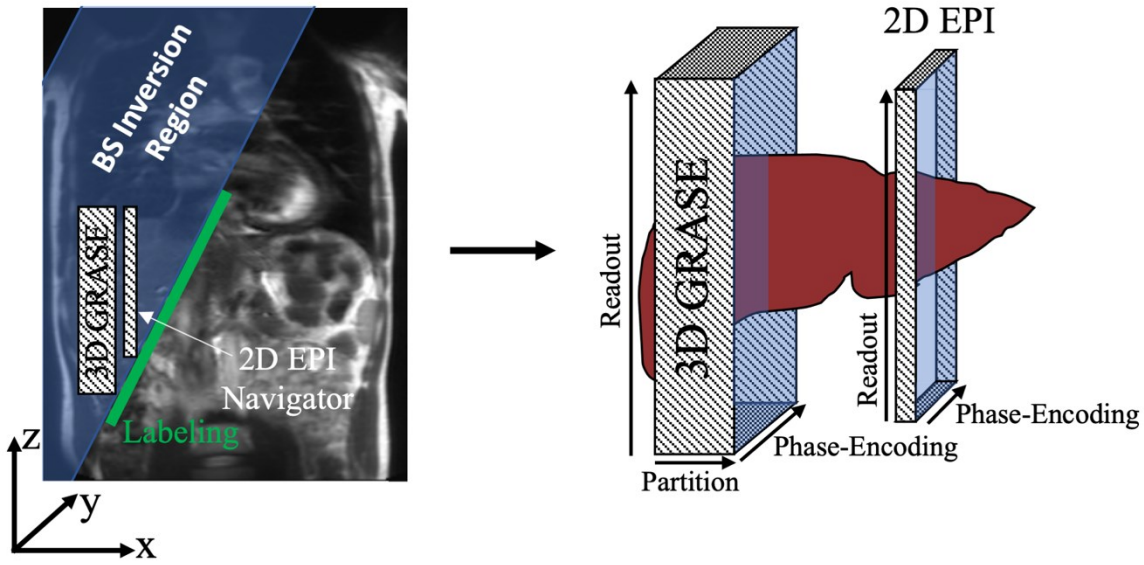

Figure 5.34: Schematic representation of the sagittal positioning of the 2D EPI readouts together with a sagittal positioned 3D GRASE readout.

3D GRASE image reconstruction

The 3D GRASE image reconstruction pipeline is demonstrated in Figure 5.35. Additional 2D in-plane B-spline nonrigid elastic registration was performed, using algorithms from the Insight Toolkit (76). The image registration was based on the magnitude data of the respective label control images. 2D image retrospective image registration was preferred over 3D registration, due to the restricted number of partitions in single-shot 3D GRASE experiments. After retrospective image registration, a subject-dependent region was specified, covering the upper boundary of the liver in the central slice. Subsequently, a 2D

translational registration was performed for analysis of residual liver motion in acquired images. All image reconstruction steps were implemented in C++ within the Siemens ICE framework (Siemens Healthineers, Erlangen).

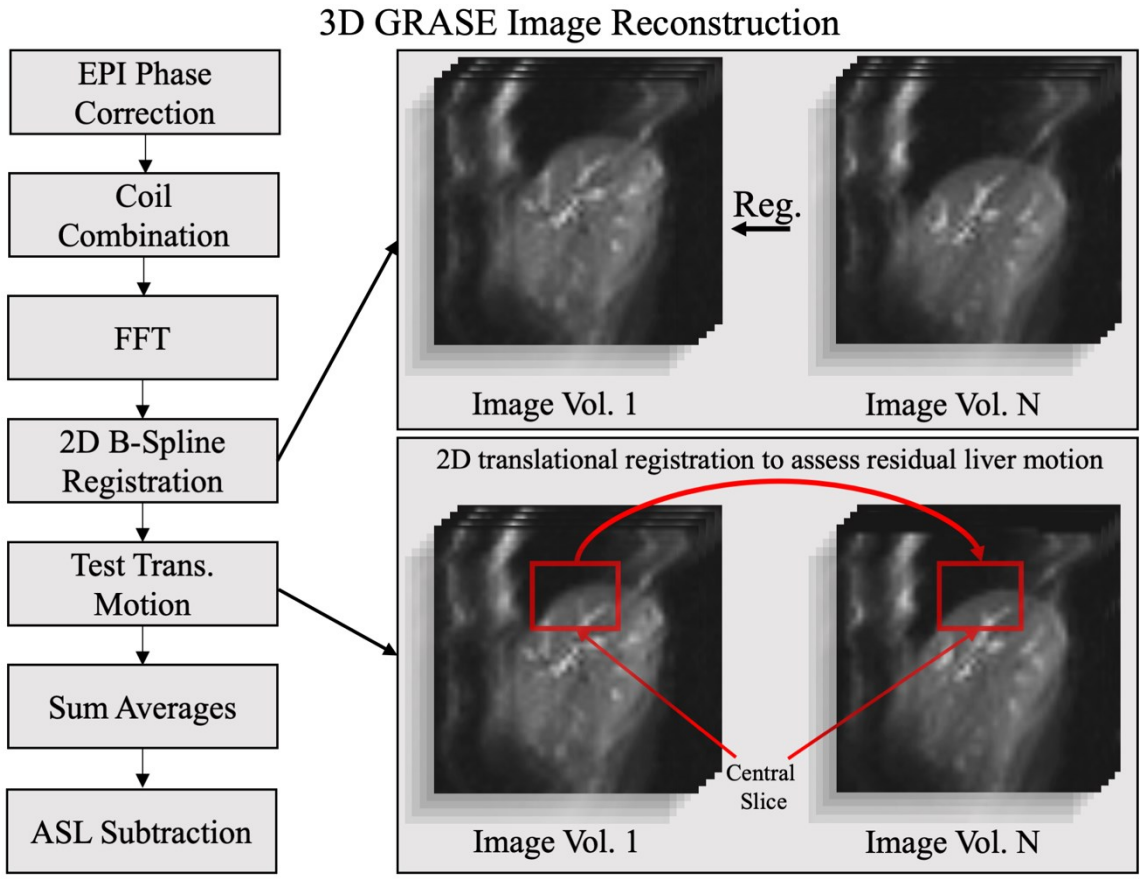

Figure 5.35: 3D GRASE image reconstruction pipeline as applied in this work. Images were reconstructed with/without the 2D B-Spline image registration step. Therefore, the first acquired control volume was used as the reference image. A simple difference metric was used during image registration. The testing of translational motion did not introduce any additional resampling of the data but was only performed to estimated residual motion in the indicated subject-dependent upper liver region.

Adjustment of optimized fixed BS algorithm

In this work, a small residual amount of static liver signal was desired at excitation to avoid difficulties during the elastic registration and to allow estimation of residual motion in the liver region using different imaging protocols. In addition, good fat suppression was anticipated to reduce potential subtraction errors arising from the off-resonant signal mismatches after image subtraction. Therefore, three C-shape FOCI pulses (cf. section

2.8.1) were applied after initial saturation. Timings were calculated using the optimized fixed BS scheme. Liver tissue was targeted to 10% of its nominal M_0 value while signal arising from fat was reduced to 0% at excitation. A detailed list of parameters of the BS algorithm is given in Table 5.6. Selected T_1 values correspond to literature reports (63)(101). Lists of calculated inversion timings are given in Table 5.7 and Table 5.8.

	Liver	**Fat**
T_1 values [ms]	700, 800, 900	300, 350, 400
$w(T_1)$	0.23	0.1
$M_{\mathrm{res}}(T_1)$	0.1	0.0

Table 5.6: Selected parameters of the optimized fixed BS scheme in this study. Indicated weightings were applied for each of the given T_1 values. The same holds for the residual magnetization levels.

BS Inversion Timings: Timed-Breathing/Free-Breathing

PLD	**1. Inversion**	**2. Inversion**	**3. Inversion**
700ms	990 ms	2158 ms	2578 ms
1500ms	1630 ms	2929 ms	3371 ms
2000ms	2071 ms	3419 ms	3869 ms
2500ms	2532 ms	3912 ms	4366 ms

Table 5.7: Calculated inversion timings for the indicated PLD during the timed-breathing/free-breathing experiments, where no additional constraint in terms of forbidden pulse timings during the navigator readout apply.

BS Inversion Timings: Prospective

PLD	1. Inversion	2. Inversion	3. Inversion
700ms	123 ms	1887 ms	2514 ms
1500ms	524 ms	2670 ms	3310 ms
2000ms	931 ms	3182 ms	3814 ms
2500ms	1404 ms	3679 ms	4314 ms

Table 5.8: Calculated inversion timings for the indicated PLD during the prospectively corrected experiments, where additional constraint in terms of forbidden pulse timings during the navigator readout apply.

Experiments

Eight healthy volunteers (4m, 4w, aged 24-40) were scanned at 3T (Siemens MAGNETOM Skyra, Siemens Healthineers, Erlangen). All subjects provided written informed consent prior to scanning and the study was approved by the local ethics committee.

As a reference, pCASL scans using a timed-breathing protocol were performed, referred to as “Timed-Breathing” in the following sections. The first exhaled breathhold was triggered by automatic commands of the MRI system. The breathhold extended over the following pCASL labeling, post-labeling delay and 3D GRASE phase. Subjects were instructed to take one deep breath during the following empty time span until a TR of 10 s was reached and to go back into the exhaled breathhold as soon as possible. Parameters related to the pCASL preparation were: label duration LD = 2000 ms, post-labeling delays PLD = 700 ms/1500 ms/2000 ms/2500 ms (58). Experiments were repeated under free-breathing with a TR of 6 seconds, referred to as “Free-Breathing”. Last, free-breathing measurements were performed with a TR of 6 s and enabled prospective motion correction, referred to as “Prospective”.

Imaging parameters of the 2D EPI readouts were TR/TE = 100 ms/24.3 ms, matrix size = 64 x 64, FoV = (220 x 220) mm^2, slab thickness = 5 mm. For the reference series, 100 repetitions were acquired prior to the pCASL experiment. This resulted in a temporal coverage of 10 s of the reference EPI series, which should cover the duration of a normal breathing cycle. During acquisition of the reference series, a flip angle of 90° was used.

The flip angle was decreased to 20° for navigator images acquired during the ASL experiment. The whole acquisition time of a single EPI navigator was 47 ms. An additional 50 ms temporal gap was inserted between the end of the navigator and the following saturation/3D GRASE module, covering time for image reconstruction and feedback broadcasting.

The 3D GRASE imaging module consisted of three Q2Tips pulses (102) followed by a spectral fat saturation pulse (103) and the 90° excitation pulse with 3D GRASE encoding technique, as described in (18). Imaging parameters of the 3D GRASE readout were: TE = 23.9 ms, Bandwidth = 2264 HZ/Px, FoV = (250 x 208 x 40) mm^3 with a matrix size of 48 x 40 x 8 pixels, yielding a voxel size of 5.2 x 5.2 x 5 mm^3. Seven pairs of label/control images were obtained in each measurement, yielding a total acquisition time of 2:20 minutes for the timed-breathing protocol and 1:24 for free-breathing/prospective protocols.

Data analysis

The analysis of acquired data aimed to clarify whether the proposed prospective motion compensation technique can achieve accurate alignment of the liver position throughout the pCASL experiment. In addition, it should be verified whether the motion correction techniques allow reconstruction of high-quality perfusion-weighted images of the human liver under free-breathing conditions. Therefore, free-breathing as well as prospective data were reconstructed with/without the elastic registration depicted in Figure 5.35. The latter are referred to as “Free-Breathing + Elastic” and “Prospective + Elastic”. Note that the elastic registration of free-breathing data (without prospective correction) was only reasonable due to the sagittal positioning. In oblique positionings, pure retrospective correction is not promising due to major though-plane components of the cranial-caudal liver shifts. In addition, prospective data was resampled using the inverse prospective motion updates of each 3D GRASE volume, yielding uncorrected pseudo free-breathing images (“Prospective Inverted”). Reconstructed label, control and perfusion-weighted images were then qualitatively compared to timed-breathing data.

Residual cranial-caudal motion estimates, obtained from retrospective registration of the upper liver boundary (cf. Figure 5.35), were further quantitatively compared. Therefore, the standard deviation $\sigma_{\Delta z}$ of residual motion estimates for a specific subject and PLD was first calculated. Then, standard deviations were averaged across PLDs to allow a subject-

specific statement about the effectiveness of the prospective motion compensation. Finally, standard deviations were averaged across all subjects and PLDs to enable a general evaluation. Note that datasets using a PLD of 700 ms were excluded from this analysis, because label and control images showed large differences in macrovascular compartments, which were problematic for the translational registration routine.

In addition, the acquired navigator images were retrospectively resampled after finishing the pCASL experiment, using the corresponding motion estimates from the lookup table. After manual selection of a region which contains visible vessel structures of the liver the saturation and imaging navigators were separately registered (2D translational) to the first image of the corresponding series to assess the residual motion in the cranial-caudal direction. The accuracy of navigator registration was then compared to the previously described 3D GRASE analysis by performing the analogous calculation of mean $\sigma_{\Delta z}$ estimates. This way, potential effects of the temporal gap between EPI navigator and 3D GRASE excitation could be assessed. This step was only performed for those subjects where residual signal from vessels was assessable in EPI navigator data. Note that these additional navigator registration tasks, which were used for data analysis only, were also implemented in the Siemens ICE framework.

Last, reproducibility of pCASL experiments was assessed by calculating the mean variance of pairwise subtracted label/control images. This was possible, because multiple repetitions of the experiment were performed for subsequent signal averaging. Variance of the information in subtraction images was calculated by first defining a quadratic region of interest, covering the position of the liver in the first subtraction pair. Afterwards, variance of the difference information was calculated voxel wise and averaged over the central four slices of all PLDs of all subjects. The variance analysis was accomplished using Octave.

5.3.2.2 Results

Achieved signal suppression using the optimized fixed BS scheme is demonstrated in Figure 5.36. Theoretical suppression levels are given in Table 5.9. Comparable levels of residual static tissue signal were achieved for all PLDs using the timed-breathing protocol. Only minor shifted fat signal was observed here. In the prospective case, variation in residual fat signal was observed, especially for the two latest PLDs.

Visual examples of the processing of the reference timeseries and EPI navigators are given in Figure 5.37, Figure 5.38 and Figure 5.39.

Mean standard deviation $\overline{\sigma_{\Delta z}}$ in navigator data was reduced when applying LUT shifts (cf. Figure 5.40a). For subject three, no distinct vessel structure could be selected for the image registration procedure. The same situation showed for the saturation navigators of subject five and eight. Figure 5.40b shows the impact of the motion correction strategies. The right diagram shows that application of prospective correction resulted in an average reduction of residual motion to 43% of the uncorrected value. Further application of 2D B-splines registration allowed a decrease to 26% of the respective uncorrected fluctuation, which is in accordance with estimated residual motion using timed-breathing protocols (also cf. exemplarily trajectories in Figure 5.41).

Figure 5.42 illustrates the visual effect of prospective motion compensation on acquired 3D GRASE images. The prospective correction visibly aligned the liver throughout different repetitions of the experiment, resulting in reduced image blurring of label/control data (cf. Figure 5.42b). An analogous observation was made when applying the 2D elastic registration (cf. Figure 5.43). Note, how prospective data was already adequately aligned prior to this step.

Figure 5.44 demonstrates the effect of the motion compensation algorithms on perfusion-weighted images. The timed-breathing protocol showed the expected inflow from macrovascular to microvascular compartments with later PLDs (also cf. further examples in Figure 5.45). Free-breathing and prospective inverted images show a reduction of subtraction errors by application of the elastic registration and prospective correction with additional elastic registration, respectively.

Figure 5.46 finally shows that lowest variance in subtraction images was observed in the timed-breathing case. Highest variance showed for free-breathing and prospective inverted data. The latter was slightly reduced by application of prospective motion correction (also cf. Figure 5.47).

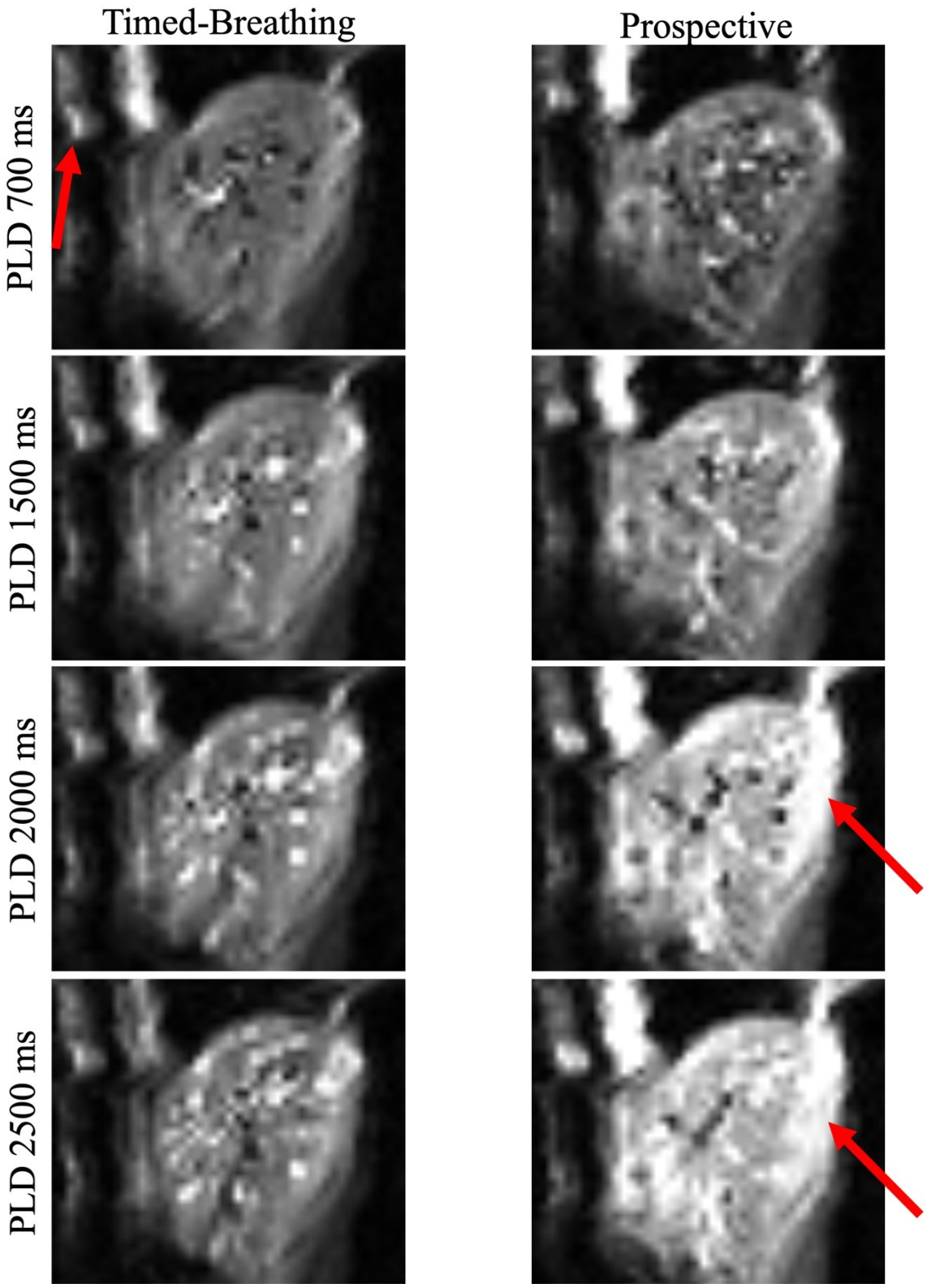

Figure 5.36: Measured static tissue signal in control images of one of the volunteers. Rows show the different PLDs. Columns show images obtained under the timed-breathing protocol and with prospective motion correction enabled. Arrows indicate regions with chemical shift artifacts.

	Timed		Prospective	
	Liver	**Fat**	**Liver**	**Fat**
PLD = 700ms	9.93%	1.01%	9.55%	2.76%
PLD = 1500ms	9.94%	0.81%	9.59%	2.68%
PLD = 2000ms	9.95%	0.73%	9.51%	3.02%
PLD = 2500ms	9.95%	0.96%	9.76%	1.95%

Table 5.9: Theoretical suppression of static tissue achieved with the proposed BS design. Percentual values were averaged over the T_1 ranges, given in Table 5.6. The left part of the table shows results using the timed-breathing protocol. The right part of the table shows results using the prospective correction, where the window of possible pulse timings is slightly reduced due to the additional EPI navigator.

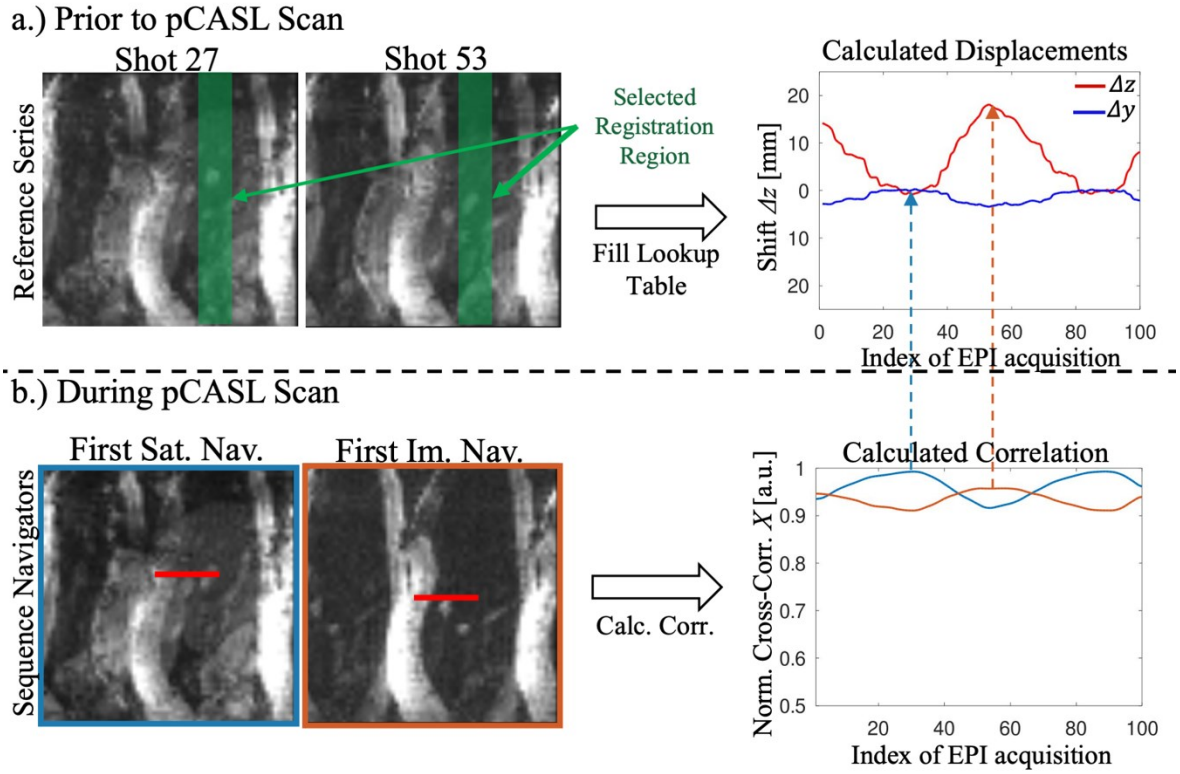

Figure 5.37: a.) Exemplary results from the prospective motion compensation technique for one of the volunteers. The liver region is identified in the EPI reference series as indicated by the green bars and the lookup table is filled with corresponding shifts; and b.) During the pCASL experiment, the calculated cross-correlation between navigators and the reference series shows clear maxima. Corresponding shifts (indicated by the arrows) are sent back to the sequence. Red bars in the navigator images indicate the position of prominent vessels and thus the global liver position.

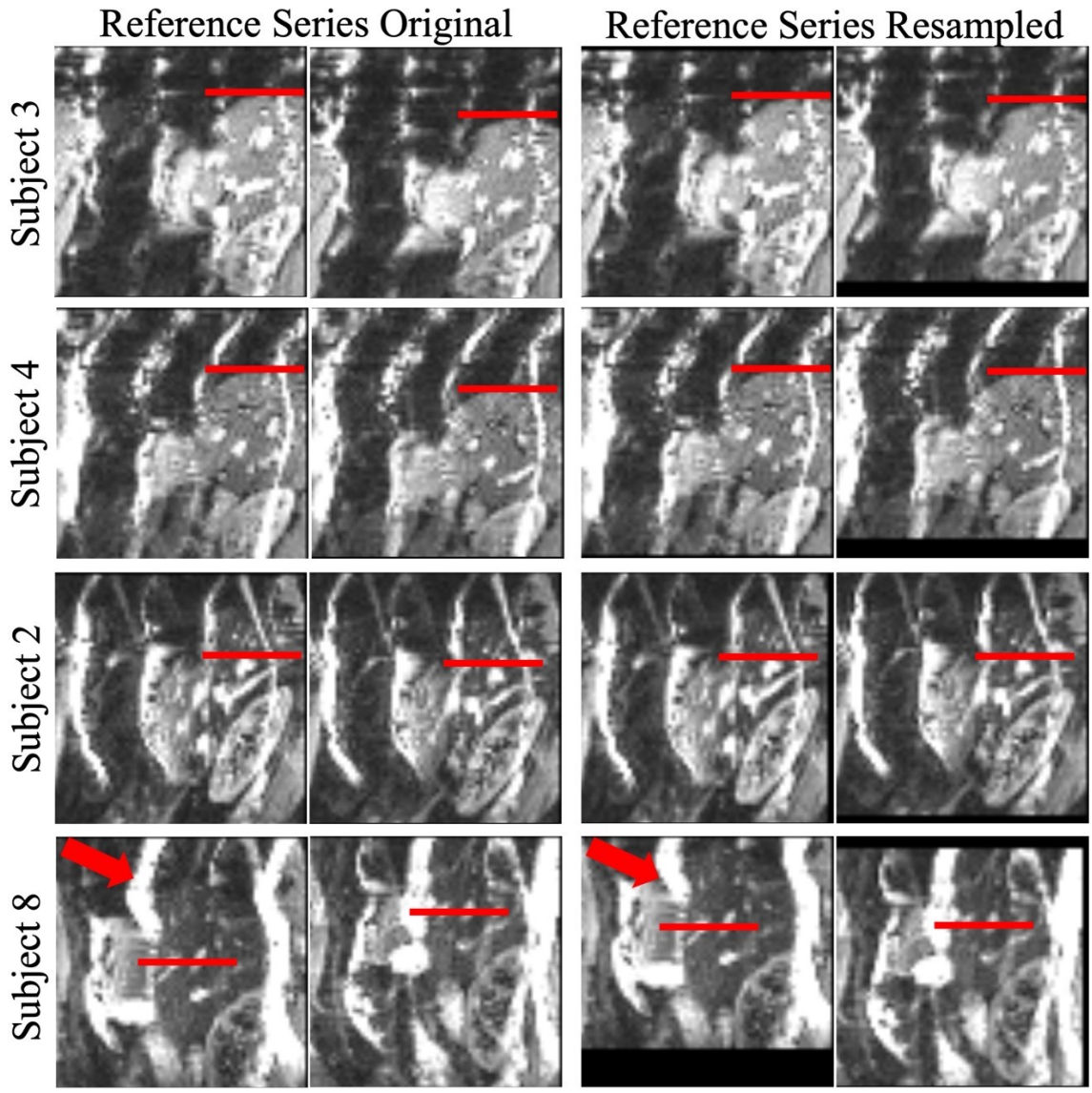

Figure 5.38: Exemplary 2D EPI images from the reference timeseries of different subjects. Two of hundred images are shown with maximum visible cranial-caudal shifts. Red bars are inserted as landmarks corresponding to fixed structures of the liver e.g., the upper boundary or distinctive vessels. Cranial-caudal shifts of liver tissue are visibly reduced after resampling using parameters estimated from the image registration algorithm, which was described in this work. Note how especially for the last subject, high intensity artifacts corresponding to fat are not aligned anymore (cf. red arrows) after resampling while the liver tissue clearly is.

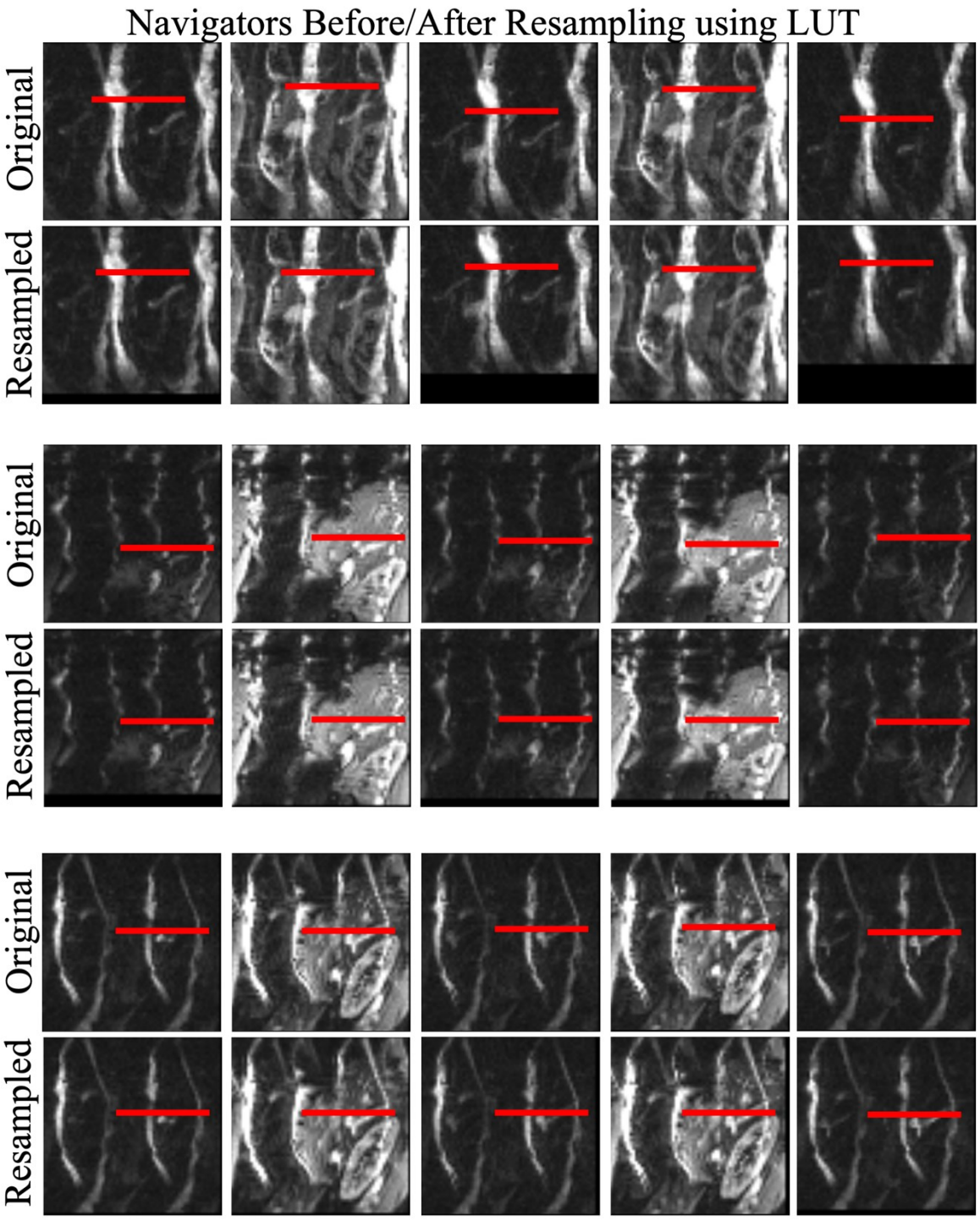

Figure 5.39: Exemplary series of navigator images from different subjects. Five of 28 images are shown. Rows show the original navigator images and navigator images resampled using the motion estimate with highest correlation value from the lookup table.

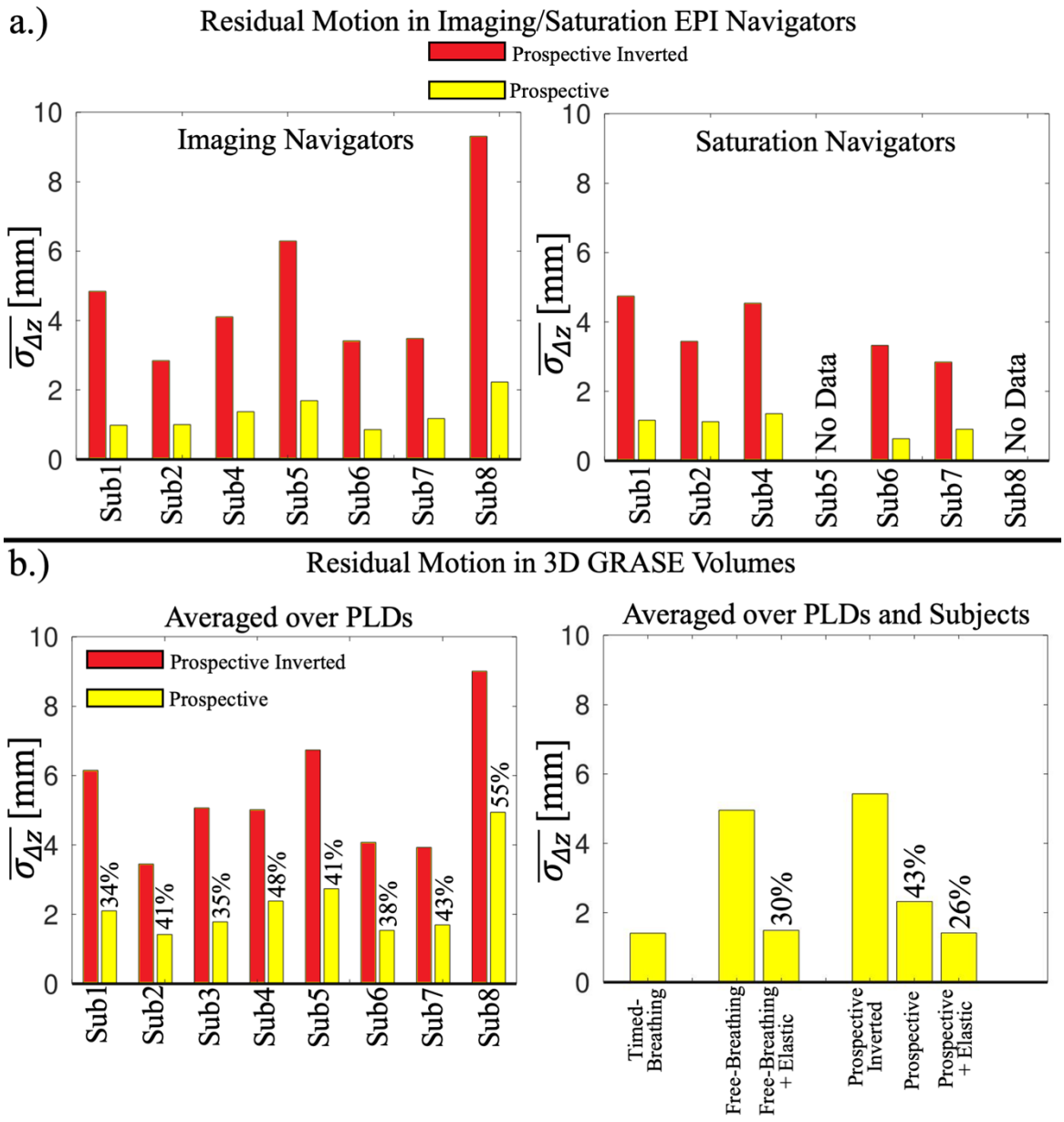

Figure 5.40: a.) Calculated mean standard deviations (averaged over all PLDs) of Δz motion estimates from acquired navigator data before and after resampling, using motion estimates from the lookup table. Note that resampling of navigators was performed retrospectively and is not required for the prospective motion correction algorithm. No direct registration of images was possible for subject three due to the lack of clear vessel structures. The same holds for the saturation navigators of subject five and eight; and b.) Left: Calculated mean standard deviations of Δz motion estimates from 3D GRASE data, averaged over different PLDs (except PLD = 700 ms). Red bars show results for prospective inverted data while yellow bars show results with applied prospective correction. Right: Calculated mean standard deviations of Δz motion estimates from 3D GRASE data, averaged over all PLDs (except PLD = 700 ms) and subjects, using different motion compensation strategies. Percentage values indicate the decrease when compared to the respective free-breathing/prospective inverted value.

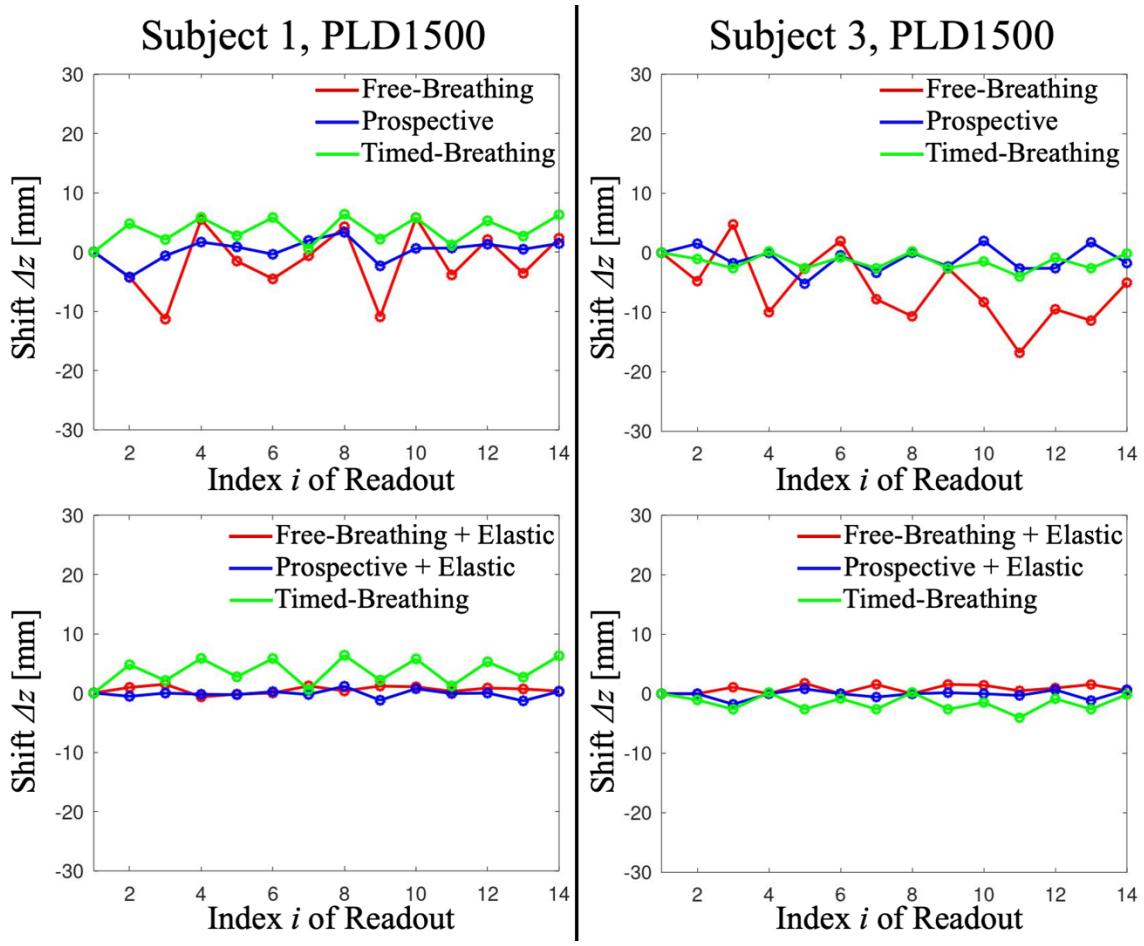

Figure 5.41: Comparison of estimated translational motion in z direction with/without application of prospective/retrospective correction algorithms. The first row shows a comparison of the timed-breathing, free-breathing and prospective datasets. The second row compares free-breathing and prospective data with additional nonrigid elastic registration with the timed-breathing protocol.

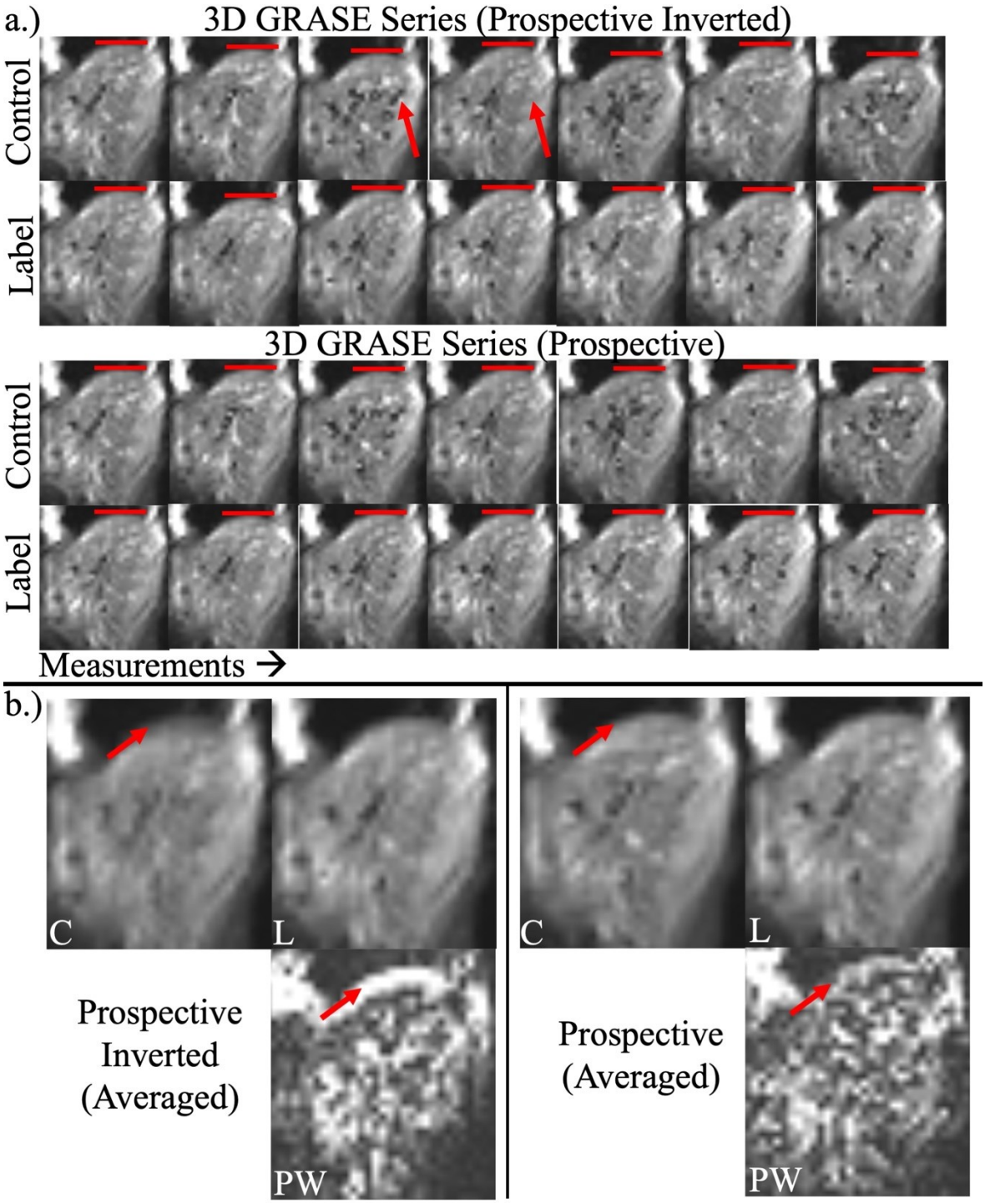

Figure 5.42: a.) Comparison between label/control data acquired under free-breathing with/without prospective correction during the scan (PLD = 2500 ms). Columns show individual repetitions/measurements. The upper part shows images with inverted prospective motion correction by retrospectively resampling the data using the inverse motion estimates. The lower part shows data as reconstructed with the prospective motion feedback. Note the change in position of the upper part of the liver (red bar) if the prospective correction was negated and visible through-plane motion of vessels, as indicated by the red arrows; and b.) Control (C), Label (L) and perfusion-weighted (PW) images obtained by averaging individual measurements/repetitions from a.). Note the increased blurring in the control image and the prominent subtraction artifact at the upper

boundary of the liver, which is visibly reduced when applying the prospective motion compensation technique.

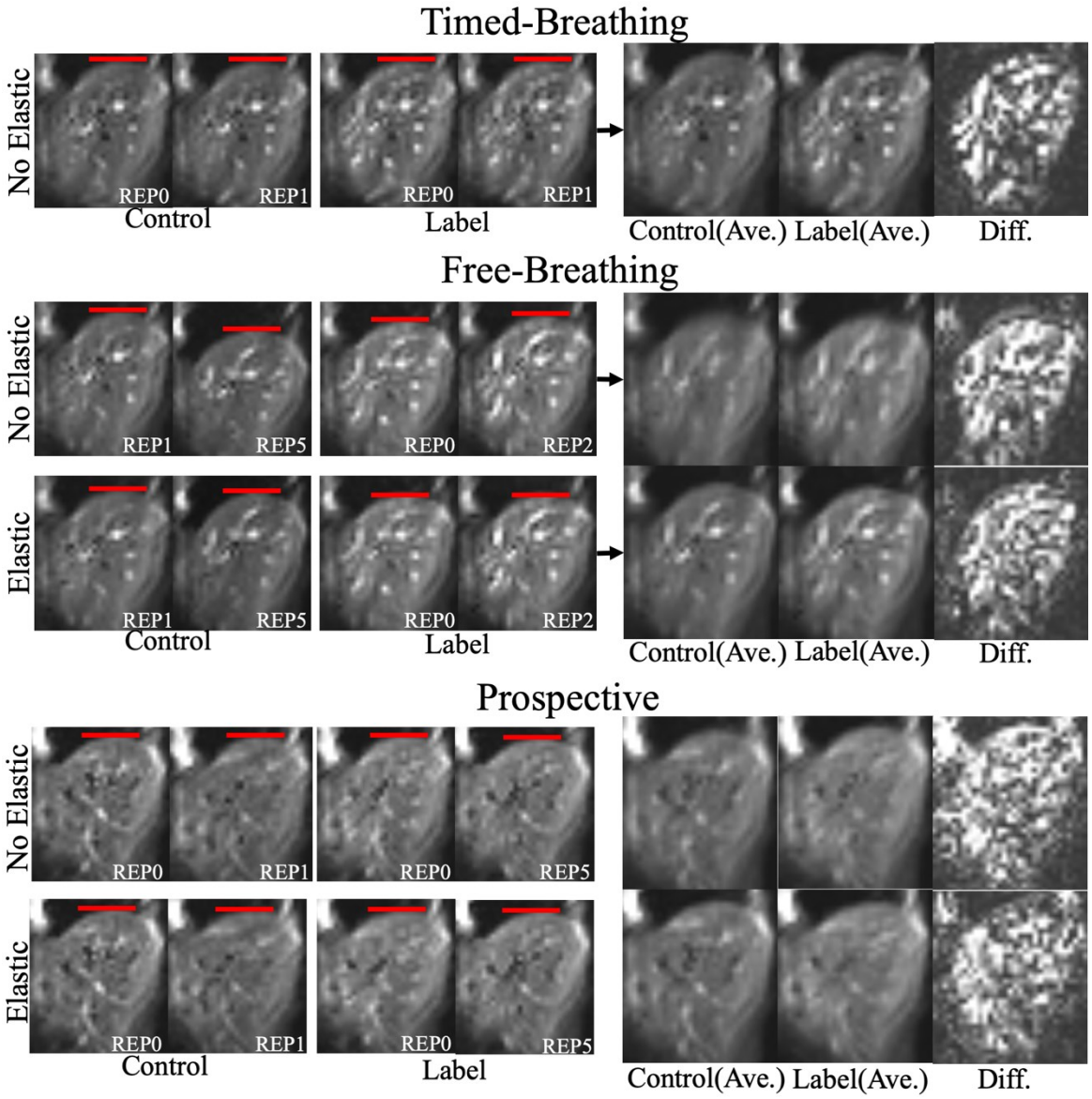

Figure 5.43: Exemplary demonstration of the retrospective 2D elastic image registration. The upper row shows the timed-breathing protocol as a reference. Data acquired under free-breathing shows large deviations of the liver position between individual measurements/repetitions. The elastic registration allows to compensate for the motion by some extend (cf. upper part of liver, indicated by red bar). Using the prospective correction, the liver position is already aligned prior to the elastic registration step, which then has only minor impact on individual images. The indicated repetitions were selected due to the visible displacement of the liver.

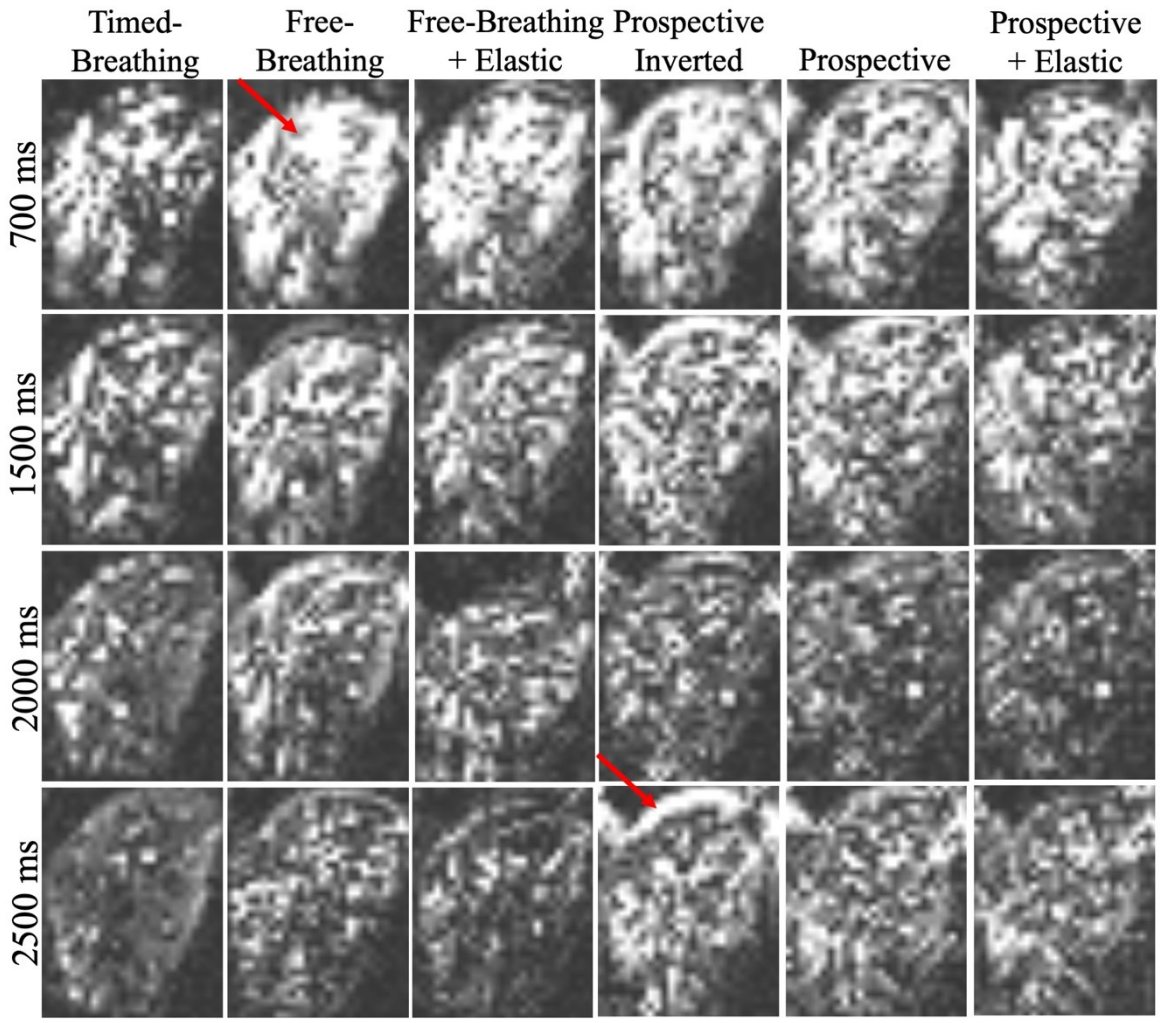

Figure 5.44: Reconstructed perfusion-weighted images (central slice) of an exemplary volunteer using the indicated techniques for compensation of motion related artifacts. Different PLDs are shown in different rows. Arrows indicate areas with distinct subtraction errors and blurred signals.

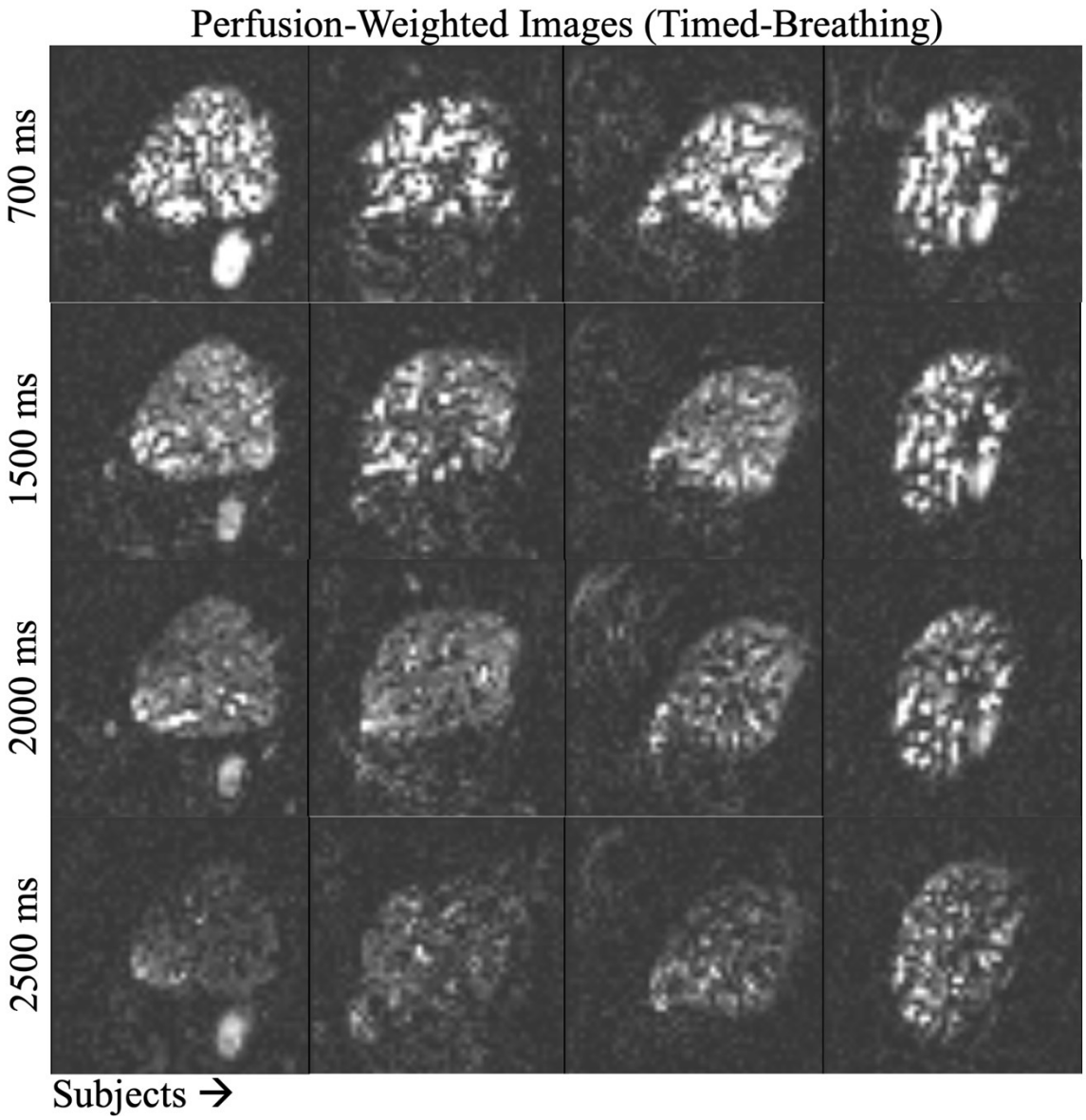

Figure 5.45: Comparison of perfusion-weighted images (central slice) for different PLDs (rows) using the timed-breathing approach. Columns show data from different subjects. The inflow from macrovascular to microvascular compartments clearly shows. In addition, relaxation of perfusion-weighted signal, due to increased T_1 decay, shows for later PLDs.

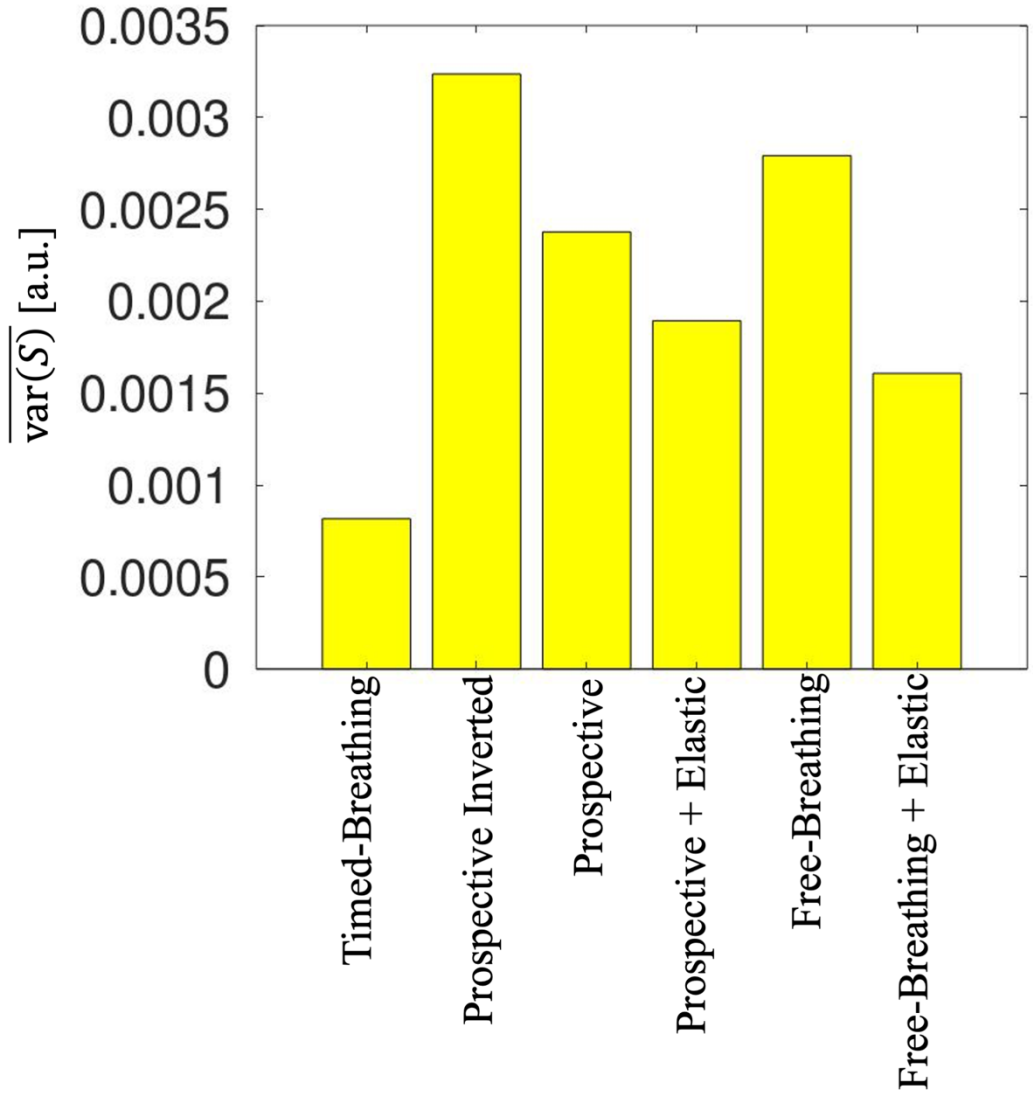

Figure 5.46: Calculated mean variance of individually subtracted perfusion-weighted images. Averaging was performed over the central four slices of all PLDs from all volunteers of this study.

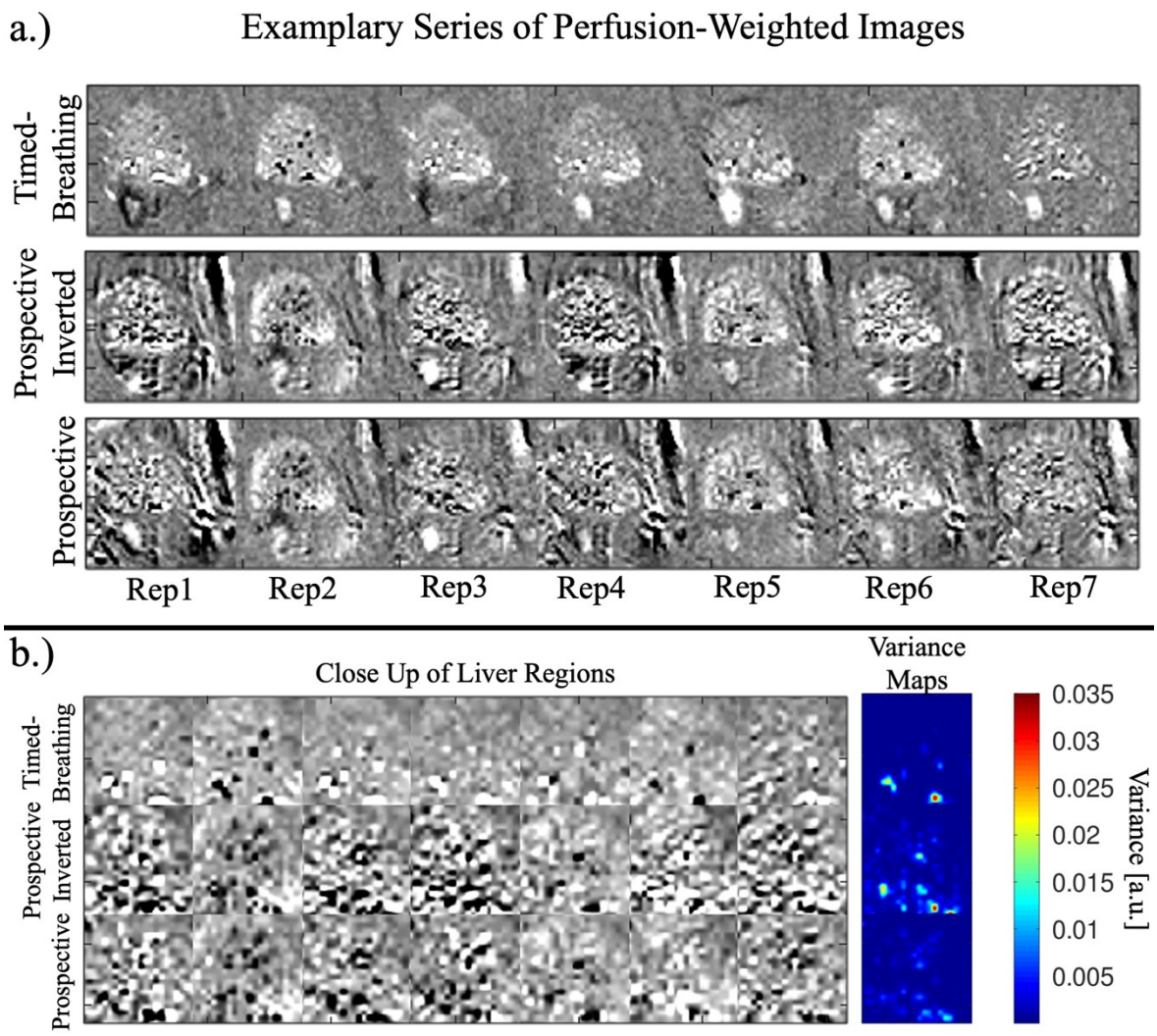

Figure 5.47: a.) Exemplary demonstration of the timeseries of subtraction images used for variance calculation as shown in Figure 5.46; and b.) Close ups of liver regions used to calculate the variance of the timeseries. The variance image shows some localized spots for the timed-breathing protocol, most likely corresponding to pulsation in larger vessels. In case of free-breathing, a larger image variance is distributed over the whole region of interest. The prospective technique allows a minor reduction of this value, corresponding to observations from Figure 5.46.

5.3.2.3 Discussion

The prospective motion correction technique achieved a significant reduction of cranial-caudal liver motion in acquired label/control 3D GRASE volumes. Different aspects of the experiments will be subsequently discussed.

Optimized fixed BS in Liver pCASL imaging

Calculated inversion timings for the timed-breathing protocol achieved comparable signal suppression for all PLDs (cf. Figure 5.36). The residual signal level was suitable for calculation of high-quality perfusion-weighted images of the human liver, as verified by Figure 5.45. However, minor chemical shift artifacts were still visible, which were also observed in the previous FAIR PASL study (cf. section 5.3.1). It is therefore likely, that a subject-specific T_1 estimate of fat together with knowledge about achieved inversion efficiency and efficiency of the spectral fat saturation would allow even better fat suppression in future work. Note that in contrast to the FAIR PASL study, the increased saturation of static tissue signal with inflow time was not observed here, manifesting the assumption that the long train of Q2Tips pulses saturated the static tissue in the PASL experiment. Using the prospective motion compensation, signal levels for later inflows appeared to be slightly higher. This is related to the fact that the navigator blocks additional time during the ASL preparation phase, and a poorer compromise for inversion timings was found when compared to the timed-breathing protocol. Higher amounts of residual static tissue signal were not directly predicted by the algorithm (cf. Table 5.9). It can therefore be concluded that the subject-specific liver T_1 might slightly differ from assumed values. Additional analysis by application of the developed adaptive BS technique could therefore be helpful in future studies. Increased amounts of residual fat using the prospective technique were however predicted by the optimized fixed BS algorithm and are visible in prospective images, especially in later PLDs. This might have an impact on achievable image quality in motion corrected data, which is discussed in a subsequent paragraph (“Quality of perfusion-weighted images”).

Quality of the EPI reference timeseries registration

The developed reference cycle registration technique allowed robust estimation of the liver’s trajectory, which was verified by visual inspection of resampled images (cf. Figure 5.37 and Figure 5.38). For some datasets, the estimated Δy shift was discarded. This did not significantly affect the visual correspondence of resampled EPI reference images, verifying the assumption that the major amount of translational motion showed in the cranial-caudal direction. The results indicate that the selected threshold MSE < 2 was suitable for the given task to identify the most agile region in the cranial-caudal direction

of the reference image series. This threshold should therefore be considered as a guideline value for future applications of the proposed algorithm.

Reliability of navigator matches during the pCASL experiments

The prospective technique allowed highly accurate estimation of the current liver position by the cross-correlation matching approach. This was verified by a strong decline in the estimated residual cranial-caudal motion in resampled navigators (cf. Figure 5.39 and Figure 5.40a). Except for subject eight, estimated mean standard deviations were below $\overline{\sigma_{\Delta z}}$ = ± 2 mm. These standard deviations were found to be suitably low for accurate motion compensation in single-shot 3D GRASE pCASL experiments with typical voxel sizes > 4 mm^3. The fact that no direct registration of navigator data for subject three was possible indicates the importance of a robust indirect solution for motion estimation in background suppressed pCASL imaging. Note that the accuracy of navigator matches should also be robust against temporal variation of the breathing cycle as long as a variety of liver positions were sampled by the reference series.

Prospective motion compensation in acquired 3D GRASE data

The accurate detection of motion states from the navigator data resulted in the expected reduction of cranial-caudal shifts in 3D GRASE images for all volunteers of this study (cf. Figure 5.40b, “Prospective Inverted”, “Prospective”). The mean standard deviation $\overline{\sigma_{\Delta z}}$ = ± 2.3 mm using prospective correction corresponds to a 57% decrease when compared to the prospective inverted value and was in the range of the voxel size of the single-shot 3D GRASE experiments, performed in this work (cf. Figure 5.40b, right). Depending on how much of the cranial-caudal motion shows as through-plane displacements, acquired data might therefore show corrupted most outer imaging slices, which usually are unusable due to residual aliasing, nonetheless. The proposed prospective technique is therefore found to be applicable to arbitrary positionings other than sagittal which should be further investigated in future studies. A high accuracy of position updates was also validated by the label/control data given in Figure 5.42. The fact that residual motion in 3D GRASE data was slightly higher than what was observed from the navigator data (cf. Figure 5.40a, left and Figure 5.40b, left) can be partly explained by the temporal gap of 160 ms between excitation of navigator and 3D GRASE volumes. A reduction of the temporal distance by

either decreasing the navigator resolution or the duration of Q2Tips pulses and the time needed for post-processing of navigator data is therefore likely to further reduce the residual fluctuation in 3D GRASE data. Second, residual motion was estimated from different parts of the liver. For the navigator series, vessel structures were chosen for registration, while the upper part of the liver was considered in case of 3D GRASE.

Prospective motion compensation of the saturation plane

Since residual motion in corrected saturation navigator data (cf. Figure 5.40a) was in the same range as for the imaging navigators, the accuracy of saturation updates should lie within the same range, which was observed for the 3D GRASE region ($\overline{\sigma_{\Delta z}}$ = ± 2.3 mm). It is even likely that position updates are more accurate for the saturation plane, due to a shorter temporal gap (no fat saturation and Q2Tips pulses).

Retrospective elastic motion compensation in acquired 3D GRASE data

Additional retrospective elastic image registration further reduced the mean standard deviation to levels of timed-breathing protocols ($\overline{\sigma_{\Delta z}}$ ≈ 2 mm), which holds for free-breathing as well as prospective data (cf. Figure 5.40b, "Timed-Breathing", "Free-Breathing + Elastic", "Prospective + Elastic"). Best motion compensation was achieved using prospective and elastic registration together. It must be mentioned that the elastic B-spline registration delivered poor results for some datasets with a PLD of 700 ms (data not shown), which was not surprising, because the macrovascular signal clearly differed between label and control volumes. It is therefore recommended to further improve the elastic registration of early PLDs in future work. In general, the combination of 2D prospective and retrospective motion correction was suitable for correction of cranial-caudal motion in liver pCASL imaging. Note that the reduction of cranial-caudal motion in free-breathing data using elastic image registration was only achievable due to the sagittal positioning and a large field of view in the in-plane direction. This way, the liver did not fully or partially leave the field of view, as it would happen in oblique positionings with a restricted number of image partitions or with restricted in-plane field-of-views, which require prospective solutions.

Quality of perfusion-weighted images

The visible alignment of acquired label and control images using prospective correction with additional elastic image registration (cf. Figure 5.42 and Figure 5.43) did not result in artifact-free perfusion-weighted images (cf. Figure 5.44). Although prominent subtraction errors were reduced and the inflow characteristics were recognized, residual artifacts impeded the perfusion information. This observation was in accordance with the calculated mean variance of the perfusion-weighted image series (cf. Figure 5.46). Mean variance could only be minorly improved by application of prospective correction and/or elastic image registration. That means that residual unwanted differences were still present in subtraction images.

One reason might be the non-ideal suppression of fat signal, as was already discussed. A possible solution would be the subject-specific estimation of T_1 ranges of fat as well as adaptive optimization of the spectral fat saturation pulse. Both preparations could then be integrated into an updated adaptive BS technique.

Another source of residual artifacts in perfusion-weighted images were shifts and deformations in the medial-lateral direction, which appear as through-plane motion in sagittal positioning (cf. Figure 5.42a, arrows). A possible straightforward solution would be an extension of the nonrigid image registration to 3D. This, in turn, would require the acquisition of an increased number of k-space partitions for each label/control volume, which would be achievable using either sophisticated parallel imaging techniques such as a Caipirinha (104) or segmented readouts. Here, a 3D GRASE PROPELLER trajectory might be a promising segmentation strategy due to the potential for additional retrospective motion compensation (54)(62).

The prospective technique also has room for improvements in future work. This includes substitution of the two-dimensional EPI navigator by a one-dimensional readout, which would decrease the temporal gap between navigator and the saturation/3D GRASE module. In fact, arbitrary signals which are correlated with the acquired EPI reference series will allow to recover the motion state throughout the ASL experiments if these signals show a distinct variation for each liver position. Therefore, another interesting approach would be to correlate estimated shifts from the EPI reference series with external signals coming from e.g., respiratory cushions. This would give access to the liver position at arbitrary timepoints during the sequence without the need for navigator readouts. This would also prevent saturation bands in perfusion-weighted images, which could arise if

sagittal navigators are combined with axial 3D GRASE readouts. Finally, shortening the time needed for navigator acquisition would also be beneficial for background suppression, because no additional constraints about pulse timings need to be considered.

Compatibility with perfusion quantification

This study had a strong focus on the quality of perfusion-weighted images using the prospective motion compensation technique. Therefore, perfusion quantification was beyond the scope of this work and no additional M_0 data was acquired. For accurate quantification, different runs of prospectively corrected M_0 and pCASL sequences need to share the same reference position information, which requires a synchronization between different runs of the sequence and thus an adapted implementation, which will be addressed in future work. An updated sequence could run the EPI reference scan only once for a specific subject at the beginning of the series of examinations. The first pCASL experiment would then define the reference position of the liver, which is also used for all subsequent scans.

In addition, the role of a potentially time dependent labeling efficiency should be further investigated. Current models assume a constant labeling efficiency (58). A potential time dependency could be assessed using the ASLIF technique as proposed by Günther (105).

Scan times

While a single measurement using the timed-breathing protocol took 2:20 minutes, the prospective measurement only took 1:24 minutes + 10 seconds for the initial acquisition of the reference series, resulting in a 33% decrease of total measurement time. This indicates the future potential of motion corrected free-breathing liver ASL imaging in terms of a reduction of measurement time.

Applicability to other organs

This work demonstrated a prospective method to correct the large cranial-caudal shifts of the liver throughout the breathing cycle. The technique can however also be readily applied to other abdominal organs. The most obvious transfer would be the application to free-

breathing measurements of the kidneys. As seen from Figure 5.38, the right kidney is directly located below the liver, which allows a quite similar experimental setup. In general, the prospective technique requires that the organ is suitably large to identify corresponding spatial cranial-caudal shifts in the EPI reference series. Application to brain ASL experiments could also be interesting. Here, the registration procedure of the EPI timeseries could be easier, but increased likelihood for additional random motion, which is not covered by the proposed technique, must be considered.

5.3.2.4 Conclusion

A prospective motion compensation technique with additional 2D elastic image registration, which allowed to reduce cranial-caudal shifts of the liver in sagittal free-breathing 3D GRASE pCASL to levels of a timed-breathing protocol, was successfully demonstrated. The prospective technique did not rely on residual liver signal in navigator images, and thus is compatible with background suppressed pCASL imaging. The prospective solution further enables free-breathing experiments using arbitrary positionings without the risk of losing information due to through-plane motion. Future work will focus on optimal fat suppression as well as improvements of the prospective and retrospective motion correction techniques and the 3D GRASE readout. This way, the proposed techniques might pave the way for robust free-breathing pCASL imaging of the human liver and other abdominal organs.

6 General Discussion and Future Work

Diseases like stroke, tumors or liver cirrhosis are accompanied by a change in tissue perfusion, making techniques for perfusion measurement a high clinical interest. Arterial spin labeling is a promising non-invasive alternative to other perfusion measurement techniques, such as dynamic susceptibility contrast and dynamic contrast enhanced imaging. However, the low intrinsic SNR of ASL is problematic, because many averages and long measurements times are usually required to generate a single perfusion-weighted image. This increases the likelihood of random motion and the sensitivity to respiratory motion during the scan. Sophisticated techniques for motion correction and a reliable reduction of static tissue signal prior to the data acquisition step are therefore mandatory for robust ASL imaging in brain and abdominal organs such as liver. The new methodological approaches in this work focused on increasing the robustness of ASL against random and respiratory motion and were validated in brain and liver imaging.

Background Suppression

This work introduced two novel optimization algorithms for calculation of background suppression-related inversion timings. Background suppression is a crucial component of ASL sequences to reduce the motion sensitivity by reducing the amount of static tissue magnetization in acquired label and control images. Standard background suppression (BS) techniques were designed to suppress a given range of T_1 values at a distinct timepoint (42)(43)(45). Usually, the nulling of static tissue is selected to occur a few milliseconds before application of the excitation pulse to prevent subtraction errors during the subsequent ASL image reconstruction. This, however, also allows short off-resonant fat components to recover some amount of magnetization, which might not be perfectly cancelled using spectral saturation techniques. If motion during the scan occurs, image registration can be applied to align the mismatched on-resonant static tissue. Unfortunately, this does not hold for the off-resonant fat. These non-aligned chemical shift artifacts are subsequently not cancelled out during the ASL subtraction step, resulting in artifacts in perfusion-weighted images. Therefore, the novel optimized fixed BS scheme was proposed to selectively reduce the magnetization of on-resonant static tissue signal of the organ of interest to small positive offsets, while simultaneously nulling unwanted T_1

components arising from fat (cf. section 4.1.2). The optimized BS scheme was applied to pCASL experiments in brain (cf. section 5.2.1) in a study with five healthy volunteers, and PASL as well as pCASL scans of the liver with one and eight healthy volunteers, respectively (cf. sections 5.3.1 and 5.3.2). The algorithm achieved sufficient suppression of fat in brain ASL imaging together with a spectral fat saturation pulse and thus allowed significant reduction of motion-related artifacts in combination with the applied 3DGP readout strategy and retrospective motion compensation techniques. A somewhat different picture emerged in liver ASL experiments. Here, residual signal from fat was clearly visible in reconstructed label and control images. Residual fat clearly affected the quality of perfusion-weighted liver images in combination with the prospective motion compensation technique. It was concluded that the accuracy of the underlying signal model was slightly decreased in abdominal experiments, and that spectral saturation is not as effective as in brain experiments. This can be mainly attributed to the fact that perfect saturation as well as inversion efficiencies were assumed in the optimized fixed BS scheme, which might not hold for the fat signal in abdominal imaging due to increased off-resonance. The latter could also drastically reduce the efficiency of the spectral fat saturation pulse if a fixed off-resonance for subcutaneous fat is assumed here.

Another major drawback of all BS related algorithms is the need for a-priori assumptions about the T_1 distribution in the region of interest. If operators are not familiar with the underlying algorithm or the specific organ, this could easily result in poor BS setups, which might not sufficiently reduce the static tissue magnetization and thus lead to poor image quality. A novel technique, which allows to incorporate the subject-specific T_1 distribution in the region of interest, was introduced in this work in terms of the adaptive BS algorithm. In contrast to the optimized fixed BS scheme and literature algorithms, the actual T_1 distribution is first estimated from a preceding M_0 scan and subsequently used to calculate optimal inversion timings to achieve a specific level of static tissue reduction (cf. section 4.1.3). The technique was validated in brain pCASL imaging using two healthy volunteers, and it showed that high-quality perfusion-weighted images could be reconstructed using two or more inversion pulses together with residual signal levels of 4% to 12% (cf. section 5.1.2). Future work should therefore focus on the application of the adaptive BS technique in studies with a larger number of subjects. In addition, application to abdominal organs is of high interest. As a minor drawback, the current implementation of the technique did not allow to recover the subject-specific T_1 value of off-resonant fat due to reduction of related signal in M_0 scans by the additional spectral saturation pulses.

This leads to possible future developments in the field of background suppression, which combine the benefits of both BS algorithms, which were proposed in this work.

In the future, a single adaptive solution could be applied, which addresses both, the complexity of current BS adjustments and the optimal suppression of fat in ASL experiments. Therefore, the on-resonant static tissue spectrum could first be measured by applying a selective excitation with subsequent Look-Locker readout (96) without further image encoding strategy. The major components of the measured signal evolution are subsequently fitted, and the procedure is repeated with a spatial-spectral excitation of the off-resonant fat signal or a combination of spectral saturation of on-resonant static tissue and subsequent excitation of off-resonant fat signal. This way, a subject-specific fat T_1 estimate could be obtained, which might allow more accurate prediction of the evolution of the fat signal. Depending on what kind of preparation scans were performed, the adaptive BS algorithm will adjust the timing of following ASL measurements, such that the on-resonant spectrum is reduced to an amount between 5% and 10% of its respective M_0 signal to prevent errors during magnitude image subtraction. In addition, measured or assumed fat T_1 will be targeted to 0%. The algorithm could then also recommend the number of inversion pulses which are needed for accurate background suppression in the current scenario. Finally, the algorithm can be combined with additional preparation scans, which e.g., estimate mean inversion efficiency of the BS pulses or optimal flip angles for the spectral fat saturation pulse. The resulting method could drastically simplify the setup of an ASL sequence, which would be especially helpful for operators or clinicians which do not have further knowledge about suitable setups for background suppression-related parameters. In addition, measured ASL data would always be perfectly suitable for potential additional retrospective motion correction techniques if desired. The discussed future development of the adaptive BS technique therefore is a promising step towards increased motion robustness of ASL and thus a step towards clinical reality.

3D GRASE PROPELLER

ASL in combination with 3D GRASE PROPELLER (3DGP) allows retrospective in-plane correction of rigid body motion (54). The accuracy of motion estimates however was restricted by the presence of rotated geometric distortion with each acquired brick (71). Therefore, this work introduced a novel reconstruction algorithm called 3DGP-JET, which allowed joint estimation of motion and geometric distortion from the acquired data,

without the need for additional reference scans (cf. section 4.2.2). The algorithm was successfully applied to brain pCASL imaging in combination with the optimized fixed BS technique in a study with five healthy volunteers (cf. section 5.2.1). It was shown that simultaneous estimation of in-plane motion and geometric distortion in brain ASL imaging is possible using the 3DGP-JET algorithm, which not only allowed to additionally correct for distortion-related signal smearing in final images, but also reduced fluctuation of motion estimates and thus increased the accuracy of the latter. It showed that the algorithm was most effective in case of slow intentional motion patterns, making it a promising solution for occasional random motion during clinical experiments. Application to data which was acquired under realistic scenarios should therefore be investigated in future studies. In addition, application to abdominal organs should be further investigated.

One aspect which was not addressed by the proposed 3DGP-JET algorithm is the question whether three-dimensional rigid body motion estimation and correction is possible using a 3DGP segmentation. It could have a positive impact on the SNR in perfusion-weighted images if data containing through-plane motion is corrected instead of filtered. To this aim, feasibility of three-dimensional rigid body correction using 3DGP was assessed by proposing a novel image space-based 3DGP-3D reconstruction algorithm (cf. section 4.2.3). The technique was validated as a proof of principle in pCASL scans with a healthy volunteer (cf. section 5.2.2). Successful application in terms of identified three-dimensional rotations and visual improvement of the quality of perfusion-weighted images was demonstrated. A potential drawback of the approach was the neglection of geometric distortion, resulting in systematic fluctuation of estimated motion parameters.

Potential areas of future developments using 3DGP segmentation in ASL imaging arise from the previous discussions of experiments. Successful identification of three-dimensional motion trajectories motivates the extension of the 3DGP-JET algorithm to include a six-parameter rigid body motion model. This would allow to estimate and correct through-plane motion, without the influence of geometric distortion on estimated motion parameters. However, the full potential of the 3DGP technique will most likely only be achieved when combining the retrospective 3DGP-JET routine with a prospective technique, which aims for alignment of saturation and imaging plane in the through-plane direction, prior to the data acquisition step. This follows from the fact that potential spin history artifacts, arising from mismatches between saturation and image excitation, cannot be corrected retrospectively during the 3DGP reconstruction. Using e.g., orthogonal fat navigators (97) for prospective correction of these mismatches during the scan in addition

to a 3DGP-JET routine with three-dimensional rigid body correction is a promising approach for increased motion robustness in segmented ASL imaging. Such prospective fat navigation would however require that the fat and the organ show the same motion. While this assumption might be reasonable in brain ASL imaging, further analysis in this thesis demonstrated that abdominal fat moves differently when compared to e.g., the liver and adapted solutions, as presented in section 4.3.3., might be needed. Finally, a 3DGP-JET reconstruction with additional prospective sequence adaption could also allow to recover time dependent field maps from small subsets of bricks since the timepoints of motion are known. This might allow to investigate changes in off-resonance induced by motion during the scan. Note that a perfect suppression of off-resonant fat would be needed, especially if the 3DGP-JET technique is applied to abdominal organs. Therefore, a combination of a prospective 3DGP-JET algorithm with the previously described extended adaptive BS technique would have the potential to be highly effective against low-frequent and high-frequent rigid body motion during experiments and will be further investigated in future work. Finally, compensation of non-rigid motion might also be achievable in 3DGP imaging and future studies are recommended.

Compensation of Respiratory Motion

While sophisticated background suppression and retrospective motion correction are most effective in case of slow drifts or low-frequent random motion, respiratory motion can be a major challenge in abdominal ASL imaging. Among all abdominal organs, liver is most affected, due to the proximity to the lungs. The respiratory motion leads to large cranial-caudal shifts of the liver throughout the long ASL scans and is high-frequent in its pattern. In liver ASL imaging, breathing motion is therefore typically tackled by timed-breathing protocols, which are uncomfortable for subjects and increase the scan time when compared to free-breathing examinations.

This work presented novel methods, which were especially designed for compensation of the high-frequent respiratory motion in abdominal liver ASL imaging. First, an extension of timed-breathing protocols was proposed, which aims to improve the comfort during liver ASL examinations using automatic multi-breathhold detection (cf. section 4.3.2). Feasibility of the developed technique was demonstrated in liver FAIR PASL scans of a healthy volunteer as a proof of principle. The proposed multi-breathhold method achieved significant reduction of motion artifacts in perfusion-weighted images of the liver.

However, scan times using multi-breathhold detection might be even longer when compared to a strict timed-breathing protocol, which might be a limiting factor for the application in clinical reality. Future work should therefore compare multi-breathhold detection with timed-breathing protocols in terms of scan time and subject comfort during scans.

To overcome the need for breathholds or strict breathing patterns, a novel prospective motion compensation technique, using additional EPI navigators during a pCASL scan, was proposed. Instead of directly registering acquired navigator images, corresponding data were matched to a series of EPI reference images, which were acquired prior to the pCASL experiment. This way, strong background suppression could be applied, because no signal coming from the liver was required in acquired navigator data. By calculating the maximum correlation between navigator and reference series, an estimated of the current liver position was sent to the sequence and the position of saturation plane as well as 3D GRASE image module was updated accordingly (cf. section 4.3.3). The technique was evaluated in a pCASL study with eight healthy volunteers in combination with the optimized fixed BS scheme and achieved significant reduction of the livers cranial-caudal shift during free-breathing examinations (cf. section 5.3.2). However, the quality of perfusion-weighted images using the prospective method was not as high as the image quality when using timed-breathing protocols. This was mainly related to non-ideal fat suppression in addition to a large temporal gap of about 160 ms between navigator and image readout as well as additional three-dimensional deformations of the liver, which were not addressed using the prospective technique.

Conclusions about future work in the field of motion compensation in abdominal ASL imaging, especially liver ASL imaging, can be drawn from the work of this thesis. As a first step, the correlation of calculated shifts from the reference times series with external signals should be investigated. This would remove the need for additional navigators during the ASL sequence and would allow to access the current liver position at arbitrary timepoints during the sequence within a few milliseconds, while simultaneously removing constraints in the timing of background suppression related inversion pulses. Therefore, the external signal from e.g., a respiratory cushion should be stored during acquisition of the reference series. After image registration, each signal value would then be assigned a specific shift from the lookup table. This approach would also remove the need for residual abdominal fat signal in navigator images, which most likely improves and simplifies the image registration procedure, especially in smaller abdominal organs. By inserting

additional pulses, which saturate signal from unwanted abdominal regions, the robustness of the navigator registration could possibly be greatly improved. In addition, a hybrid approach between triggering and prospective motion correction could be investigated in following experiments, which could potentially reduce the amount of elastic deformation, which needs to be retrospectively corrected. The idea would be to estimate the average duration of the breathing cycle from the acquired data and to trigger the initial saturation such that the image readout occurs during exhaled phases (cf. Figure 6.1). Residual deviations in the positioning are then corrected by the prospective motion compensation technique.

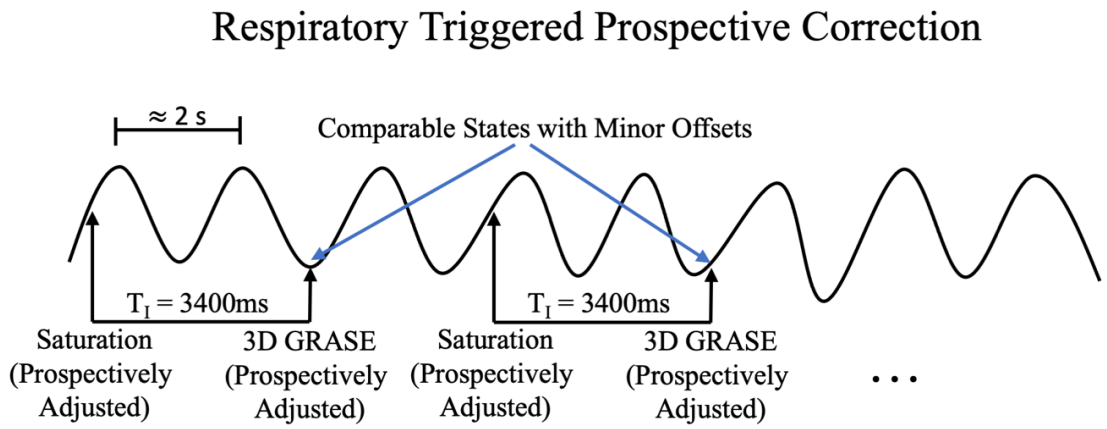

Figure 6.1: Concept of hybrid triggering and prospective compensation of respiratory motion. The sequence timing is adjusted based on the desired inflow time *TI* and an estimate of the average duration of the breathing cycle. This way, it is likely that the image readout occurs in the exhaled phase. Residual offsets in the position are nevertheless corrected by the prospective technique.

Finally, a combination with the 3DGP readout as discussed in the previous paragraph or parallel imaging techniques would potentially allow to increase the number of acquired partitions within a single shot. This, in turn, could allow to apply three-dimensional retrospective motion correction algorithms to compensate for residual elastic deformations of the liver or other abdominal organs.

Conclusion

Motion is one of the major remaining challenges of ASL in clinical routine. This work presented a variety of novel methods for compensation of motion-related artifacts in

perfusion-weighted ASL images. Novel approaches for background suppression, in terms of the optimized fixed BS scheme and the adaptive BS algorithm, were first introduced and their feasibility was demonstrated in brain and liver ASL imaging. Retrospective motion in-plane rigid body correction with additional estimation of geometric distortion in segmented 3D GRASE ASL imaging was further demonstrated in brain ASL imaging using a 3D GRASE PROPELLER readout with JET reconstruction. In addition, the feasibility of estimation and correction of three-dimensional rigid body motion in brain imaging was shown. Finally, the problem of respiratory motion in liver ASL imaging was tackled by the multi-breathhold approach and the prospective navigator matching technique.

The novel techniques provide solutions for different kinds of motion during ASL scans. Thus, presented work is of high value for the reduction of motion sensitivity of ASL sequences in different organs or scenarios. By combining different ideas from this thesis, ASL could finally become a robust candidate for substitution of contrast agent-based perfusion measurements in clinical reality.

List of Figures

List of tables

Bibliography

1. OpenStax College. Anatomy & physiology. OpenStax; 2013.

2. Zaharchuk G. Arterial spin-labeled perfusion imaging in acute ischemic stroke. Stroke 2014;45:1202–1207 doi: 10.1161/STROKEAHA.113.003612.

3. Wolk DA, Detre JA. Arterial spin labeling MRI: An emerging biomarker for Alzheimer's disease and other neurodegenerative conditions. Curr. Opin. Neurol. 2012;25:421–428 doi: 10.1097/WCO.0b013e328354ff0a.

4. Van Beers BE, Leconte I, Materne R, Smith AM, Jamart J, Horsmans Y. Hepatic Perfusion Parameters in Chronic Liver Disease. Am. J. Roentgenol. 2001;176:667–673 doi: 10.2214/ajr.176.3.1760667.

5. Lassen NA, Ingvar DH. The blood flow of the cerebral cortex determined by radioactive krypton85. Experientia 1961;17:42–43 doi: 10.1007/BF02157946.

6. Ollinger JM, Fessler JA. Positron-emission tomography. IEEE Signal Process. Mag. 1997;14:43–55 doi: 10.1109/79.560323.

7. LAUTERBUR PC. Image Formation by Induced Local Interactions: Examples Employing Nuclear Magnetic Resonance. Nature 1973;242:190–191 doi: 10.1038/242190a0.

8. Edward M, Quinn J, Mukherjee S, et al. Gadodiamide contrast agent 'activates' fibroblasts: a possible cause of nephrogenic systemic fibrosis. J. Pathol. 2008;214:584–593 doi: 10.1002/path.2311.

9. Detre JA, Leigh JS, Williams DS, Koretsky AP. Perfusion imaging. Magn. Reson. Med. 1992;23:37–45 doi: 10.1002/mrm.1910230106.

10. Thamm T, Zweynert S, Piper SK, et al. Diagnostic and prognostic benefit of arterial spin labeling in subacute stroke. Brain Behav. 2019;9:e01271 doi: 10.1002/brb3.1271.

11. Pan X, Qian T, Fernandez-Seara MA, et al. Quantification of liver perfusion using multidelay pseudocontinuous arterial spin labeling. J. Magn. Reson. Imaging 2016;43:1046–1054 doi: 10.1002/jmri.25070.

12. Do RKG, Rusinek H, Taouli B. Dynamic Contrast-Enhanced MR Imaging of the Liver: Current Status and Future Directions. Magn. Reson. Imaging Clin. N. Am. 2009;17:339–349 doi: 10.1016/j.mric.2009.01.009.

13. Schuppan D, Afdhal NH. Liver cirrhosis. Lancet 2008;371:838–851 doi: 10.1016/S0140-6736(08)60383-9.

14. Faivre J, Forman D, Estève J, Obradovic M, Sant M. Survival of patients with primary liver cancer, pancreatic cancer and biliary tract cancer in Europe. Eur. J. Cancer 1998;34:2184–2190 doi: 10.1016/S0959-8049(98)00330-X.

15. Fujima N, Kudo K, Yoshida D, et al. Arterial Spin labeling to determine tumor viability in head and neck cancer before and after treatment. J. Magn. Reson. Imaging 2014;40:920–928 doi: 10.1002/jmri.24421.

16. Davis FG, Freels S, Grutsch J, Barlas S, Brem S. Survival rates in patients with primary malignant brain tumors stratified by patient age and tumor histological type: an analysis based on Surveillance, Epidemiology, and End Results (SEER) data, 1973–1991. J. Neurosurg. 1998;88:1–10 doi: 10.3171/jns.1998.88.1.0001.

17. Lautt WW. Hepatic Circulation. Colloq. Ser. Integr. Syst. Physiol. From Mol. to Funct. 2009;1:1–174 doi: 10.4199/C00004ED1V01Y200910ISP001.

18. Bernstein MA, King KF, Zhou XJ. Handbook of MRI Pulse Sequences. Elsevier Academic Press; 2004. doi: 10.1016/B978-0-12-092861-3.X5000-6.

19. Kety SS, Schmidt CF. THE DETERMINATION OF CEREBRAL BLOOD FLOW IN MAN BY THE USE OF NITROUS OXIDE IN LOW CONCENTRATIONS. Am. J. Physiol. Content 1945;143:53–66 doi: 10.1152/ajplegacy.1945.143.1.53.

20. Lee JJ, Powers WJ, Faulkner CB, Boyle PJ, Derdeyn CP. The Kety-Schmidt Technique for Quantitative Perfusion and Oxygen Metabolism Measurements in the MR Imaging Environment. Am. J. Neuroradiol. 2013;34:E100–E102 doi: 10.3174/ajnr.A3270.

21. Villringer A, Rosen BR, Belliveau JW, et al. Dynamic imaging with lanthanide chelates in normal brain: Contrast due to magnetic susceptibility effects. Magn. Reson. Med. 1988;6:164–174 doi: 10.1002/mrm.1910060205.

22. Aronhime S, Calcagno C, Jajamovich GH, et al. DCE-MRI of the liver: Effect of linear and nonlinear conversions on hepatic perfusion quantification and reproducibility. J. Magn. Reson. Imaging 2014;40:90–98 doi: 10.1002/jmri.24341.

23. Jajamovich GH, Calcagno C, Dyvorne HA, Rusinek H, Taouli B. DCE-MRI of the Liver: Reconstruction of the Arterial Input Function Using a Low Dose Pre-Bolus Contrast Injection Hoffmann A-C, editor. PLoS One 2014;9:e115667 doi: 10.1371/journal.pone.0115667.

24. Schieda N, Blaichman JI, Costa AF, et al. Gadolinium-Based Contrast Agents in Kidney Disease: A Comprehensive Review and Clinical Practice Guideline Issued by the Canadian Association of Radiologists. Can. J. Kidney Heal. Dis. 2018;5:205435811877857 doi: 10.1177/2054358118778573.

25. Kanda T, Fukusato T, Matsuda M, et al. Gadolinium-based contrast agent accumulates in the brain even in subjects without severe renal dysfunction: Evaluation of autopsy brain specimens with inductively coupled plasma mass spectroscopy. Radiology 2015;276:228–232 doi: 10.1148/radiol.2015142690.

26. McDonald RJ, McDonald JS, Kallmes DF, et al. Intracranial gadolinium deposition after contrast-enhanced MR imaging. Radiology 2015;275:772–782 doi: 10.1148/radiol.15150025.

27. Gulani V, Calamante F, Shellock FG, Kanal E, Reeder SB. Gadolinium deposition in the brain: summary of evidence and recommendations. Lancet Neurol. 2017;16:564–570 doi: 10.1016/S1474-4422(17)30158-8.

28. Liang, Zhi-Pei; Lauterbur PC. Principles of Magnetic Resonance Imaging: A Signal Processing Perspective. IEEE Press Series on Biomedical Engineering; 2000.

29. Hanson LG. Is quantum mechanics necessary for understanding magnetic resonance? Concepts Magn. Reson. Part A 2008;32A:329–340 doi: 10.1002/cmr.a.20123.

30. Griffiths DJ, Harris EG. Introduction to Quantum Mechanics. Pearson Prentice Hall; 1995. doi: 10.1119/1.18098.

31. Gruber B, Froeling M, Leiner T, Klomp DWJ. RF coils: A practical guide for nonphysicists. J. Magn. Reson. Imaging 2018;48:590–604 doi: 10.1002/jmri.26187.

32. Chavhan GB, Babyn PS, Thomas B, Shroff MM, Haacke EM. Principles, Techniques, and Applications of T2*-based MR Imaging and Its Special Applications. RadioGraphics 2009;29:1433–1449 doi: 10.1148/rg.295095034.

33. Yongbi MN, Branch CA, Helpern JA. Perfusion imaging using FOCI RF pulses. Magn. Reson. Med. 1998;40:938–943 doi: 10.1002/mrm.1910400622.

34. Ordidge RJ, Wylezinska M, Hugg JW, Butterworth E, Franconi F. Frequency offset corrected inversion (FOCI) pulses for use in localized spectroscopy. Magn. Reson. Med. 1996;36:562–566 doi: 10.1002/mrm.1910360410.

35. Payne GS, Leach MO. Implementation and evaluation of frequency offset corrected inversion (FOCI) pulses on a clinical MR system. Magn. Reson. Med. 1997;38:828–833 doi: 10.1002/mrm.1910380520.

36. Dixon WT, Du LN, Faul DD, Gado M, Rossnick S. Projection angiograms of blood labeled by adiabatic fast passage. Magn. Reson. Med. 1986;3:454–462 doi: 10.1002/mrm.1910030311.

37. Alsop DC, Detre JA, Golay X, et al. Recommended implementation of arterial spin-labeled Perfusion mri for clinical applications: A consensus of the ISMRM Perfusion Study group and the European consortium for ASL in dementia. Magn. Reson. Med. 2015;73:102–116 doi: 10.1002/mrm.25197.

38. Edelman RR, Siewert B, Darby DG, et al. Qualitative mapping of cerebral blood flow and functional localization with echo-planar MR imaging and signal targeting with alternating radio frequency. Radiology 1994;192:513–520 doi: 10.1148/radiology.192.2.8029425.

39. Knutsson L, Xu J, Ahlgren A, van Zijl PC. CEST, ASL, and magnetization transfer contrast: How similar pulse sequences detect different phenomena. Magn. Reson. Med. 2018;80:1320–1340 doi: 10.1002/mrm.27341.

40. Alsop DC, Detre JA. Multisection cerebral blood flow MR imaging with continuous arterial spin labeling. Radiology 1998;208:410–416 doi: 10.1148/radiology.208.2.9680569.

41. Dai W, Garcia D, de Bazelaire C, Alsop DC. Continuous flow-driven inversion for arterial spin labeling using pulsed radio frequency and gradient fields. Magn. Reson. Med. 2008;60:1488–1497 doi: 10.1002/mrm.21790.

42. Mani S, Pauly J, Conolly S, Meyer C, Nishimura D. Background suppression with multiple inversion recovery nulling: Applications to projective angiography. Magn. Reson. Med. 1997;37:898–905 doi: 10.1002/mrm.1910370615.

43. Günther M, Oshio K, Feinberg DA. Single-shot 3D imaging techniques improve arterial spin labeling perfusion measurements. Magn. Reson. Med. 2005;54:491–498 doi: 10.1002/mrm.20580.

44. Garcia DM, Duhamel G, Alsop DC. Efficiency of inversion pulses for background suppressed arterial spin labeling. Magn. Reson. Med. 2005;54:366–372 doi: 10.1002/mrm.20556.

45. Maleki N, Dai W, Alsop DC. Optimization of background suppression for arterial spin labeling perfusion imaging. Magn. Reson. Mater. Physics, Biol. Med. 2012;25:127–133 doi: 10.1007/s10334-011-0286-3.

46. Dietrich O, Raya JG, Reeder SB, Reiser MF, Schoenberg SO. Measurement of signal-to-noise ratios in MR images: Influence of multichannel coils, parallel imaging, and reconstruction filters. J. Magn. Reson. Imaging 2007;26:375–385 doi: 10.1002/jmri.20969.

47. Mansfield P. Multi-planar image formation using NMR spin echoes. J. Phys. C Solid State Phys. 1977;10:L55–L58 doi: 10.1088/0022-3719/10/3/004.

48. Hoge WS, Tan H, Kraft RA. Robust EPI Nyquist ghost elimination via spatial and temporal encoding. Magn. Reson. Med. 2010;64:1781–1791 doi: 10.1002/mrm.22564.

49. Xiang Q-S, Ye FQ. Correction for geometric distortion and N/2 ghosting in EPI by phase labeling for additional coordinate encoding (PLACE). Magn. Reson. Med. 2007;57:731–741 doi: 10.1002/mrm.21187.

50. Andersson JLR, Skare S, Ashburner J. How to correct susceptibility distortions in spin-echo echo-planar images: application to diffusion tensor imaging. Neuroimage 2003;20:870–888 doi: 10.1016/S1053-8119(03)00336-7.

51. Hennig J. Multiecho imaging sequences with low refocusing flip angles. J. Magn. Reson. 1988;78:397–407 doi: 10.1016/0022-2364(88)90128-X.

52. Andre JB, Bresnahan BW, Mossa-Basha M, et al. Toward quantifying the prevalence, severity, and cost associated with patient motion during clinical MR examinations. J. Am. Coll. Radiol. 2015;12:689–695 doi: 10.1016/j.jacr.2015.03.007.

53. Uecker M, Lai P, Murphy MJ, et al. ESPIRiT-an eigenvalue approach to autocalibrating parallel MRI: Where SENSE meets GRAPPA. Magn. Reson. Med. 2014;71:990–1001 doi: 10.1002/mrm.24751.

54. Tan H, Hoge WS, Hamilton CA, Günther M, Kraft RA. 3D GRASE PROPELLER: Improved image acquisition technique for arterial spin labeling perfusion imaging. Magn. Reson. Med. 2011;66:168–173 doi: 10.1002/mrm.22768.

55. Pipe JG. Motion correction with PROPELLER MRI: Application to head motion and free-breathing cardiac imaging. Magn. Reson. Med. 1999;42:963–969 doi: 10.1002/(SICI)1522-2594(199911)42:5<963::AID-MRM17>3.0.CO;2-L.

56. Stöcker T, Vahedipour K, Pflugfelder D, Shah NJ. High-performance computing MRI simulations. Magn. Reson. Med. 2010;64:186–193 doi: 10.1002/mrm.22406.

57. Hoinkiss DC, Erhard P, Breutigam N-J, von Samson-Himmelstjerna F, Günther M, Porter DA. Prospective motion correction in functional MRI using simultaneous multislice imaging and multislice-to-volume image registration. Neuroimage 2019;200:159–173 doi: 10.1016/j.neuroimage.2019.06.042.

58. Martirosian P, Pohmann R, Schraml C, et al. Spatial-temporal perfusion patterns of the human liver assessed by pseudo-continuous arterial spin labeling MRI. Z. Med. Phys. 2019;29:173–183 doi: 10.1016/j.zemedi.2018.08.004.

59. Matakos A, Balter JM, Cao Y. A Robust Method for Estimating B0 Inhomogeneity Field in the Liver by Mitigating Fat Signals and Phase-Wrapping. Tomography 2017;3:79–88 doi: 10.18383/j.tom.2017.00003.

60. Huber J, Hoinkiss DC, Günther M. Robust Implementation of a 3D Pulsed ASL Sequence for Assessment of Liver Perfusion. In: Proceedings of the 29th Annual Meeting of the International Society for Magnetic Resonance in Medicine. Virtual Conference; 2021.

61. Huber J, Hoinkiss DC, Günther M. Joint Estimation and Correction of Motion and Geometric Distortion in segmented Arterial Spin Labeling Perfusion Imaging. In: Proceedings of the 29th Annual Meeting of the International Society for Magnetic Resonance in Medicine. Virtual Conference; 2021.

62. Huber J, Hoinkiss DC, Günther M. Joint estimation and correction of motion and geometric distortion in segmented arterial spin labeling. Magn. Reson. Med. 2021 doi: 10.1002/mrm.29083.

63. Gold GE, Han E, Stainsby J, Wright G, Brittain J, Beaulieu C. Musculoskeletal MRI at 3.0 T: Relaxation times and image contrast. Am. J. Roentgenol. 2004;183:343–351 doi: 10.2214/ajr.183.2.1830343.

64. Huber J, Hoinkiss D, Günther M. Subject-Specific Background Suppression in 3D Pseudo-Continuous Arterial Spin Labeling Perfusion Imaging. In: Proceedings of the 28th Annual Meeting of the International Society for Magnetic Resonance in Medicine. Paris; 2020.

65. Huber J, Hoinkiss DC, Günther M. Adaptive Adjustment of Background Suppression in Pseudo-Continuous Arterial Spin Labeling. In: Proceedings of the 37th Annual Scientific Meeting of the European Society of Magnetic Resonance in Medicine and Biology. Virtual Conference; 2021.

66. Guennebaud G, Jacob B. Eigen Library. https://eigen.tuxfamily.org/. Accessed February 3, 2022.

67. Kellman P, Xue H, Chow K, Spottiswoode BS, Arai AE, Thompson RB. Optimized saturation recovery protocols for T1-mapping in the heart: influence of sampling strategies on precision. J. Cardiovasc. Magn. Reson. 2014;16:55 doi: 10.1186/s12968-014-0055-3.

68. Mutsaerts HJMM, Petr J, Groot P, et al. ExploreASL: An image processing pipeline for multi-center ASL perfusion MRI studies. Neuroimage 2020;219:117031 doi: 10.1016/j.neuroimage.2020.117031.

69. Wang Z. Improving cerebral blood flow quantification for arterial spin labeled perfusion MRI by removing residual motion artifacts and global signal fluctuations. Magn. Reson. Imaging 2012;30:1409–1415 doi: 10.1016/j.mri.2012.05.004.

70. Beatty PJ, Nishimura DG, Pauly JM. Rapid gridding reconstruction with a minimal oversampling ratio. IEEE Trans. Med. Imaging 2005;24:799–808 doi: 10.1109/TMI.2005.848376.

71. Huber J, Vicari M, Günther M. Motion Robust Distortion-Free Arterial Spin Labeling. In: Proceedings of the 27th Annual Meeting of the International Society for Magnetic Resonance in Medicine. Montreal; 2019.

72. Huber J, Hoinkiss DC, Vicari M, Günther M, Wilke R. 3D Rigid Body Motion Correction in ASL Perfusion Imaging using 3D GRASE PROPELLER. In: Proceedings of the 36th Annual Scientific Meeting of the European Society of Magnetic Resonance in Medicine and Biology. Rotterdam; 2019.

73. Skare S, Andersson J, Bammer R. Calibration free distortion correction for propeller EPI. In: Proceedings of the 16th Annual Meeting of the International Society for Magnetic Resonance in Medicine. Vol. Toronto. Toronto; 2008. p. 417.

74. Uecker M, Hohage T, Block KT, Frahm J. Image reconstruction by regularized nonlinear inversion - Joint estimation of coil sensitivities and image content. Magn. Reson. Med. 2008;60:674–682 doi: 10.1002/mrm.21691.

75. Walsh DO, Gmitro AF, Marcellin MW. Adaptive reconstruction of phased array MR imagery. Magn. Reson. Med. 2000;43:682–690 doi: 10.1002/(SICI)1522-2594(200005)43:5<682::AID-MRM10>3.0.CO;2-G.

76. Mccormick M, Liu X, Jomier J, Marion C, Ibanez L. Itk: Enabling reproducible research and open science. Front. Neuroinform. 2014;8:13 doi: 10.3389/fninf.2014.00013.

77. Hansen MS, Sørensen TS. Gadgetron: An open source framework for medical image reconstruction. Magn. Reson. Med. 2013;69:1768–1776 doi: 10.1002/mrm.24389.

78. Yancey SE, Rotenberg DJ, Tam F, et al. Spin-history artifact during functional MRI: Potential for adaptive correction. Med. Phys. 2011;38:4634–4646 doi: 10.1118/1.3583814.

79. Cheng H, Puce A. Reducing respiratory effect in motion correction for EPI images with sequential slice acquisition order. J. Neurosci. Methods 2014;227:83–89 doi: 10.1016/j.jneumeth.2014.02.007.

80. Kino A, Takahashi M, Ashiku SK, Decamp MM, Lenkinski RE, Hatabu H. Optimal breathing protocol for dynamic contrast-enhanced MRI of solitary pulmonary nodules at 3T. Eur. J. Radiol. 2007;64:397–400 doi: 10.1016/j.ejrad.2007.08.014.

81. Huber J, Hoinkiss DC, Günther M. A Prospective Motion Correction Algorithm Suitable for pCASL Imaging of the Moving Liver. In: Proceedings of the 37th Annual Scientific Meeting of the European Society of Magnetic Resonance in Medicine and Biology. Virtual Conference; 2021.

82. Rohlfing T, Maurer CR, O'Dell WG, Zhong J. Modeling liver motion and deformation during the respiratory cycle using intensity-based nonrigid registration of gated MR images. Med. Phys. 2004;31:427–432 doi: 10.1118/1.1644513.

83. Nguyen TD, Spincemaille P, Prince MR, Wang Y. Cardiac fat navigator-gated steady-state free precession 3D magnetic resonance angiography of coronary arteries. Magn. Reson. Med. 2006;56:210–215 doi: 10.1002/mrm.20938.

84. Stanisz GJ, Odrobina EE, Pun J, et al. T1, T2 relaxation and magnetization transfer in tissue at 3T. Magn. Reson. Med. 2005;54:507–512 doi: 10.1002/mrm.20605.

85. Zhang B, Wang K, Jiang T. RF power design optimization in MRI system. Magn. Reson. Lett. 2021;1:89–98 doi: 10.1016/j.mrl.2021.100006.

86. Sengupta A, Gupta RK, Singh A. Evaluation of B1 inhomogeneity effect on DCE-MRI data analysis of brain tumor patients at 3T. J. Transl. Med. 2017;15:242 doi: 10.1186/s12967-017-1349-7.

87. Wansapura JP, Holland SK, Dunn RS, Ball WS. NMR relaxation times in the human brain at 3.0 Tesla. J. Magn. Reson. Imaging 1999;9:531–538 doi: 10.1002/(SICI)1522-2586(199904)9:4<531::AID-JMRI4>3.0.CO;2-L.

88. Zhu DC, Penn RD. Full-brainT1 mapping through inversion recovery fast spin echo imaging with time-efficient slice ordering. Magn. Reson. Med. 2005;54:725–731 doi: 10.1002/mrm.20602.

89. Werz K, Braun H, Vitha D, et al. T1-, T2- und T2*-Relaxationswerte von Äpfeln, Birnen, Zitrusfrüchten und Kartoffeln im Vergleich zu menschlichen Geweben. Z. Med. Phys. 2011;21:206–215 doi: 10.1016/j.zemedi.2010.12.006.

90. Henkelman RM, Stanisz GJ, Graham SJ. Magnetization transfer in MRI: a review. NMR Biomed. 2001;14:57–64 doi: 10.1002/nbm.683.

91. De Vita E, Günther M, Golay X, Thomas DL. Magnetisation transfer effects of Q2TIPS pulses in ASL. Magn. Reson. Mater. Physics, Biol. Med. 2012;25:113–126 doi: 10.1007/s10334-011-0298-z.

92. Petr J, Schramm G, Hofheinz F, Maus J, van den Hoff J. Estimating the influence of magnetization transfer effects on cerebral blood flow quantification in pseudo-continuous arterial spin labeling. In: Proceedings of the 23rd Annual Meeting of the International Society for Magnetic Resonance in Medicine. Milan; 2014.

93. Bley TA, Wieben O, François CJ, Brittain JH, Reeder SB. Fat and water magnetic resonance imaging. J. Magn. Reson. Imaging 2010;31:4–18 doi: 10.1002/jmri.21895.

94. Pinto J, Chappell MA, Okell TW, et al. Calibration of arterial spin labeling data—potential pitfalls in post-processing. Magn. Reson. Med. 2020;83:1222–1234 doi: 10.1002/mrm.28000.

95. Deichmann R, Haase A. Quantification of T1 values by SNAPSHOT-FLASH NMR imaging. J. Magn. Reson. 1992;96:608–612 doi: 10.1016/0022-2364(92)90347-A.

96. Nacif MS, Turkbey EB, Gai N, et al. Myocardial T1 mapping with MRI: Comparison of look-locker and MOLLI sequences. J. Magn. Reson. Imaging 2011;34:1367–1373 doi: 10.1002/jmri.22753.

97. Skare S, Hartwig A, Mårtensson M, Avventi E, Engström M. Properties of a 2D fat navigator for prospective image domain correction of nodding motion in brain MRI. Magn. Reson. Med. 2015;73:1110–1119 doi: 10.1002/mrm.25234.

98. Martirosian P, Kühn B, Weiss J, et al. 3D Arterial Spin Labeling Imaging of Arterial and Portal-Venous Perfusion in Human Liver at 3 Tesla under Free Breathing: Preliminary Results. In: Proc. Intl. Soc. Mag. Reson. Med. 27. Montreal; 2019.

99. Cai W, Li F, Wang J, et al. A comparison of arterial spin labeling perfusion MRI and DCE-MRI in human prostate cancer. NMR Biomed. 2014;27:817–825 doi: 10.1002/nbm.3124.

100. Buchbender S, Obenauer S, Mohrmann S, et al. Arterial spin labelling perfusion MRI of breast cancer using FAIR TrueFISP: Initial results. Clin. Radiol. 2013;68:e123–e127 doi: 10.1016/j.crad.2012.10.011.

101. de Bazelaire CMJ, Duhamel GD, Rofsky NM, Alsop DC. MR Imaging Relaxation Times of Abdominal and Pelvic Tissues Measured in Vivo at 3.0 T: Preliminary Results. Radiology 2004;230:652–659 doi: 10.1148/radiol.2303021331.

102. NOGUCHI T, NISHIHARA M, HARA Y, et al. A Technical Perspective for Understanding Quantitative Arterial Spin-labeling MR Imaging using Q2TIPS. Magn. Reson. Med. Sci. 2015;14:1–12 doi: 10.2463/mrms.2013-0064.

103. Delfaut EM, Beltran J, Johnson G, Rousseau J, Marchandise X, Cotten A. Fat Suppression in MR Imaging: Techniques and Pitfalls. RadioGraphics 1999;19:373–382 doi: 10.1148/radiographics.19.2.g99mr03373.

104. Boland M, Stirnberg R, Pracht ED, et al. Accelerated 3D-GRASE imaging improves quantitative multiple post labeling delay arterial spin labeling. Magn. Reson. Med. 2018;80:2475–2484 doi: 10.1002/mrm.27226.

105. Günther M. Arterial Spin Labeled Input Function (ASLIF): signal acquisition during pseudo-continuous arterial spin labeling. In: Proceedings of the 26th Annual Meeting of the International Society for Magnetic Resonance in Medicine. ; 2018. p. 305.

Acknowledgements

Working on this thesis was one of the most challenging, sometimes frustrating and at the same time fun things to do. This thesis gave me the opportunity to be creative in many fields and to combine my interests in programming and physics. In the following, I want to thank the great people who made the completion of this thesis possible.

First, I want to thank my supervisor Matthias Günther, who gave me the opportunity to do this PhD. It was always a pleasure to discuss novel ideas with you and you were really inspiring to me. Most important, you gave me the freedom to pursue my ideas, while guiding me the right direction in situations of frustration. During my time as a PhD student, I have undergone great personal development, and this would not have been possible without you as my supervisor. Thank you.

I also want to thank Oliver Speck for reading this thesis and taking part in my defense as the second referee.

A big thank you goes to Daniel Hoinkiss. You were a great discussion partner and I really profited from your deep knowledge in the field of motion correction. You were basically involved in all topics of this thesis, so I would not have come so far in comparable time without your help. Most important however, you also became a good friend, and I am looking forward to further work with you in the future.

I want to thank my friends David Krogmann and Philip Kerner. Your friendship was an important constant throughout my life since we left school, and you always supported me in good as well as frustrating times.

I thank Stefan Bokelmann for reading my thesis, but more important for being a great friend. You were a great support, especially during the last year, and I appreciate that.

Further thank goes to Henrik Asendorf, Kevin Sökel and Tuncer Kaya for being good friends for many years. Your company was always a well appreciated time out from stressful phases.

I also want to thank Amnah Mahroo, Mareike Buck and Nora Breutigam for the many fun MRI sessions and discussions we had together. I learned a lot from you, so many thanks!

A big thank you goes to the other members of the imaging physics group. The many discussions of abstracts and other valuable input helped to give this thesis the final shape. Special thank goes to Sven for being my mentor and helping me to find my way around.

I want to thank Marco Vicari. You supported me during my bachelor and master thesis, and I had many fruitful discussions with you. You were one of the reasons, I started writing this PhD thesis. Thank you!

Special thank goes to my parents and sister. You were a great support during this time, and you were always there, whenever I needed help or advice.

Finally, I want to thank you, Rebecca. You accompanied my long way and were always there for me, especially during the hard times. You never complained and were always understanding during stressful phases. You were my sanctuary and therefore contributed a lot to this thesis.